STUDIES OF METAL-ORGANIC POLYHEDRA: SYNTHESIS AND APPLICATIONS IN GAS STORAGE AND SEPARATION

A thesis presented to

The School of Physical Sciences

at

The University of Adelaide

in fulfilment of the requirements for

The Degree of

Doctor of Philosophy in Chemical Science

by

Jesse Teo

Adelaide, Australia

March 2017

DECLARATION

I certify that this work contains no material which has been accepted for the award of any other degree or diploma in my name, in any university or other tertiary institution and, to the best of my knowledge and belief, contains no material previously published or written by another person, except where due reference has been made in the text. In addition, I certify that no part of this work will, in the future, be used in a submission in my name, for any other degree or diploma in any university or other tertiary institution without the prior approval of the University of Adelaide and where applicable, any partner institution responsible for the joint-award of this degree.

I give consent to this copy of my thesis when deposited in the University Library, being made available for loan and photocopying, subject to the provisions of the Copyright Act 1968.

The author acknowledges that copyright of published works contained within this thesis resides with the copyright holder(s) of those works.

I also give permission for the digital version of my thesis to be made available on the web, via the University's digital research repository, the Library Search and also through web search engines, unless permission has been granted by the University to restrict access for a period of time.

Jesse Teo

ACKNOWLEDGEMENTS

First and foremost I would like to thank my supervisors, Prof. Chris Sumby and Prof. Christian Doonan for their constant support, guidance and advice while pushing me to achieve my best.

I would also like to give special thanks to Dr. Cam Coghlan for his teamwork, insight and friendship throughout much of my candidature.

To my past and present lab mates, Wit, Damien, Oli, Rosemary, Tash, Harley, Rob and James, thank you for the hours of advice, jokes and good times and for making the lab a pleasant place to be.

Thank you to my friends and colleagues in the Sumby/Doonan research group, Alex, Jack, Andrew, Michael, Pat, Kate and the inspirational Prof. Richard Keene who helped make this time so enjoyable.

Finally, thank you to my caring family and friends for their endless support in every possible way. I could never have made it this far without you.

Dedicated to Jwee Tai & Christina Teo

TABLE OF CONTENTS

ABBREVIATIONS

BET	Brunauer-Emmett-Teller
b^{m}*bdc*	5-*tert*-butyl *m*-benzene dicarboxylate
BSE	Back-scattered electron
CCS	Carbon capture and storage
COC	Covalent-organic cage
COF	Covalent-organic framework
CSD	Cambridge Structural Database
DEF	*N*,*N*-diethylformamide
DFT	Density functional theory
DMA	*N*,*N*-dimethylacetamide
DMF	*N*,*N*-dimethylformamide
DNA	Deoxyribonucleic acid
dobdc	2,5-dioxido-1,4-benzenedicarboxylate
DOE	Department of Energy
EDX	Energy-dispersive X-ray spectroscopy
EPA	Environmental Protection Agency
EtOAc	Ethyl acetate
h^{m}*bdc*	5-hydroxy *m*-benzene dicarboxylate
HOMO	Highest Occupied Molecular Orbital
hs	High spin
IPCC	Intergovernmental Panel on Climate Change
ls	Low spin
^{m}*bdc*	*m*-benzene dicarboxylate
MEA	Monoethanolamine
MeOH	Methanol
MOF	Metal-organic framework
MOP	Metal-organic polyhedron
NBS	*N*-Bromosuccinimide
OMIM	Organic molecule of intrinsic microporosity
PTFE	Polytetrafluroethane

PTMSP	Poly[1-(trimethylsilyl)-1-propyne]
$scCO_2$	Supercritical CO_2
SE	Secondary electron
SEM	Scanning electron microscopy
TBDMSCl	*tert*-butyldimethylsilyl chloride
TGA	Thermogravimetric analysis
THF	Tetrahydrofuran
VAZO-88	1,1′-Azo bis(cyclohexanecarbonitrile)
ZIF	Zeolitic imidazolate framework

ABSTRACT

Metal-organic polyhedra (MOPs) are a class of porous materials, comprised of metal ions and organic ligands, which form discrete cage-like structures. Possessing large internal void volumes, the physical and chemical properties of MOPs can be tuned by appropriate selection of the metal and organic building units. The work presented in this thesis investigates the application of MOPs to environmentally significant gas storage and separation.

The first chapter introduces MOPs as an emerging class of promising materials and discusses their historical development since the first examples of synthetic supramolecular structures. As microporous materials, MOPs demonstrate strong interactions with small molecules giving them promise as a medium for selective gas adsorption. These attributes are of interest in the areas of H_2 storage and the capture of CO_2. As such, Chapter 1 discusses the benefits and challenges of utilising porous materials in these areas.

Chapter 2 presents synthetic routes to MOPs containing both internal and external functionalisation by modifying both the metal nodes and the organic components which constitute the supramolecular structure. Presented herein are the first permanently porous examples of this class of materials to incorporate two different metal elements into a single paddlewheel unit in a controlled manner. These bimetallic MOPs demonstrate a strong binding affinity as well as an impressive volumetric capacity for H_2 gas furthering development of a suitable H_2 storage solution.

Chapter 3 explores the decoration of MOPs with various external functionality and the effect these motifs have on MOP packing in the crystalline matrix. The synthesis of several new organic pro-ligands and subsequent MOPs is also detailed within. A method of modelling single crystal X-ray diffraction data is described that provides insight into the interactions between MOP structures which are dominated by the chemistry of the MOP exteriors. The tendency of these large structural entities to reduce porosity is further studied using X-ray diffraction data and computational methods.

The work in Chapter 4 focuses on the use of MOPs in a composite system rather than as a singular material. By combining MOPs with a highly permeable polymer, poly[1-

(trimethylsilyl)-1-propyne] (PTMSP), a series of mixed matrix membranes are synthesised for application in separating N_2 and CO_2 gases, a challenge of global significance from both an environmental and economic perspective. The compatibility of these constituents is shown to have a significant impact on the physical properties as well as the gas separation performance of the resulting composites.

CHAPTER 1.

INTRODUCTION

Chapter 1. Introduction

1.1. Supramolecular Chemistry

The field of supramolecular chemistry has shown dramatic growth and increasing interest for decades.[1-5] While the term 'supramolecular chemistry' has gained widespread use since its use by Jean-Marie Lehn in the second half of the 20th century, the underlying principles of chemistry beyond covalent bonding have fascinated scientists for a hundred years. The pioneering work by Lehn, Cram and Pedersen, which was awarded the Nobel Prize in Chemistry in 1987, exemplifies the importance of molecular recognition in chemical systems.[6,7] Such recognition was shown to be a result of the secondary, weaker intermolecular forces, yet critical for biological function.

Supramolecular chemistry is the study of the interactions between molecules which are often governed by weaker forces such as hydrogen bonding, π-π stacking, electrostatic interactions, metal-ligand bonding, halogen bonding and Van der Waals forces.[8-14] As such, the roots of supramolecular chemistry can be traced back to the 19th century where the first postulations of intermolecular forces are found. Nobel laureate Herman Emil Fisher suggested that many biological systems might operate based on molecular recognition, inspiring many of the earliest host-guest chemistry investigations.[15]

It is now understood that intermolecular forces fulfil a myriad of crucial roles throughout the physical world. For example, the double helical structure of DNA is a result of hydrogen bonding between complimentary base pairs, and this supramolecular construction allows the duplication of each strand.[16] Host-guest interactions are pivotal in the function of many biological receptor systems, where molecular recognition is possible due to the physical conformation of the guest species.[17,18] The principles of supramolecular chemistry are by no means limited to biological systems however. The broad spectrum of supramolecular concepts also covers many areas of synthetic nanotechnology including molecular self-assembly, mechanical interlocking, host-guest complexation and the development of molecular machinery.[19-21]

One of the most powerful aspects of supramolecular synthesis lies in the relative simplicity with which complex structures can be designed. Careful consideration of the physical parameters of molecules allows them to be used as building blocks for higher order architectures, allowing design and tuning control over the resulting structure in an approach that is simple when compared to a complete atomistic design.[22-24] Control over the physical

and mechanical aspects at the molecular level gives a promising avenue for the development of new materials, which has driven the prolific growth seen in the field of supramolecular chemistry.[25,26]

Supramolecular chemistry is now being explored as a potential way to address many issues faced by the modern world.[27,28] Indeed, the promise provided by such materials is so significant that the 2016 Nobel Prize in Chemistry was awarded to Stoddart, Sauvage and Feringa for their work toward the development of molecular machinery. Interestingly, the possible scope of application is far greater than might be intuitively predicted, given that the field often focuses on weaker, non-covalent interactions. Materials which are designed on supramolecular principles may also have an impact on global scale issues such as climate change, energy production, agriculture and medicine.[29-34] As is addressed in this thesis, supramolecular materials have shown incredible potential for host-guest interactions with small molecules in a gas state, as the exceptional structural control can be used to capture, separate or store gas molecules.[35-37] To this end, the supramolecular structures described herein are designed for such interactions, pursuing suitable solutions to industrially relevant issues.

1.2. Coordination Polymers

One of the most intensively researched areas of supramolecular chemistry is that of coordination polymers, which feature a repeating pattern of metal ions and bridging ligands.[38] As metal-ligand bonding tends to be weaker than covalent bonding, coordination polymers are generally synthesised using a supramolecular approach in which the ligand and metal ions can be considered as building units for the supramolecular structure.[39] Synthesis of these materials is typically carried out by the reaction of a metal salt with a potential ligand under conditions that promote molecular self-assembly of the polymeric material.[40] This reaction methodology often leads to the synthesis of crystalline products, producing highly ordered materials that are suitable for structure determination by X-ray crystallographic analysis.[41]

The architecture of coordination polymers is often described in terms of structural dimensionality.[42,43] Not to be confused with physical dimensionality, the term describes the polymerisation of the structure which is derived from the ligand and coordination geometries. One of the most well-known examples of coordination polymers is MOF-5, which was first described by Yaghi and co-workers almost 20 years ago, consisting of zinc oxide metal clusters as octahedral nodes and linear terephthalate ligands.[44] The coordination geometry of

the metal nodes results in an architecture that extends linearly from each node in all three spatial dimensions and thus is described as a three dimensional coordination polymer (Figure 1). The rigid, well-defined framework structure of such materials has given rise to the term metal-organic framework (MOF), from which MOF-5 derives its name. Metal-ligand polymerisation however, does not necessarily form products of such high symmetry and polymerisation is often restricted to fewer dimensions.[45-48] Factors such as metal ion coordination number, molecular sterics, competing ligands and thermodynamic considerations have all been shown to influence the resulting topology of coordination polymers.[49] As such, coordination polymers can repeat in one or two dimensions to form chains or sheets respectively (Figure 1). In a crystalline state these structures usually facilitate intermolecular attraction between sheets or chains such as hydrogen bonding or π-π interactions.[50,51]

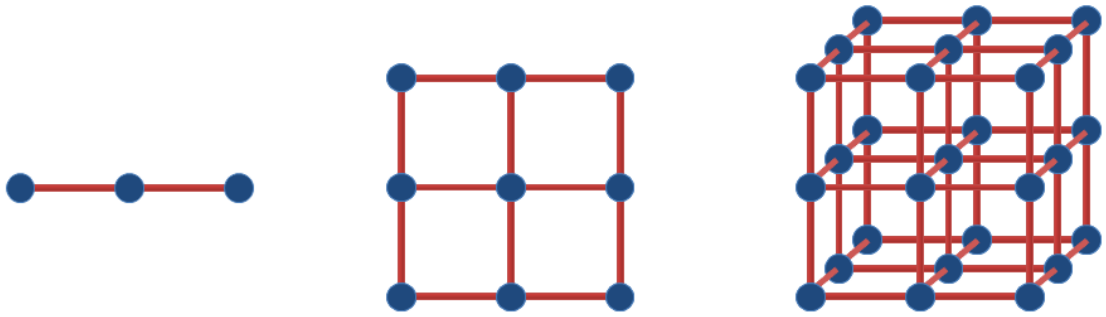

Figure 1. Schematic representation of 1-D, 2-D and 3-D polymerisation (left to right).

The nature of the required intermolecular forces that constitute framework dimensionality is somewhat inconsistent in the literature. For example, the $[M(H_2O)_6][M'(dipicolinate)_2]\cdot nH_2O$ (M/M′ = Zn/Ni or Ni/Ni) materials synthesised by Kirillova *et al*. are described as three-dimensional metal-organic frameworks constructed by means of hydrogen bonds.[52] Similarly, the hydrogen bonded organic framework, HOF-5, by Chen and associates is described by the authors as three-dimensional, in which the hydrogen bonding is included as formal structural bonding.[53] Conversely, other authors have refrained from including hydrogen bonding when describing framework dimensionality.[54] A noteworthy example of this is $[Cu_2F(HF)(HF_2)(pyz)_4][(SbF_6)_2]_n$ (*pyz* = pyrazine) which is

described by Li and associates as a two-dimensional framework in which 2-D $[Cu_2(pyz)_2]^{2+}$ layers are bridged by hydrogen bonds.[55] This two-dimensional specification is given despite the strong H-F···H bonding between layers being comparable to the strength of the systems coordination bonds. As such, the definition of structural dimensionality remains somewhat open to interpretation, being used to highlight significant structural information, rather than a definitive description of bonding within a structure.

The supramolecular approach to material design has allowed the synthesis of discrete entities in which the repeating metal-ligand bonding is limited through the use of constraining geometric properties, such as angular bridging ligands.[56] Unlike conventional coordination polymers, these resulting macromolecular structures show no indefinite bonding in any spatial dimension, often being referred to as 0-dimensional materials.[57-59] With the potential to rationally design their size and structure, these materials can be synthesised to have a specific atomic content and defined geometry on the nano-scale. Examples of such include two and three dimensional objects such as molecular squares, cubes and complex polyhedra (Figure 2).[60-65]

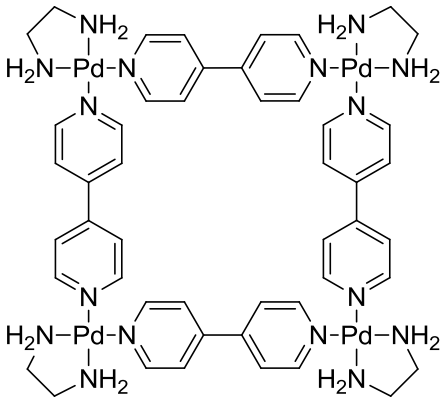

Figure 2. A two-dimensional supramolecular square.

1.3. Porous Materials

One of the most exploited properties of coordination polymers is their permanent porosity. Indeed, research into porous materials has grown rapidly over the last several decades. Historically, zeolites have found widespread use in industry with millions of tonnes of zeolitic material mined annually for commercial use.[66] These naturally occurring, inorganic, crystalline materials feature cavities as a result of the repeating atomic arrangement.[67] Synthetic aluminosilicate frameworks have also been created with varying

pore sizes, that demonstrate the diversity of synthetic porous materials.[68] More recently, MOFs and COFs (covalent-organic frameworks) have emerged as promising synthetic materials as they similarly have the potential to display porosity, differing from zeolites and each other in the nature of the building blocks that comprise the structure; metal-organic in the case of MOFs and purely organic in the case of COFs.

Porous materials possess several properties that make them commercially and industrially useful, particularly in the fields of efficient gas storage and selective gas separation.[69-72] The inherent porosity of these materials permits physical and chemical interactions that would otherwise be unfeasible on an industrial scale. Notably, highly porous materials can exhibit extremely high surface areas, with numerous examples of MOFs featuring surface areas in excess of 4000 m^2/g.[73,74] An extremely high surface area allows surface specific interactions to readily occur on a relatively small amount of porous substrate and thereby opens porous materials to a multitude of industrial applications.

Interactions of gas molecules with a surface have been extensively investigated, with literature showing that surface-gas adsorption is much greater than gas-gas attraction.[75-77] High surface area materials allow for the high density storage of gases, such as H_2, CO_2 or ethylene, at much lower pressure than conventional compression without the increased energy demands of cryogenic methods.[78-80] One factor relevant for any adsorbing material considered for gas storage is the gas binding affinity, which is known to be influenced by several factors in the matrix.[81,82] Pore size in particular is shown to be a relevant feature, showing optimal adsorption when pore diameter is similar to the size of the adsorbate.[83] This is due to the significant overlap of the attractive net forces from the pore walls as described by the Lennard-Jones potential:[84,85]

$$V(r) = 4\varepsilon\left[\left(\frac{\sigma}{r}\right)^{12} - \left(\frac{\sigma}{r}\right)^{6}\right]$$

Where V = the potential between the pore surface and the adsorbing molecule, ε = depth of the potential well, σ = Van der Waals radius, r = distance between surface and adsorbate.

The Lennard-Jones equation describes the interaction potential at the surface as a summation of the attractive and repulsive forces. At long (non-infinite) distances, the dominating contributions are Van der Waals forces, which pull the adsorbate to the surface. As the surface-adsorbate distance becomes smaller than the combined Van der Waals radii, repulsion due to forced electron orbital overlap becomes the dominant force. The potential results in an equilibrium adsorption site at a distance roughly equal to the combined Van der Waals radii. As both covalent and metal-organic frameworks feature tuneable architectures, their pore dimensions can be tailored to a specific storage or gas separation requirement, and it is this design element that gives them a conceptual advantage over naturally occurring materials.[86]

Design and synthesis of COFs is a relatively new field of research and as such is less established than the coordination polymer equivalents.[71] The absence of metallic constituents presents both challenges and benefits in the synthesis of suitable covalent framework materials. Unlike the metal-ligand interactions encountered in MOFs, covalent frameworks must be generated from less labile bonds, providing a significant synthetic obstacle.[87] Efforts to overcome this hurdle have employed the use of somewhat reversible covalent linkages such as boronate and hydrazone motifs, however the resulting materials generally show reduced crystallinity due to the relatively high occurrence of unresolved crystal defects.[71,88,89] As the building units involved in COFs innately lack metallic elements, the resultant materials have the benefit of being lightweight and theoretically much cheaper than MOF counterparts, two properties which are of vast importance for consideration of any potential material for industrial application.[90,91]

While the innate properties of porous materials makes them promising for gas storage and separations, functionalisation of the pore architecture can bring about dramatic improvements in capacity and selectivity of guest species.[92-97] Utilizing organic building units with accessible functionality has been shown to enhance the performance of porous materials and provides a direct pathway for the decoration of the pore surface with a multitude of useful functional groups including alkyl, ether and amine motifs, providing sites for chemical and physical interactions with guest molecules.[98-101] This methodology has been heavily employed in the functionalisation of MOFs. The framework backbone is often directed by the thermodynamic stability of chelating motifs, such as carboxylate groups, while the moieties intended for guest interaction exhibit a lower affinity for the metallic building unit, reducing

the presence of defects in the matrix and retaining availability of the functional groups to guest species.[37]

Metal-organic framework functionalisation can extend beyond the organic building unit. The rigidity of MOFs coupled with tuneable pore architectures allows the stabilisation of metal geometries that leave the metal node accessible to guest molecules.[69] The presence of coordinatively unsaturated metals in a MOF can dramatically increase the ability to separate or store gas molecules by providing sites of high substrate affinity and favourable kinetics.[102] MOF-74/CPO-27, which features a distinctive topology arising from the 2,5-dioxido-l,4-benzenedicarboxylate (*dobdc*) organic linker, exemplifies the potential for the inclusion of novel functionality in a porous material and since its first publication a decade ago has been the focus of much further research due to the promise displayed in the fields of gas separation and storage.[103]

To further enhance the activity of a porous material, functionality beyond that of the original building units can be added through the use of traditional chemical modification.[104] As the pores allow solvents and potential reactants to travel throughout the material, the post-synthetic addition of desired functionality can be performed, assuming the framework is stable and remains uncompromised. Literature examples of such post-synthetic modifications range from relatively simple deprotection of functional groups to more orchestrated covalent alterations that allow for further complexation of secondary metals in an existing framework.[105,106] Post-synthetic modification has also been exploited to suppress framework interpenetration or stabilise motifs that would otherwise decompose during framework synthesis.[107]

Despite the vast research into extended framework materials, the potential of their discrete counterparts remains relatively unexplored as the synthesis of discrete porous structures can be challenging when compared to analogous frameworks, particularly in the case of metal-organic cages. The solvothermal conditions that are commonly used to synthesise coordination polymers favour the formation of thermodynamically stable products which, in the case of metal ion and bridging ligand pairs, is often an extended framework.[108] While in solution, the formation of a dissolved discrete species is entropically favourable over an extended framework, however it is generally desirable to obtain the product of reaction as a crystalline solid. The process of crystallisation minimises the entropic contribution of dissolution, driving synthesis towards extended framework materials that exhibit extensive

cooperative bonding throughout the structure.[109] Polymerisation to form denser, extended framework materials therefore is the thermodynamically favourable product of the self-assembly process, following typical Ostwald-Volmer behaviour. In line with this relationship, the synthesis of discrete structures is frequently achieved as the kinetic product of a reaction, using relatively low temperatures and more dilute reaction conditions.[109-112] In addition to the thermodynamic aspects, geometrical considerations must be taken into account to synthesise a discrete porous assembly. Formation of an enclosed molecular structure requires that either a metal node or bridging ligand be of non-linear geometry, thus limiting the potential building block combinations that can be practically applied.[56]

1.4. Porosity in Discrete Nano-structures

Much of the interest in porous materials arises from their ability to interact with guest species, in particular gas phase molecules, due to their high surface areas.[113,114] In order to take advantage of this porosity a molecular solid must be structurally robust, such that the porous structure is maintained upon removal of solvent molecules; a property often referred to as permanent porosity.[115,116] In a 3-D framework the effect of cooperative bonding can enhance structural integrity, which in turn can maintain permanent porosity. In a discrete molecular structure however, this effect is reduced as cooperative bonding is limited.[109] While the literature shows many examples of discrete supramolecules with pores, the proportion of these that remain porous in the absence of supporting solvent molecules is significantly lower.[117-119]

A porous material composed of discrete structures contains two types of pore space; the intrinsic and extrinsic volumes.[120,121] The intrinsic pore space is that which is encompassed by the structure thus is likely to be conserved upon removal of solvent molecules, unless structural bonds are broken. The accessibility of this void space to guest bodies however is dependent on the presence of transport permitting windows or channels. The extrinsic space is that which is created between individual structures as a result of packing forces (Figure 3). In the absence of directing intermolecular forces, the extrinsic volume in these materials can be extremely challenging to predict.[121]

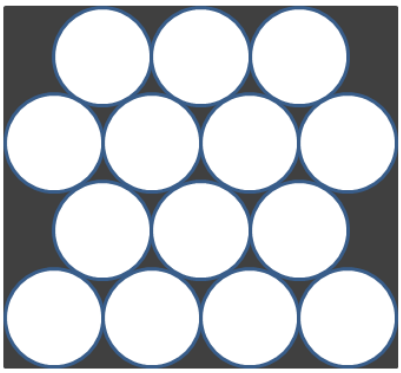

Figure 3. Schematic representation of intrinsic (white) and extrinsic (grey) space in packed circles.

Like extended framework materials, discrete porous structures are often categorised by the elemental constituents. Covalent organic cages (COCs) and metal-organic polyhedra (MOPs), like their extended framework counterparts, are constructed from organic or metal-ligand building units respectively.[122,123] As such, the potential advantages and weaknesses for the organic and metal-organic approaches are shared with those of COFs and MOFs. Interestingly, zeolites which are well established as an extended porous medium have a very limited number of discrete analogues due to the lack of well defined, angular building units. While particle size of such inorganic materials can be controlled to the nanometer scale, the synthetic methodologies are typically based on 'top-down' syntheses as opposed to a supramolecular 'bottom-up' approach.[124,125] As such, the atomistic structural control found in COCs and MOPs is generally unseen in an inorganic equivalent.

1.5. Development of Metal-Organic Polyhedra

Metal-organic polyhedra are an emerging class of materials that have been explored extensively for the last two decades.[126-128] Early reports of metal-organic supramolecules were largely fundamental research, aimed at increasing molecular complexity in rationally designed architectures. Such research is exemplified by the work of Fujita and associates showing self-assembly of multiple components into highly ordered, discrete structures that exhibit an engineered architecture.[129,130] While this work provided insight into the possibilities of nano-structural design, in addition to the inherently fascinating assemblies, small cavity sizes and instability limit the potential for any industrial application. These early structures generally used pyridine-type ligands, often coupled with transition metals such as platinum or

palladium, to form the structural backbone of the molecule.[131] As an unfortunate drawback, this often leads to structures that are not robust enough to withstand removal of solvent molecules, rendering them incapable of permanent porosity, excluding them from repeated host-guest interactions in the absence of solvent.

The term ‘metal-organic polyhedron’ was first used to describe the aptly named MOP-1 structure by Eddaoudi and associates (Figure 4).[126] Under suitable reaction conditions, the combination of copper ions and isophthalate ligands produces an Archimedean (truncated cuboctahedral) polyhedron with large pore windows on the square faces. Despite relative structural simplicity when compared to other multi-component supramolecular structures, MOP-1 features two highly desirable characteristics for host-guest interactions. Firstly the large size of the structure, pore cavity and pore windows of MOP-1 allow for interactions on both the external surface and interior of the structure. Secondly the combination of rigid linkers, carboxylate donors and copper paddle-wheel motifs provides for a structurally robust backbone, producing a permanently porous structure. This pairing of desirable properties has led to a vast increase in interest and development in MOP design and synthesis. In recent years, further research has allowed for control of the pore size and geometry, metal substitution and structuralisation of MOPs.[132-136] As is seen with MOFs, zeolites and other porous materials, the combination of permanent porosity and the ability to control pore size has made MOPs particularly interesting in the development of new materials for gas sorption and separation.

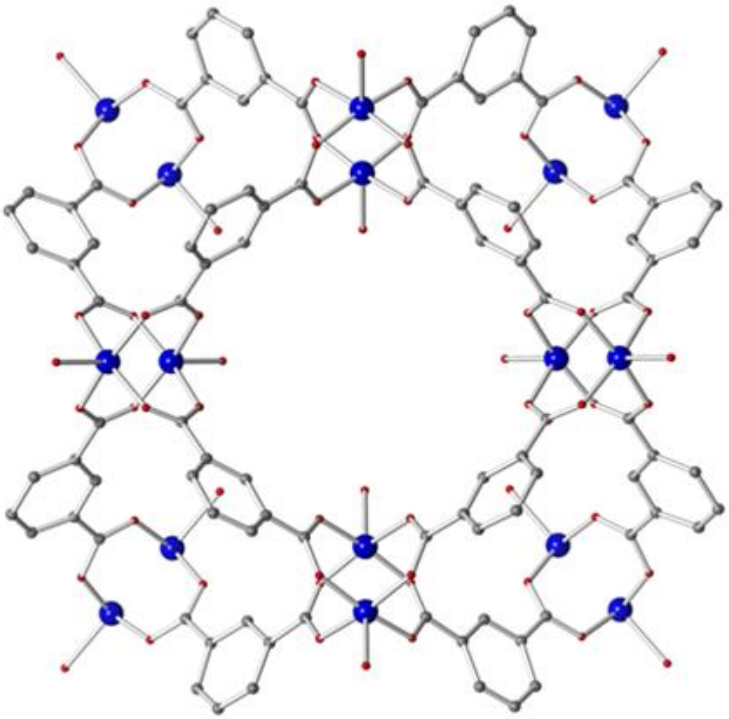

Figure 4. The structure of metal-organic polyhedron MOP-1. Hydrogen atoms are omitted and only the oxygen atoms of solvent molecules are shown for clarity.

1.5.1. Structural Diversification of MOP-1

Despite the relatively infantile stage of MOP research, literature shows a keen interest in the development of these materials. Since the publication of MOP-1, significant research has since been undertaken to modify and functionalise this archetypical structure. Most commonly, the organic bridging unit is the target of such modification and advantageously the effects of modification can often be predicted from the known MOP-1 structure. Two noteworthy examples of this are the structures produced by Furukawa *et al.*[137] and Tonigold *et al.*[138] which are isoreticular to MOP-1. Furukawa's structure, termed MOP-18, is synthesised by replacing the isophthalic acid reagent with one that contains an appended alkoxy chain in the 5-position. Upon formation of the MOP, these long chains are positioned on the exterior of the cage and confer increased solubility to the structure. This solubility was then exploited to disperse MOP-18 onto a graphite surface in a thin film which could then be analysed by scanning tunnelling microscopy, allowing the packing of individual polyhedra to be monitored. Using the same synthetic methodology, the MOP synthesised by Tonigold and associates features ethylene glycol groups on the MOP surface that confers additional solubility in polar solvents. Being both robust and soluble, these MOPs are shown to be

available for synthetic reaction with phenylisocyanate to generate urethane functionalised MOPs via post-synthetic modification.

When considering the geometric and coordination requirements of metal ions in a MOP, it is unsurprising that structural modification of the metal node is relatively rare for these structures. Synthesis of a di-molybdenum analogue has been successfully carried out by Ke *et al.* which interestingly features a quadruple bond between the molybdenum ions.[136] The instability of this material however presents a significant barrier to any real-world application. Recently, Young *et al.* published a method to synthesise di-ruthenium analogues of the MOP-1 structure.[139] Cyclic voltammetry measurements of these compounds show that reversible redox between the Ru_2^{4+} and Ru_2^{5+} oxidation states should be possible under mild conditions. Despite the known catalytic potential of ruthenium,[140-142] the authors make no report of catalytic activity. Similarly, no mentions are made as to whether the material is permanently porous, or whether the ruthenium ions are available for interaction with other entities.

1.6 Gas Storage and Separation Using Porous Materials

The gas adsorption properties of porous materials have resulted in a wide ranging field of potential applications. MOFs in particular have been explored extensively as a platform for storing fuel gases such as methane, as well as addressing traditionally challenging chemical separations such as olefin/paraffin mixtures.[143,144] Indeed, the possible applications of porous materials extend into exotic separations in highly specialised areas such as the separation of hydrogen from deuterium through the process of quantum sieving.[86] Two of the most significant and heavily researched areas of porous materials are that of carbon capture and hydrogen storage, as they pose significant challenges for modern society. As such, the difficulties of these fields are discussed in further detail in this section.

1.6.1 Carbon Capture and Sequestration

Anthropogenic greenhouse gas emission has been a focus of scientific research, environmental groups and government bodies for decades yet a solution continues to elude the global community. Since the dawn of the industrial revolution, the atmospheric concentration of CO_2 has increased alarmingly, with a pronounced increase of over 30% in the last few decades.[92] Ice core samples show that the normal atmospheric concentration of CO_2 has been between 180 and 300 ppm for more than half a million years, however in 2005 concentrations had risen to almost 380 ppm. The increase in atmospheric carbon dioxide shows a direct link to increases in anthropogenic sources with annual emissions rising from

approximately 23.5 to 26.4 Gt(CO_2) between the 1990's and early 2000's.[145] Without improvement over current carbon dioxide emission control or a reduction in global dependence on fossil fuels, atmospheric CO_2 concentrations will continue to increase.

The major concern surrounding CO_2 emission is the capability of CO_2 to act as a greenhouse gas and the inherent association with global climate change.[96] Carbon dioxide is the most significant anthropogenic greenhouse gas due in part to its long atmospheric life. In 2007 the Intergovernmental Panel on Climate Change (IPCC) estimated the global radiative forcing of CO_2 to be 1.66 W/m^2 which is almost equivalent to the overall calculated effect of all anthropogenic sources. The same report showed that the preceding fifty years exhibited an average temperature increase of 0.13 °C per year, nearly double that of the previous century.[145]

Global energy production is highly dependent on fossil fuels, with up to 85% of primary energy production arising from fossil fuel combustion, accounting for over 55% of all anthropogenic greenhouse gas emission.[146] Fossil fuel power generation facilities are one of the largest contributors to this production of CO_2 and as such, represent an ideal target for implementation of effective carbon sequestration methods.[86,94,147] While the capture of CO_2 from combustion has been in practice for many decades, current methodologies are inefficient and exhibit several drawbacks that result in an increased financial and energetic expense of power generation.[148] Current methods of carbon capture and storage (CCS) often employ solutions of aqueous amine scrubbers, such as monoethanolamine (MEA), to chemically remove the carbon dioxide from the post combustion flue stream and are able to capture up to 90% of CO_2. However the associated energy of the capture process, transport and storage of the CO_2 and subsequent regeneration of the absorbent can increase energy requirements by up to 40%.[149] The energy demanding approaches used in current CCS systems are believed to increase the cost of energy production by up to 70%.[148]

A second method to improve CCS is pre-combustion capture (Figure 5). While generally not useful for coal or oil based power generation facilities, pre-combustion methods are viewed as a viable approach for natural gas purification where CO_2 capture takes place at elevated pressures. Unlike post-combustion carbon capture which requires the separation of environmentally benign N_2 from CO_2, the removal of CO_2 from natural gas reserves concerns separation of CO_2 and CH_4, presenting a different set of challenges for any promising platform.

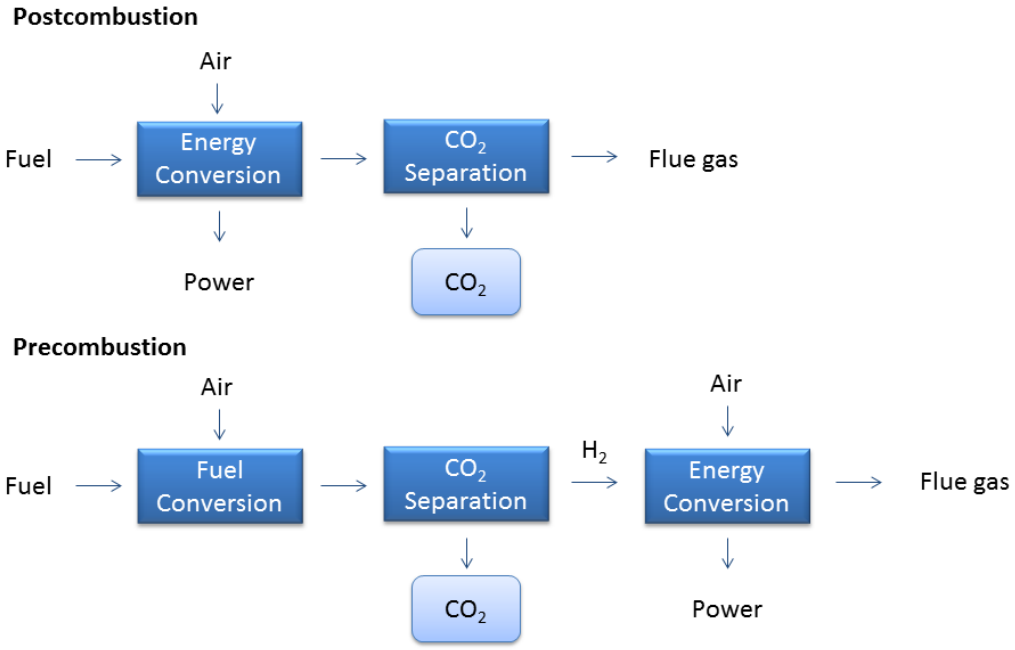

Figure 5. Post- and pre- combustion CO_2 capture processes.[150]

Porous materials are an attractive alternative to conventional separation techniques for CCS as they have the potential to address the significant cost associated with solution based absorption.[93] The large energetic cost of amine sorbent regeneration comes from the stability of the formed carbamate species (Figure 6), thus is an inherent problem of all systems based on this chemisorption methodology.[151,152] Porous materials however are able to bind CO_2 molecules with much weaker physisorptive interactions, avoiding the formation of highly stable carbamates thus reducing the cost of sorbent regeneration. Research in recent years has shown not only that porous materials can facilitate physisorptive processes, but also that the strength of the binding interaction can be tuned through control of the pore architecture.[36,92,147] As the pore structure of many synthetic frameworks can be organised at an atomic level, the gas-binding enthalpy can also be controlled to meet the needs of a given application.

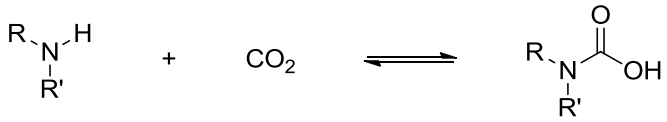

Figure 6. Amine facilitated capture of CO_2 to form carbamic acid.

The highly ordered structure of porous materials allows for an alternative approach to separating gaseous mixtures that is not based upon chemical interactions. A porous material with a well-defined pore structure may also separate guests based purely on physical and steric properties.[153,154] Despite the small difference in the kinetic diameters of CO_2 and other relevant gas molecules such as N_2 and CH_4, fine control of the pore architecture potentially allows for separation based on a molecular sieving approach thus an energetically expensive sorption-desorption cycle is not necessary.[155,156]

1.6.2 Materials Based Hydrogen Storage

With the growing need for clean energy sources, interest in the use of hydrogen as a fuel has gained significant momentum over the last few decades. As an alternative to petroleum products, hydrogen gas is particularly appealing for use in the transport sector which is one of the major global contributors of greenhouse gases. A recent study by the United States Environmental Protection Agency (EPA) found that approximately 27% of total greenhouse gas emission in the United States resulted from transportation, making it the second largest contributor of greenhouse gases behind primary energy production.[157] Under ideal conditions, the combustion of hydrogen however produces only energy and water resulting in an environmentally benign fuel system. As such, the replacement of petroleum fuels with cleanly burning hydrogen gas could have a dramatic impact on greenhouse gas emission.

In order to be a suitable petroleum fuel replacement, a fuel system needs to be both competitively lightweight and compact.[158] H_2 possesses the highest known energy per mass as a combustion fuel, with a gravimetric energy density of 120 MJ/kg. This value is two to three times greater than those for petroleum products, which generally contain 40 – 60 MJ/kg.[159] Despite the high energy density per molecule of H_2, the volumetric energy density is relatively low which presents one of the most significant challenges to the implementation of hydrogen fuel systems for transport applications. Unlike molecular energy density which is an intrinsic property of a fuel, the volumetric density is governed by the phase and compression

of the material. As petroleum products are generally liquids at room temperature and atmospheric pressure, they inherently have volumetric energy densities suitable for use in automotive applications.[158] Conversely, H_2 at atmospheric pressure is a gas at temperatures above 20K and in this state has an energy density that is unsuitable for use as a transport fuel. Even under high compression (700 bar) the volumetric energy density of H_2 is approximately 5 MJ/L and vastly outperformed by fuels such as gasoline (44 MJ/L).[159] Storage of hydrogen as a liquid increases the energy density to 8 MJ/L, however the low critical temperature of 33K means that the storage processes can be both expensive and potentially hazardous in a working environment due to factors such as oxygen condensation.

Material based storage of H_2 provides an alternative to physical based methods, drawing its distinction from the interactions that govern gas compression. In physical methods, the intermolecular interactions of H_2 determine the compression efficiency, giving rise to the low density (70 kg/m^3 for liquid H_2).[160] In a sorbent based material, hydrogen storage is based upon gas-sorbent interactions, thus the hydrogen binding interaction can be much stronger. Solid state chemical absorption of hydrogen as metal hydrides have shown particular success, reaching 150 kg H_2/m^3 in Mg_2FeH_6, however the high content of transition metals in such hydride materials often has a prohibitively negative effect on the gravimetric hydrogen density.[161]

The combination of organic and inorganic components used in coordination polymers makes them a promising candidate for hydrogen storage. MOF architectures can be constructed such that metal ions, either constituent or added post-synthesis, are accessible to guests within the pore space. The presence of available metal sites found in many of these materials provide strong binding sites for H_2 gas, increasing both the adsorption capacity and enthalpy, due to the polarizing effect that open metal sites have on adsorbing gas molecules and their ability to act as Lewis acids.[162-164] While this is also true for metal hydrides, the light-weight organic scaffold in coordination polymers is advantageous from a gravimetric perspective. The organic component not only facilitates transport to the metal sites, but can actively adsorb H_2 through guest-pore interactions. A prominent example of this is the M_2(*dobdc*) (*dobdc*$^{4-}$ = 2,5-dioxido-1,4-benzenedicarboxylate) family of MOFs in which the pore channels are lined with a high density of open metal sites including Mg, Mn, Fe, Co, Ni and Zn.[165] H_2 adsorption in these materials is accurately described by a dual-Langmuir function (described in further detail in Chapter 2) which demonstrates preferential gas adsorption at the metal sites and subsequently within the 1-D channels.

1.7. Thesis Coverage

This thesis presents the study of metal-organic polyhedra from the perspectives of design, synthesis, and characterisation with a specific focus on environmentally significant gas phase applications. Chapters 1 and 5 are introduction and conclusion chapters respectively. The first chapter has provided a developmental history of metal-organic polyhedra and background information on the applications they are targeted toward in this work, while the final chapter gives a brief conclusion and summary of the work presented in this thesis. Both of these aim to give an understanding of the overall direction of the presented work. As such, some of the key results and successes of the work are summarised in the conclusion and placed into context of their relative potential for application.

Chapter 2 presents a synthetic route to MOPs containing both internal and external functionalisation by modifying the metal nodes rather than organic component, which is conventionally targeted for modification. Described in the chapter is an isoreticular series of MOPs which feature Pd(II)/M(II) (M = Cu, Ni, Co, Zn) bimetallic paddle-wheel motifs. Due to its coordination requirements, the Pd(II) ion is selectively positioned on the inner surface of the cage while the corresponding divalent metal is located on the outer faces of the structure. The bimetallic MOPs that have been synthesised are the first permanently porous examples of this class of materials to incorporate two different metal elements into a single paddlewheel unit. These metal sites are available for interactions with guest molecules and show promising hydrogen adsorption characteristics. Additionally, this work shows that judicious choice of the bimetallic nodes can dramatically enhance the hydrogen binding properties over analogous materials by substituting only a single metal element and in doing so, expand the future possibilities of using MOPs for gas storage. Some of the results presented in Chapter 2 have been published in a peer-reviewed, international journal.[166]

Chapter 3 describes the synthesis of a series of $M_{24}L_{24}$ MOPs which feature surface decoration with structural motifs designed to influence the interactions between individual cages and the surrounding environment. The ligand of each MOP, to which the functional group is bound, is an isophthalate di-anion with the substituent in the 5 position. Investigation by single crystal X-ray diffraction shows that the series of resulting MOPs share a conserved structural core, but exhibit a range of packing arrangements due to the peripheral groups. The flexible nature of some of these side chains makes them fundamentally challenging to characterise by X-ray crystallography hence structural information is obtained using a combined crystallographic-computational modelling approach. The advantages and

limitations of this methodology are discussed with respect to the materials presented in the chapter, including rationalisation of the technique in the absence of conclusive crystallographic information.

Chapter 4 explores the use of polymer membranes doped with MOPs for the purpose of separating gaseous mixtures. MOPs, which are soluble in common laboratory solvents, are dissolved in a polymer casting solution to produce mixed matrix membranes in which the MOPs are dispersed throughout the supporting polymer matrix. Analysis of these membranes by electron microscopy investigates the impact that the surface functionality has upon MOP aggregation. The effectiveness of the resulting membranes was determined for the separation of CO_2 from N_2 to explore the potential of such materials in post-combustion carbon capture. In addition to promising separation properties, these MOP additives also show the ability to stabilise meta-stable polymer phases, potentially extending the operational life time of any resulting membrane system. Some of the results of this chapter have been published in an international, peer-reviewed journal.[167]

Appended to the thesis are copies of the published data from this work. Similarly, details of the crystal structure solutions can be found in .cif format on the accompanying data drive.

1.8. References

(1) Lehn, J.-M. *Science* **2002**, *295*, 2400.

(2) Lee, J. W.; Samal, S.; Selvapalam, N.; Kim, H.-J.; Kim, K. *Acc. Chem. Res.* **2003**, *36*, 621.

(3) Fyfe, M. C. T.; Stoddart, J. F. *Acc. Chem. Res.* **1997**, *30*, 393.

(4) Lehn, J.-M. *Chem. Soc. Rev.* **2007**, *36*, 151.

(5) Zeng, F.; Zimmerman, S. C. *Chem. Rev.* **1997**, *97*, 1681.

(6) Lehn, J.-M. *Angew. Chem., Int. Ed. Engl.* **1988**, *27*, 89.

(7) Lehn, J.-M. *Stud. Org. Chem.* **1983**, *13*, 163

(8) Metrangolo, P.; Meyer, F.; Pilati, T.; Resnati, G.; Terraneo, G. *Angew. Chem., Int. Ed.* **2008**, *47*, 6114.

(9) Slater, A. G.; Perdigão, L. M. A.; Beton, P. H.; Champness, N. R. *Acc. Chem. Res.* **2014**, *47*, 3417.

(10) Ye, B.-H.; Tong, M.-L.; Chen, X.-M. *Coord. Chem. Rev.* **2005**, *249*, 545.

(11) Schneider, H.-J. *Angew. Chem., Int. Ed.* **2009**, *48*, 3924.

(12) Holliday, B. J.; Mirkin, C. A. *Angew. Chem., Int. Ed.* **2001**, *40*, 2022.

(13) Stang, P. J.; Olenyuk, B. *Acc. Chem. Res.* **1997**, *30*, 502.

(14) Atwood, J. L.; Barbour, L. J.; Jerga, A. *Science* **2002**, *296*, 2367.

(15) Fischer, E. *Berichte der deutschen chemischen Gesellschaft* **1894**, *27*, 2985.

(16) Watson, J. D.; Crick, F. H. C. *Nature* **1953**, *171*, 737.

(17) Blondeau, P.; Segura, M.; Perez-Fernandez, R.; de Mendoza, J. *Chem. Soc. Rev.* **2007**, *36*, 198.

(18) Fish, R. H.; Jaouen, G. *Organometallics* **2003**, *22*, 2166.

(19) Kay, E. R.; Leigh, D. A.; Zerbetto, F. *Angew. Chem., Int. Ed.* **2007**, *46*, 72.

(20) Balzani, V.; Credi, A.; Raymo, F. M.; Stoddart, J. F. *Angew. Chem., Int. Ed.* **2000**, *39*, 3348.

(21) Li, F.; Clegg, J. K.; Lindoy, L. F.; Macquart, R. B.; Meehan, G. V. *Nat. Commun.* **2011**, *2*, 205.

(22) Leininger, S.; Olenyuk, B.; Stang, P. J. *Chem. Rev.* **2000**, *100*, 853.

(23) Korevaar, P. A.; George, S. J.; Markvoort, A. J.; Smulders, M. M. J.; Hilbers, P. A. J.; Schenning, A. P. H. J.; De Greef, T. F. A.; Meijer, E. W. *Nature* **2012**, *481*, 492.

(24) Schenning, A. P. H. J.; Elissen-Román, C.; Weener, J.-W.; Baars, M. W. P. L.; van der Gaast, S. J.; Meijer, E. W. *J. Am. Chem. Soc.* **1998**, *120*, 8199.

(25) Davis, J. T. *Angew. Chem., Int. Ed.* **2004**, *43*, 668.

(26) Uhlenheuer, D. A.; Petkau, K.; Brunsveld, L. *Chem. Soc. Rev.* **2010**, *39*, 2817.

(27) Geng, Y.; Ali, M. A.; Clulow, A. J.; Fan, S.; Burn, P. L.; Gentle, I. R.; Meredith, P.; Shaw, P. E. *Nat. Commun.* **2015**, *6*.

(28) Palacios, M. A.; Nishiyabu, R.; Marquez, M.; Anzenbacher, P. *J. Am. Chem. Soc.* **2007**, *129*, 7538.

(29) Li, Y.; Yang, R. T. *Langmuir* **2007**, *23*, 12937.

(30) Chen, B.; Xiang, S.; Qian, G. *Acc. Chem. Res.* **2010**, *43*, 1115.

(31) Morris, R. E.; Bu, X. *Nat. Chem.* **2010**, *2*, 353.

(32) Dias, E. M.; Petit, C. *J. Mater. Chem. A* **2015**, *3*, 22484.

(33) Zhao, D.; Tan, S.; Yuan, D.; Lu, W.; Rezenom, Y. H.; Jiang, H.; Wang, L.-Q.; Zhou, H.-C. *Adv. Mater.* **2011**, *23*, 90.

(34) Vallet-Regí, M.; Balas, F.; Arcos, D. *Angew. Chem., Int. Ed.* **2007**, *46*, 7548.

(35) Krishna, R.; van Baten, J. M. *Phys. Chem. Chem. Phys.* **2011**, *13*, 10593.

(36) Zhang, Z.; Yao, Z.-Z.; Xiang, S.; Chen, B. *Energy Environ. Sci.* **2014**, *7*, 2868.

(37) Morris, R. E.; Wheatley, P. S. *Angew. Chem., Int. Ed.* **2008**, *47*, 4966.

(38) Janiak, C. *Dalton Trans.* **2003**, 2781.

(39) Kitagawa, S.; Kitaura, R.; Noro, S.-i. *Angew. Chem., Int. Ed.* **2004**, *43*, 2334.

(40) Robin, A. Y.; Fromm, K. M. *Coord. Chem. Rev.* **2006**, *250*, 2127.

(41) Riddell, I. A.; Hristova, Y. R.; Clegg, J. K.; Wood, C. S.; Breiner, B.; Nitschke, J. R. *J. Am. Chem. Soc.* **2013**, *135*, 2723.

(42) Khlobystov, A. N.; Blake, A. J.; Champness, N. R.; Lemenovskii, D. A.; Majouga, A. G.; Zyk, N. V.; Schröder, M. *Coord. Chem. Rev.* **2001**, *222*, 155.

(43) Zaworotko, M. J. *Chem. Commun.* **2001**, 1.

(44) Li, H.; Eddaoudi, M.; Groy, T. L.; Yaghi, O. M. *J. Am. Chem. Soc.* **1998**, *120*, 8571.

(45) Kondo, A.; Noguchi, H.; Carlucci, L.; Proserpio, D. M.; Ciani, G.; Kajiro, H.; Ohba, T.; Kanoh, H.; Kaneko, K. *J. Am. Chem. Soc.* **2007**, *129*, 12362.

(46) Zhu, X.; Zhao, J.-W.; Li, B.-L.; Song, Y.; Zhang, Y.-M.; Zhang, Y. *Inorg. Chem.* **2010**, *49*, 1266.

(47) Wang, L.; Yang, M.; Shi, Z.; Chen, Y.; Feng, S. *J. Solid State Chem.* **2005**, *178*, 3359.

(48) Chen, C.-T.; Suslick, K. S. *Coord. Chem. Rev.* **1993**, *128*, 293.

(49) Smulders, M. M. J.; Riddell, I. A.; Browne, C.; Nitschke, J. R. *Chem. Soc. Rev.* **2013**, *42*, 1728.

(50) Zhao, M.; Wang, Y.; Ma, Q.; Huang, Y.; Zhang, X.; Ping, J.; Zhang, Z.; Lu, Q.; Yu, Y.; Xu, H.; Zhao, Y.; Zhang, H. *Adv. Mater.* **2015**, *27*, 7372.

(51) Chen, C.; Kang, B.; Su, C. *Aust. J. Chem.* **2006**, *59*, 3.

(52) Kirillova, M. V.; Kirillov, A. M.; Guedes da Silva, M. F. C.; Kopylovich, M. N.; Fraústo da Silva, J. J. R.; Pombeiro, A. J. L. *Inorg. Chim. Acta* **2008**, *361*, 1728.

(53) Wang, H.; Li, B.; Wu, H.; Hu, T.-L.; Yao, Z.; Zhou, W.; Xiang, S.; Chen, B. *J. Am. Chem. Soc.* **2015**, *137*, 9963.

(54) Eddaoudi, M.; Li, H. L.; Yaghi, O. M. *J. Am. Chem. Soc.* **2000**, *122*, 1391.

(55) Li, W.; Kiran, M. S. R. N.; Manson, J. L.; Schlueter, J. A.; Thirumurugan, A.; Ramamurty, U.; Cheetham, A. K. *Chem. Commun.* **2013**, *49*, 4471.

(56) Tranchemontagne, D. J.; Ni, Z.; O'Keeffe, M.; Yaghi, O. M. *Angew. Chem., Int. Ed.* **2008**, *47*, 5136.

(57) Yang, J.; Wu, B.; Zhuge, F.; Liang, J.; Jia, C.; Wang, Y.-Y.; Tang, N.; Yang, X.-J.; Shi, Q.-Z. *Cryst. Growth Des.* **2010**, *10*, 2331.

(58) Deng, Z.-P.; Huo, L.-H.; Qi, H.-L.; Zhu, L.-N.; Zhao, H.; Gao, S. *Cryst. Eng. Comm.* **2011**, *13*, 4218.

(59) Zhuang, W.; Zheng, X.; Li, L.; Liao, D.; Ma, H.; Jin, L. *Cryst. Eng. Comm.* **2007**, *9*, 653.

(60) Jaya Prakash, M.; Oh, M.; Liu, X.; Han, K. N.; Seong, G. H.; Lah, M. S. *Chem. Commun.* **2010**, *46*, 2049.

(61) Lee, S. J.; Lin, W. *J. Am. Chem. Soc.* **2002**, *124*, 4554.

(62) Kieltyka, R.; Englebienne, P.; Fakhoury, J.; Autexier, C.; Moitessier, N.; Sleiman, H. F. *J. Am. Chem. Soc.* **2008**, *130*, 10040.

(63) Sheikh, J. A.; Goswami, S.; Adhikary, A.; Konar, S. *Inorg. Chem.* **2013**, *52*, 4127.

(64) Argent, S. P.; Adams, H.; Harding, L. P.; Ward, M. D. *Dalton Trans.* **2006**, 542.

(65) Lu, Z.; Knobler, C. B.; Furukawa, H.; Wang, B.; Liu, G.; Yaghi, O. M. *J. Am. Chem. Soc.* **2009**, *131*, 12532.

(66) *Zeolites - USGS Mineral Commodity Summaries*; United States Geological Survey, **2011**.

(67) Seo, J. S.; Whang, D.; Lee, H.; Jun, S. I.; Oh, J.; Jeon, Y. J.; Kim, K. *Nature* **2000**, *404*, 982.

(68) Cheetham, A. K.; Férey, G.; Loiseau, T. *Angew. Chem., Int. Ed.* **1999**, *38*, 3268.

(69) Glover, T. G.; Peterson, G. W.; Schindler, B. J.; Britt, D.; Yaghi, O. *Chem. Eng. Sci.* **2011**, *66*, 163.

(70) Rosi, N. L.; Eckert, J.; Eddaoudi, M.; Vodak, D. T.; Kim, J.; O'Keeffe, M.; Yaghi, O. M. *Science* **2003**, *300*, 1127.

(71) Cote, A. P.; Benin, A. I.; Ockwig, N. W.; O'Keeffe, M.; Matzger, A. J.; Yaghi, O. M. *Science* **2005**, *310*, 1166.

(72) Zuttel, A. *Naturwissenschaften* **2004**, *91*, 157.

(73) Chae, H. K.; Siberio-Perez, D. Y.; Kim, J.; Go, Y.; Eddaoudi, M.; Matzger, A. J.; O'Keeffe, M.; Yaghi, O. M. *Nature* **2004**, *427*, 523.

(74) Koh, K.; Van Oosterhout, J. D.; Roy, S.; Wong-Foy, A. G.; Matzger, A. J. *Chem. Sci.* **2012**, *3*, 2429.

(75) Walton, K. S.; Snurr, R. Q. *J. Am. Chem. Soc.* **2007**, *129*, 8552.

(76) Skoulidas, A. I.; Sholl, D. S. *J. Phys. Chem. A* **2003**, *107*, 10132.

(77) Sing, K. *Colloids Surf. A* **2001**, *187–188*, 3.

(78) Yang, S.; Lin, X.; Lewis, W.; Suyetin, M.; Bichoutskaia, E.; Parker, J. E.; Tang, C. C.; Allan, D. R.; Rizkallah, P. J.; Hubberstey, P.; Champness, N. R.; Mark Thomas, K.; Blake, A. J.; Schröder, M. *Nat. Mat.* **2012**, *11*, 710.

(79) Rabbani, M. G.; El-Kaderi, H. M. *Chem. Mat.* **2012**, *24*, 1511.

(80) Xiang, Z.; Cao, D. *J. Mater. Chem. A* **2013**, *1*, 2691.

(81) Rowsell, J. L. C.; Yaghi, O. M. *J. Am. Chem. Soc.* **2006**, *128*, 1304.

(82) Rowsell, J. L. C.; Millward, A. R.; Park, K. S.; Yaghi, O. M. *J. Am. Chem. Soc.* **2004**, *126*, 5666.

(83) Chun, H.; Dybtsev, D. N.; Kim, H.; Kim, K. *Chem.- Eur. J.* **2005**, *11*, 3521.

(84) Yazaydın, A. Ö.; Snurr, R. Q.; Park, T.-H.; Koh, K.; Liu, J.; LeVan, M. D.; Benin, A. I.; Jakubczak, P.; Lanuza, M.; Galloway, D. B.; Low, J. J.; Willis, R. R. *J. Am. Chem. Soc.* **2009**, *131*, 18198.

(85) Babarao, R.; Hu, Z.; Jiang, J.; Chempath, S.; Sandler, S. I. *Langmuir* **2007**, *23*, 659.

(86) Li, J. R.; Kuppler, R. J.; Zhou, H. C. *Chem. Soc. Rev.* **2009**, *38*, 1477.

(87) Ding, S.-Y.; Wang, W. *Chem. Soc. Rev.* **2013**, *42*, 548.

(88) Uribe-Romo, F. J.; Doonan, C. J.; Furukawa, H.; Oisaki, K.; Yaghi, O. M. *J. Am. Chem. Soc.* **2011**, *133*, 11478.

(89) Wan, S.; Guo, J.; Kim, J.; Ihee, H.; Jiang, D. *Angew. Chem.* **2008**, *120*, 8958.

(90) Feng, X.; Ding, X.; Jiang, D. *Chem. Soc. Rev.* **2012**, *41*, 6010.

(91) Dawson, R.; Cooper, A. I.; Adams, D. J. *Prog. Polym. Sci.* **2012**, *37*, 530.

(92) Choi, S.; Drese, J. H.; Jones, C. W. *Chem. Sus. Chem.* **2009**, *2*, 796.

(93) D'Alessandro, D. M.; Smit, B.; Long, J. R. *Angew. Chem., Int. Ed.* **2010**, *49*, 6058.

(94) McDonald, T. M.; D'Alessandro, D. M.; Krishna, R.; Long, J. R. *Chem. Sci.* **2011**.

(95) Torrisi, A.; Bell, R. G.; Mellot-Draznieks, C. *Cryst. Growth Des.* **2010**, *10*, 2839.

(96) Yang, H.; Xu, Z.; Fan, M.; Gupta, R.; Slimane, R. B.; Bland, A. E.; Wright, I. *J. Environ. Sci.* **2008**, *20*, 14.

(97) Zheng, C.; Liu, D.; Yang, Q.; Zhong, C.; Mi, J. *Ind. Eng. Chem. Res.* **2009**, *48*, 10479.

(98) Eddaoudi, M.; Kim, J.; Rosi, N.; Vodak, D.; Wachter, J.; O'Keeffe, M.; Yaghi, O. M. *Science* **2002**, *295*, 469.

(99) Tanabe, K. K.; Wang, Z.; Cohen, S. M. *J. Am. Chem. Soc.* **2008**, *130*, 8508.

(100) Nguyen, J. G.; Cohen, S. M. *J. Am. Chem. Soc.* **2010**, *132*, 4560.

(101) Henke, S.; Schmid, R.; Grunwaldt, J.-D.; Fischer, R. A. *Chem.- Eur. J.* **2010**, *16*, 14296.

(102) Caskey, S. R.; Wong-Foy, A. G.; Matzger, A. J. *J. Am. Chem. Soc.* **2008**, *130*, 10870.

(103) Rosi, N. L.; Kim, J.; Eddaoudi, M.; Chen, B.; O'Keeffe, M.; Yaghi, O. M. *J. Am. Chem. Soc.* **2005**, *127*, 1504.

(104) Wang, Z.; Cohen, S. M. *J. Am. Chem. Soc.* **2007**, *129*, 12368.

(105) Deshpande, R. K.; Minnaar, J. L.; Telfer, S. G. *Angew. Chem., Int. Ed.* **2010**, *49*, 4598.

(106) Doonan, C. J.; Morris, W.; Furukawa, H.; Yaghi, O. M. *J. Am. Chem. Soc.* **2009**, *131*, 9492.

(107) Burrows, A. D.; Frost, C. G.; Mahon, M. F.; Richardson, C. *Chem. Commun.* **2009**, 4218.

(108) Furukawa, H.; Kim, J.; Ockwig, N. W.; O'Keeffe, M.; Yaghi, O. M. *J. Am. Chem. Soc.* **2008**, *130*, 11650.

(109) Tonigold, M.; Volkmer, D. *Inorg. Chim. Acta* **2010**, *363*, 4220.

(110) Li, J.-R.; Zhou, H.-C. *Nat. Chem.* **2010**, *2*, 893.

(111) Hamilton, T. D.; Papaefstathiou, G. S.; Friščić, T.; Bučar, D.-K. i.; MacGillivray, L. R. *J. Am. Chem. Soc.* **2008**, *130*, 14366.

(112) Larsen, R. W. *J. Am. Chem. Soc.* **2008**, *130*, 11246.

(113) Ma, J.; Ying, Y.; Yang, Q.; Ban, Y.; Huang, H.; Guo, X.; Xiao, Y.; Liu, D.; Li, Y.; Yang, W.; Zhong, C. *Chem. Commun.* **2015**, *51*, 4249.

(114) Augustyniak, A. W.; Fandzloch, M.; Domingo, M.; Lakomska, I.; Navarro, J. A. R. *Chem. Commun.* **2015**, *51*, 14724.

(115) Dybtsev, D. N.; Chun, H.; Yoon, S. H.; Kim, D.; Kim, K. *J. Am. Chem. Soc.* **2004**, *126*, 32.

(116) Dybtsev, D. N.; Nuzhdin, A. L.; Chun, H.; Bryliakov, K. P.; Talsi, E. P.; Fedin, V. P.; Kim, K. *Angew. Chem., Int. Ed.* **2006**, *45*, 916.

(117) Zhao, L.; Northrop, B. H.; Stang, P. J. *J. Am. Chem. Soc.* **2008**, *130*, 11886.

(118) Lee, J.; Ghosh, K.; Stang, P. J. *J. Am. Chem. Soc.* **2009**, *131*, 12028.

(119) Zheng, Y.-R.; Stang, P. J. *J. Am. Chem. Soc.* **2009**, *131*, 3487.

(120) Jiang, S.; Jones, J. T. A.; Hasell, T.; Blythe, C. E.; Adams, D. J.; Trewin, A.; Cooper, A. I. *Nat. Commun.* **2011**, *2*, 207.

(121) Pyzer-Knapp, E. O.; Thompson, H. P. G.; Schiffmann, F.; Jelfs, K. E.; Chong, S. Y.; Little, M. A.; Cooper, A. I.; Day, G. M. *Chem. Sci.* **2014**, *5*, 2235.

(122) Perry, J. J.; Kravtsov, V. C.; Zaworotko, M. J.; Larsen, R. W. *Cryst. Growth Des.* **2011**, *11*, 3183.

(123) Hasell, T.; Wu, X.; JonesJames, T. A.; Bacsa, J.; Steiner, A.; Mitra, T.; Trewin, A.; Adams, D. J.; Cooper, A. I. *Nat. Chem.* **2010**, *2*, 750.

(124) Rhodes, K. H.; Davis, S. A.; Caruso, F.; Zhang, B.; Mann, S. *Chem. Mat.* **2000**, *12*, 2832.

(125) Doussineau, T.; Smaïhi, M.; Mohr, G. J. *Adv. Funct. Mater.* **2009**, *19*, 117.

(126) Eddaoudi, M.; Kim, J.; Wachter, J. B.; Chae, H. K.; O'Keeffe, M.; Yaghi, O. M. *J. Am. Chem. Soc.* **2001**, *123*, 4368.

(127) Hamilton, T. D.; MacGillivray, L. R. *Cryst. Growth Des.* **2004**, *4*, 419.

(128) Alkordi, M. H.; Belof, J. L.; Rivera, E.; Wojtas, L.; Eddaoudi, M. *Chem. Sci.* **2011**, *2*, 1695.

(129) Fujita, M.; Yazaki, J.; Ogura, K. *J. Am. Chem. Soc.* **1990**, *112*, 5645.

(130) Fujita, M.; Sasaki, O.; Mitsuhashi, T.; Fujita, T.; Yazaki, J.; Yamaguchi, K.; Ogura, K. *Chem. Commun.* **1996**, 1535.

(131) Fujita, M.; Umemoto, K.; Yoshizawa, M.; Fujita, N.; Kusukawa, T.; Biradha, K. *Chem. Commun.* **2001**, 509.

(132) Park, J.; Hong, S.; Moon, D.; Park, M.; Lee, K.; Kang, S.; Zou, Y.; John, R. P.; Kim, G. H.; Lah, M. S. *Inorg. Chem.* **2007**, *46*, 10208.

(133) Li, J.-R.; Yu, J.; Lu, W.; Sun, L.-B.; Sculley, J.; Balbuena, P. B.; Zhou, H.-C. *Nat. Commun.* **2013**, *4*, 1538.

(134) Stoeck, U.; Senkovska, I.; Bon, V.; Krause, S.; Kaskel, S. *Chem. Commun.* **2015**, *51*, 1046.

(135) Han, Y.; Li, J.-R.; Xie, Y.; Guo, G. *Chem. Soc. Rev.* **2014**, *43*, 5952.

(136) Ke, Y.; Collins, D. J.; Zhou, H.-C. *Inorg. Chem.* **2005**, *44*, 4154.

(137) Furukawa, H.; Kim, J.; Plass, K. E.; Yaghi, O. M. *J. Am. Chem. Soc.* **2006**, *128*, 8398.

(138) Tonigold, M.; Hitzbleck, J.; Bahnmuller, S.; Langstein, G.; Volkmer, D. *Dalton Trans.* **2009**, *0*, 1363.

(139) Young, M. D.; Zhang, Q.; Zhou, H.-C. *Inorg. Chim. Acta* **2015**, *424*, 216.

(140) Duan, L.; Bozoglian, F.; Mandal, S.; Stewart, B.; Privalov, T.; Llobet, A.; Sun, L. *Nat. Chem.* **2012**, *4*, 418.

(141) Karvembu, R.; Prabhakaran, R.; Natarajan, K. *Coord. Chem. Rev.* **2005**, *249*, 911.

(142) Harvey, M. E.; Musaev, D. G.; Du Bois, J. *J. Am. Chem. Soc.* **2011**, *133*, 17207.

(143) Peng, Y.; Krungleviciute, V.; Eryazici, I.; Hupp, J. T.; Farha, O. K.; Yildirim, T. *J. Am. Chem. Soc.* **2013**, *135*, 11887.

(144) Böhme, U.; Barth, B.; Paula, C.; Kuhnt, A.; Schwieger, W.; Mundstock, A.; Caro, J.; Hartmann, M. *Langmuir* **2013**, *29*, 8592.

(145) IPCC *IPCC, 2007: Summary for Policymakers. In: Climate Change 2007: The Physical Science Basis*; Cambridge University Press: United Kingdom and New York, NY, USA, **2007**.

(146) IPCC *Special Report on Renewable Energy Sources and Climate Change Mitigation*; Cambridge University Press: United Kingdom and New York, NY, USA, **2011**.

(147) Sayari, A.; Belmabkhout, Y.; Serna-Guerrero, R. *Chem. Eng. J.* **2011**, *171*, 760.

(148) Haszeldine, R. S. *Science* **2009**, *325*, 1647.

(149) IPCC *IPCC Special Report on Carbon Dioxide Capture and Storage*; Cambridge University Press: Cambridge, UK, **2005**.

(150) Feron P. H. M., H. C. A. *Oil Gas Sci. Technol.* **2005**, *60*, 451.

(151) Rao, A. B.; Rubin, E. S. *Env. Sci. Technol.* **2002**, *36*, 4467.

(152) Desideri, U.; Paolucci, A. *Energy Conversion and Management* **1999**, *40*, 1899.

(153) Bux, H.; Liang, F.; Li, Y.; Cravillon, J.; Wiebcke, M.; Caro, J. *J. Am. Chem. Soc.* **2009**, *131*, 16000.

(154) Ma, S.; Sun, D.; Wang, X.-S.; Zhou, H.-C. *Angew. Chem., Int. Ed.* **2007**, *46*, 2458.

(155) An, J.; Geib, S. J.; Rosi, N. L. *J. Am. Chem. Soc.* **2010**, *132*, 38.

(156) Bastin, L.; Bárcia, P. S.; Hurtado, E. J.; Silva, J. A. C.; Rodrigues, A. E.; Chen, B. *J. Phys. Chem. C* **2008**, *112*, 1575.

(157) *Inventory of US Greenhouse Gas Emissions and Sinks: 1990-2013*; United States Environmental Protection Agency, **2015**.

(158) Schapbach, L.; Zuttel, A. *Nature* **2001**, *414*, 353.

(159) United States Department of Energy: Office of Energy Efficiency & Renewable Energy: http://energy.gov/eere/fuelcells/hydrogen-storage; last accessed 14/03/2016.

(160) NIST Chemistry WebBook, Thermophysical Properties of Fluid Systems: http://webbook.nist.gov; last accessed 01/05/2016.

(161) Didisheim, J. J.; Zolliker, P.; Yvon, K.; Fischer, P.; Schefer, J.; Gubelmann, M. *Inorg. Chem.* **1984**, *23*, 1953.

(162) Bordiga, S.; Regli, L.; Bonino, F.; Groppo, E.; Lamberti, C.; Xiao, B.; Wheatley, P. S.; Morris, R. E.; Zecchina, A. *Phys. Chem. Chem. Phys.* **2007**, *9*, 2676.

(163) Dincă, M.; Long, J. R. *J. Am. Chem. Soc.* **2007**, *129*, 11172.

(164) Dincă, M.; Long, J. R. *Angew. Chem., Int. Ed.* **2008**, *47*, 6766.

(165) Kapelewski, M. T.; Geier, S. J.; Hudson, M. R.; Stück, D.; Mason, J. A.; Nelson, J. N.; Xiao, D. J.; Hulvey, Z.; Gilmour, E.; FitzGerald, S. A.; Head-Gordon, M.; Brown, C. M.; Long, J. R. *J. Am. Chem. Soc.* **2014**, *136*, 12119.

(166) Teo, J. M.; Coghlan, C. J.; Evans, J. D.; Tsivion, E.; Head-Gordon, M.; Sumby, C. J.; Doonan, C. J. *Chem. Commun.* **2015**.

(167) Kitchin, M.; Teo, J.; Konstas, K.; Lau, C. H.; Sumby, C. J.; Thornton, A. W.; Doonan, C. J.; Hill, M. R. *J. Mater. Chem. A* **2015** , 3 ,15241.

CHAPTER 2.

HETERO-BIMETALLIC METAL-ORGANIC POLYHEDRA

Part of this work appears in the following publication:

Hetero-bimetallic Metal-Organic Polyhedra.[1]

Chapter 2. Hetero-bimetallic Metal-Organic Polyhedra

2.1. Introduction

One of the key properties of coordination polymers is the potential for design of the pore and surface architectures.[2-5] The structure of a supramolecular entity can often be predicted through the use of known structural components, allowing these porous materials to be designed and tuned for a specific purpose.[6,7] Commonly, the structure of a coordination polymer is designed through consideration of the relevant metal ion and ligand geometries.[4,8] While ab initio structural prediction can be extremely challenging, the literature provides a vast library of known structures that can be used as a guide for structural design. Based on known architectures and through consideration of the geometric angles of the organic links, useful structural predictions can be made using a reticular approach. Generally, these types of syntheses use metal salt starting materials which dissociate in solution to afford the required solvated metal ions.[9] These solvated metal ions subsequently form the metal nodes of the coordination polymer, frequently adapting the coordination environments and structural geometries that are commonplace in molecular inorganic species such the thermodynamically stable Cu(II) 'paddlewheel' unit.[10-12] Solvothermal or hydrothermal methods are almost exclusively employed as the final synthetic step in the formation of coordination polymers, as this has several beneficial characteristics.[13,14] Firstly, the synthesis of highly ordered crystalline materials is aided by the high temperatures, pressures and reaction times allowing for the correction of irregularities during the self-assembly process. Secondly, these conditions drive the reaction system towards the most thermodynamically stable product, which can add a degree of structural predictability through rational design.[15] Reaction conditions that favour thermodynamic products however can prevent the inclusion of meta-stable motifs, limiting the potential diversity and complexity of the structure. Upon consideration of the fact that discrete structures are thermodynamically less favourable than extended frameworks, in combination with the propensity to form structurally simple products, it can be concluded that the use of solvothermal or hydrothermal approaches is often not ideal for synthesizing structurally complex MOPs.[16]

The work presented in this chapter focuses on the use of pre-organised bimetallic nodes and subsequent synthesis of metal-organic polyhedra that feature internal palladium ions and accessible first row metal ions decorating the external surface. While the development of novel metal nodes acts as a platform for further research into coordination chemistry, the resulting generation of open metal sites is significant. As mentioned previously

(see section 1.6.2), accessible metal sites are highly desirable for their gas sorption properties, which are of key interest in this work.

2.1.1. Preorganisation of Metal Nodes

The synthesis of materials with increasingly complex structures has been explored extensively in recent literature.[17-19] While the pursuit of molecular complexity is fundamentally interesting, the driving force behind this research is the potential applications that become available with access to new pore architectures and surfaces.[17,20,21] The inclusion of functionality in porous materials has historically been added through reticulation of existing materials, an approach that has been highly successful and is exemplified by the prominent work of Yaghi and co-workers.[4,13,22] Interestingly, organic ligands are almost exclusively used as the platform for introduction of functionality.[23] This is not surprising as organic synthesis provides an exceptional toolset for supramolecular chemistry, in which structures can be designed to mimic and facilitate known interactions.[24] Sites of activity have been introduced using a plethora of methods including post synthetic covalent modification of ligands themselves, or coordination of an active moiety to exposed metal centres.[25,26]

In order to expand the design possibilities of metal-organic polyhedra, this work explores modification of the metal node as an alternative avenue for controlling MOP pore surface chemistry. Despite investigation by researchers such as Ke *et al.* most examples to date have focussed on simple inorganic building units containing one metal as a node.[27] However, using well-established methods, metal clusters can be isolated with interesting and useful coordination environments in the form of discrete complexes, which may in turn contain combinations of metal ions in specific geometric and electronic configurations that are unseen in coordination polymers or MOPs. Careful selection of both the metal complex and reaction conditions can allow the inclusion of these meta-stable building units, which would normally not be found as the product of solvothermal conditions, into porous molecular materials. As dissociation of the bimetallic unit must be avoided, synthesis conditions must be mild in comparison to commonly used solvothermal techniques.[28] While the prototypical MOP-1 was synthesised in a *N*,*N*-dimethylformamide (DMF)/EtOH mixture at 80°C in a pressurised reaction vessel, the synthetic methods described herein are at ambient temperature and pressure.[29]

This approach also avoids the potentially chaotic metal distributions obtained by metal ion exchange methods.[30-32] A previous study by Yao *et al.* has shown di-copper paddlewheels

are susceptible to cation exchange when exposed to solutions of chemically similar transition metals such as cobalt, nickel and zinc, however the extent of these exchanges are unpredictable and tend to result in the disordered occupation of metal sites within the material.[28] As a second consideration, metal exchange methods can take several months to reach the desired elemental content. By using a preformed metal node, the well-defined distribution of metals can be achieved rapidly in a more controlled manner.

2.1.2. Palladium-3d Transition Metal Paddle-wheel Acetates

Bimetallic paddle-wheel acetates represent convenient starting materials for creating new metal-organic materials due to the predefined metal arrangement. Previous work by Zhou *et al*. exploited the ligand exchange process as a route to accessing new metal-organic polyhedra structures.[23] Through the process of ligand exchange, the bimetallic species can be used as building units in which the metal geometries and configurations are preserved in the resulting supramolecule. As mentioned previously, the Cu(II) binuclear paddle-wheel building block is widespread throughout supramolecular chemistry.[16,33] These paddle-wheel motifs exhibit a plane of symmetry, defined by the carboxylate carbon atoms (Figure 7). The work described herein uses paddle-wheel acetates in which a single Pd(II) ion is combined with either a Co(II), Ni(II), Cu(II) or Zn(II) ion to produce an asymmetric paddle-wheel unit that does not have this symmetry element. The asymmetry of these acetates is subsequently exploited to selectively position the different metal ions in the resulting MOPs. Synthesis of the hetero-bimetallic acetates in this work was performed using the methods described by Moiseev *et al*. to produce crystalline samples of $PdM(\mu\text{-}OOCMe)_4(OH_2)(HOOCMe)_2$ (M = Co (**2.1**), M = Ni (**2.2**), M = Zn (**2.3**) and M = Cu (**2.4**)).[34]

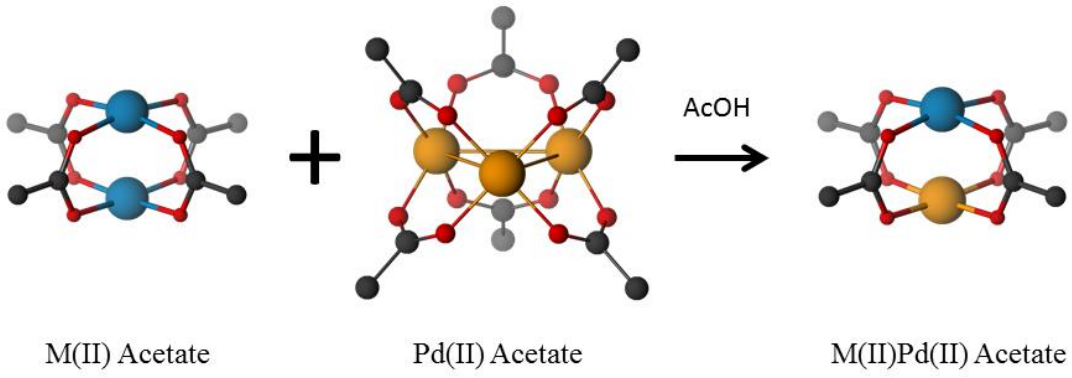

Figure 7. Reaction schematic for the synthesis of asymmetric hetero-bimetallic acetates **2.1 - 2.4.**

2.2. Synthesis of Hetero-bimetallic Metal-Organic Polyhedra

Synthesis of the hetero-bimetallic MOPs (**2.5** - **2.14**) was carried out using methods adapted from the work of Zhou and co-workers to facilitate ligand exchange processes in MOPs.[23] As such, the reagents were dissolved in amide solvents and allowed to react at room temperature for several days until large prism-shaped crystals were formed. *N*,*N*-Dimethylacetamide (DMA) was used in all cases as this was found to yield large, regular-shaped single crystals. Reactions were attempted with similar solvents such as DMF and *N*,*N*-diethylformamide (DEF), however in these cases the products were very small particles that appeared to be non-crystalline by visual inspection, and expectedly yielded no X-ray diffraction pattern amenable to structure determination.

Precautions were necessary to prevent exposure of the reaction mixture to oxygen and atmospheric moisture as this was found to have a negative impact on formation of the desired products, instead resulting in decomposition of the material. The direct use of DMA from commercial suppliers resulted in the formation of non-crystalline solids that could not be characterised. As such, all DMA used in the synthesis was distilled from CaH_2 under argon directly onto 4 Å molecular sieves and stored under argon. The MOP synthesis reactions were carried out in glass vials and purged with argon after mixing to minimise atmospheric exposure. This sensitivity to oxygen is not observed in syntheses to form the analogous di-copper MOPs, indicating that the palladium ion is the likely site of oxidative degradation.[29] Interestingly the synthesis conditions for the bimetallic MOPs seemed to be consistent, regardless of the organic unit involved, providing a general synthetic method for producing the bimetallic MOPs.

2.3. Structure and Composition of Hetero-bimetallic Metal-Organic Polyhedra

The structure of 10 hetero-bimetallic MOPs was determined by X-ray crystallography. All of the characterised compounds form an isostructural series in which all members consist of 12 paddle-wheel units connected by 24 isophthalate bridges to produce a cuboctahedral structure (Figure 8). The large unit cells of over 23000 $Å^3$ are characteristic of MOPs that share this topology.[29] Each polyhedron features an internal void space of approximately 15 Å diameter, accessible by six square and eight triangular pore windows of 9 Å and 5 Å respectively. In order to more accurately describe the metal distribution throughout the material, each sample was also subjected to analysis by EDX to measure the relative

concentrations of the metallic elements. This was found to indicate a 1:1 atomic ratio of palladium to the first row metal in all cases, with the exception of the Cu-Pd MOP (**2.14**) which is discussed in further detail in 2.3.2.1.

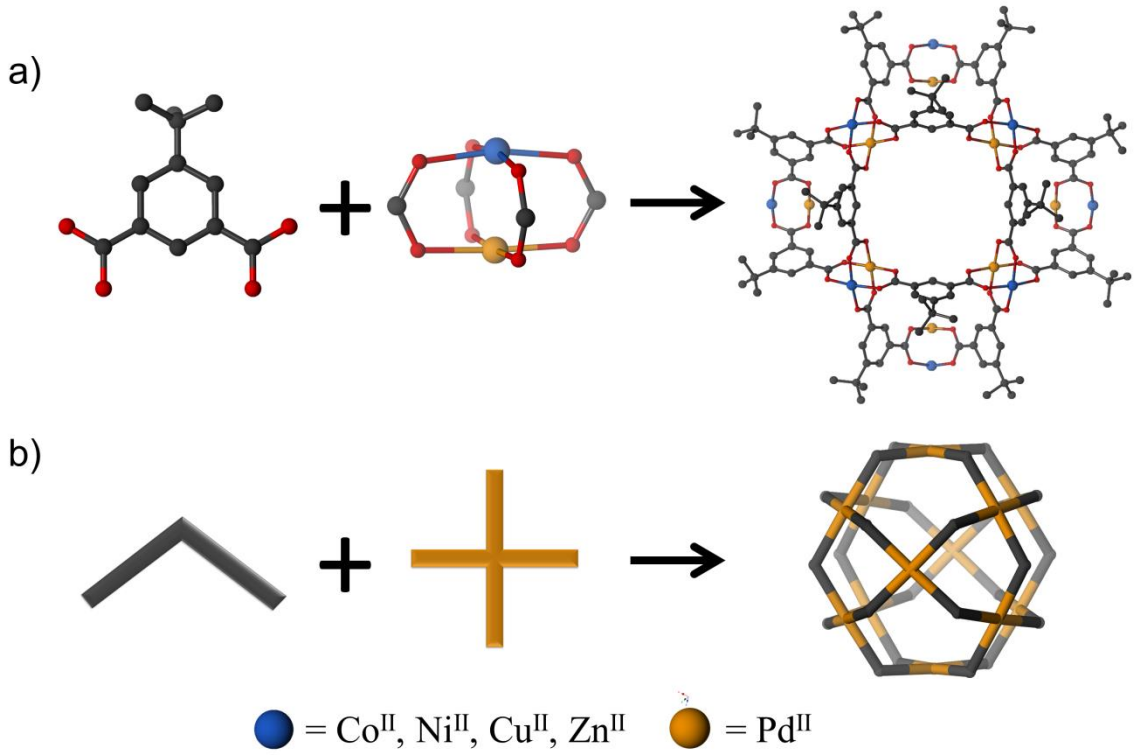

Figure 8. Structural (a) and schematic (b) representations of cuboctahedral bimetallic MOPs containing 12 heteronuclear paddlewheel nodes. Pd(II) sites are preferentially positioned within the void cavity, while a divalent first row metal occupies the external sites.

As the metal positions and occupancies were of significant interest, a consistent approach to determine these parameters was developed and applied across the series of bimetallic structures. Each endo- and exohedral metal site was refined in two parts, with each part assigned to either palladium or the relevant first row metal. Each bimetallic node in the asymmetric unit had to be refined individually to establish the orientation and the relative occupancy of the site, i.e. an exo- or endohedrally positioned palladium(II). After trial refinement of an individual node, the occupancy factors for each metal site were fixed and the new parameters used as a reference for trial refinement of the second metal node in the asymmetric unit. This process was repeated until the identity, position and occupancy of all metal nodes was established. Importantly, the position and site occupancy factors (including at minimum the O atom of the coordinated solvent molecules) were refined prior to removal of unassigned electron density by SQUEEZE software. In determining the node orientation

and metal occupancies it has been established that this series of hetero-bimetallic structures show preferential endohedral positioning of the palladium ion, while the relevant first row transition metal preferentially occupies the external site in the paddle-wheel nodes. It is worth noting that as the asymmetric units described in this chapter each contains a half-occupied (on a plane of symmetry) and fully-occupied bimetallic pair, the refined occupancy value for the metal ions can be more accurately determined using the fully-occupied site. This is due to the error associated with the electron densities, which is lower for the fully-occupied metal atoms than for those with symmetry generated electron density.

Analysis of the X-ray diffraction data reveals the presence of solvent molecules situated at the axial sites of the paddle-wheels. This was confirmed by acid digestion of the MOPs with DCl/*d6*-DMSO followed by ^{1}H NMR spectroscopy. After the removal of excess solvent, first by pipette then under vacuum, integration of the relevant NMR resonances combined with the crystal diffraction data determined that each bimetallic MOP contains 12 bound DMA molecules prior to activation, with the solvent molecule coordinated to the first row metal ion.

2.3.1. Structure of Isophthalate Bimetallic MOPs

The reaction of the hetero-bimetallic acetates (**2.1**, **2.2** and **2.3**) with *m*-benzene dicarboxylic acid ($H_2{}^{m}bdc$) in DMA resulted in the formation of three different bimetallic MOPs; $Co_{12}Pd_{12}(^{m}bdc)_{24}(C_4H_9NO)_{12}$ (**2.5**), $Ni_{12}Pd_{12}(^{m}bdc)_{24}(C_4H_9NO)_{12}$ (**2.6**) and $Zn_{12}Pd_{12}(^{m}bdc)_{24}(C_4H_9NO)_{12}$ (**2.7**) respectively. These materials crystallise in the tetragonal space group *P*4/*mnc*, with two bimetallic nodes and three ^{m}bdc ligands in the asymmetric unit (Appendix, Figures 35 – 37). Within this unit, one of these pairs of metal ions is located on a plane of symmetry with a site occupancy factor of 0.5. Trial refinement established that the internal metal site occupancy for palladium is approximately 75%, with the respective first row metal making up the remaining 25% of the internally directed metal site. The isophthalate ligands bridge between the metal nodes at an angle of 120(1)° and undergo dihedral rotations of 4(2)°, as measured across the carboxylate oxygen pairs, to compensate for the strain induced by the MOP. Individual polyhedra pack efficiently with no significant hydrogen bonding or π-stacking contributions. While many pore windows are obscured by adjacent cages, the internal void space remains accessible through the larger square apertures when viewed down the *c* axis. Accessible inter-polyhedral void space can be seen when viewed along both *b* and *c* axes (Figure 9).

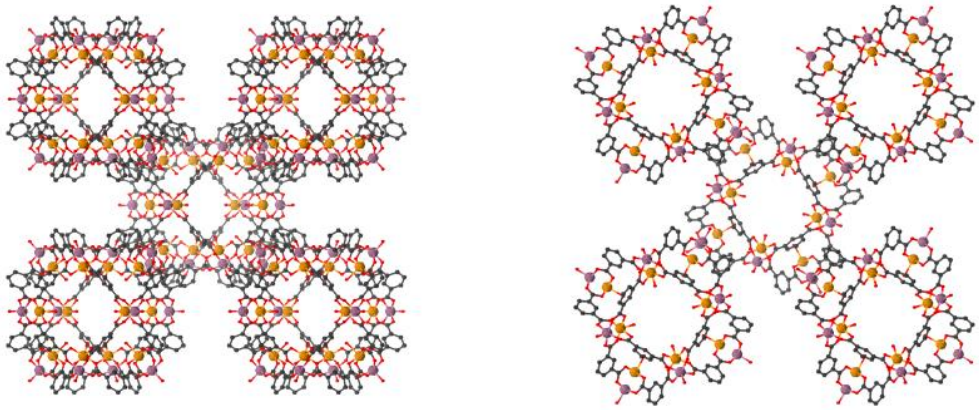

Figure 9. Crystal packing of $M_{12}Pd_{12}$-*m*-*bdc* polyhedra when viewed along the *b* (left) and *c* (right) crystallographic axes.

Analysis of the bond angles in structures **2.5**, **2.6** and **2.7** reveals that the Pd(II) coordination environment is close to an ideal square-planar geometry in the endo-Pd orientation in all cases. When in an endohedral position, first row metals also favour a planar arrangement with the carboxylate oxygens, as shown by the corresponding angles shifting towards 180° (Table 1).

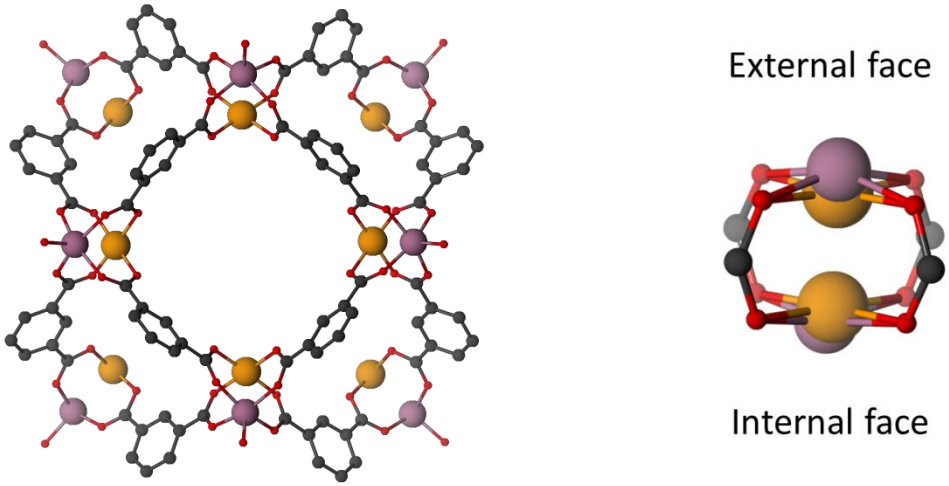

Figure 10. (Left) A perspective view of **2.5**. Metals with a site occupancy factor below 0.5 and hydrogen atoms are omitted for clarity. Only the oxygen atom of coordinating DMA molecules is shown. (Right) Overlay image of endo-Pd and exo-Pd paddlewheel node. Co and Pd atoms are coloured in mauve and orange respectively.

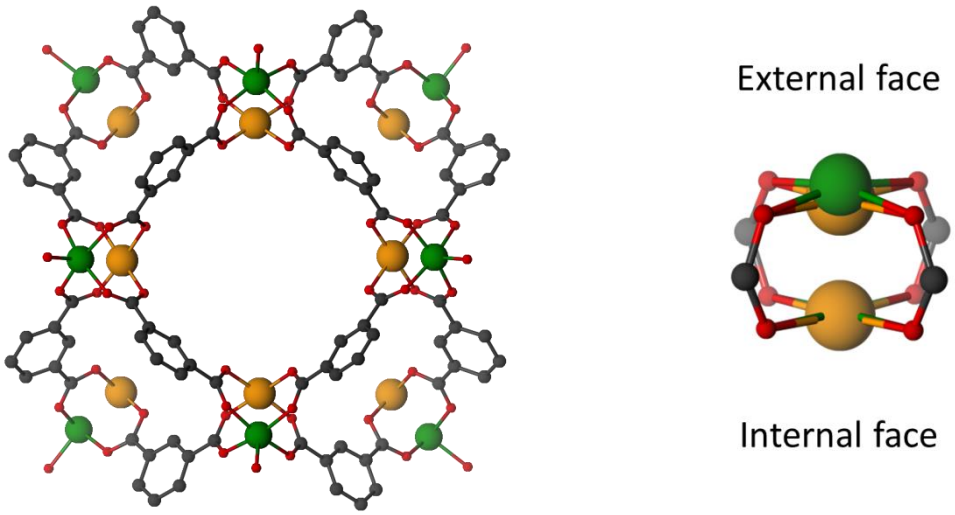

Figure 5. (Left) A perspective view of **2.6**. Metals with a site occupancy factor below 0.5 and hydrogen atoms are omitted for clarity. Only the oxygen atom of coordinating DMA molecules is shown. (Right) Overlay image of endo-Pd and exo-Pd paddlewheel node. Ni and Pd atoms are coloured in green and orange respectively.

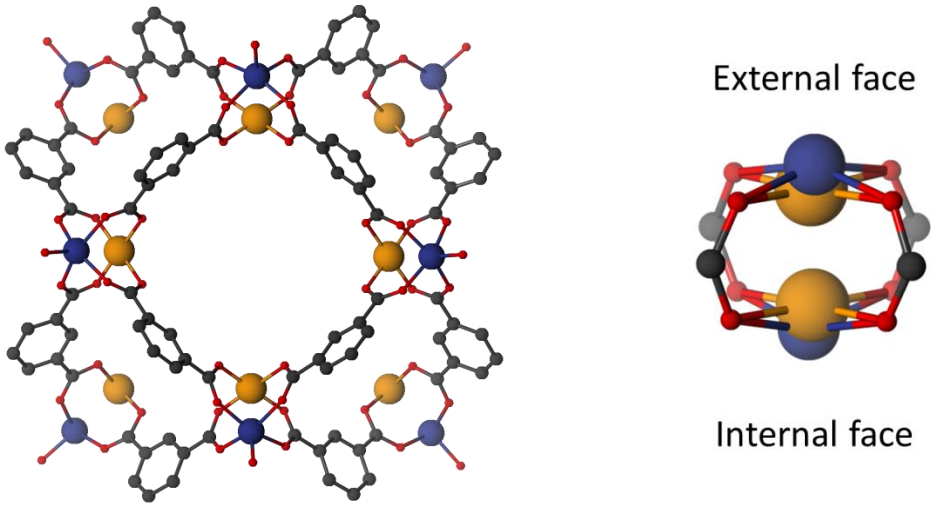

Figure 6. (Left) A perspective view of **2.7**. Metals with a site occupancy factor below 0.5 and hydrogen atoms are omitted for clarity. Only the oxygen atom of coordinating DMA molecules is shown. (Right) Overlay image of endo-Pd and exo-Pd paddlewheel node. Zn and Pd atoms are coloured in blue and orange respectively.

Table 1. Metal node bond lengths and angles for ^{m}bdc polyhedra.

	Structure	O-M-O (°)	O-Pd-O (°)	M-O (Å)	Pd-O (Å)
Endo-Pd Orientation	**2.5**	158(1)	178(1)	2.05(2)	2.00(2)
	2.6	166(3)	177(1)	2.05(3)	1.99(2)
	2.7	156(1)	178(1)	2.07(2)	2.01(1)
Exo-Pd Orientation	**2.5**	166(2)	176(1)	2.03(13)	2.01(3)
	2.6	169(1)	175(3)	2.01(20)	1.99(9)
	2.7	156(3)	177(2)	2.01(4)	2.01(3)

2.3.2. Structure of 5-t-Butyl Isophthalate Bimetallic MOPs

5-*t*-Butyl *m*-benzene dicarboxylic acid ($H_2b^{m}bdc$) was reacted with **2.1**, **2.2** and **2.3** to yield prism shaped crystals of $Co_{12}Pd_{12}(b^{m}bdc)_{24}(C_4H_9NO)_{12}$ (**2.8**), $Ni_{12}Pd_{12}(b^{m}bdc)_{24}(C_4H_9NO)_{12}$ (**2.9**) and $Zn_{12}Pd_{12}(b^{m}bdc)_{24}(C_4H_9NO)_{12}$ (**2.10**)**,** respectively. These crystallise in the tetragonal space group *I*4/*m*, in which each polyhedron has 12 hydrophobic *t*-butyl groups decorating the periphery. The asymmetric units consist of three *t*-butyl isophthalate bridging ligands that show significant thermal motion orthogonal to the plane of the aromatic rings. Precise structural refinement of these *t*-butyl groups was difficult due to the combined thermal and rotational motion of these motifs which, in all cases, was restrained using AFIX and DFIX commands. Additionally, the structures of **2.8** and **2.10** contain butyl groups that were solved over two positions to account for more diffuse electron density.

One of the two bimetallic nodes in each asymmetric unit sits on a mirror plane with a site occupancy factor of 0.5. Unrestricted refinement of the metal sites indicates an endohedral occupancy of palladium of approximately 75% for all three structures presented below. The zinc-palladium MOP (**2.10**) structure displays a slight discrepancy between the overall metal content and the EDX data, however this difference is likely due to the quality of the diffraction data obtained.

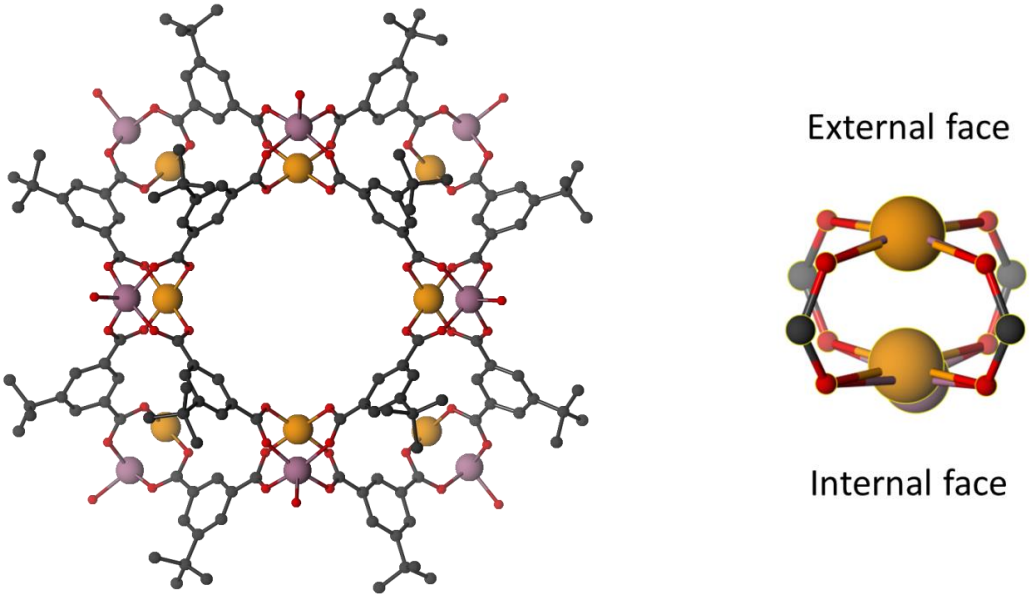

Figure 7. (Left) A perspective view of **2.8**. Metals with a site occupancy factor below 0.5 and hydrogen atoms are omitted for clarity. Only the oxygen atom of coordinating DMA molecules is shown. (Right) Overlay image of endo-Pd and exo-Pd paddlewheel node. Co and Pd atoms are coloured in mauve and orange respectively.

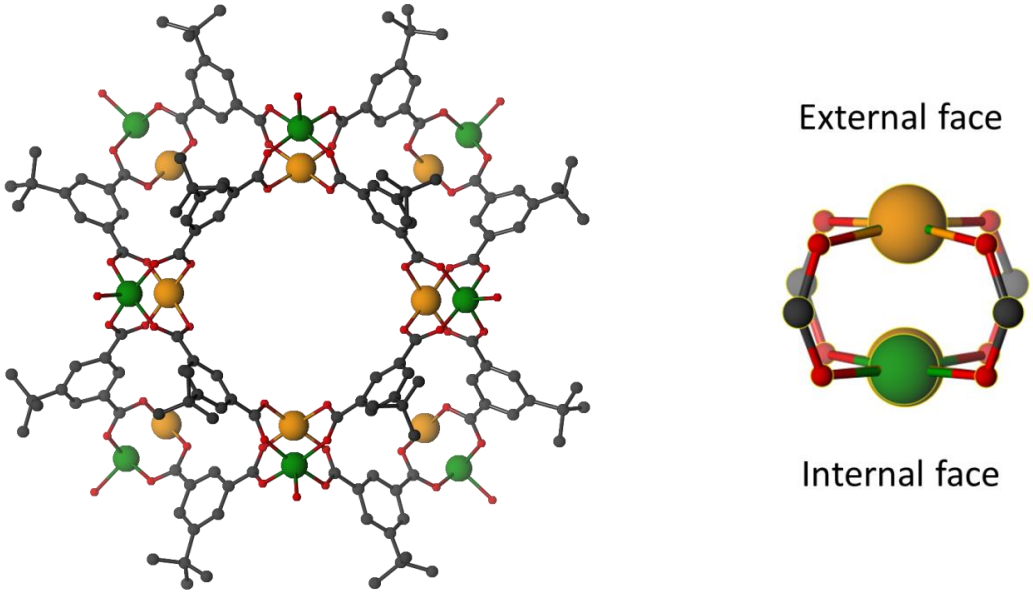

Figure 8. (Left) A perspective view of **2.9**. Metals with a site occupancy factor below 0.5 and hydrogen atoms are omitted for clarity. Only the oxygen atom of coordinating DMA molecules is shown. (Right) Overlay image of endo-Pd and exo-Pd paddlewheel node. Ni and Pd atoms are coloured in green and orange respectively.

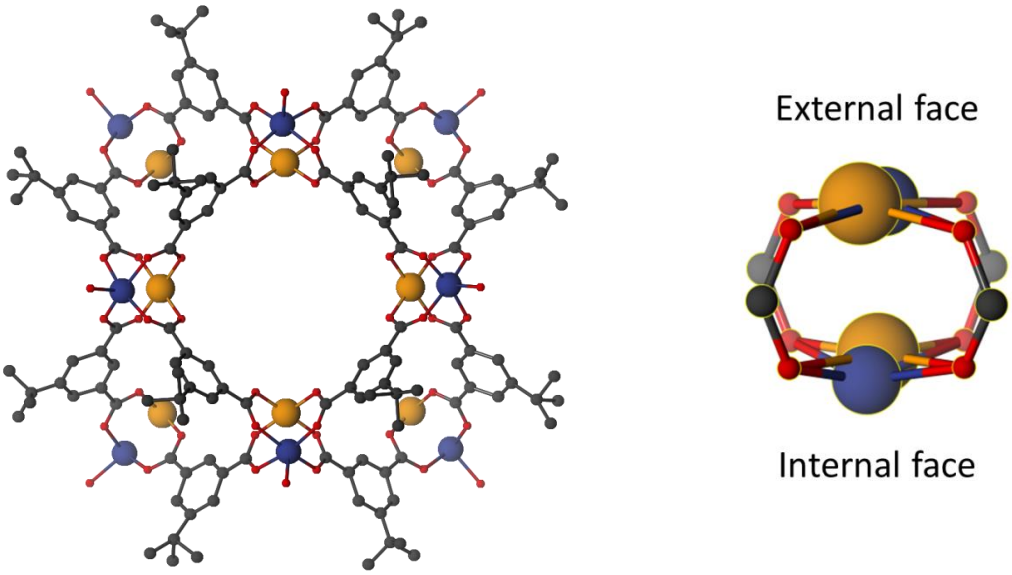

Figure 9. (Left) A perspective view of **2.10**. Metals with a site occupancy factor below 0.5 and hydrogen atoms are omitted for clarity. Only the oxygen atom of coordinating DMA molecules is shown. (Right) Overlay image of endo-Pd and exo-Pd paddlewheel node. Zn and Pd atoms are coloured in blue and orange respectively.

Table 2. Metal node bond lengths and angles for *b*^{m}*bdc* polyhedra.

	Structure	O-M-O (°)	O-Pd-O (°)	M-O (Å)	Pd-O (Å)
Endo-Pd Orientation	**2.8**	167(1)	177(2)	2.00(5)	2.04(4)
	2.9	171(1)	176(1)	2.02(4)	1.97(5)
	2.10	165(1)	177(3)	2.03(8)	1.99(4)
Exo-Pd Orientation	**2.8**	161(7)	166(2)	1.93(15)	2.11(15)
	2.9	167(3)	168(5)	2.10(20)	1.99(6)
	2.10	158(5)	161(2)	2.02(2)	2.04(25)

The effects of endo- and exohedral positioning on metal atom bond angles in **2.8**, **2.9** and **2.10** are similar to that observed in the non-functionalised analogues described in section 2.3.1. Significantly, the packing of individual polyhedra is drastically different due to the *t*-butyl groups on the outer surfaces. Three of these groups cluster together in the crystal lattice

altering the packing of individual polyhedra with respect to the tetragonal *P*4/*mnc* solution and expanding the void space and unit cells to over 34000 Å^3 (Section 2.3.3, Figure 20).

*2.3.2.1. A Copper-Palladium Bimetallic Metal-Organic Polyhedron (**2.11**)*

The reaction of PdCu(μ-OOCMe)$_4$(OH$_2$)(HOOCMe)$_2$ (**2.4**) with 5-*t*-butyl isophthalic acid produced green prism-shaped crystals of Cu$_x$Pd$_y$(*b*^{m}*bdc*)$_{24}$(C$_4$H$_9$NO)$_{12}$ (**2.11**); however, the structural composition of the metal nodes was found to deviate from the ideal 50:50 metal distribution seen in the Co, Ni and Zn species. Single crystal X-ray diffraction experiments reveal that the compound is isostructural to the other *t*-butyl MOPs presented in section 2.3.2, however the occupation of each metal within the paddle-wheel is unequal. Unlike **2.8**, **2.9** and **2.10**, EDX analysis of the copper-palladium analogue shows a higher ratio of the 3*d* transition metal, such that the atomic content of copper is approximately 50% greater than that of palladium, with some variance between individual crystals. This results in a molecular formula of approximately Cu$_{14}$Pd$_{10}$(*b*^{m}*bdc*)$_{24}$.

The original work by Moiseev *et al*. to prepare the bimetallic acetate starting materials reported a similar trend when the copper-palladium acetate **2.4** was formed.[34] After acetate synthesis, Moiseev *et al*. found that the hetero-bimetallic species would decompose into mononuclear Cu(II) acetate and trinuclear Pd$_2$Cu(μ-OOCMe)$_6$ rapidly when stored as a crystalline solid at ambient temperature. Consideration of this decomposition provides a plausible explanation for the relatively high content of first row metal found in Cu$_{14}$Pd$_{10}$(*b*^{m}*bdc*)$_{24}$ **2.11**, when compared to the other bimetallic MOPs. The analogues that do not contain copper (**2.8 – 2.10**) are synthesised under conditions in which the bimetallic acetate is stable, thus there is a single possible metal cluster available for reaction during synthesis and crystallisation. Instability of the CuPd acetate **2.4** however results in the availability of mononuclear copper acetate, which can form competing di-copper paddlewheels under these reaction conditions. Conversely, despite the large number of palladium based coordination polymers, none are known to form based on carboxylate linkers. It is therefore unsurprising that the MOP forms with Cu(II) ions occupying the majority of the metal sites.

Crystallographic analysis suggests that the exohedral metal sites in **2.11** have a Cu(II) occupancy of 75%, consistent with the other members of the bimetallic *t*-butyl MOP series, however the Cu(II) occupancy at the internal site increases to approximately 50%. This

suggests that the increased copper content in **2.11** is predominantly due to the increased presence of Cu(II) ions at the endohedral metal site.

Crystals of **2.11** decompose rapidly, even when stored under an inert atmosphere. If left to stand in the reaction mixture the crystals, which are initially green prisms with clearly defined edges, become opaque with many defects over the course of several days. Washing fresh crystals with DMA leads to a gradual olive green colouring of the solution and formation of an insoluble green precipitate, which also begins to darken over several days. The decomposition products show no permanent porosity and were not characterised further. Due to the intrinsic thermodynamic instability of **2.11**, as well as the relevant bimetallic CuPd starting material, no additional structures were synthesised from the copper-palladium acetate **2.4**.

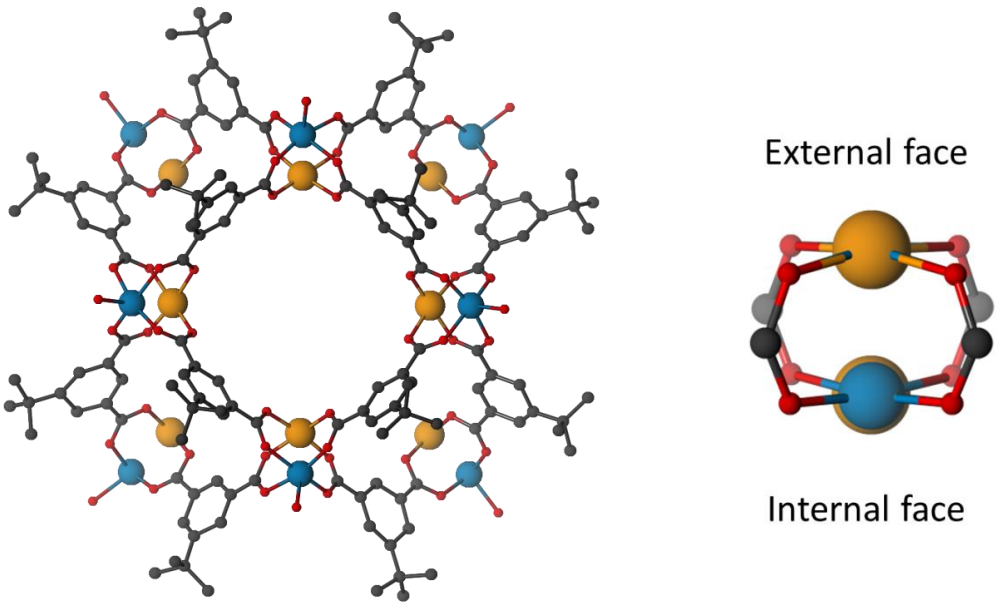

Figure 10. (Left) A perspective view of **2.11**. Metals with a site occupancy factor below 0.5 and hydrogen atoms are omitted for clarity. Only the oxygen atom of coordinating DMA molecules is shown. (Right) Overlay image of endo-Pd and exo-Pd paddlewheel node. Cu and Pd atoms are coloured in blue and orange respectively.

Table 3. Metal node bond lengths and angles for $Cu_{14}Pd_{10}(b^{m}bdc)_{24}$ polyhedra.

	O-M-O (°)	O-Pd-O (°)	M-O (Å)	Pd-O (Å)
Endo-Pd Orientation	168(1)	174(1)	2.00(22)	1.99(9)
Exo-Pd Orientation	174(1)	168(1)	1.98(10)	2.00(11)

2.3.3. Structure of 5-Hydroxy-Isophthalate Bimetallic MOPs

$Co_{12}Pd_{12}(h^{m}bdc)_{24}(C_4H_9NO)_{12}$ (**2.12**), $Ni_{12}Pd_{12}(h^{m}bdc)_{24}(C_4H_9NO)_{12}$ (**2.13**) and $Zn_{12}Pd_{12}(h^{m}bdc)_{24}(C_4H_9NO)_{12}$ (**2.14**) are afforded from the reaction of 5-hydroxy *m*-benzene dicarboxylic acid ($H_2h^{m}bdc$) with dimetallic acetates **2.1**, **2.2** and **2.3** respectively. The asymmetric unit of these materials (Appendix, Figures 42 – 44), as with the previously described MOP species contains three ligands and two metallic nodes, one of which is situated on a mirror plane. Similar to the $b^{m}bdc$ analogues, these materials crystallise in the tetragonal *I4/m* space group. Each of the ligands features a non-coordinating hydroxyl group located on the exterior of the cage, while the structure solution gives an occupancy factor for the endohedrally located Pd(II) of between 70 and 75%.

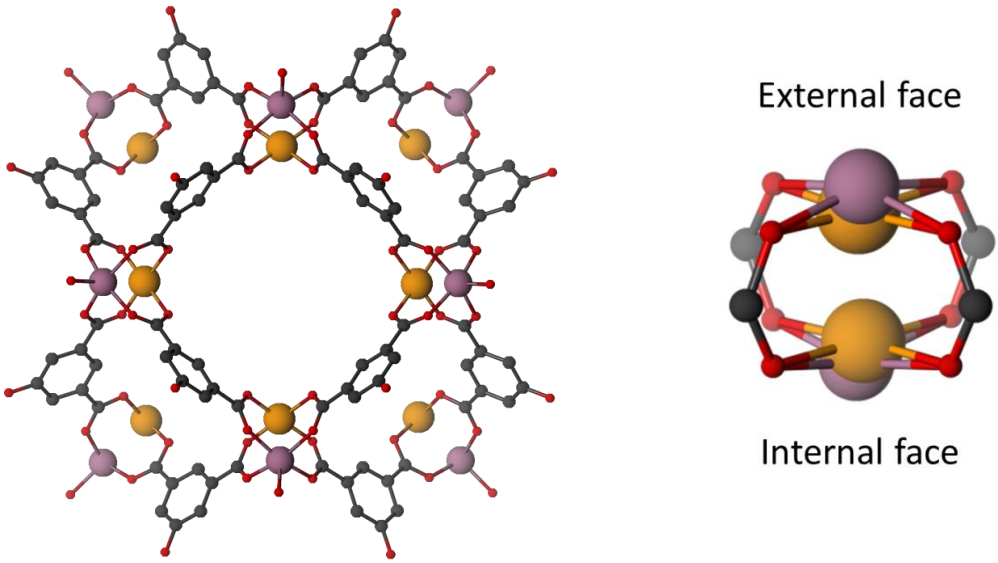

Figure 11. (Left) A perspective view of **2.12**. Metals with a site occupancy factor below 0.5 and hydrogen atoms are omitted for clarity. Only the oxygen atom of coordinating DMA molecules is shown. (Right) Overlay image of endo-Pd and exo-Pd paddlewheel node. Co and Pd atoms are coloured in mauve and orange respectively.

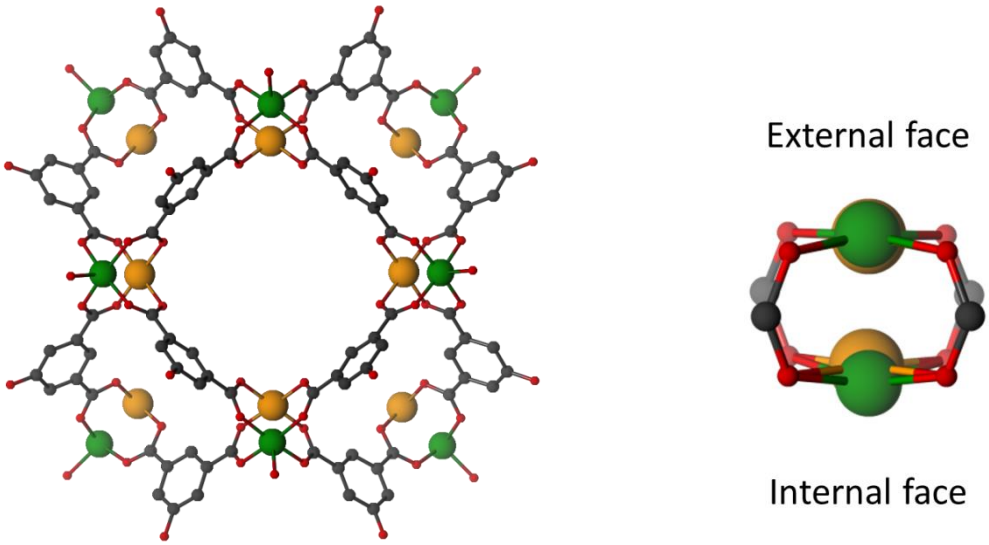

Figure 12. (Left) A perspective view of **2.13**. Metals with a site occupancy factor below 0.5 and hydrogen atoms are omitted for clarity. Only the oxygen atom of coordinating DMA molecules is shown. (Right) Overlay image of endo-Pd and exo-Pd paddlewheel node. Ni and Pd atoms are coloured in green and orange respectively.

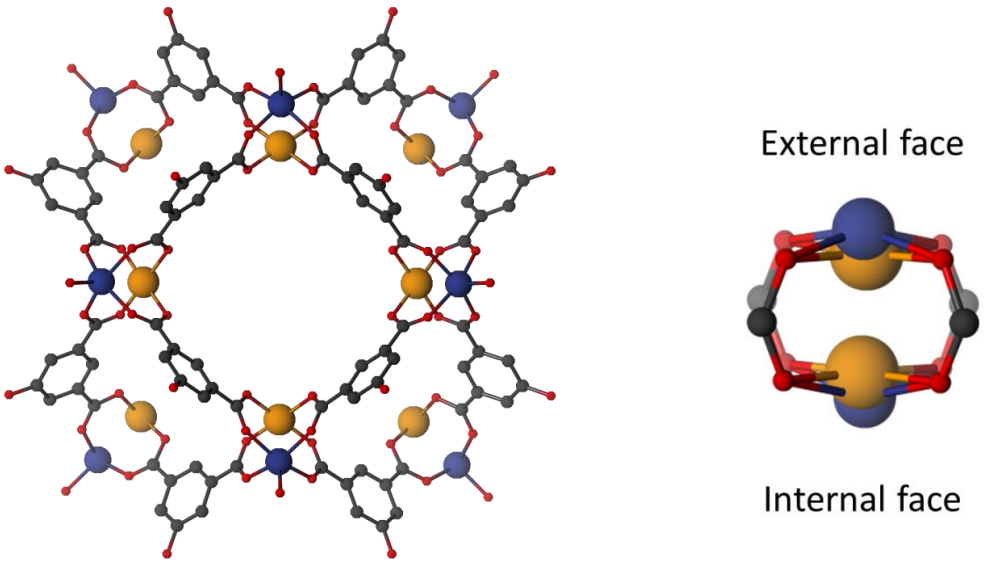

Figure 13. (Left) A perspective view of **2.14**. Metals with a site occupancy factor below 0.5 and hydrogen atoms are omitted for clarity. Only the oxygen atom of coordinating DMA molecules is shown. (Right) Overlay image of endo-Pd and exo-Pd paddlewheel node. Zn and Pd atoms are coloured in blue and orange respectively.

Table 4. Metal node bond lengths and angles for $h^m bdc$ polyhedra.

	Structure	O-M-O (°)	O-Pd-O (°)	M-O (Å)	Pd-O (Å)
Endo-Pd Orientation	**2.12**	159(1)	178(1)	2.05(2)	1.98(1)
	2.13	169(3)	178(1)	2.03(2)	2.01(1)
	2.14	156(1)	178(1)	2.07(3)	2.01(2)
Exo-Pd Orientation	**2.12**	161(1)	174(1)	2.07(6)	2.05(4)
	2.13	163(1)	174(2)	2.00(5)	2.00(2)
	2.14	156(1)	176(1)	2.04(4)	2.01(4)

As is observed in the other bimetallic MOP structures, the position of the Ni(II) ions is almost co-localised with the corresponding Pd(II) site due to the similarities in electronic configuration, as the *d*8 electronic configuration of these elements favours a planar arrangement with the oxygen atoms.[35,36] The Co(II) and Zn(II) ions are situated further to the cage exterior due to their more flexible coordination geometries.[37,38]

These compounds are truncated cuboctahedra that crystallise in the *I*4*/m* space group as do the *t*-butyl compounds described in 2.3.2, however the cage packing is subtly different. Unlike packing of the analogous *t*-butyl crystals which is aided by formation of a 3 member hydrophobic cluster of organic groups, the 5-hydroxy substituents create hydrogen bonding between two hydroxyl groups from the ligands of adjacent cages. The crystallographically determined donor-acceptor distance of 3.29(1) Å is commensurate with moderate-weak hydrogen bonding of a mostly electrostatic nature.[39] The resulting compacted arrangement results in a smaller unit cell than is observed in the *t*-butyl cages, yet is larger than the non-functionalised isophthalate analogues.

Interestingly, the crystal packing of the bimetallic $h^m bdc$ MOPs differs to that of the di-copper analogue. While it displays similar hydrogen bonding motifs, when crystallised in the *I*4/*m* space group, the homometallic copper MOP has cell dimensions of $a = b = 25.87$ Å and $c = 39.13$ Å has a cell volume of 26183 Å^3. This is 10% smaller than the heterometallic counterparts average of 29333 Å^3, which have more similar cell lengths of approximately $a = b = 30.7$ Å, $c = 31.1$ Å.

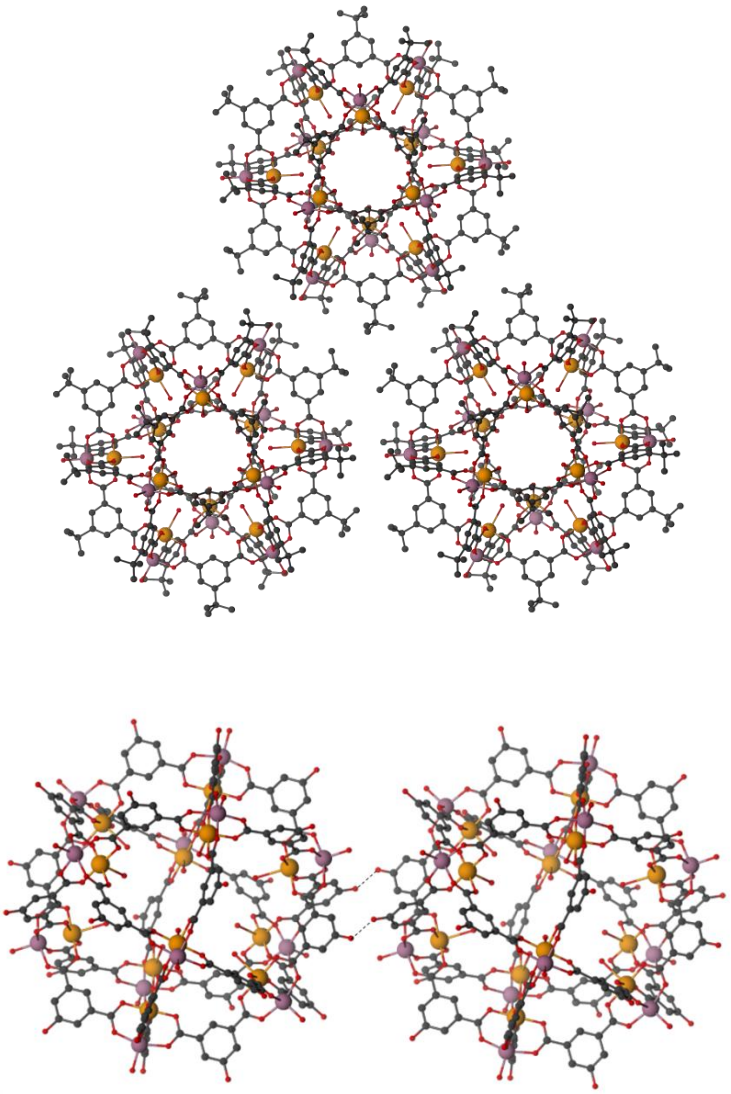

Figure 20. Packing of polyhedra in *t*-butyl (top) and hydroxyl (above) cages is influenced by respective hydrophobic and hydrogen bonding interactions between adjacent MOPs.

2.4. Endo/Exo Selectivity of Metal Ions

An explanation of the endo/exo selectivity in these bimetallic MOPs has been proposed, yet remains difficult to conclusively prove. Initially it was theorised that preferential positioning of palladium would arise from a combination of angular and steric contributors, in which case the resultant node orientation would be determined by the thermodynamic stability of the supramolecular assembly. As these MOPs have nearly spherical internal and external surfaces, it was predicted that the Pd(II) ions would be positioned exohedrally due to a larger atomic radius than the first row metals. Investigation into the coordination environment of the Pd(II) ions however reveals that the opposite holds

true in these compounds, as the endohedral position facilitates a more ideal square planar environment. In general however, the angular difference between exo- and endo-conformations is less than 5° and not solely responsible for the significant positional preference.

An alternative explanation for the preferential metal positioning arises as a consequence of the solvation of the metal in the bimetallic acetate reagent. As shown by the single crystal structures of the bimetallic starting materials, the Pd(II) ion has a 4-coordinate square planar geometry, while the relevant first row metal is 5-coordinate, bound to a solvent molecule.[34] During the self-assembly process, 12 bimetallic acetates must aggregate to form the complete structure. In order for all the solvated first row metals to be positioned endohedrally, 12 corresponding solvent molecules must be directed inwards, creating substantial steric hindrance. If the internal cavity is assumed to be a sphere of 15 Å diameter, the expected cavity volume is calculated to be under 1800 $Å^3$. Considering the elemental composition of 12 DMA molecules, $(C_4H_9NO)_{12}$, it can be determined that even at an atomic level, the required volume to encapsulate 12 DMA molecules (almost 2200 $Å^3$) is beyond that of the internal cavity. Not taking into account geometric restraints due to molecular bonding, nor accounting for imperfect packing of solvent molecules, this approximation is a significant under-estimate of the true required volume. As such, it is suspected that the kinetics of cage formation and the associated internal steric interactions suppress the exo-Pd conformation when using these solvated starting materials.

2.5. Determination of Metal-Metal Bonding

Paddle-wheel motifs have been extensively studied as the bridging carboxylates hold the metal atoms in close proximity, allowing the possibility of metal-metal bonding and electron transfer. The extent of this interaction has been thoroughly investigated in literature for both homo- and heterometallic paddle-wheel complexes, as these interactions give rise to possible applications in molecular magnetism and electronics, in addition to a strong influence in adsorption in porous materials.[40-46]

Computational chemistry is a powerful tool for examining the interactions between the metal ions and has been used with great success in work by Ke *et al*. to investigate a di-molybdenum MOP, showing the presence of a quadruple bond between each pair of 2nd row metals.[27] Using computational studies, Markov and associates have investigated heterometallic acetates, yet found no bonding electron interaction between the metal ions.[47]

The same methodology has been used in this work to study the heterometallic paddle-wheels in the MOPs presented in this chapter. While Pd(II)-M(II) (M = Co, Ni, Zn) paddle-wheel complexes are thoroughly investigated in this manner in the literature, the structural influence of the MOP architecture, as well as the presence of metal-bound solvent molecules, alters the paddle-wheel geometry and potentially the metal-metal distance and electronic properties.[47]

The inter-metal distance for each heterometallic pair was determined from the corresponding MOP single crystal structures to verify that the metal ions are close enough to facilitate an inter-metal interaction (Table 5). In all cases the metal-metal distance is between 2 and 3 Å, thus the most intuitive physical condition is satisfied.[48]

Table 5. Crystallographically measured metal-metal distances of the fully occupied node.

	Metal-Metal Distance (Å)		
Metal Node	**Isophthalate MOPs**	**5-*t*-Butylisophthalate MOPs**	**5-Hydroxyisophthalate MOPs**
CoPd	2.463	2.509	2.471
NiPd	2.442	2.462	2.418
ZnPd	2.527	2.558	2.514
CuPd	-	2.552	-

Consideration of the molecular orbitals and 3*d*-valence electrons for each metal atom allows for a prediction of bond order, suggesting bond orders between 2.5 and 1 (for Pd-Co and Pd-Zn, respectively). Calculations made in such simplified methods however must be used with caution due to the energetic similarities between the relevant 3*d*, 4*p* and 5*s* orbitals as well as the possible spin states for the involved metals.[49] Furthermore, crystal packing forces exert an influence on the metal-metal distances in such paddle-wheel complexes.[50] Therefore approximations made in such calculations, particularly in high electron count systems, add some uncertainty to such results.

To provide further insight into the inter-metal interactions, the metal nodes were investigated by co-workers using computational methods at B97-D3/def2-tzvpd level theory. As an entire MOP structure consists of hundreds of atoms, modelling an entire MOP unit was not viable because the computational time for such calculations increases as the square (or

greater depending on the level of theory) of the number of atoms. To reduce computational expense, the metal nodes were modelled as discrete formate paddle-wheel units, and the relevant metal orbitals visualised for signs of metal-metal bonding.[1] To ensure a valid comparison between DFT methods and experimental data, the modelled formate cluster was compared to the crystallographic data for reasonable geometric agreement. In the case of each bi-metallic pair, the anti-bonding nature of the highest occupied molecular orbitals (HOMOs) suggests there is no significant bonding interaction between the metal ions (Figure 21). The absence of orbital overlap indicates that the metals are not electronically bound to each other, but are instead held in close proximity by the bridging acetate groups. These results are unsurprising when considering the chemical similarity to the heterometallic complexes studied by Markov *et al*.[47]

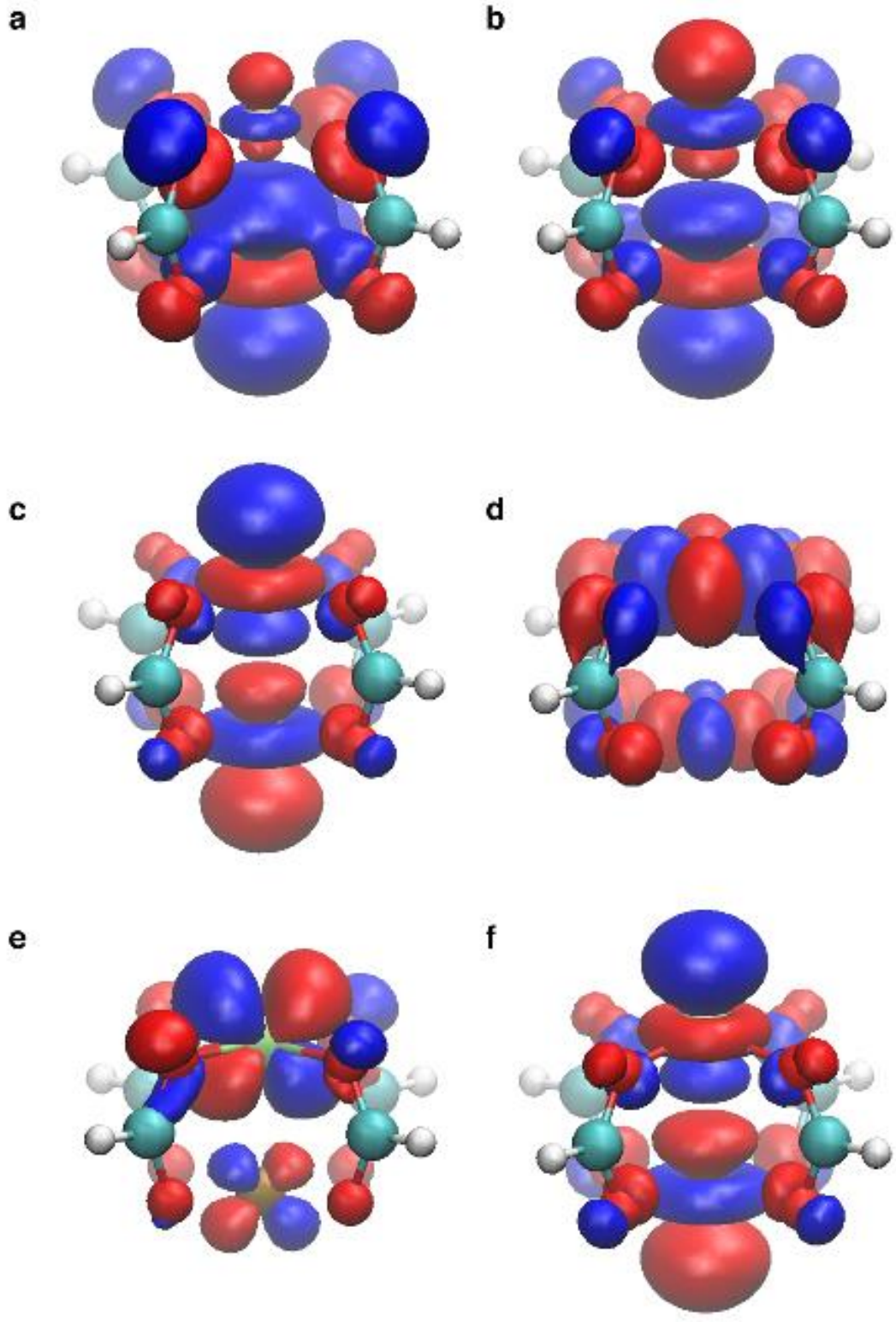

Figure 14. Highest occupied molecular orbital diagrams for (**a**) ZnPd, (**b**) CuPd, (**c**) NiPd (singlet), (**d**) NiPd (triplet), (**e**) CoPd (doublet) and (**f**) CoPd (quartet) acetate clusters, calculated at B97-D3/def2-tzdvp level theory.

2.6. Gas Adsorption Studies of Hetero-bimetallic Metal-Organic Polyhedra

Being permanently porous structures, the interactions of MOPs with small gas molecules have been studied intensively over the last several years. The tuneable surface and internal void space make these materials particularly attractive platforms for gas storage and separation.

The paddle-wheel metal nodes in this series of bimetallic MOPs are interesting, as the metal sites within porous materials are often associated with strong adsorbate interactions.[51-53] Coordination polymers with di-copper paddle-wheels are well documented as having promising interactions with hydrogen gas. A literature search for HKUST-1, a di-copper paddle-wheel based MOF, returns over 150 references directly associated with hydrogen and demonstrates the amount of research focussed on these materials. Much of the interest in paddle-wheel containing structures comes from their ability to stabilise coordinatively unsaturated metal sites in a manner that is accessible to guest species. These open metal sites are often capable of interacting with guests that are traditionally difficult to bind, by inducing polarity or through Lewis acid-base interactions.[54,55]

While the copper paddle-wheel has shown great potential for gas phase applications, enhancing or tuning of the metal-adsorbate interaction is historically limited to the relatively subtle influences of ligands that impinge electronically or sterically on the site.[56-58] By incorporating different metal ions into the paddle-wheel geometry, the electronic properties and strength of the resultant guest interaction can be drastically altered as is shown in this investigation wherein the enthalpy of adsorption for hydrogen gas is significantly increased through the application of the hetero-bimetallic metal nodes.

2.6.1. Activation of Hetero-bimetallic MOPs

In order to take advantage of a coordinatively unsaturated metal site, solvent molecules that are bound to the relevant metal ion must first be removed. In the instances of the bimetallic MOPs, this requires the removal of the axially coordinated DMA molecule from the first row metal site, which was shown by the X-ray crystallographic structure and confirmed by NMR spectroscopy on digested MOP samples.

Activation of the bimetallic MOPs was achieved in a multiple step method as the implementation of literature procedures, previously used to activate analogous di-copper MOPs, left 12 DMA molecules bound to each MOP as determined by ^{1}H NMR analysis. Typical literature activation protocols are based upon washing the crystals with MeOH to

remove coordinated solvent molecules, and subsequent removal of the MeOH with a combination of heat and reduced pressure to yield an activated material. This methodology was found to be incompatible with the bimetallic MOPs for several reasons.

Firstly the bond between the relevant metal ion and the coordinated synthesis solvent (DMA) was too strong to be displaced by MeOH (12 DMA molecules remain bound after 4 days in MeOH as determined by ^{1}H NMR). Soaking MOP crystals in MeOH for several days afforded DMA solvated structures which, while porous, do not have the desired open metal sites. Exchanging the solvent with acetone was found to exchange the DMA molecules however the process was very slow due to the coordinating ability of DMA compared to acetone. After several days in acetone, ^{1}H NMR analysis shows only residual traces of DMA is present in the crystals. Acetone itself was found to interact strongly with the bimetallic MOPs which were subject to supercritical CO_2 ($scCO_2$) drying for several hours to remove most of the acetone, followed by heating at 50°C for 200 minutes to yield the activated materials.

The second shortcoming in applying established activation methods was brought about by the low thermal stability of the bimetallic MOPs. Exposing the crystals to temperatures over 70°C or prolonged periods at 50°C was found to give drastically reduced porosity and cause a rapid darkening of samples. Thermogravimetric analysis reveals a corresponding gradual mass loss at temperatures above 50°C. The colour change and insolubility of these decomposition products suggests the formation of metal oxides and unregulated polymerisation, however subsequent characterisation was not performed.

A further obstacle to the successful activation of the bimetallic MOPs was the instability of these materials in the presence of oxygen or water. All solvent used during activation required meticulous drying and degassing prior to use. Once activated, exposure to atmospheric moisture and oxygen must be avoided to maintain the maximised surface area and hydrogen enthalpies observed.

This method of activation also dramatically increases the surface area of previously characterised MOPs. N_2 isotherms at 77 K of $Cu_{24}(b^mbdc)_{24}$ using a MeOH activation procedure reveal a negligible internal surface area, as shown by Li *et al.*[23] and confirmed by this work. After activation by the acetone exchange protocol however, the material exhibits a near type I isotherm with a corresponding BET surface area of 300 m^2/g (Figure 22). To determine the cause of this change in adsorption properties, ^{1}H NMR spectroscopy was used

to quantify the amount of DMA that remained in the activated materials. As was seen in the hetero-bimetallic materials, MeOH exchange did not remove coordinating DMA molecules, thus it is concluded that the difference in surface area is a result of the presence of bound solvent molecules and not simply a case of differing packing of individual cages. Interestingly, this gives rise to the potential of using the coordinated solvent as a switch to inhibit adsorption of N_2 on $Cu_{24}(b^m bdc)_{24}$•xS. Upon activation, these materials undergo a crystalline to amorphous transition, as observed by powder X-ray diffraction (PXRD). This transformation is consistent with many discrete porous structures in which crystallinity is lost as solvent molecules are removed.[20,59]

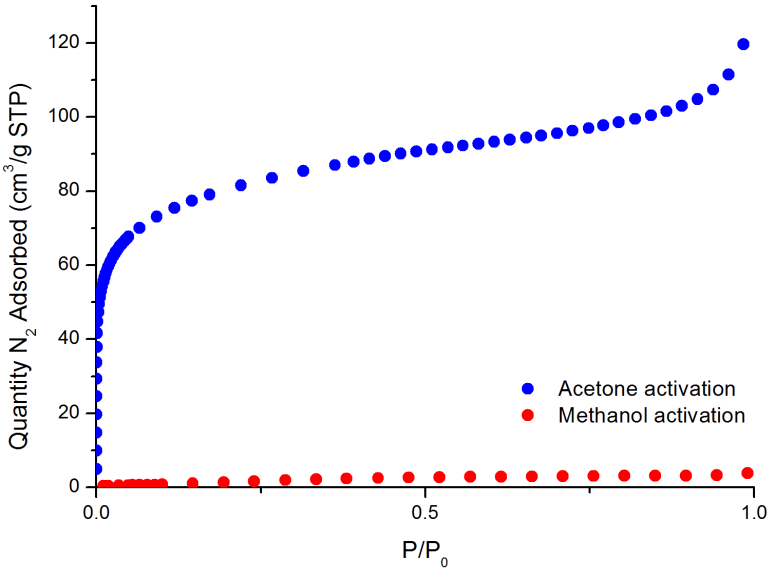

Figure 15. N_2 adsorption isotherm of $Cu_{24}(b^m bdc)_{24}$ after acetone/$scCO_2$ or methanol activation protocols (77 K).

2.6.2. Gas Adsorption Studies of Isophthalate Bimetallic MOPs

The bimetallic isophthalate MOPs exhibit type I N_2 isotherms (Figure 23), with the nickel analogue having the highest surface area of 930 m^2/g and a minor hysteresis at P/P_0 = 0.5. BET analysis determines that the surface areas for the zinc and cobalt species are 650 and 750 m^2/g respectively. Analysis of the pore size distribution (Appendix, Figure 54) shows that gas uptake is largely due to a dominating microporosity between 5 and 10 Å in all three MOPs, which is attributable to the internal cavity of the structure.

Hydrogen adsorption isotherms show high capacity for all three ^{m}bdc MOPs up to atmospheric pressure (Figure 24). The high hydrogen capacity of these MOPs is expected due to the large surface area and pore volumes. Most of the hydrogen adsorption occurs in the low pressure regions of the isotherms, with all 3 ^{m}bdc MOPs exceeding 3 mmol/g at 250 mbar.

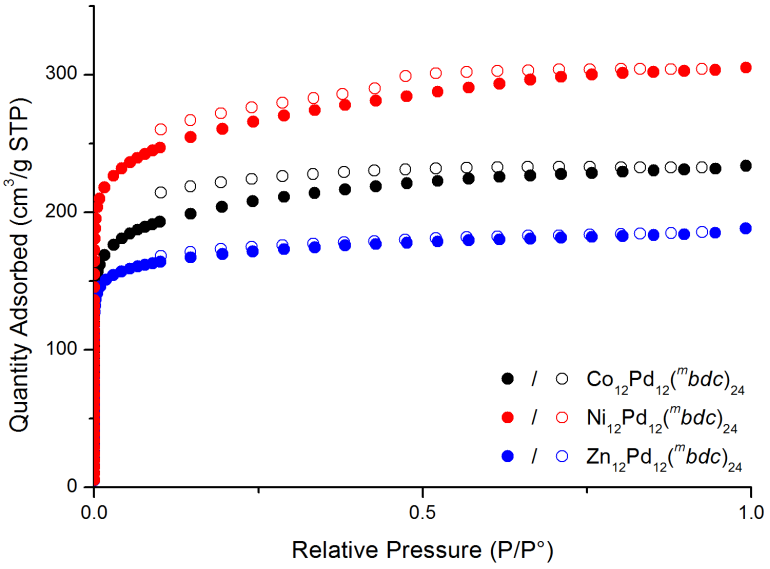

Figure 16. N_2 adsorption isotherms collected at 77 K for M-Pd isophthalate MOPs following activation with acetone. Closed and open symbols represent adsorption and desorption data, respectively.

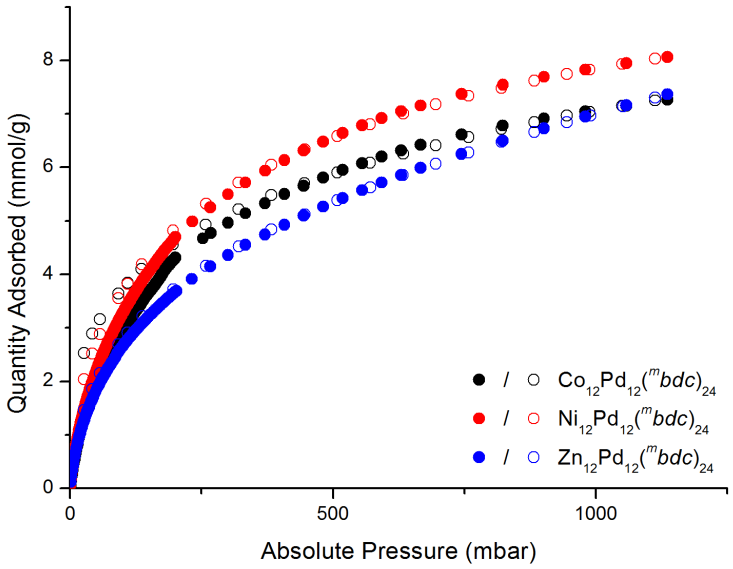

Figure 17. H_2 adsorption isotherms collected at 77 K for M-Pd isophthalate MOPs following activation with acetone. Closed and open symbols represent adsorption and desorption data, respectively.

2.6.3. Gas Adsorption Studies of t-Butyl Isophthalate Bimetallic MOPs

Nitrogen adsorption experiments (Figure 25) show that *t*-butyl isophthalate bimetallic MOPs have high BET surface areas of up to 1100 m^2/g. $Ni_{12}Pd_{12}(b^m bdc)_{24}$ and $Zn_{12}Pd_{12}(b^m bdc)_{24}$ isotherms exhibit type I profiles with BET surface areas of 700 and 900 m^2/g respectively. DFT pore size calculations align with the X-ray crystal structure, with the majority of the void space in 5-10 Å cavities. $Co_{12}Pd_{12}(b^m bdc)_{24}$, which has the highest surface area, shows a slight hysteresis in the adsorption isotherm suggesting that the packing of polyhedra in the activated state is less dense than that of the nickel and zinc analogues. Indeed, subtle changes in packing arrangements have been known to cause significant changes in adsorption as is seen in the work of Mastalerz and associates. Their studies of organic molecules of intrinsic microporosity (OMIMs) shows examples of frustrated packing manifesting as an isotherm hysteresis, attributed to breathing during the sorption process.[60] This is further implied by the pore size distribution of the CoPd MOP showing significant pore structure of a diameter greater than 15 Å, larger than the internal diameter of the polyhedron. As extremely mild conditions are used during both synthesis and activation of these materials, the amorphous packing is not the thermodynamic minimum for these

materials. As such, differences in pore structure between materials, such as frustrated packing of MOPs, are not unexpected.

The N_2 adsorption isotherm of the $Cu_{14}Pd_{10}(b^mbdc)_{24}$ structure **2.11** shows generally type I character with a much lower surface area than other bimetallic MOPs, showing similar behaviour to the analogous di-copper material. Notably, the Cu-Pd desorption curve shows that N_2 remains sorbed to the material in a non-reversible manner. Both of these features can be attributed to the instability and decomposition of the MOP as collapse of the pore structure not only reduces the available surface area, but can also trap adsorbed gas molecules giving rise to the non-reversible adsorption profile.[61] This is further evidenced by the pore size distribution of **2.11** revealing a significant reduction in microporosity compared to the other *b*^{m}*bdc* analogues.

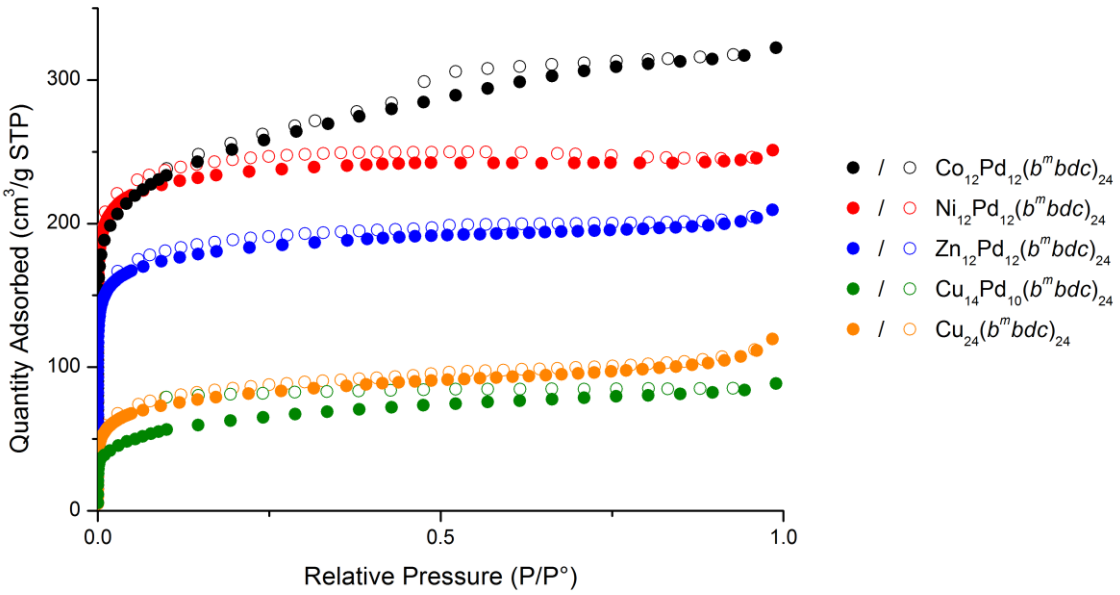

Figure 18. N_2 adsorption isotherms collected at 77 K for *t*-butyl isophthalate MOPs following activation with acetone. Closed and open symbols represent adsorption and desorption data, respectively.

Cryogenic hydrogen adsorption isotherms show reversible uptake up to atmospheric pressure (Figure 26). The gas adsorption is characterised by a steep uptake at pressures below 250 mbar, which begins to plateau after 750 mbar. At atmospheric pressure, the hydrogen capacities at 77 K for the *t*-butyl MOPs range from approximately 3 to 5 mmol/g. This

capacity is significantly lower than the non-substituted isophthalate analogues which have H_2 capacities between 7 and 8 mmol/g. Unsurprisingly, the two copper containing MOPs show the lowest hydrogen uptake, due to their low surface areas.

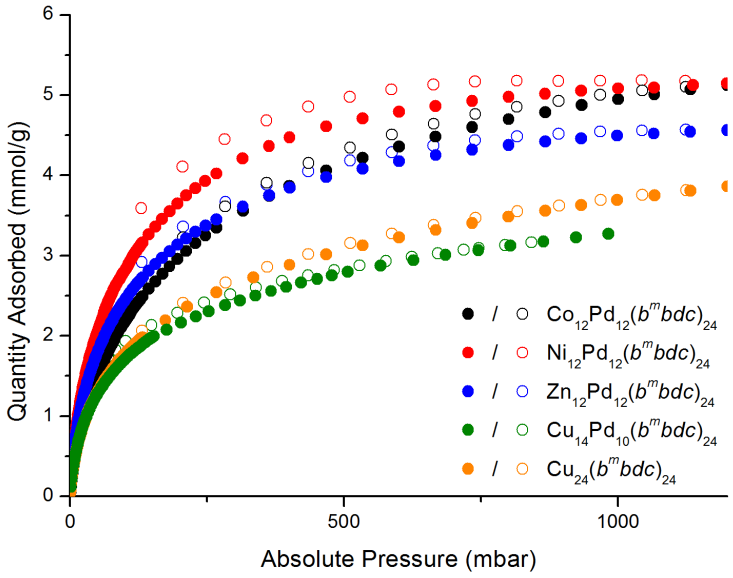

Figure 19. H_2 adsorption isotherms collected at 77 K for *t*-butyl isophthalate MOPs following activation with acetone. Closed and open symbols represent adsorption and desorption data, respectively.

2.6.4. Gas Adsorption Studies of Hydroxy Isophthalate Bimetallic MOPs

The three hydroxy isophthalate MOPs have type I nitrogen adsorption profiles (Figure 20), with BET surface areas close to 800 m^2/g. The $Zn_{12}Pd_{12}(h^mbdc)_{24}$ isotherm shows a very slight hysteresis which appeared in repeat experiments. As with the other bimetallic MOPs which display this adsorption behaviour, this suggests the presence of accessible mesoporous regions between individual cages, resulting from the non-thermodynamic, amorphous packing.

Surface areas for the 5-hydroxyisophthalate MOPs are all lower than the respective *t*-butyl analogues indicating that the peripheral motifs play a substantial role in available surface area. Li *et al.* proposed that external functional groups on MOPs obscure pore windows in adjacent cages thus altering the accessible pore space within the material.[23] While this proposal can explain some of the changes observed in the surface area of these materials, it cannot adequately describe differences observed between the hetero-bimetallic species and

the analogous di-copper materials, which have significantly lower surface areas. Therefore it stands to reason that the accessible surface areas are influenced not only by the organic unit, but also by the metal node and the subtly different overall structures of the homo and heterometallic cages.

The difference in surface areas between MOPs highlights the significance of packing effects in the amorphous state. The ability of external groups to influence packing in discrete porous structures and alter extrinsic void space has been explored by Cooper and associates in their studies of covalent organic cages.[62] Their work found that the introduction of external aryl groups dramatically changed the gas adsorption properties of their organic cages, by altering both the extrinsic void space and also the intrinsic pore connectivity. Both dispersion forces and π-electron interactions were found to be significant factors in their work, thus it is unsurprising that the external functionality in this work shows a similar effect. As is discussed in section 2.3.3, hydroxyl groups and *t*-butyl groups were found to influence the MOP packing in the crystalline state through hydrogen bonding and hydrophobic forces respectively. It is expected then that these interactions, in particular the stronger hydrogen bonding, would influence the gas adsorption of MOPs even in the amorphous state and indeed this is observed in these materials.

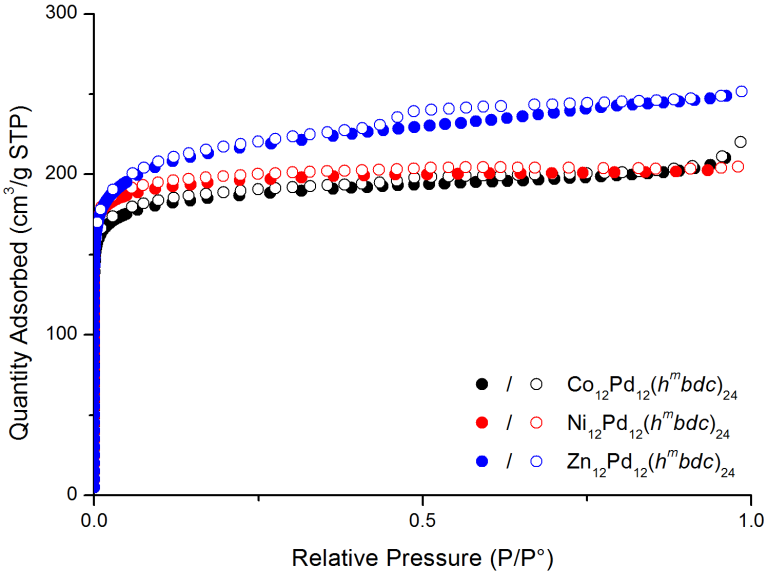

Figure 20. N_2 adsorption isotherms collected at 77 K for M-Pd hydroxy isophthalate MOPs following activation with acetone. Closed and open symbols represent adsorption and desorption data, respectively.

Hydrogen adsorption in the *h*^{m}*bdc* series of materials follows a similar trend to the other bimetallic MOPs in this chapter, such that the adsorption is predominantly driven by the highly accessible surface area, with a large uptake in the low pressure region of the isotherm. The gravimetric adsorption capacity of these materials is comparable to that of the *b*^{m}*bdc* analogues (4 – 5 mmol/g at 1 atm), but is significantly lower than the unfunctionalised ^{m}*bdc* variants. Interestingly, consideration of the gas adsorption relative to the molecular weight of each MOP shows that the *h*^{m}*bdc* structures have the lowest H_2 uptake per MOP unit.

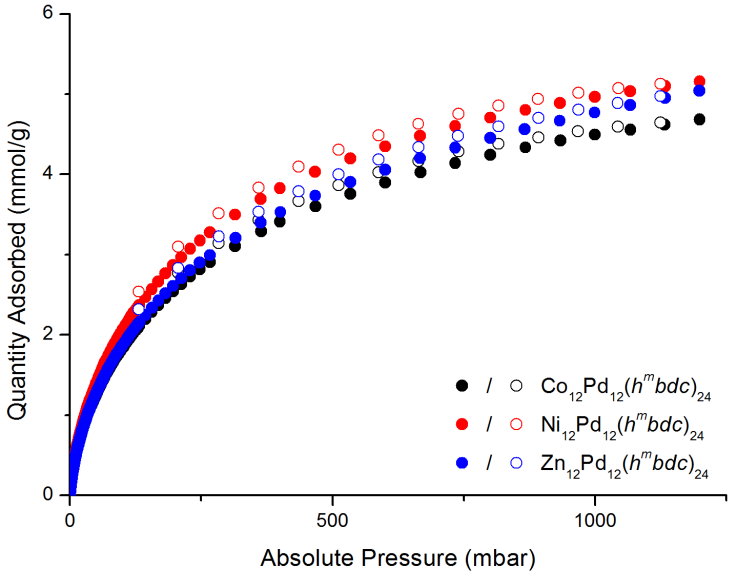

Figure 21. H_2 adsorption isotherms collected at 77 K for M-Pd hydroxy isophthalate MOPs following activation with acetone. Closed and open symbols represent adsorption and desorption data, respectively.

2.6.5. Experimental Determination of H_2 Binding Enthalpy

The enthalpy of adsorption is one of the key factors that can determine the potential of a porous material as a candidate for gas storage.[63,64] As such, the accurate determination of enthalpy has been widely discussed in literature, with several methods finding ubiquity in adsorption analyses. Unfortunately, little agreement over which method to use is found in the literature despite the significance of enthalpy calculations. HKUST-1, a thoroughly investigated candidate for hydrogen storage for example, has reported enthalpies of hydrogen adsorption that range from 4.5 to 10.1 kJ/mol.[65-67] While it is well documented that differences in sample preparation and activation can influence adsorption properties, much of the disagreement between reported enthalpy values is a direct result of the different calculation methods used.[68,69]

MOPs can be particularly challenging subjects for gas enthalpy determination, as the gas adsorption behaviour can be difficult to accurately describe due to the complicated, non-crystalline nature of the activated material.[23] In order to address this issue, several prevailing

methods of enthalpy were considered to find the most suitable description of the hydrogen-MOP interaction.

2.6.5.1. Van't Hoff & Clausius Clapeyron Relationships

Two of the most commonly applied relationships to determine isosteric gas adsorption enthalpy are the Clausius-Clapeyron equation and the Van't Hoff equation. Theoretically the two models differ in their intended application, but are nearly identical in isosteric adsorption enthalpy calculations. The Clausius-Clapeyron equation describes the thermodynamics of a phase transition, such as a gas to liquid condensation by considering the vapour pressure exerted by the gas phase. In this way, the theory closely matches the assumptions made in BET theory, in which formation of a gas multilayer is energetically equivalent to the energy of condensation.[70] The Van't Hoff equation determines the thermodynamic parameters of a given equilibrium by considering the change in equilibrium constant at different temperatures. In order to calculate the isosteric enthalpy of adsorption, both of these methods treat the gas adsorption process as an equilibrium quantified by the adsorbate gas phase pressure. For determination of isosteric enthalpy at low pressure, both the Clausius-Clapeyron and Van't Hoff relationships commonly take the form of:[71]

$$Q_{st} = RT^2 \left(\frac{\delta \ln P}{\delta T}\right)$$

Where P = equilibrium pressure, T = absolute temperature, Q_{st} = isosteric heat of adsorption, R = specific gas constant.

This relationship is commonly applied in the literature as experimental data can be used directly in calculations, as well as the ease with which the calculations can be justified. The most significant drawbacks to this methodology lie in the accuracy of the calculations, as the value of Q_{st} is highly susceptible to error propagation from adsorption measurements and greatly influenced by relatively small temperature changes.[68,72] Ideally several isotherms are measured over a range of close temperatures, with Q_{st} determined graphically to minimise this error, however this is not often achievable due to experimental limitations.

The heat of hydrogen adsorption for the bimetallic MOPs was calculated from Van't Hoff isochore plots (Appendix, Figures 57 - 59) using 77 K and 87 K adsorption data, with the low coverage (5 cm^3/g STP) Q_{st} values given in Table 6. While the calculated values are generally within the range expected of physisorptive interactions, they show inconsistencies with values predicted by computational studies (section 2.6.6.) as well as unrealistic values at near zero coverage. These discrepancies however are expected due to the aforementioned inaccuracies associated with Van't Hoff type calculations.

Table 6. Low Coverage enthalpy of H_2 adsorption calculated from the Van't Hoff relationship.

	Enthalpy of H_2 Adsorption (-kJ.mol^{-1})		
Metal Node	**Isophthalate MOPs**	***t*-butyl isophthalate MOPs**	**Hydroxy isophthalate MOPs**
CoPd	4.5	7.2	7.8
NiPd	6.9	7.1	7.4
ZnPd	7.8	10.9	7.3
CuPd	-	10.1	-
CuCu	-	8.1	-

2.6.5.2. Dual-Site Langmuir Expression of Surface Coverage

As exposed metal sites in porous materials can facilitate a very strong metal-gas interaction, the zero-coverage adsorption enthalpy of the MOPs synthesised in this chapter is of great interest. In order to address the inaccuracy associated with Clausius-Clapeyron type analysis at very low pressure, gas uptake can be described mathematically as a function of pressure prior to calculation of Q_{st}.

The Langmuir adsorption expression was the first equation to explain solid-gas adsorption through physical parameters.[73] As such, it relies on several assumptions that have seen its direct application decrease in favour of more comprehensive physical models, such as BET theory, for the purposes of determining specific surface areas of porous materials. The most significant consideration for Langmuir-type equations is that only monolayer gas adsorption is considered, thus the model begins to break down as surface coverage reaches saturation. For the purposes of very low coverage adsorption enthalpy calculations however, the assumptions are more realistic.

In an attempt to accurately determine the low coverage enthalpy of hydrogen adsorption using a physically justifiable model, a double-Langmuir-type function was explored. Gaining popularity in recent literature, this approach has several desirable factors that make it appealing for the application of this work.[74-76] A superpositioning of Langmuir functions, referred to as a generalised Langmuir equation, can fit most experimental adsorption data with relative ease. The form of the equation itself has promising characteristics for describing gas adsorption. Firstly, a generalised Langmuir expression produces a monotonically increasing function which is the expected behaviour of a physisorptive process. Secondly, a dual-Langmuir function reflects the gas adsorption characteristics of a porous material with two inequivalent gas binding domains. For the purposes of this work, the open metal sites can be viewed as a distinct gas binding domain, while the remaining accessible surface area is another. The dual-site Langmuir expression therefore provides a model of simultaneous physisorption in both domains, each with its own gas adsorption profile. As such, the H_2 adsorption data was fitted to a dual-site Langmuir equation:[77]

$$q_{total} = q_A + q_B = \frac{q_{sat,A} b_A P}{1 + b_A P} + \frac{q_{sat,B} b_B P}{1 + b_B P}$$

For two adsorbing surfaces *A*, *B* where: q = molar loading of adsorbate, q_{sat} = molar saturation loading, P = equilibrium pressure, b = parameter in the pure component Langmuir adsorption isotherm.

While Langmuir-type fitting has been successful in highly ordered materials, one must be aware of the non-ideality of the accessible surface area in a MOP and the subsequent effect on the applicability of the model. Unlike a crystalline MOF which has an extremely well defined surface area, MOPs tend to become amorphous upon activation, thus the adsorbing surface is less regular than their extended framework counterparts. Accessible metal sites within the amorphous solid may be partially obscured by adjacent cages creating a distribution of inequivalent adsorption sites. Although the dual-site Langmuir model showed great promise as a description of the hydrogen adsorption in these materials, a suitable fit to

the experimental data was not able to be achieved due to non-ideal adsorption behaviour in the very low pressure region.

2.6.5.3. Virial-Type Equation of Gas-Solid Adsorption

In recent years the application of virial form equations has become increasingly popular in order to accurately calculate the isosteric enthalpy of gas adsorption. [78-80] As with a dual-site Langmuir methodology, fitting virial type equations to experimental adsorption data minimises analysis error, particularly at low surface coverage. Virial expressions describe the experimental data as an expansion of polynomial functions, giving the gas adsorption in the form of:

$$\ln P = \frac{1}{T}\sum_{i=0}^{n1} a_i v^i + \sum_{i=0}^{n2} b_i v^i + \ln v$$

Where: v = amount adsorbed, P = equilibrium pressure, T = absolute temperature, *n1* & *n2* = number of parameters in thermally dependant and independent terms respectively.[68]

The virial equation is fit to the experimental data over the low pressure region where Henry's law is observed, to a best fit measured by the coefficient of determination (R^2) and the expansion can then be used directly to calculate Q_{st}. As the virial equation allows further expansion through the introduction of additional parameters, expressing gas adsorption in this form prior to Van't Hoff analysis provides a smoother and more realistic determination of Q_{st}. While the expansion itself is an empirical description of the adsorption profile, the parameters (*a*, *b* etc.) are often related to a physical phenomenon or property such as the enthalpy of adsorption at zero-coverage.[68]

Caution must be exercised when determining Q_{st} through virial type calculations, as the calculated value is susceptible to significant variance during the fitting process, being influenced by both polynomial order and the pressure range over which the function is fit. Using excessively high order polynomials produces undulations within the fitting function that inaccurately describe the gas adsorption process, while fitting a curve beyond the Henry's law region can lead to poor fitting of the very low pressure data.

To provide the best description of the adsorption profiles, thermally independent fourth order polynomials were fit to the adsorption data sets to prevent the generation of artificial inflexions in the function, while maintaining a good fit to the experimental data. Coverage dependant Q_{st} was calculated up to a hydrogen loading of 2 mmol/g for all samples, with the exceptions of the copper containing species, $Cu_{14}Pd_{10}(b^{m}bdc)_{24}$ and $Cu_{24}(b^{m}bdc)_{24}$), which were calculated up to 1 mmol/g due to their reduced H_2 adsorption capacity.

Isosteric heats of adsorption (Figures 29 - 31) were obtained from temperature independent virial fits to the isotherms. The isosteric curves show a broad range of initial *Qst* values ranging from -4.5 to -12.1 kJ/mol. To provide a better understanding of the hydrogen binding in these structures, the experimental results were compared to DFT studies, as described in 2.6.6.

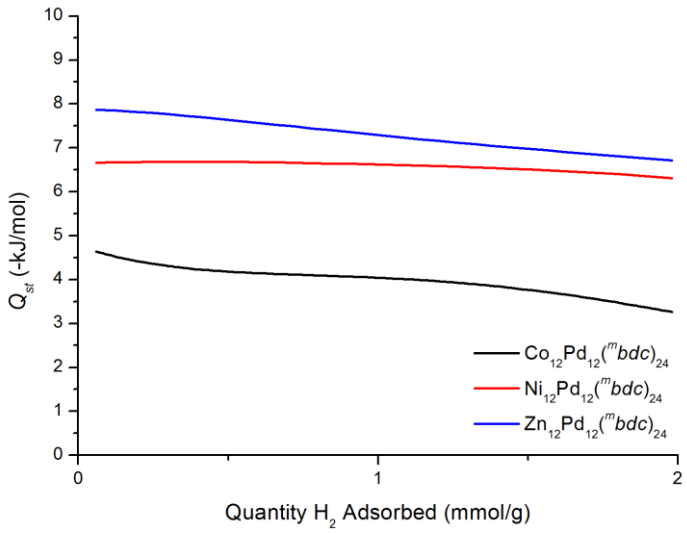

Figure 29. Coverage dependant isosteric heats of H_2 adsorption for M-Pd isophthalate MOPs.

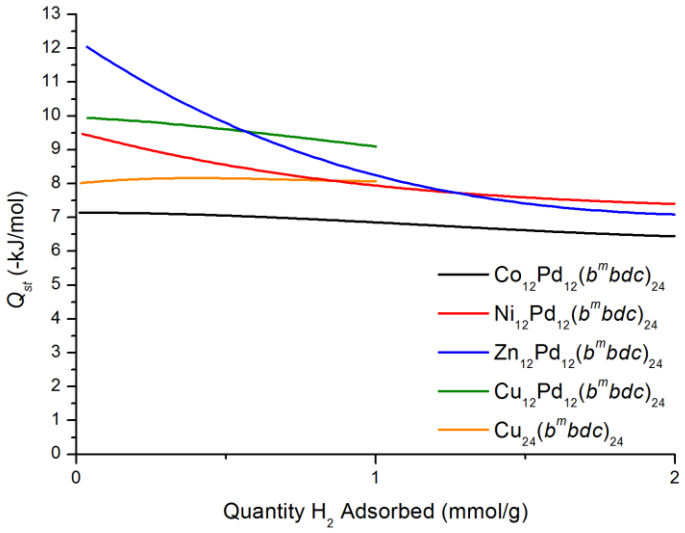

Figure 30. Coverage dependant isosteric heats of H_2 adsorption for *t*-butyl isophthalate MOPs.

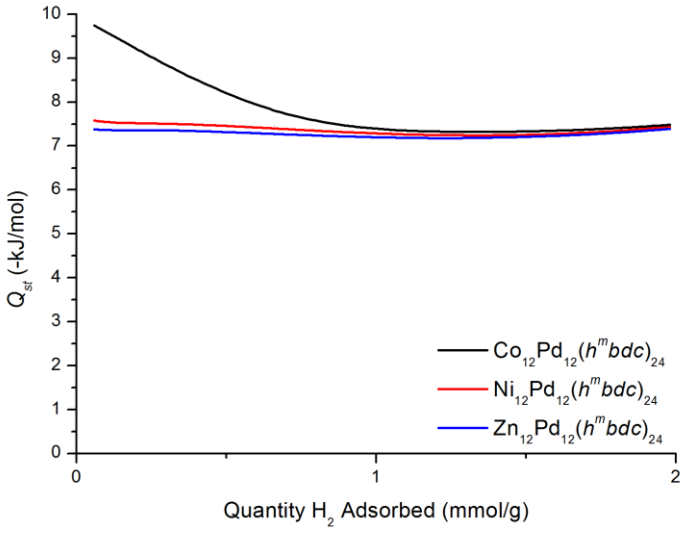

Figure 31. Coverage dependant isosteric heats of H_2 adsorption for M-Pd hydroxy isophthalate MOPs.

2.6.6. DFT Determination of Hydrogen Adsorption Enthalpy

To provide further insight into the hydrogen binding modes, bimetallic paddle-wheel clusters were investigated through DFT calculations by co-workers.[1] Gaussian09 software with PBE0 and B97D3 functionals paired with the TZDVP basis set was used to explore Pd(II)-M(II) clusters with four bridging formate ligands. As discussed in section 2.5, this motif was found to accurately reflect the geometry seen in the single crystal X-ray structures, and thus was a suitable modelling tool.

While high spin (hs) and low spin (ls) states are possible for both the CoPd and NiPd systems, a number of DFT functionals give the high spin states as the most energetically favourable. Realistically however, the local environment of the cluster can have a large effect on spin populations, thus calculations of this type must be used with caution.[81] To address this concern, the interaction energy with H_2 was considered for both possible spin states. While the Pd(II) showed no substantial interaction with H_2, it was observed that the M(II) sites showed strong interaction energies in the descending order of Co(hs), Ni(hs), Zn, Co(ls), Cu and Ni(ls). The strong interaction energies, which are calculated to be in excess of 10 kJ/mol for the high spin structures is explained by partial occupation of σ* orbitals that stabilise the H_2 gas binding as seen in Kubas-type complexes.[82] In the absence of high spin state clusters however, the H_2 binding is an effect of the polarizing nature of the M(II) partial positive charge.

Table 9. Calculated Energies of Metal Formate – H_2 Interaction.

	Multiplicity	**H_2-Metal Distance (Å)**	**H-H Distance (Å)**	**H_2-M Interaction Energy (kJ/mol)**
CuCu	Triplet	2.418	0.750	-6.54
ZnPd	Singlet	2.206	0.754	-8.81
CuPd	Doublet	2.434	0.750	-3.94
NiPd	Singlet	3.096	0.746	-2.04
NiPd	Triplet	1.998	0.760	-11.4
CoPd	Doublet	2.065	0.757	-14.1
CoPd	Quartet	1.986	0.765	-24.5

2.6.6.1. Hydrogen Adsorption Domains in Isophthalate MOPs

The weakest interaction energies are experimentally observed for the *^{m}bdc* structures (**2.5**, **2.6** and **2.7**) with initial *Qst* values of -4.5, -6.7 and -7.9 kJ/mol for the CoPd, NiPd and ZnPd analogues respectively. While the adsorption energy for the ZnPd material decreases as the H_2 loading increases, the initial *Qst* value closely matches that of the calculated interaction energy. This is strong evidence that H_2 guests bind preferentially to the Zn centres, with a subsequent decrease in binding energy as the Zn sites reach saturation.

Conversely, the CoPd and NiPd species show much lower adsorption energies over the isosteric curve. The linear profile and reduced enthalpy of the NiPd isostere is indicative of H_2 binding due to wall-wall overlaps created by the porous structure.[6] The CoPd analogue exhibits the lowest H_2 binding energy with an interaction much weaker than predicted by the computational analysis. Hydrogen adsorption in both materials suggests that the metal sites are therefore inaccessible to H_2 guests and that adsorption occurs in the inter- and intramolecular cavities (where the 3*d* transition metal site is inaccessible) of the structures.

2.6.6.2. Hydrogen Adsorption Domains in t-butylisophthalate MOPs.

The strongest H_2 adsorption energies are observed in the bimetallic MOPs that contain exohedral *t*-butyl groups. The isosteric curves for the NiPd and ZnPd MOPs (**2.10** and **2.11**) indicate strong adsorption with initial Q_{st} values of -9.50 and -12.1 kJ/mol. These experimentally determined values are in good agreement with simulation and are competitive with exposed metal ion MOFs such as HKUST-1 and CPO-27-Ni, which have interaction enthalpies of -10.1 and -13.5 kJ/mol, respectively.[83] The enthalpy of adsorption decreases to approximately -7.5 kJ/mol in both cases, as the high affinity sites reach saturation. The H_2 interaction energy for **2.10** and **2.11** is much greater than that observed for the di-copper paddle-wheel analogue, which has an enthalpy of approximately -8 kJ/mol over the hydrogen loading range.

The CoPd and CuPd MOPs (**2.8** and **2.11**) exhibit more linear enthalpy profiles with initial *Qst* values of -7.2 and -10.0 kJ/mol. The difference in profile as well as the poor agreement with simulated data indicates that strong H_2 adsorption occurs due to wall-wall overlap in these materials, and is unlikely to be due to exposed metal sites. The difference in adsorption enthalpy between the two is explained by the difference in pore structure, as can be seen in the N_2 pore size distribution data (Appendix, Figure 55).

2.6.6.3. Hydrogen Adsorption Domains in Hydroxyisophthalate MOPs.

Initial *Qst* values for the 5-hydroxyisophthalate MOPs range from -7.4 to -9.8 kJ/mol. The isosteric curves for the NiPd and ZnPd materials (**2.13** and **2.14**), which are almost identical, show *Qst* values of -7.6 and -7.4 kJ/mol respectively. The linear nature of these isosteres indicates that the strong H_2 adsorption again occurs due cavity size and pore architecture, rather than at the metal sites. This is further evidenced by the similarities in N_2 adsorption experiments, which indicate a common pore structure between the materials.

The isosteric curve for the CoPd MOP **2.12** shows that H_2 adsorption occurs at the high affinity metal centre at low gas loadings. The interaction strength reduces from 9.8 to 7.5 kJ/mol as the high affinity sites become saturated. The initial *Qst* value is in reasonable agreement with the calculated Co(ls)-H_2 interaction strength, indicating that low loading H_2 adsorption occurs at the exposed Co(II) sites.

2.7. Thermogravimetric Analysis of Hetero-bimetallic Metal-Organic Polyhedra

All of the MOPs described in this chapter were analysed by thermogravimetric analysis (TGA) to confirm activation and investigate thermal stability (Figures 32 – 34). Activated MOP samples were analysed before and after gas adsorption, with the results indicating that the sorption experiments had no observable effect on the thermal stability of the MOPs. TGA of the MOPs show only minor weight losses before 200 °C, confirming the success of the activation protocol. The activation procedure (as described in section 2.6.1) involves heating the samples under vacuum at 50 °C for several hours. In spite of this, TGA shows that the MOPS lose a small amount of weight upon heating to this temperature which is accounted for by absorption of atmospheric water. Despite efforts to minimise exposure to the atmosphere, the analysis of completely unexposed samples was not possible due to equipment limitations. After the small initial weight loss, the MOPs all show thermal stability to approximately 200 °C, before significant weight loss signifying decomposition of the materials.

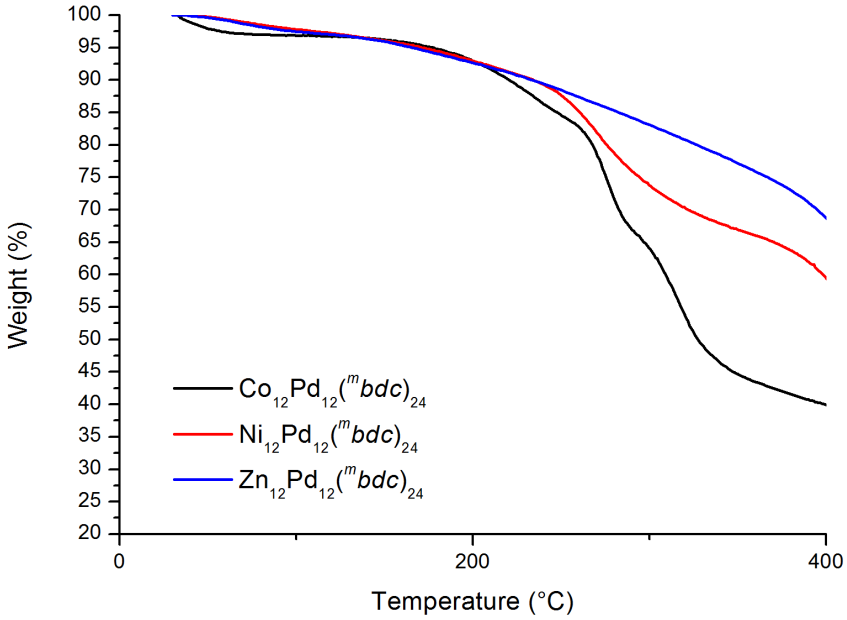

Figure 32. Thermogravimetric analysis of bimetallic isophthalate MOPs.

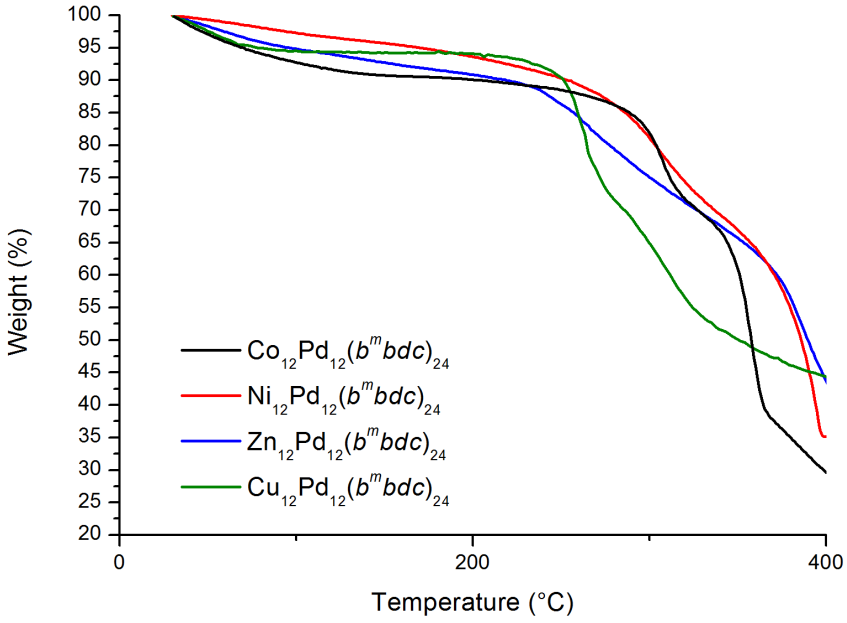

Figure 33. Thermogravimetric analysis of bimetallic *t*-butyl isophthalate MOPs.

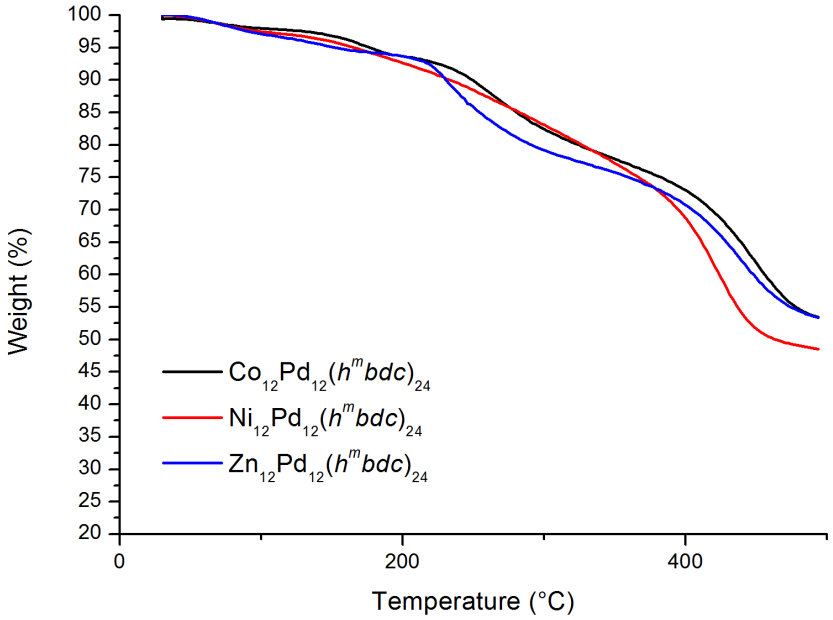

Figure 34. Thermogravimetric analysis of bimetallic hydroxy isophthalate MOPs.

2.8. Summary

In summary, a series of discrete metal-organic polyhedra have been synthesised using heterometallic building units and isophthalic acid derivatives. By using mild synthesis conditions that encourage ligand exchange, the preformed geometry and elemental composition of the hetero-bimetallic starting materials is maintained in the resulting MOPs. X-Ray crystallography shows that the structures exhibit preferential endohedral positioning of square planar Pd(II) metals, with the relevant first row metal decorating the cage exterior. Introducing external surface functionality, such as *t*-butyl or hydroxyl groups, has been shown to influence the crystal packing of these MOPs, such that the unit cell volumes range from 23000 to 35000 $Å^3$. Computational studies have shown that there is no formal bonding between the metal ions despite the close proximity, which is induced by the conformation of the ligands. Gas adsorption studies reveal permanent porosity after activation, giving rise to high surface areas up to 1100 m^2/g. The exohedral metal sites are available for interactions with guest molecules, giving rise to strong H_2 binding enthalpies in excess of -12 kJ/mol. Such adsorption enthalpies are competitive with other high performing frameworks with exposed metal ions.

2.9. Experimental

Materials and Measurements

Unless otherwise stated, all chemicals were obtained from commercial sources and used as received. DMA and MeOH were distilled from CaH_2 and degassed with Ar. Acetone was dried over $CaSO_4$ and distilled under Ar. Thermogravimetric analyses (TGA) were performed on a Perkin−Elmer STA-6000 instrument under a constant flow of N_2 at a temperature increase rate of 10 °C/min. Infrared spectra were recorded on a Perkin−Elmer Fourier-transform infrared (FT-IR) spectrometer on a zinc−selenide crystal. MOP samples for acid digestion analysis were dissolved in d_6-DMSO (1 mL) containing 1 drop of DCl solution (45% in D_2O). NMR spectra were recorded on a Varian 500 MHz spectrometer at 23 °C using a 5 mm probe. Powder X-ray diffraction data were collected on a Bruker D8 Advance diffractometer (capillary stage) using Cu Kα radiation (λ = 1.5418 Å, 50 kW/40mA, 2θ = 2 – 55°). Energy-dispersive X-ray spectroscopy (EDX) was performed on a Philips XL30 field emission scanning electron microscope. Supercritical CO_2 activation was conducted using a Samdri-PVT-3D Critical-Point-Dryer.

Synthetic Methods

$PdM(\mu\text{-}OOCMe)_4(OH_2)(HOOCMe)_2$ (M = Co (**2.1**), M = Ni (**2.2**), M = Zn (**2.3**) and M = Cu (**2.4**)) were synthesised using the methods described by Moiseev *et al*.[34]

*$Co_{12}Pd_{12}$isophthalate$_{24}$($C_4H_9NO)_{12}$ (**2.5**).*

In a screw cap vial, a solution of $[Pd(\mu\text{-}OOCMe)_4Co(OH_2)(HOOCMe)_2]$ (50 mg, 0.09 mmol) in DMA (2 mL) was mixed with a solution of isophthalic acid (15.0 mg, 0.09 mmol) in DMA (2 mL) and sonicated for 2 min. The mixture was left at room temperature for 2 days resulting in deep red prism-shaped crystals (25 mg, 56% after activation). ν_{max} (neat, cm^{-1}): 2954(w), 1606(s), 1588(m), 1401(m), 1343(s); 1267(m), 913(w);

*$Ni_{12}Pd_{12}$isophthalate$_{24}$($C_4H_9NO)_{12}$ (**2.6**).*

In a screw cap vial, a solution of $[Pd(\mu\text{-}OOCMe)_4Ni(OH_2)(HOOCMe)_2]$ (50 mg, 0.09 mmol) in DMA (2 mL) was mixed with a solution of isophthalic acid (15.0 mg, 0.09 mmol) in DMA (2 mL) and sonicated for 2 min The mixture was left at room temperature for 2 days resulting in yellow prism-shaped crystals (22 mg, 50% after activation). ν_{max} (neat, cm^{-1}): 2962(w), 1621(s), 1548(m), 1434(m), 1344(s), 1270(m) 911(w);

*$Zn_{12}Pd_{12}$isophthalate$_{24}$($C_4H_9NO)_{12}$ **(2.7)**.*

In a screw cap vial, a solution of [Pd(μ-OOCMe)$_4$Zn(OH$_2$)(HOOCMe)$_2$] (50 mg, 0.09 mmol) in DMA (2 mL) was mixed with a solution of isophthalic acid (15.0 mg, 0.09 mmol) in DMA (2 mL) and sonicated for 2 min. The mixture was left at room temperature for 2 days resulting in pale yellow prism-shaped crystals (36 mg, 80% after activation). ν_{max} (neat, cm^{-1}): 2962(w), 1615(m), 1588(m), 1404(m), 1349(s), 1261(m), 912(w);

*$Co_{12}Pd_{12}$(5-t-Butyl isophthalate)$_{24}$($C_4H_9NO)_{12}$ **(2.8)**.*

In a screw cap vial, a solution of [Pd(μ-OOCMe)$_4$Co(OH$_2$)(HOOCMe)$_2$] (50 mg, 0.09 mmol) in DMA (2 mL) was mixed with a solution of 5-*tert*-butyl isophthalic acid (20.6 mg, 0.09 mmol) in DMA (2 mL) and sonicated for 2 min. The mixture was left at room temperature for 2 days resulting in deep red prism-shaped crystals (24 mg, 44% after activation). ν_{max} (neat, cm^{-1}): 2952(w), 1605(s), 1585(m), 1400(m), 1345(s); 1267(m), 912(w);

*$Ni_{12}Pd_{12}$(5-t-Butyl isophthalate)$_{24}$($C_4H_9NO)_{12}$ **(2.9).***

In a screw cap vial, a solution of [Pd(μ-OOCMe)$_4$Ni(OH$_2$)(HOOCMe)$_2$] (50 mg, 0.09 mmol) in DMA (2 mL) was mixed with a solution of 5-*tert*-butyl isophthalic acid (20.6 mg, 0.09 mmol) in DMA (2 mL) and sonicated for 2 min. The mixture was left at room temperature for 20 days resulting in yellow prism-shaped crystals (35 mg, 64% after activation). ν_{max} (neat, cm^{-1}): 2964(w), 1623(s), 1550(m), 1436(m), 1347(s), 1269(m) 911(w);

*$Zn_{12}Pd_{12}$(5-t-Butyl isophthalate)$_{24}$($C_4H_9NO)_{12}$ **(2.10)**.*

In a screw cap vial, a solution of [Pd(μ-OOCMe)$_4$Zn(OH$_2$)(HOOCMe)$_2$] (50 mg, 0.09 mmol) in DMA (2 mL) was mixed with a solution of 5-*tert*-butyl isophthalic acid (20.6 mg, 0.09 mmol) in DMA (2 mL) and sonicated for 2 min. The mixture was left at room temperature for 2 days resulting in pale yellow prism-shaped crystals (28 mg, 51% after activation). ν_{max} (neat, cm^{-1}): 2962(w), 1605(m), 1586(m), 1401(m), 1349(s), 1268(m), 912(w);

*$Cu_{14}Pd_{10}$(5-t-Butyl isophthalate)$_{24}$($C_4H_9NO)_{12}$ **(2.11)**.*

In a screw cap vial, a solution of [Pd(μ-OOCMe)$_4$Cu(OH$_2$)(HOOCMe)$_2$] (50 mg, 0.09 mmol) in DMA (2 mL) was mixed with a solution of 5-*tert*-butyl isophthalic acid (20.6 mg, 0.09 mmol) in DMA (2 mL) and sonicated for 2 min. The mixture was left at room temperature for 2 days resulting in green prism-shaped crystals (18 mg, 33% after activation). ν_{max} (neat, cm^{-1}): 2960(w), 1610(s), 1550(m), 1414(m), 1356(s), 1265(m) 911(w);

*$Co_{12}Pd_{12}$(5-hydroxy isophthalate)$_{24}$($C_4H_9NO)_{12}$ (**2.12**).*

In a screw cap vial, a solution of [Pd(μ-OOCMe)$_4$Co(OH$_2$)(HOOCMe)$_2$] (50 mg, 0.09 mmol) in DMA (2 mL) was mixed with a solution of 5-hydroxy isophthalic acid (16.4 mg, 0.09 mmol) in DMA (2 mL) and sonicated for 2 min. The mixture was left at room temperature for 2 days resulting in deep red prism-shaped crystals (32 mg, 68% after activation). ν_{max} (neat, cm^{-1}): 3309(w), 1698(w), 1588(m), 1363(s); 1212(m), 1127(w);

*$Ni_{12}Pd_{12}$(5-hydroxy isophthalate)$_{24}$($C_4H_9NO)_{12}$ (**2.13**).*

In a screw cap vial, a solution of [Pd(μ-OOCMe)$_4$Ni(OH$_2$)(HOOCMe)$_2$] (50 mg, 0.09 mmol) in DMA (2 mL) was mixed with a solution of 5-hydroxy isophthalic acid (16.4 mg, 0.09 mmol) in DMA (2 mL) and sonicated for 2 min. The mixture was left at room temperature for 20 days resulting in yellow prism-shaped crystals (31 mg, 66% after activation). ν_{max} (neat, cm^{-1}): 3307(w), 1701(w), 1589(m), 1347(s); 1228(m), 1127(w);

*$Zn_{12}Pd_{12}$(5-hydroxy isophthalate)$_{24}$($C_4H_9NO)_{12}$ (**2.14**).*

In a screw cap vial, a solution of [Pd(μ-OOCMe)$_4$Zn(OH$_2$)(HOOCMe)$_2$] (50 mg, 0.09 mmol) in DMA (2 mL) was mixed with a solution of 5-hydroxy isophthalic acid (16.4 mg, 0.09 mmol) in DMA (2 mL) and sonicated for 2 min. The mixture was left at room temperature for 2 days resulting in pale yellow prism-shaped crystals (30 mg, 63% after activation). ν_{max} (neat, cm^{-1}): 3300(w), 1698(w), 1587(m), 1363(s); 1216(m), 1127(w);

Single Crystal X-ray Diffraction.

Single crystals were mounted in paratone-N oil on a nylon loop. X-ray diffraction data were collected at 150(2) K with Mo Kα radiation (λ = 0.7107 Å) at 100(2) K on the MX-1 beamline of the Australian Synchrotron (λ = 0.7107 Å).[84] Data sets were corrected for absorption using a multi-scan method, and structures were solved by direct methods using SHELXS-2013, and refined by full-matrix least squares on F^2 by SHELXL-2014, interfaced through the program X-Seed.[85-88]

In general, all non-hydrogen atoms were refined anisotropically and hydrogen atoms were included as invariants at geometrically estimated positions, unless specified otherwise. While the hetero-bimetallic paddlewheels are incorporated into the MOPs with a significant preference for the palladium(II) centre on the interior surface, some disorder of these sites is observed by careful structural analysis. For each crystallographically unique paddlewheel the endohedral palladium and the exohedral 3d transition metal were refined at 75% occupancy

and an endohedral 3d transition metal and exohedral palladium centre at 25% occupancy based on trial refinements. The minor paddlewheel component was refined using EXYZ and EADP restraints. The solvent molecule associated with each transition metal was assigned as an oxygen atom due to a high degree of disorder. DMA solvate molecules were disordered and refinement was accomplished using the SQUEEZE routine of Platon to remove electron density corresponding to these entities. Disorder of the *t*-butyl sites was also common to all the structures and was restrained accordingly.[89] All MOP crystals were only weakly diffracting despite the use of synchrotron radiation and this is noted as required for the individual structures.

Structural data for the compounds synthesised in this chapter can be found on the accompanying data disk. Full details of the structure determinations for **2.8**, **2.9** and **2.10** have also been deposited with the Cambridge Crystallographic Data Centre as CCDC #s 1423403-1423405. Copies of this information may be obtained free of charge from The Director, CCDC, 12 Union Street, Cambridge CB2 1EZ, U.K. (fax, +44-1223-336-033; e-mail, deposit@ccdc.cam.ac.uk).

Activation Protocol.

In a typical activation procedure, crystals of the hetero-bimetallic MOPs were washed in DMA (×3) over a 2 day period. The crystals were then exchanged into acetone (×5) over a 5 day period. The samples were dried with supercritical carbon dioxide and subsequently heated to 50°C for 200 min to yield the activated samples.

Gas adsorption measurements.

Gas adsorption isotherms were measured using volumetric methods on a Micromeritics 3-Flex analyser or ASAP2020 analyser (Micromeritics Instrument Corporation, Norcross, GA, USA) at 77 K and 87 K (utilizing liquid N_2 and Ar baths respectively or a cryo-cooler circulator). Brunauer–Emmett–Teller (BET) surface areas were calculated using experimental points at a relative pressure of P/P_0=0.05–0.25. Pore size distributions were calculated from N_2 or Ar isotherms using DFT modelling software on a Micromeritics 3-Flex analyser, or ASAP2020 analyser. UHP grade (99.999%) N_2 and (99.999%) H_2 was used for all measurements.

Thermogravimetric analysis.

Thermogravimetric analyses (TGA) were performed on a Perkin−Elmer STA-6000 instrument under a constant flow of N_2 at a temperature increase rate of 10 °C/min in a

ceramic crucible. Samples were activated using the indicated methods for each sample prior to analysis.

2.10. References

(1) Teo, J. M.; Coghlan, C. J.; Evans, J. D.; Tsivion, E.; Head-Gordon, M.; Sumby, C. J.; Doonan, C. J. *Chem. Commun.* **2015**, 52, 276.

(2) Lu, Z.; Knobler, C. B.; Furukawa, H.; Wang, B.; Liu, G.; Yaghi, O. M. *J. Am. Chem. Soc.* **2009**, *131*, 12532.

(3) Eddaoudi, M.; Kim, J.; Rosi, N.; Vodak, D.; Wachter, J.; O'Keeffe, M.; Yaghi, O. M. *Science* **2002**, *295*, 469.

(4) Doonan, C. J.; Morris, W.; Furukawa, H.; Yaghi, O. M. *J. Am. Chem. Soc.* **2009**, *131*, 9492.

(5) Eddaoudi, M.; Li, H. L.; Yaghi, O. M. *J. Am. Chem. Soc.* **2000**, *122*, 1391.

(6) Rowsell, J. L. C.; Yaghi, O. M. *J. Am. Chem. Soc.* **2006**, *128*, 1304.

(7) Tranchemontagne, D. J.; Ni, Z.; O'Keeffe, M.; Yaghi, O. M. *Angew. Chem., Int. Ed.* **2008**, *47*, 5136.

(8) Surble, S.; Serre, C.; Mellot-Draznieks, C.; Millange, F.; Ferey, G. *Chem. Commun.* **2006**, 284.

(9) Atkins, P. W. *Physical Chemistry*; Fourth ed.; Oxford University Press, **1990**.

(10) Wen, L.; Zhao, J.; Lv, K.; Wu, Y.; Deng, K.; Leng, X.; Li, D. *Cryst. Growth Des.* **2012**, *12*, 1603.

(11) Zheng, B.; Liang, Z.; Li, G.; Huo, Q.; Liu, Y. *Cryst. Growth Des.* **2010**, *10*, 3405.

(12) Liang, Z.; Du, J.; Sun, L.; Xu, J.; Mu, Y.; Li, Y.; Yu, J.; Xu, R. *Inorg. Chem.* **2013**, *52*, 10720.

(13) Farha, O. K.; Hupp, J. T. *Acc. Chem. Res.* **2010**, *43*, 1166.

(14) Perry Iv, J. J.; Perman, J. A.; Zaworotko, M. J. *Chem. Soc. Rev.* **2009**, *38*, 1400.

(15) Rowsell, J. L. C.; Yaghi, O. M. *Microporous and Mesoporous Mater.* **2004**, *73*, 3.

(16) Tonigold, M.; Volkmer, D. *Inorg. Chim. Acta* **2010**, *363*, 4220.

(17) Hirai, K.; Furukawa, S.; Kondo, M.; Uehara, H.; Sakata, O.; Kitagawa, S. *Angew. Chem., Int. Ed.* **2011**, *50*, 8057.

(18) Reboul, J.; Furukawa, S.; Horike, N.; Tsotsalas, M.; Hirai, K.; Uehara, H.; Kondo, M.; Louvain, N.; Sakata, O.; Kitagawa, S. *Nat. Mater.* **2012**, *11*, 717.

(19) Shekhah, O.; Hirai, K.; Wang, H.; Uehara, H.; Kondo, M.; Diring, S.; Zacher, D.; Fischer, R. A.; Sakata, O.; Kitagawa, S.; Furukawa, S.; Woll, C. *Dalton Trans.* **2011**, *40*, 4954.

(20) Jiang, S.; Jones, J. T. A.; Hasell, T.; Blythe, C. E.; Adams, D. J.; Trewin, A.; Cooper, A. I. *Nat. Commun.* **2011**, *2*, 207.

(21) Kongpatpanich, K.; Horike, S.; Sugimoto, M.; Kitao, S.; Seto, M.; Kitagawa, S. *Chem. Commun.* **2014**, *50*, 2292.

(22) Hunt, J. R.; Doonan, C. J.; LeVangie, J. D.; Côté, A. P.; Yaghi, O. M. *J. Am. Chem. Soc.* **2008**, *130*, 11872.

(23) Li, J.-R.; Zhou, H.-C. *Nat. Chem.* **2010**, *2*, 893.

(24) Czaja, A. U.; Trukhan, N.; Muller, U. *Chem. Soc. Rev.* **2009**, *38*, 1284.

(25) Wang, Z.; Cohen, S. M. *J. Am. Chem. Soc.* **2007**, *129*, 12368.

(26) McDonald, T. M.; D'Alessandro, D. M.; Krishna, R.; Long, J. R. *Chem. Sci.* **2011**.

(27) Ke, Y.; Collins, D. J.; Zhou, H.-C. *Inorg. Chem.* **2005**, *44*, 4154.

(28) Yao, Q.; Sun, J.; Li, K.; Su, J.; Peskov, M. V.; Zou, X. *Dalton Trans.* **2012**, *41*, 3953.

(29) Eddaoudi, M.; Kim, J.; Wachter, J. B.; Chae, H. K.; O'Keeffe, M.; Yaghi, O. M. *J. Am. Chem. Soc.* **2001**, *123*, 4368.

(30) Botas, J. A.; Calleja, G.; Sánchez-Sánchez, M.; Orcajo, M. G. *Langmuir* **2010**, *26*, 5300.

(31) Calleja, G.; Martos, C.; Orcajo, G.; Botas, J. A.; Villajos, J. A. *Cryst. Eng. Comm.* **2015**, *17*, 338.

(32) Das, S.; Kim, H.; Kim, K. *J. Am. Chem. Soc.* **2009**, *131*, 3814.

(33) Schlichte, K.; Kratzke, T.; Kaskel, S. *Microporous and Mesoporous Mater.* **2004**, *73*, 81.

(34) Akhmadullina, N. S.; Cherkashina, N. V.; Kozitsyna, N. Y.; Stolarov, I. P.; Perova, E. V.; Gekhman, A. E.; Nefedov, S. E.; Vargaftik, M. N.; Moiseev, I. I. *Inorg. Chim. Acta* **2009**, *362*, 1943.

(35) Nicholls, D. In *The Chemistry of Iron, Cobalt and Nickel*; Pergamon: 1973, p 1109.

(36) Albéniz, A. C.; Espinet, P. In *Encyclopedia of Inorganic Chemistry*; John Wiley & Sons, Ltd: 2006.

(37) Nicholls, D. In *The Chemistry of Iron, Cobalt and Nickel*; Pergamon: 1973, p 1053.

(38) Burgess, J.; Prince, R. H. In *Encyclopedia of Inorganic and Bioinorganic Chemistry*; John Wiley & Sons, Ltd: 2011.

(39) Jeffrey, G. A. *An Introduction to Hydrogen Bonding*; Oxford University Press, **1997**.

(40) Motokawa, N.; Miyasaka, H.; Yamashita, M.; Dunbar, K. R. *Angew. Chem., Int. Ed.* **2008**, *47*, 7760.

(41) Agterberg, F. P. W.; Provó Kluit, H. A. J.; Driessen, W. L.; Oevering, H.; Buijs, W.; Lakin, M. T.; Spek, A. L.; Reedijk, J. *Inorg. Chem.* **1997**, *36*, 4321.

(42) Liu, C.-S.; Wang, J.-J.; Yan, L.-F.; Chang, Z.; Bu, X.-H.; Sañudo, E. C.; Ribas, J. *Inorg. Chem.* **2007**, *46*, 6299.

(43) Bak, J. H.; Le, V.-D.; Kang, J.; Wei, S.-H.; Kim, Y.-H. *J. Phys. Chem. C* **2012**, *116*, 7386.

(44) Hijikata, Y.; Sakaki, S. *Inorg. Chem.* **2014**, *53*, 2417.

(45) Dikarev, E. V.; Gray, T. G.; Li, B. *Angew. Chem., Int. Ed.* **2005**, *44*, 1721.

(46) Kennon, B. S.; Her, J.-H.; Stephens, P. W.; Miller, J. S. *Inorg. Chem.* **2009**, *48*, 6117.

(47) Markov, A. A.; Klyagina, A. P.; Dolin, S. P.; Akhmadullina, N. S.; Kozitsyna, N. Y.; Cherkashina, N. V.; Nefedov, S. E.; Vargaftik, M. N.; Moiseev, I. I. *Russ. J. Inorg. Chem.* **2009**, *54*, 885.

(48) Pauling, L. *Proc. Natl. Acad. Sci. U. S. A.* **1976**, *73*, 4290.

(49) Krogman, J. P.; Thomas, C. M. *Chem. Commun.* **2014**, *50*, 5115.

(50) Martín, A.; Orpen, A. G. *J. Am. Chem. Soc.* **1996**, *118*, 1464.

(51) Wu, H.; Zhou, W.; Yildirim, T. *J. Am. Chem. Soc.* **2009**, *131*, 4995.

(52) Dietzel, P. D. C.; Besikiotis, V.; Blom, R. *J. Mater. Chem.* **2009**, *19*, 7362.

(53) Chen, B.; Ockwig, N. W.; Millward, A. R.; Contreras, D. S.; Yaghi, O. M. *Angew. Chem., Int. Ed.* **2005**, *44*, 4745.

(54) Haldoupis, E.; Borycz, J.; Shi, H.; Vogiatzis, K. D.; Bai, P.; Queen, W. L.; Gagliardi, L.; Siepmann, J. I. *J. Phys. Chem. C* **2015**, *119*, 16058.

(55) Weston, M. H.; Morris, W.; Siu, P. W.; Hoover, W. J.; Cho, D.; Richardson, R. K.; Farha, O. K. *Inorg. Chem.* **2015**, *54*, 8162.

(56) Dai, F. N.; He, H. Y.; Gao, D. L.; Ye, F.; Qiu, X. L.; Sun, D. F. *Cryst. Eng. Comm.* **2009**, *11*, 2516.

(57) Wang, Z.; Zheng, B.; Liu, H.; Yi, P.; Li, X.; Yu, X.; Yun, R. *Dalton Trans.* **2013**, *42*, 11304.

(58) Gao, W.-Y.; Cai, R.; Pham, T.; Forrest, K. A.; Hogan, A.; Nugent, P.; Williams, K.; Wojtas, L.; Luebke, R.; Weseliński, Ł. J.; Zaworotko, M. J.; Space, B.; Chen, Y.-S.; Eddaoudi, M.; Shi, X.; Ma, S. *Chem. Mat.* **2015**, *27*, 2144.

(59) Sudik, A. C.; Millward, A. R.; Ockwig, N. W.; Côté, A. P.; Kim, J.; Yaghi, O. M. *J. Am. Chem. Soc.* **2005**, *127*, 7110.

(60) Kohl, B.; Rominger, F.; Mastalerz, M. *Chem.- Eur. J.* **2015**, *21*, 17308.

(61) Schneider, H. M.; Granick, S. *Macromolecules* **1992**, *25*, 5054.

(62) Bojdys, M. J.; Briggs, M. E.; Jones, J. T. A.; Adams, D. J.; Chong, S. Y.; Schmidtmann, M.; Cooper, A. I. *J. Am. Chem. Soc.* **2011**, *133*, 16566.

(63) Dincă, M.; Long, J. R. *Angew. Chem., Int. Ed.* **2008**, *47*, 6766.

(64) Glover, T. G.; Peterson, G. W.; Schindler, B. J.; Britt, D.; Yaghi, O. *Chem. Eng. Sci.* **2011**, *66*, 163.

(65) Rowsell, J. L. C.; Yaghi, O. M. *J. Am. Chem. Soc.* **2006**, *128*, 1304.

(66) Panella, B.; Hirscher, M.; Pütter, H.; Müller, U. *Adv. Funct. Mater.* **2006**, *16*, 520.

(67) Bordiga, S.; Regli, L.; Bonino, F.; Groppo, E.; Lamberti, C.; Xiao, B.; Wheatley, P. S.; Morris, R. E.; Zecchina, A. *Phys. Chem. Chem. Phys.* **2007**, *9*, 2676.

(68) Czepirski, L.; JagieŁŁo, J. *Chem. Eng. Sci.* **1989**, *44*, 797.

(69) Mertens, F. O. *Surf. Sci.* **2009**, *603*, 1979.

(70) Brunauer, S.; Emmett, P.; Teller, E. *J. Am. Chem. Soc.* **1938**, *60*, 309.

(71) Sing, K. S. W.; Rouquerol, F.; Rouquerol, J. In *Adsorption by Powders and Porous Solids (Second Edition)*; Maurin, F. R. R. S. W. S. L., Ed.; Academic Press: Oxford, 2014, p 159.

(72) Naghibi, H.; Tamura, A.; Sturtevant, J. M. Proc. Natl. Acad. Sci. **1995**, *92*, 5597.

(73) Langmuir, I. *J. Am. Chem. Soc.* **1918**, *40*, 1361.

(74) Zhang, J.; Singh, R.; Webley, P. A. *Microporous and Mesoporous Mater.* **2008**, *111*, 478.

(75) Krishna, R.; Vlugt, T. J. H.; Smit, B. *Chem. Eng. Sci.* **1999**, *54*, 1751.

(76) Chowdhury, P.; Bikkina, C.; Gumma, S. *J. Phys. Chem. C* **2009**, *113*, 6616.

(77) Mason, J. A.; Sumida, K.; Herm, Z. R.; Krishna, R.; Long, J. R. *Energy Environ. Sci.* **2011**, *4*, 3030.

(78) Sun, M. S.; Shah, D. B.; Xu, H. H.; Talu, O. *J. Phys. Chem. B* **1998**, *102*, 1466.

(79) Lin, X.; Telepeni, I.; Blake, A. J.; Dailly, A.; Brown, C. M.; Simmons, J. M.; Zoppi, M.; Walker, G. S.; Thomas, K. M.; Mays, T. J.; Hubberstey, P.; Champness, N. R.; Schröder, M. *J. Am. Chem. Soc.* **2009**, *131*, 2159.

(80) Stan, G.; Cole, M. W. *Surf. Sci.* **1998**, *395*, 280.

(81) Harvey, J. In *Principles and Applications of Density Functional Theory in Inorganic Chemistry I*; Springer Berlin Heidelberg: 2004; Vol. 112, p 151.

(82) Kubas, G. J. *Chem. Rev.* **2007**, *107*, 4152.

(83) Vitillo, J. G.; Regli, L.; Chavan, S.; Ricchiardi, G.; Spoto, G.; Dietzel, P. D. C.; Bordiga, S.; Zecchina, A. *J. Am. Chem. Soc.* **2008**, *130*, 8386.

(84) McPhillips, T. M., McPhillips, S.E., Chiu, J. H., Cohen, A.E., Deacon, A. M., Ellis, P. J., Garman, E., Gonzalez, A., Sauter, N. K., Phizackerley, R. P., Soltis, S. M., Kuhn, P. *J. Synchrotron Rad.* **2002**, 401.

(85) Sheldrick, G. M.; University of Gottingen: 2014.

(86) Sheldrick, G. M. *Acta Crystallogr.* **2008**, *A64*, 112.

(87) Sheldrick, G. M. *Acta Crystallogr.* **2015**, *C71*, 3.

(88) Barbour, L. J. *J. Supramol. Chem.* **2001**, *1*, 189.

(89) Spek, A. L. *Acta Crystallogr.* **2009**, *D65*, 148.

2.11. Appendices

Table 7. Metal Content of Bimetallic MOPs as Determined by EDX.

MOP	M (At %)	Pd (At%)
$Co_{12}Pd_{12}{}^{m}bdc_{24}(C_4H_9NO)_{12}$ (**2.5**)	52.16	47.84
$Ni_{12}Pd_{12}{}^{m}bdc_{24}(C_4H_9NO)_{12}$ (**2.6**)	48.57	51.43
$Zn_{12}Pd_{12}{}^{m}bdc_{24}(C_4H_9NO)_{12}$ (**2.7**)	50.91	49.09
$Co_{12}Pd_{12}(b^{m}bdc)_{24}(C_4H_9NO)_{12}$ (**2.8**)	51.32	48.68
$Ni_{12}Pd_{12}(b^{m}bdc)_{24}(C_4H_9NO)_{12}$ (**2.9**)	49.19	50.81
$Zn_{12}Pd_{12}(b^{m}bdc)_{24}(C_4H_9NO)_{12}$ (**2.10**)	48.30	51.70
$Cu_{14}Pd_{10}(b^{m}bdc)_{24}(C_4H_9NO)_{12}$ (**2.11**)	61.52	38.48
$Co_{12}Pd_{12}(h^{m}bdc)_{24}(C_4H_9NO)_{12}$ (**2.12**)	50.16	49.84
$Ni_{12}Pd_{12}(h^{m}bdc)_{24}(C_4H_9NO)_{12}$ (**2.13**)	49.25	50.75
$Zn_{12}Pd_{12}(h^{m}bdc)_{24}(C_4H_9NO)_{12}$ (**2.14**)	48.70	51.30

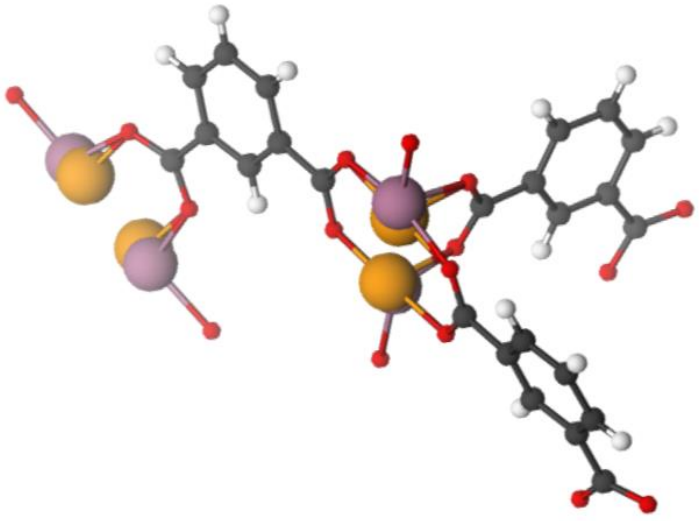

Figure 35. A perspective view of the asymmetric unit of $Co_{12}Pd_{12}{}^{m}bdc_{24}$ (**2.5**). Only the oxygen atom of coordinating solvent molecules were refined. Co and Pd atoms are coloured in mauve and orange respectively.

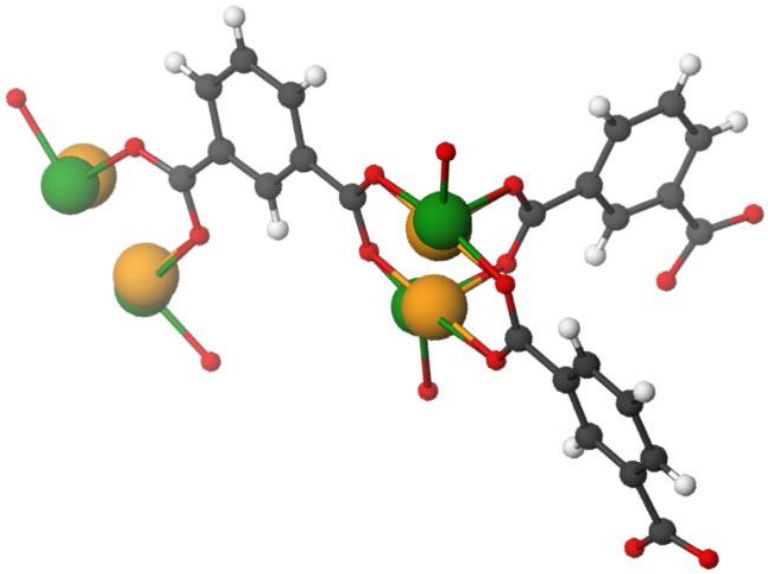

Figure 36. A perspective view of the asymmetric unit of $Ni_{12}Pd_{12}{}^{m}bdc_{24}$ (**2.6**). Only the oxygen atom of coordinating solvent molecules were refined. Ni and Pd atoms are coloured in green and orange respectively.

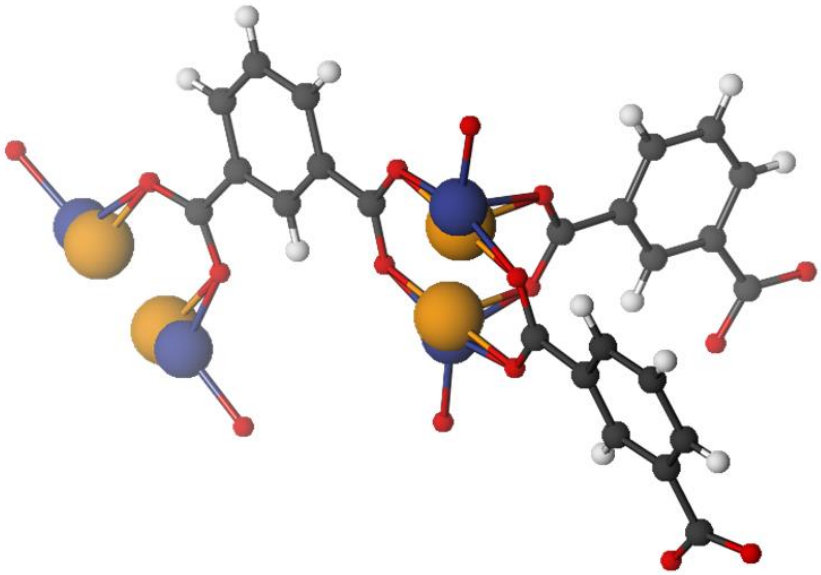

Figure 37. A perspective view of the asymmetric unit of $Zn_{12}Pd_{12}{}^{m}bdc_{24}$ (**2.7**). Only the oxygen atom of coordinating solvent molecules were refined. Zn and Pd atoms are coloured in blue and orange respectively.

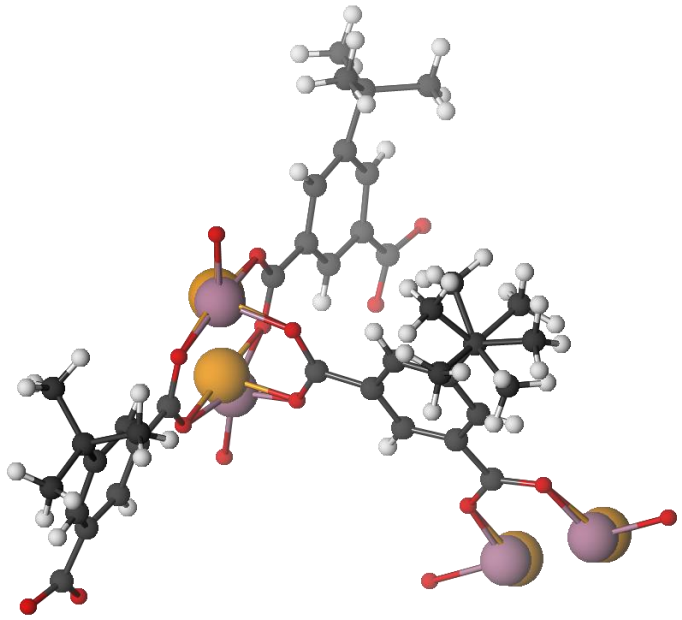

Figure 38. A perspective view of the asymmetric unit of $Co_{12}Pd_{12}b^{m}bdc_{24}$ (**2.8**). Only the oxygen atom of coordinating solvent molecules were refined. Co and Pd atoms are coloured in mauve and orange respectively.

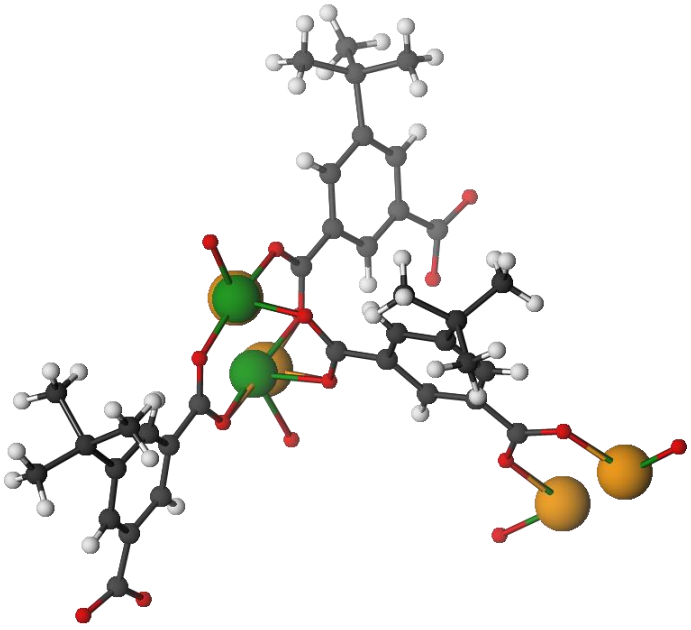

Figure 39. A perspective view of the asymmetric unit of $Ni_{12}Pd_{12}b^{m}bdc_{24}$ (**2.9**). Only the oxygen atom of coordinating solvent molecules were refined. Co and Pd atoms are coloured in mauve and orange respectively.

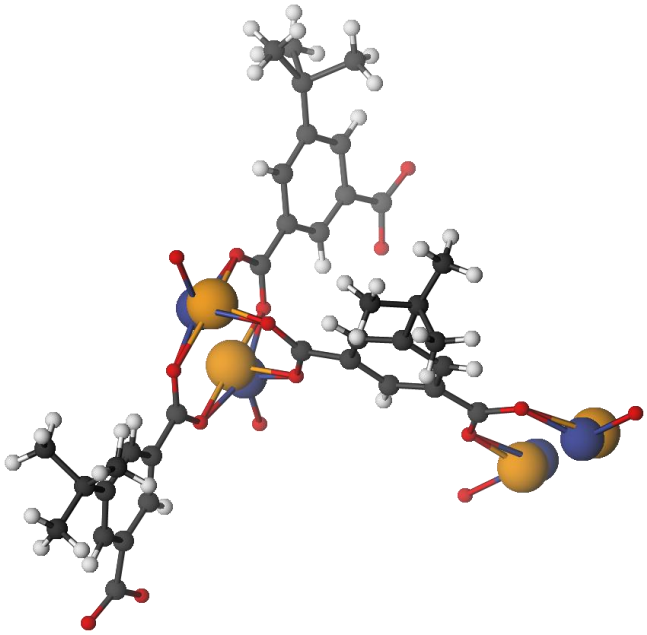

Figure 40. A perspective view of the asymmetric unit of $Zn_{12}Pd_{12}b^{m}bdc_{24}$ (**2.10**). Only the oxygen atom of coordinating solvent molecules were refined. Co and Pd atoms are coloured in mauve and orange respectively.

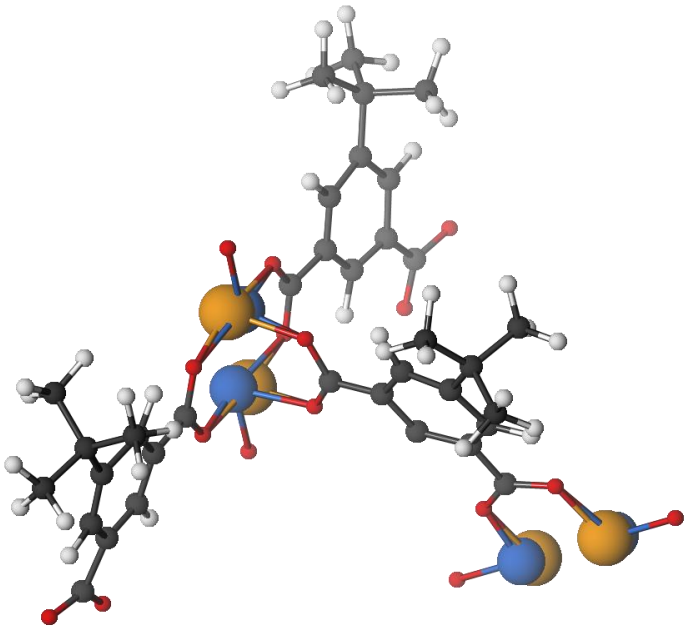

Figure 22. A perspective view of the asymmetric unit of $Cu_{14}Pd_{10}b^{m}bdc_{24}$ (**2.11**). Only the oxygen atom of coordinating solvent molecules were refined. Co and Pd atoms are coloured in mauve and orange respectively.

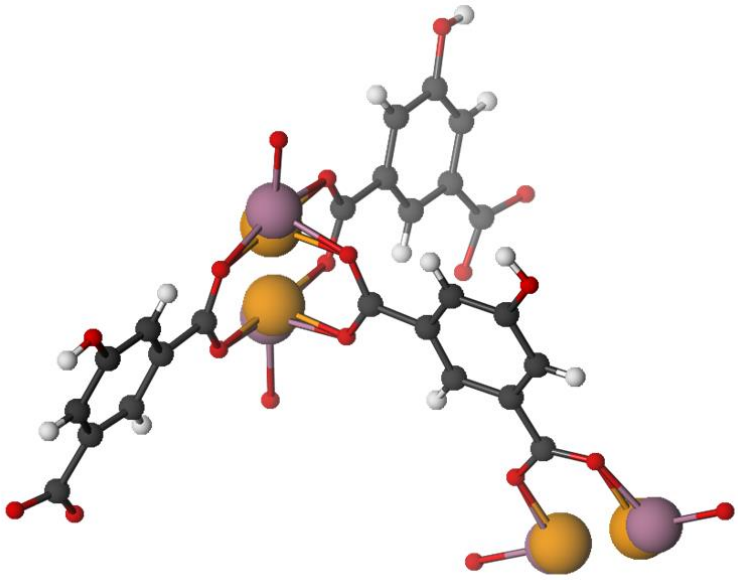

Figure 42. A perspective view of the asymmetric unit of $Co_{12}Pd_{12}h^{m}bdc_{24}$ (**2.12**). Only the oxygen atom of coordinating solvent molecules were refined. Co and Pd atoms are coloured in mauve and orange respectively.

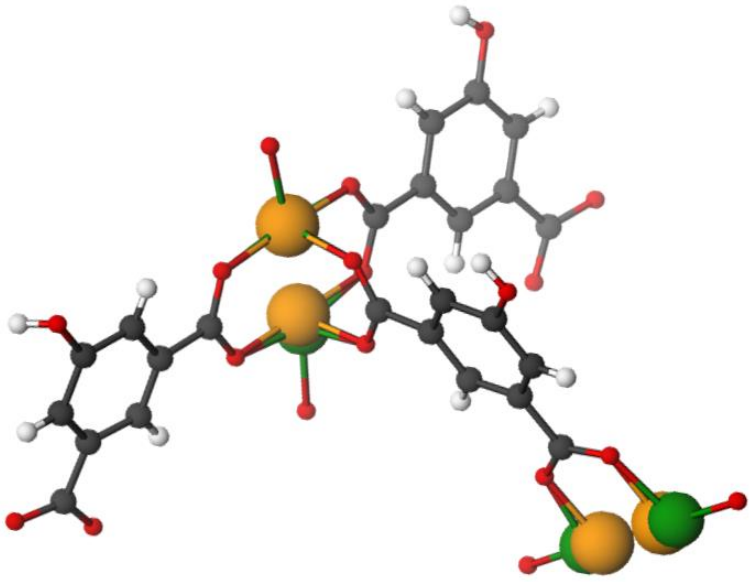

Figure 43. A perspective view of the asymmetric unit of $Ni_{12}Pd_{12}h^{m}bdc_{24}$ (**2.13**). Only the oxygen atom of coordinating solvent molecules were refined. Ni and Pd atoms are coloured in green and orange respectively.

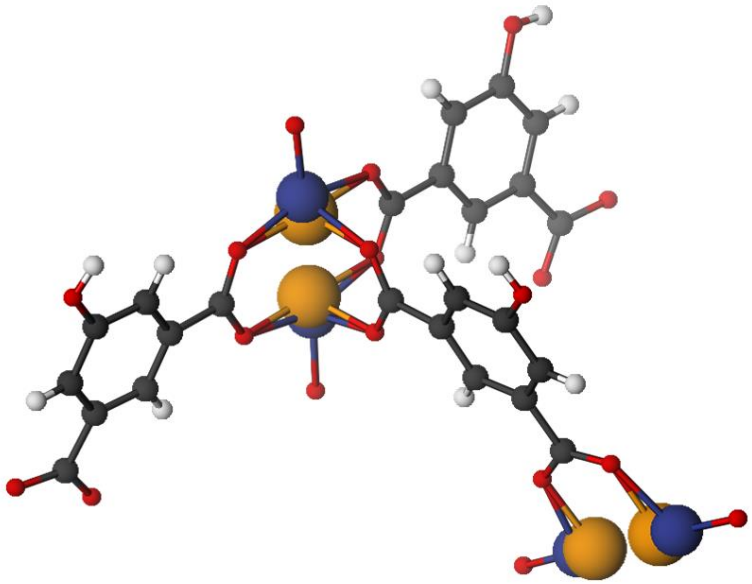

Figure 44. A perspective view of the asymmetric unit of $Zn_{12}Pd_{12}h^{m}bdc_{24}$ (**2.14**). Only the oxygen atom of coordinating solvent molecules were refined. Zn and Pd atoms are coloured in blue and orange respectively.

Table 8. Crystallographic data for isophthalate bimetallic MOPS.

Compound	**2.5**	**2.6**	**2.7**
Empirical formula	$C_{192}H_{96}Co_{12}O_{108}Pd_{12}$	$C_{192}H_{96}Ni_{12}O_{108}Pd_{12}$	$C_{192}H_{96}O_{108}Pd_{12}Zn_{12}$
Formula weight	6114.64	6112	6191.92
Crystal system	Tetragonal	Tetragonal	Tetragonal
Space group	*P4/mnc*	*P4/mnc*	*P4/mnc*
$a = b$ (Å)	28.910 (4)	28.917 (4)	28.986 (4)
c (Å)	27.719 (6)	27.680 (6)	27.798 (6)
$\alpha = \beta = \gamma$ (°)	90	90	90
Volume (Å^3)	23167 (8)	23146 (8)	23356 (8)
Z	2	2	2
Density (calc.) (mg/m^3)	0.877	0.877	0.880
Absorption coefficient (mm^{-1})	0.62	0.976	1.10
F(000)	5976	6000	6048
θ range for data collection (°)	1.0 to 26.1	1.0 to 24.7	1.0 to 27.1
Observed reflections	10279	8479	11500
Reflections collected	11795	10048	13167
[R(int)]	0.0815	0.064	0.057
Restraints/parameters	0/415	0/415	0/415
Completeness (%)	0.997	0.994	0.998
Goodness-of-fit on F^2	1.089	1.065	1.06
R_1 [I>2σ(I)]	0.0586	0.062	0.0577
wR_2 (all data)	0.191	0.206	0.192
Largest peak (e.Å^{-3})	1.675	1.311	1.587
Deepest hole (e.Å^{-3})	-1.036	-0.540	-1.325

Table 9. Crystallographic data for *t*-butyl bimetallic MOPS.

Compound	**2.8**	**2.9**	**2.10**	**2.11**
Empirical formula	$C_{288}H_{288}Co_{12}O_{108}Pd_{12}$	$C_{288}H_{288}Ni_{12}O_{108}Pd_{12}$	$C_{288}H_{288}O_{108}Pd_{12}Zn_{12}$	$C_{288}H_{288}Cu_{12}O_{108}Pd_{12}$
Formula weight	7461.13	7458.49	7538.41	7516.45
Crystal system	Tetragonal	Tetragonal	Tetragonal	Tetragonal
Space group	*I*4/*m*	*I*4/*m*	*I*4/*m*	*I*4/*m*
$a = b$ (Å)	29.012 (4)	29.174 (4)	28.935 (4)	28.980 (4)
c (Å)	41.159 (8)	41.296 (8)	41.164 (8)	40.961 (8)
$\alpha = \beta = \gamma$ (°)	90	90	90	90
Volume (Å^3)	34643 (12)	35147 (12)	34464 (12)	34400 (10)
Z	2	2	2	2
Density (calc.) (mg/m^3)	0.715	0.705	0.726	0.726
Absorption coefficient (mm^{-1})	0.62	0.65	0.75	0.71
F(000)	7512	7536	7584	7560
θ range for data collection (°)	1.0 to 22.7	1.0 to 24.7	1.0 to 20.7	1.0 to 22.7
Observed reflections	9345	12015	7333	9612
Reflections collected	11804	15259	9079	11778
[R(int)]	0.089	0.065	0.061	0.096
Restraints/parameters	27/565	8/494	21/517	21/532
Completeness (%)	0.998	0.937	0.998	0.998
Goodness-of-fit on F^2	1.06	1.07	1.04	1.04
R_1 [I>2σ(I)]	0.089	0.069	0.083	0.095
wR_2 (all data)	0.216	0.218	0.215	0.245
Largest peak (e.Å^{-3})	0.575	1.291	0.484	0.072
Deepest hole (e.Å^{-3})	-0.716	-0.603	-0.351	-1.041

Table 10. Crystallographic data for hydroxy bimetallic MOPS.

Compound	**2.12**	**2.13**	**2.14**
Empirical formula	$C_{192}H_{96}Co_{12}O_{132}Pd_{12}$	$C_{192}H_{96}Ni_{12}O_{132}Pd_{12}$	$C_{192}H_{96}O_{132}Pd_{12}Zn_{12}$
Formula weight	6498.64	6496	6575.92
Crystal system	Tetragonal	Tetragonal	Tetragonal
Space group	*I*4/*m*	*I*4/*m*	*I*4/*m*
$a = b$ (Å)	30.742 (4)	30.689 (4)	30.689 (4)
c (Å)	31.226 (6)	31.088 (6)	31.117 (6)
$\alpha = \beta = \gamma$ (°)	90	90	90
Volume (Å^3)	29510 (10)	29184 (10)	29305 (10)
Z	2	2	2
Density (calc.) (mg/m^3)	0.731	0.737	0.745
Absorption coefficient (mm^{-1})	0.725	0.777	0.882
F(000)	6360	6384	6432
θ range for data collection (°)	0.9 to 25	0.9 to 27	0.9 to 27.5
Observed reflections	11161	14497	12718
Reflections collected	13278	17141	15687
[R(int)]	0.069	0.052	0.0846
Restraints/parameters	0/434	0/446	0/415
Completeness (%)	0.995	0.992	0.914
Goodness-of-fit on F^2	0.931	1.050	1.116
R_1 [I>2σ(*I*)]	0.060	0.042	0.070
wR_2 (all data)	0.235	0.135	0.215
Largest peak (e.Å^{-3})	1.792	2.480	2.480
Deepest hole (e.Å^{-3})	-1.020	-0.790	-2.760

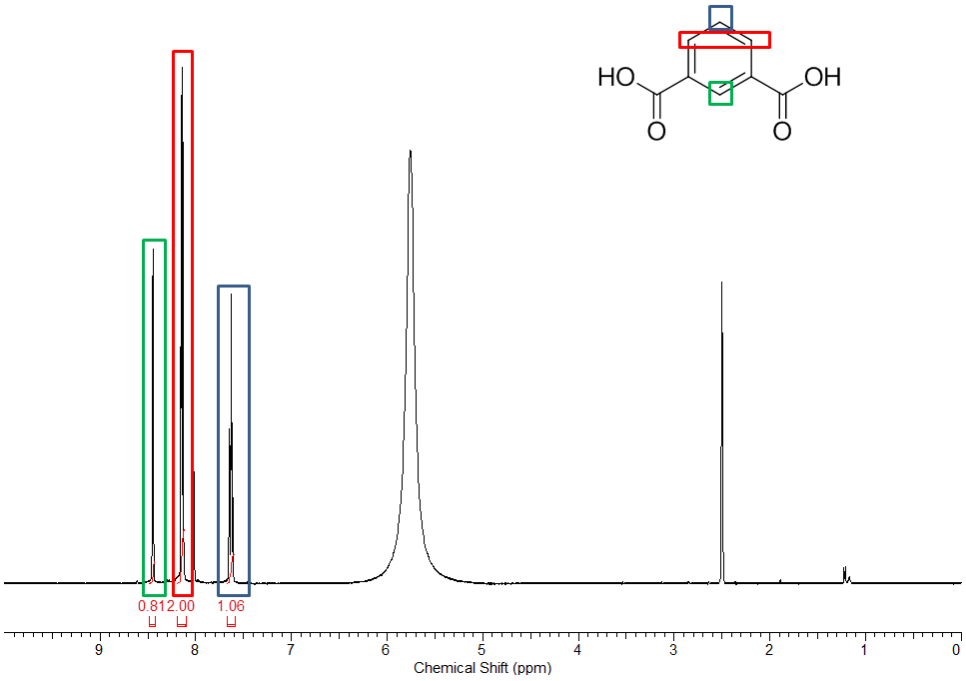

Figure 45. ^{1}H NMR spectrum of a DCl d_6-DMSO digested sample of activated $Co_{12}Pd_{12}{}^{m}bdc_{24}$. The large peak between 5-6 ppm is from residual water in the D_2O/DCl solution.

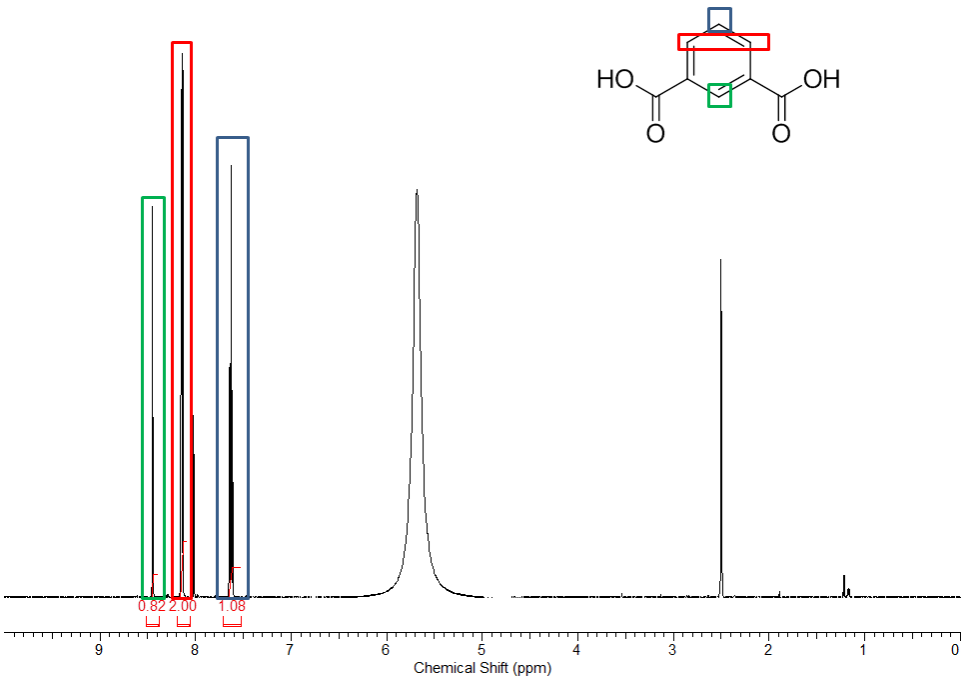

Figure 46. ^{1}H NMR spectrum of a DCl d_6-DMSO digested sample of activated $Ni_{12}Pd_{12}{}^{m}bdc_{24}$. The large peak between 5-6 ppm is from residual water in the D_2O/DCl solution.

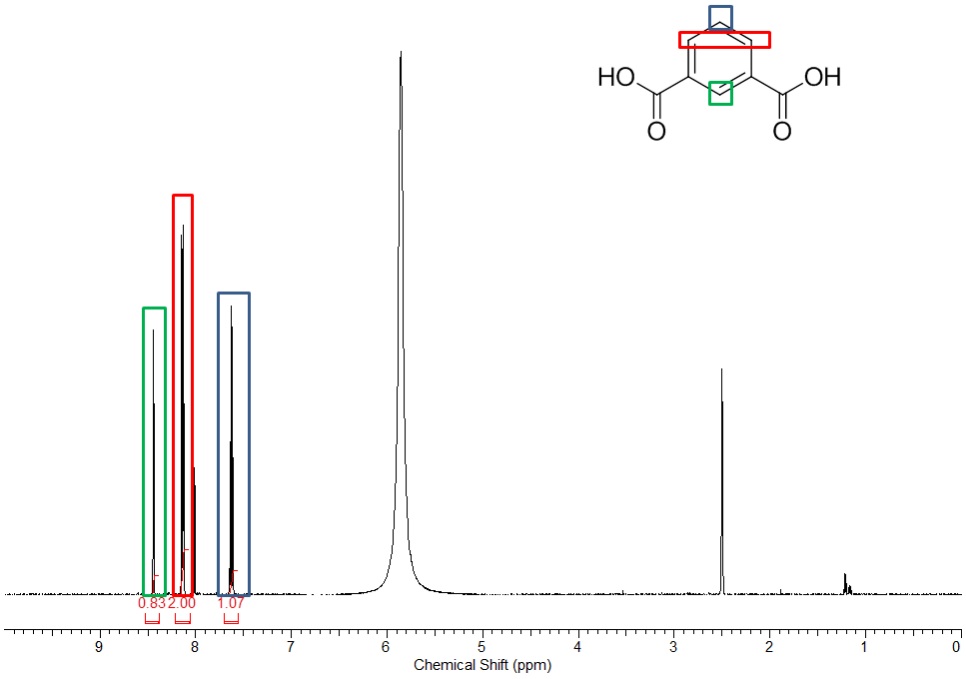

Figure 47. ^{1}H NMR spectrum of a DCl d_6-DMSO digested sample of activated $Zn_{12}Pd_{12}{}^{m}bdc_{24}$. The large peak between 5-6 ppm is from residual water in the D_2O/DCl solution.

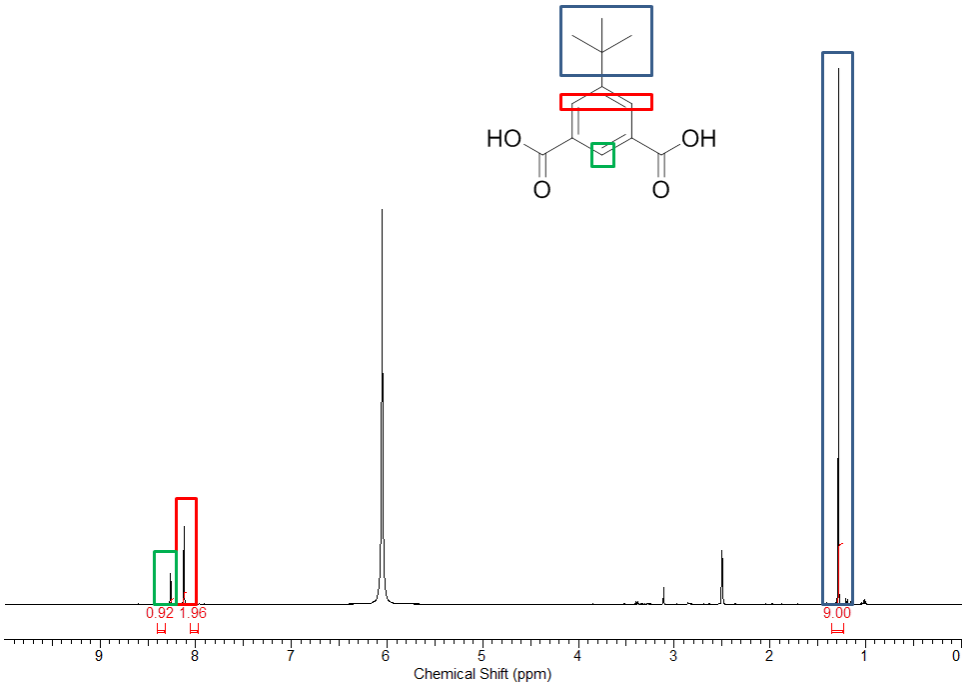

Figure 48. ^{1}H NMR spectrum of a DCl d_6-DMSO digested sample of activated $Co_{12}Pd_{12}b^{m}bdc_{24}$. The large peak at 6 ppm is from residual water in the D_2O/DCl solution.

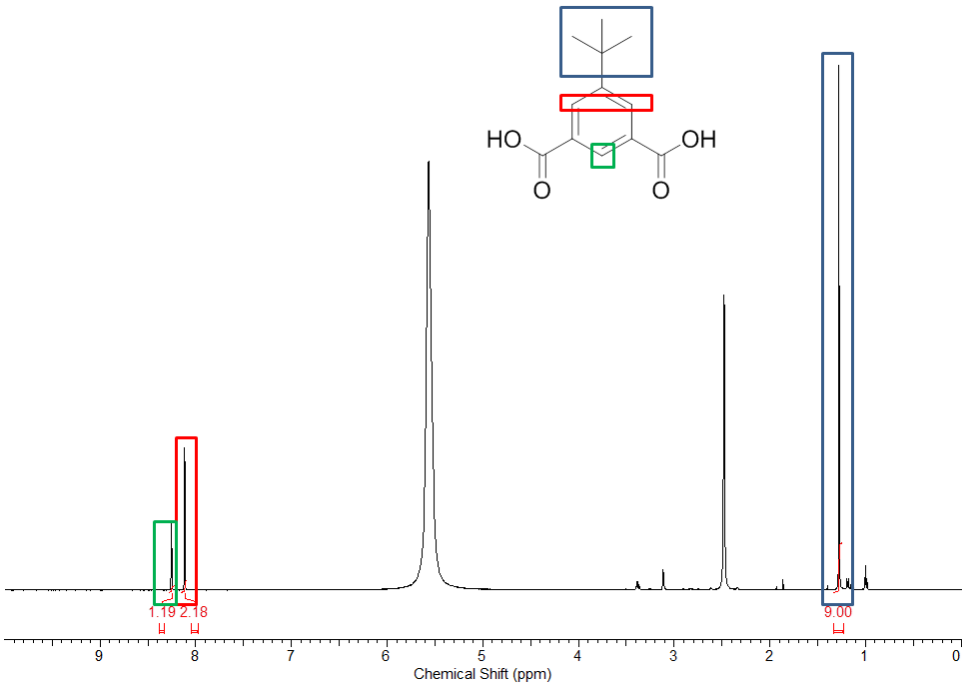

Figure 49. ^{1}H NMR spectrum of a DCl d_6-DMSO digested sample of activated $Ni_{12}Pd_{12}b^{m}bdc_{24}$. The large peak between 5-6 ppm is from residual water in the D_2O/DCl solution.

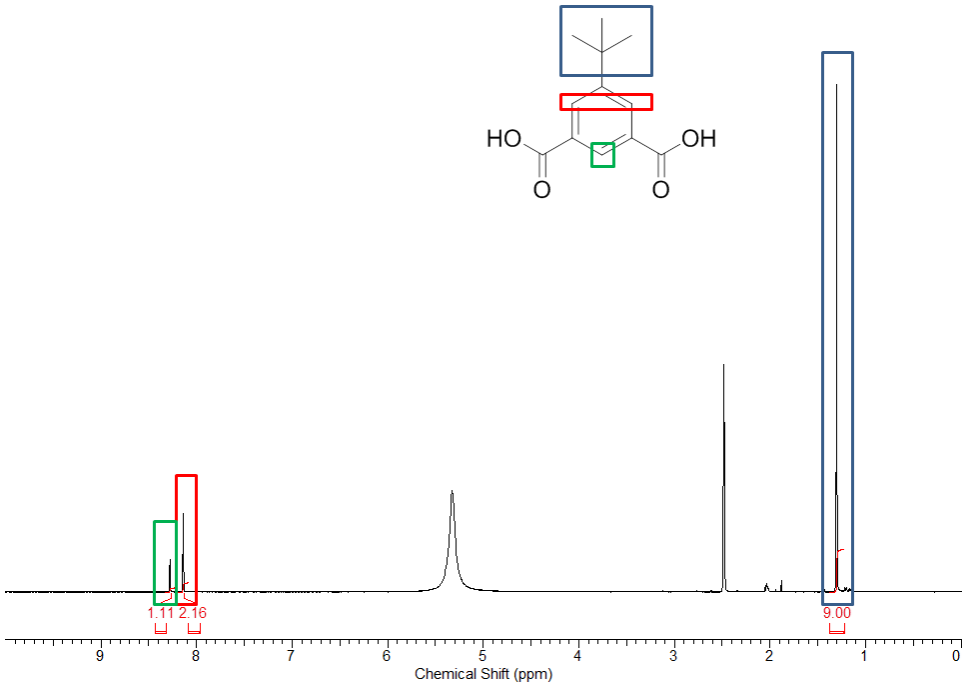

Figure 50. ^{1}H NMR spectrum of a DCl d_6-DMSO digested sample of activated $Zn_{12}Pd_{12}b^{m}bdc_{24}$. The large peak between 5-6 ppm is from residual water in the D_2O/DCl solution.

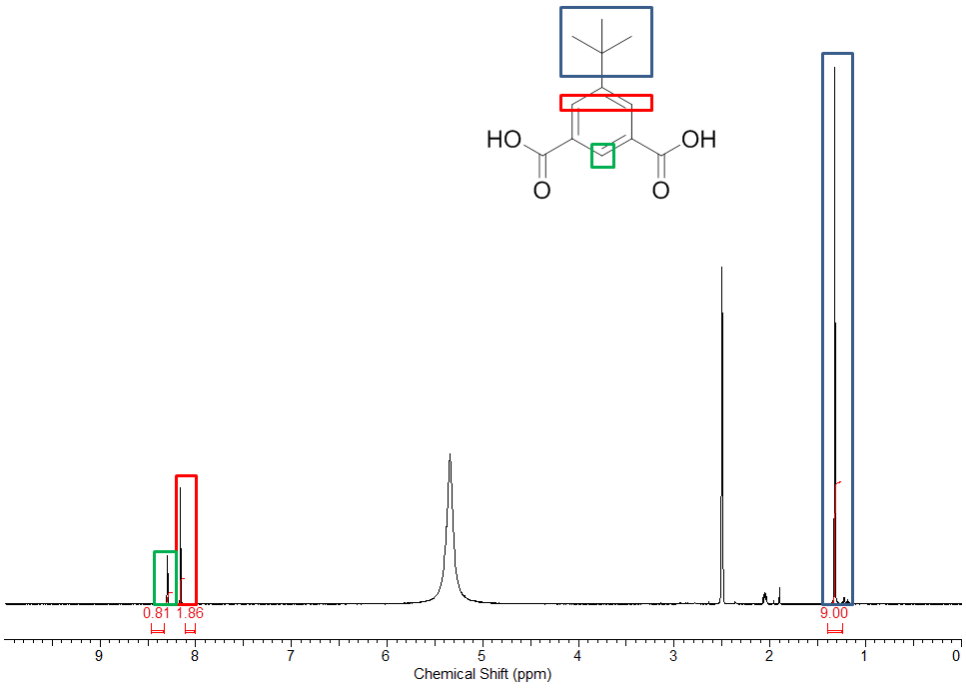

Figure 51. ^{1}H NMR spectrum of a DCl d_6-DMSO digested sample of activated $Cu_{14}Pd_{10}b^{m}bdc_{24}$. The large peak between 5-6 ppm is from residual water in the D_2O/DCl solution.

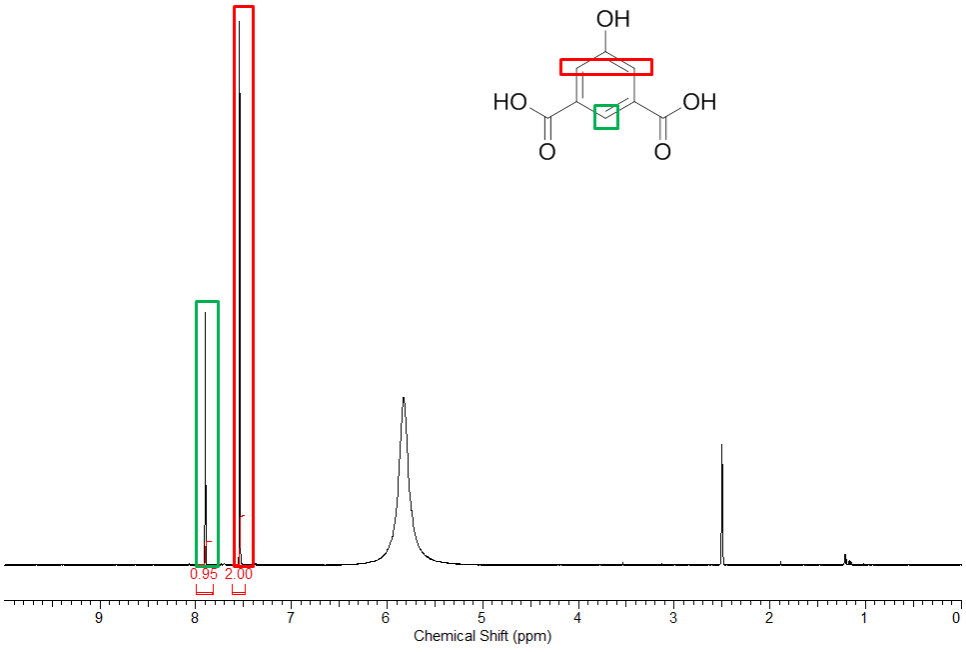

Figure 52. ^{1}H NMR spectrum of a DCl d_6-DMSO digested sample of activated $Co_{12}Pd_{12}h^{m}bdc_{24}$. The large peak between 5-6 ppm is from residual water in the D_2O/DCl solution.

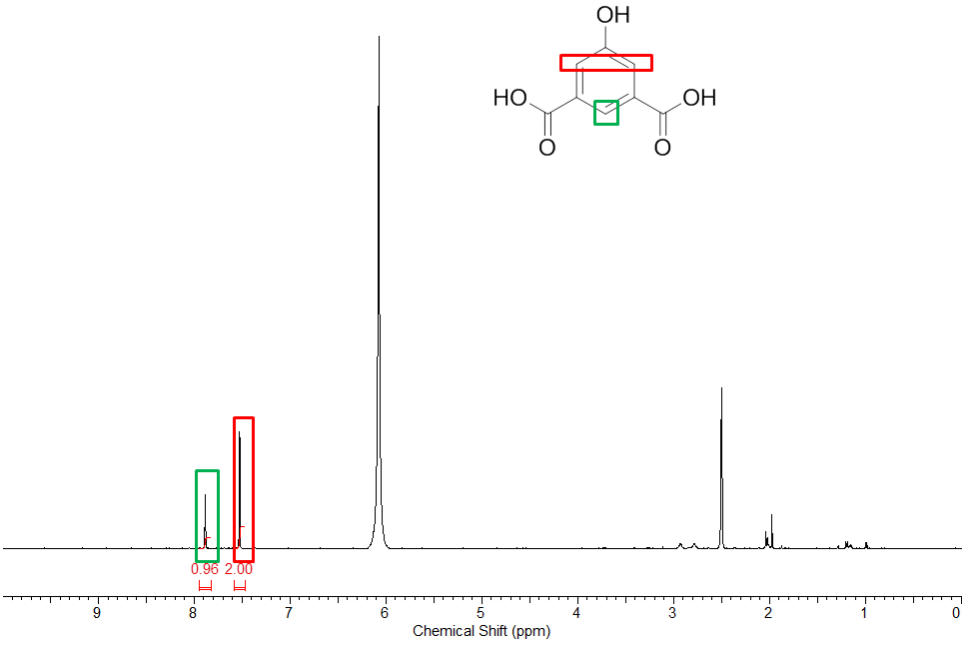

Figure 53. ^{1}H NMR spectrum of a DCl d_6-DMSO digested sample of activated $Ni_{12}Pd_{12}h^{m}bdc_{24}$. The large peak at 6 ppm is from residual water in the D_2O/DCl solution.

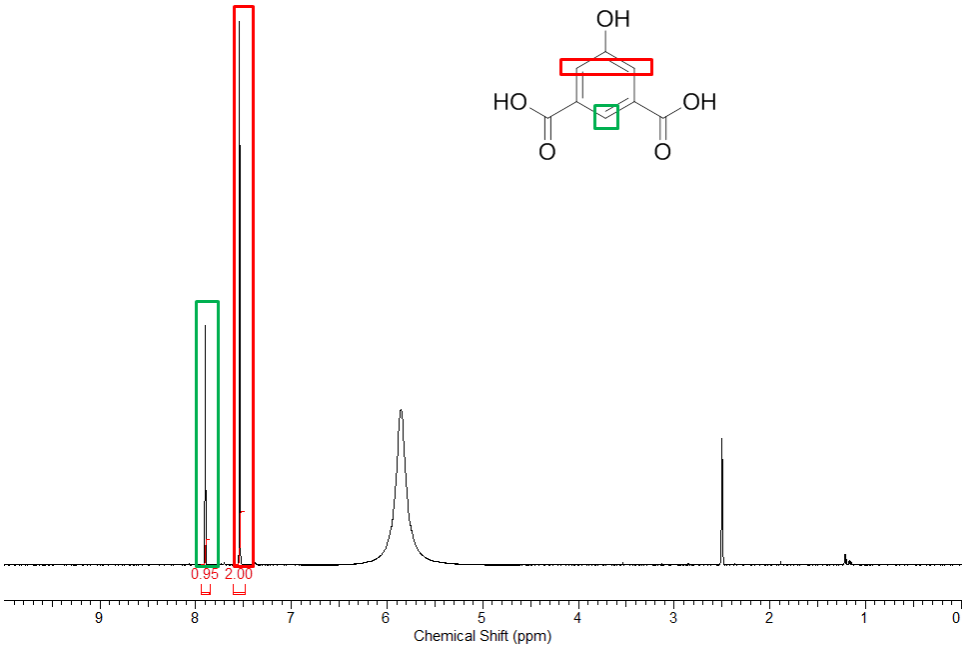

Figure 54. ^{1}H NMR spectrum of a DCl d_6-DMSO digested sample of activated $Zn_{12}Pd_{12}h^{m}bdc_{24}$. The large peak between 5-6 ppm is from residual water in the D_2O/DCl solution.

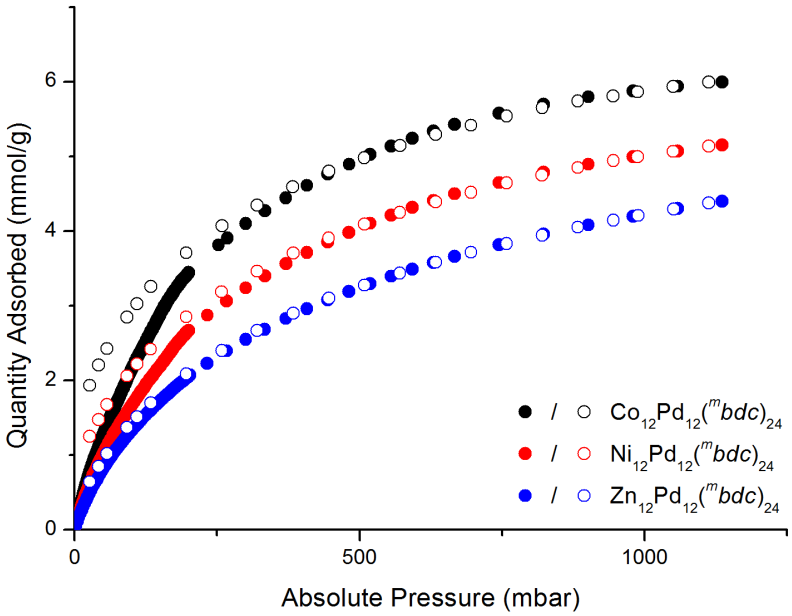

Figure 55. H_2 adsorption isotherms collected at 87 K for ^{m}bdc MOPs following activation with acetone and supercritical CO_2. Closed and open symbols represent adsorption and desorption data, respectively.

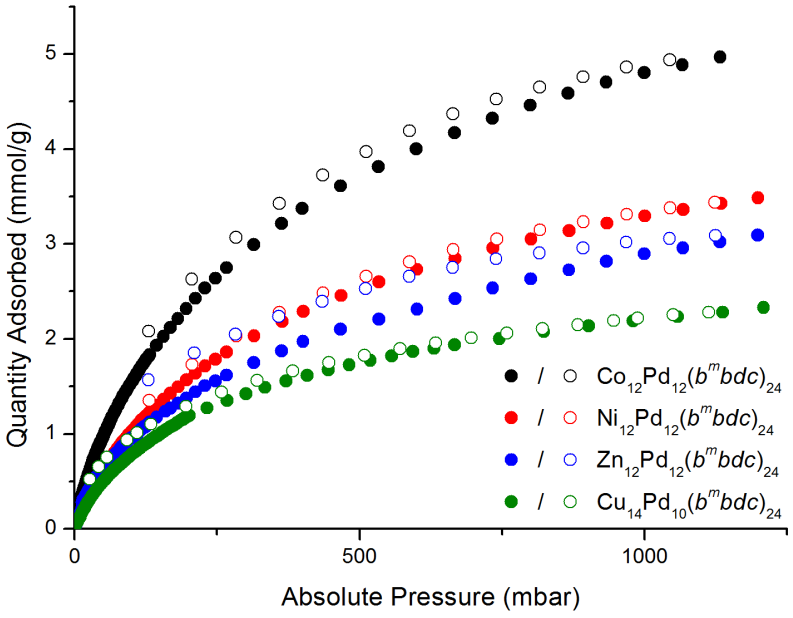

Figure 56. H_2 adsorption isotherms collected at 87 K for $b^{m}bdc$ MOPs following activation with acetone and supercritical CO_2. Closed and open symbols represent adsorption and desorption data, respectively.

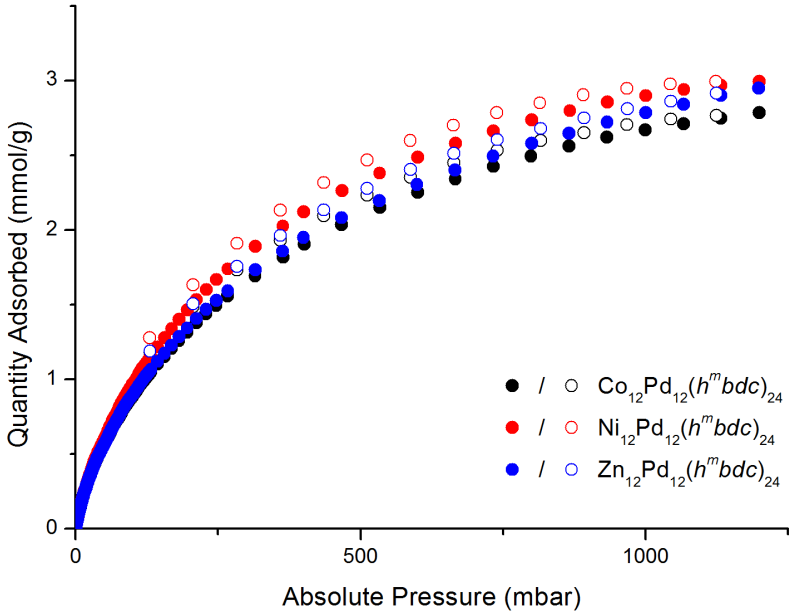

Figure 57. H_2 adsorption isotherms collected at 87 K for $h^m bdc$ MOPs following activation with acetone and supercritical CO_2. Closed and open symbols represent adsorption and desorption data, respectively.

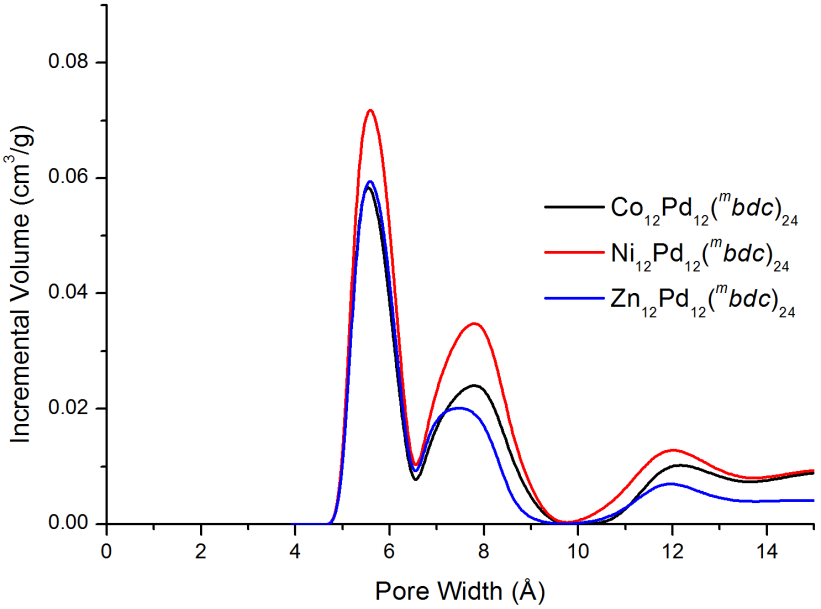

Figure 58. Pore size distribution of bimetallic $^m bdc$ MOPs determined from N_2 gas adsorption at 77 K.

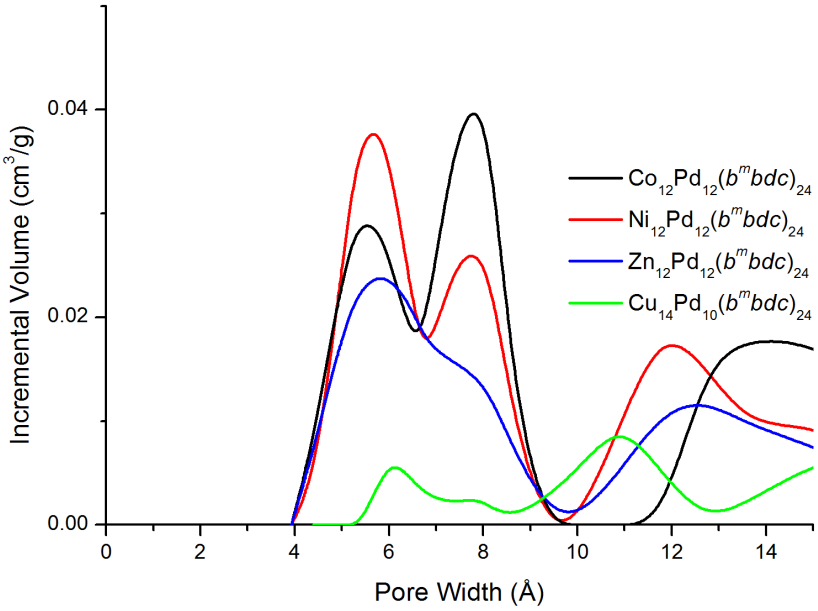

Figure 59. Pore size distribution of bimetallic *b*^{m}*bdc* MOPs determined from N_2 gas adsorption at 77K.

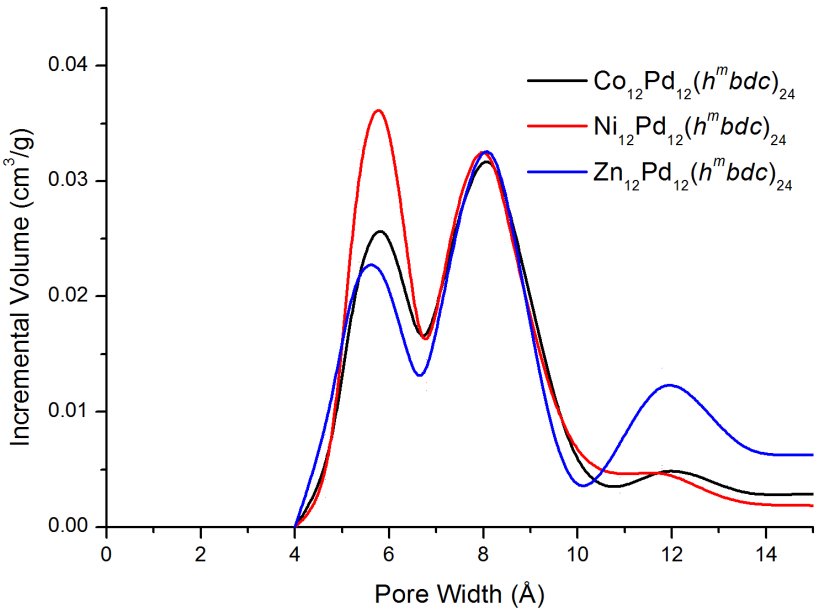

Figure 60. Pore size distribution of bimetallic *h*^{m}*bdc* MOPs determined from N_2 gas adsorption at 77K.

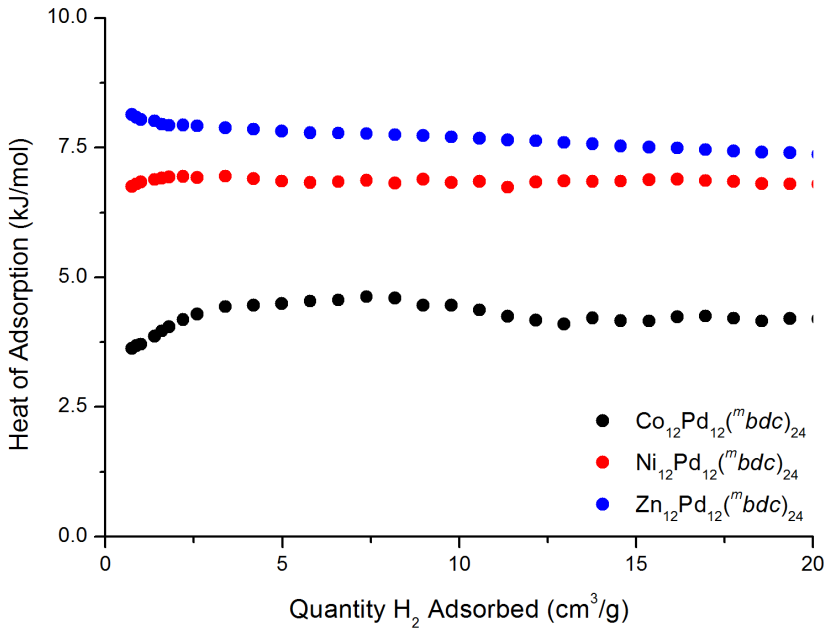

Figure 61. Van't Hoff isochore plots calculated from the 77K and 87K H_2 adsorption of bimetallic ^{m}bdc MOPs.

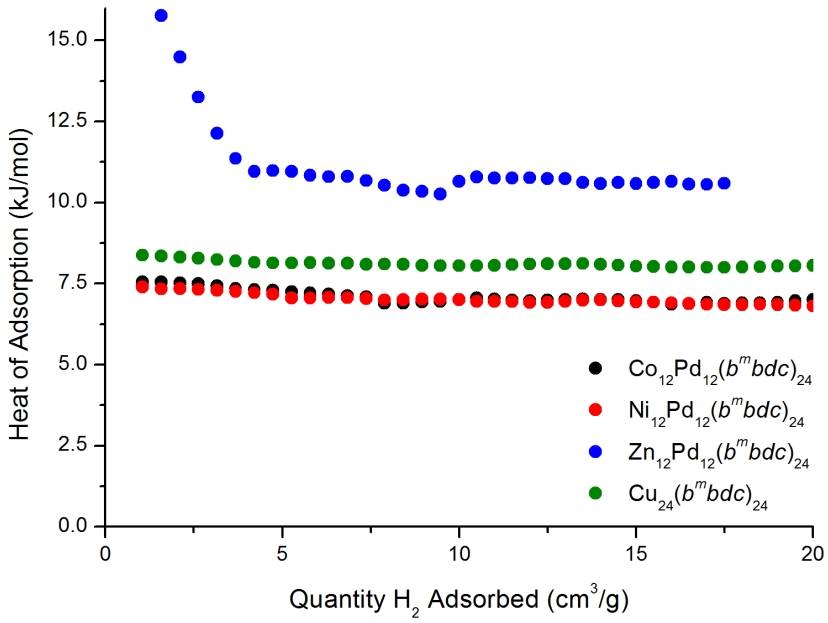

Figure 62. Van't Hoff isochore plots calculated from the 77K and 87K H_2 adsorption of bimetallic $b^{m}bdc$ MOPs.

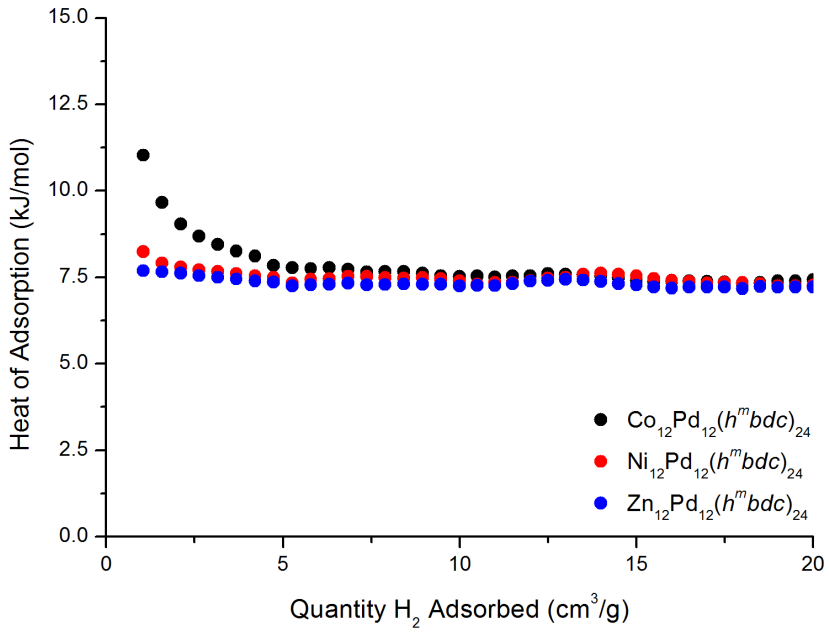

Figure 63. Van't Hoff isochore plots calculated from the 77K and 87K H_2 adsorption of bimetallic h^m*bdc* MOPs.

CHAPTER 3.

EXOHEDRALLY FUNCTIONALISED METAL-ORGANIC POLYHEDRA

Chapter 3. Exohedrally Functionalised Metal-Organic Polyhedra

3.1. Introduction

The external surface chemistry of discrete molecular structures is known to dramatically influence molecular packing, giving rise to changes in both the micro- and macroscopic properties of porous materials. This is due to the myriad of interactions that occur at the intermolecular interface, including hydrogen bonding, Van der Waals, ionic attraction, π-stacking, halogen bonding and mechanical interlocking.[1-6] These intermolecular interactions, such as the directional hydrogen bonding between carboxylic acid motifs (Figure 64), are known to govern packing arrangements in a crystalline state; hence structurally directive functionalisation has been extensively explored in the field of crystal engineering.[7-9]

One of the more obvious exploitations of hydrogen bonding is seen in the work of Karmakar *et al.* in their report of hydrogen-bonded organic frameworks (HOFs) composed of arene sulphonates and guanidinium ions.[10] These materials exhibit exceptional proton conduction properties due to the presence of an ionic backbone. The organic framework prepared by Marti-Rujas *et al.* is an example of a material that features both hydrogen and halogen bonding in its structure.[11] While the authors make no report of permanent porosity, the framework, which features two dimensional channels, is able to undergo a single-crystal-to-single-crystal transformation upon immersion in 1,3-dibromobenzene. This transformation is possible due to the more flexible nature of the non-covalent structural interactions. Examples of structural halogen bonding is exemplified by the work of Pigge *et al.* in their 4-iodophenoxy trimesoate complexes.[12] These materials display both halogen-carbonyl and halogen-π bonding, resulting in a crystalline framework with hexagonal pore channels.As such, the influence of these crystal packing forces can be exploited to tune the pore architecture and functionality of the resulting materials, by allowing or restricting guest access to any intrinsic pore space, or through secondary influences on extrinsic pore space that exists between discrete entities.[5]

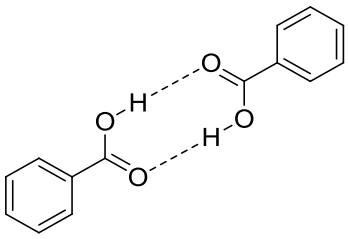

Figure 64. Representation of the directional hydrogen bonding between carboxylic acid pairs.

This chapter presents the synthesis of four new MOPs that incorporate novel ligands and details a method of elucidating structural parameters from highly disordered structural motifs. The described MOPs are isostructural to the prototypical $M_{24}L_{24}$ MOP-1 synthesised by Yaghi and co-workers, comprised of a metal paddle-wheel motif and isophthalate linkers.[13] Since this first MOP synthesis in 2001, work has been carried out to add chemical groups to the MOP exterior, including alkyl chains and hydrophilic groups, in order to increase the solubility or enhance surface interactions.[14-16] To expand on the existing work found in the literature and to advance the crystal engineering of MOP materials, the work in this chapter is focussed on the synthesis of new metal-organic polyhedra that vary in the chemical functionality of the external surface and hence demonstrate a directed packing upon crystallisation (Figure 65). While this chapter gives particular focus to the effects these exohedral groups have on the cage packing in the crystalline matrix, changes in the chemistry and structures of the MOPs have a significant role to play in the synthesis of mixed matrix materials, which is discussed in Chapter 4.

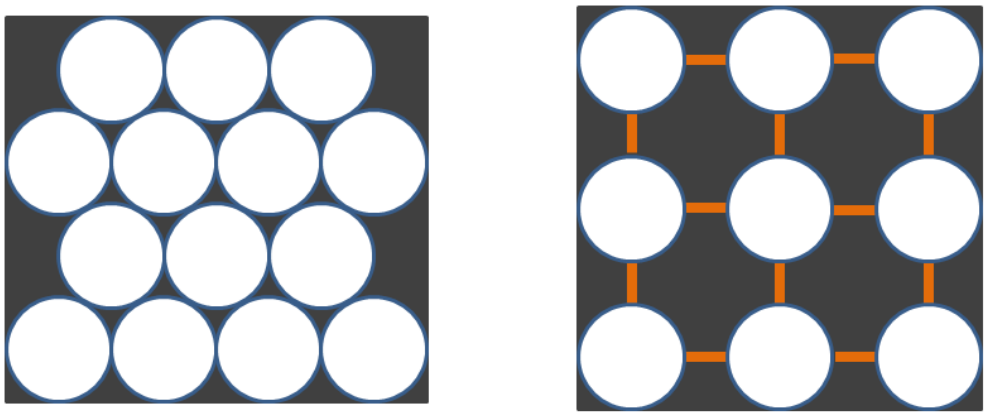

Figure 65. Schematic representations of naturally packed circles (left) and under directed packing by peripheral interactions (right).

3.2. Synthesis of Functionalised Isophthalic Acids

The structure of MOP-1 type materials allows for the introduction of external functionality through the use of isophthalate linkers with substituents in the 5-position. An overview of the organic compounds synthesised in this section is given in Figure 66. While attempts were made to include more elaborate hydrogen bonding motifs, such as diamino-triazines, these proved synthetically troublesome and were subsequently abandoned.

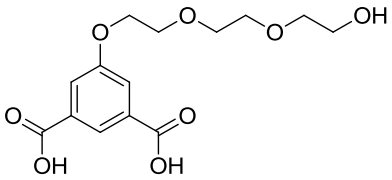

5-(2-(2-(2-hydroxyethoxy)ethoxy)ethoxy)isophthalic acid (**3.1**)

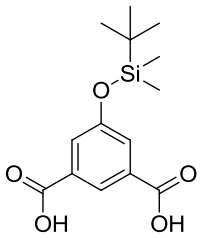

5-((*tert*-butyldimethylsilyl)oxy)isophthalic acid (**3.2**)

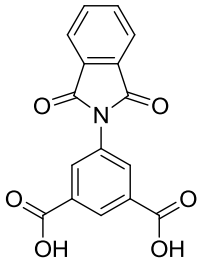

5-(1,3-dioxoisoindolin-2-yl)isophthalic acid (**3.3**)

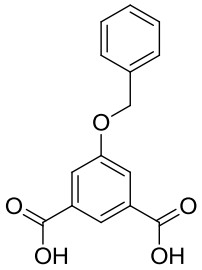

5-(benzyloxy)isophthalic acid (**3.4**)

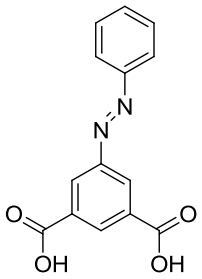

5-(phenyldiazenyl)isophthalic acid (**3.5**)

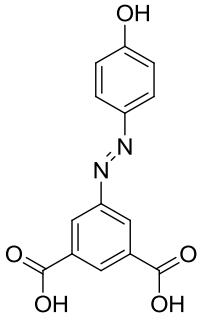

5-((4-hydroxyphenyl)diazenyl)isophthalic acid (**3.6**)

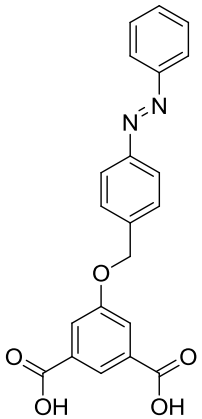

5-((4-(phenyldiazenyl)benzyl)oxy)isophthalic acid (**3.7**)

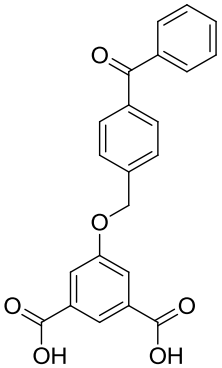

5-((4-benzoylbenzyl)oxy)isophthalic acid (**3.8**)

Figure 66. Isophthalic acids synthesised for use as organic bridges in MOPs.

*3.2.1. Synthesis of 5-(2-(2-(2-hydroxyethoxy)ethoxy)ethoxy)isophthalic acid (**3.1**)*

The addition of ethylene glycol chains to the surface of a MOP has been carried out by Tonigold and associates, conferring water solubility to the cuboctahedral MOP core.[17] As an increased solubility can be beneficial for many functional materials, such as mixed matrix membranes, drug delivery platforms and water treatment agents, **3.1** was intended to generate a hydrophilic nanostructure capable of strong interactions with its environment.[18-20]

3.1 was synthesised from 5-hydroxy isophthalic acid based on a literature procedure.[17] The first step was selective protection of the carboxylic acid groups via esterification with methanol. This allowed for reaction of a chlorinated glycol chain at the hydroxyl group to afford the desired compound which was isolated by ion exchange chromatography prior to saponification with KOH in a 52% yield over 3 steps (Figure 67).

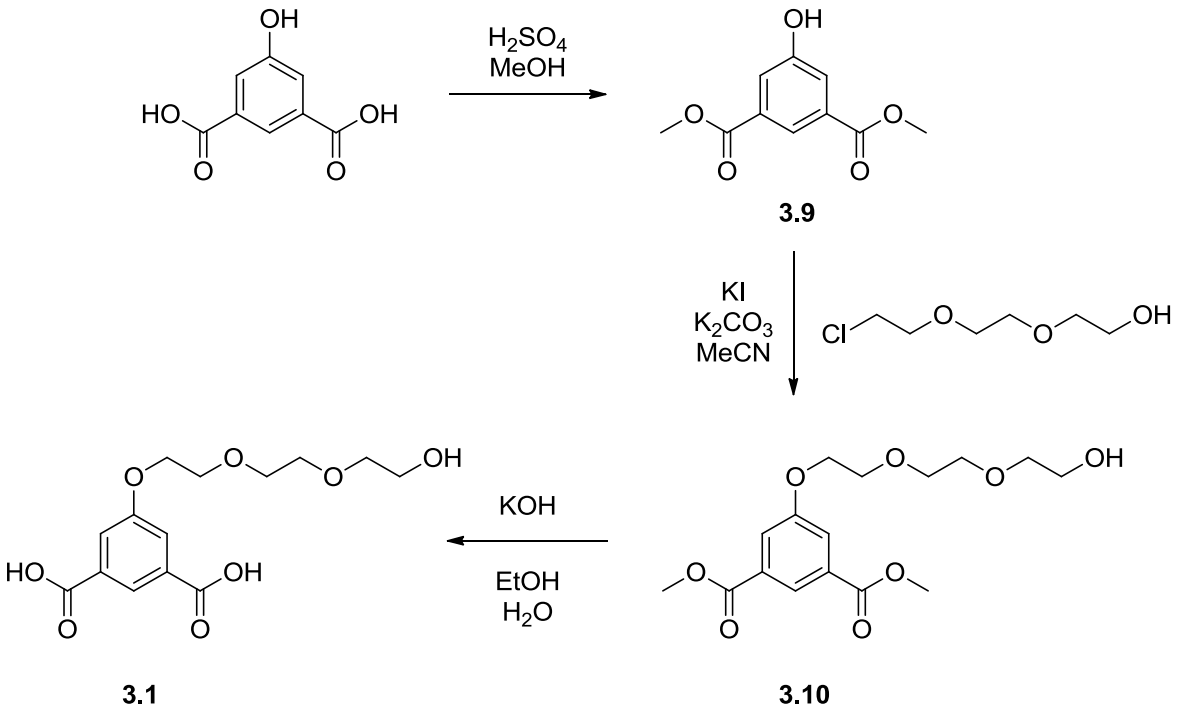

Figure 67. Synthesis of 5-(2-(2-(2-hydroxyethoxy)ethoxy)ethoxy)isophthalic acid (**3.1**)

*3.2.2. Synthesis of 5-((tert-butyldimethylsilyl)oxy)isophthalic acid (**3.2**)*

Two major aims were taken into account in the design of isophthalic acid **3.2** which contains an alkylated silyl motif. The first was to allow the construction of a MOP with an extremely hydrophobic exterior while limiting the potential for cage interweaving by long flexible surface groups, as is seen in MOP-18 which features a 12-carbon chain.[13] The bulky, alkylated silyl groups however also were intended to serve a secondary purpose in the development of mixed matrix membranes. The silyl moiety is similar to that seen in polymers of high interest for gas separation technology, such as Poly[1-(trimethylsilyl)-1-propyne] (PTMSP).[21] It was proposed that the structural similarities between **3.2** and PTMSP would allow for strong MOP-polymer interactions, addressing one of the major performance barriers in the production of mixed matrix membranes.[22,23] Initial attempts were made to synthesise a trimethyl silyl analogue as this more closely mirrors the chemical structure of PTMSP polymer, however the silyl group was found to be cleaved during deprotection of the carboxylic acids. As such, **3.2** was chosen due to its increased stability over the trimethyl counterpart.

3.2 was synthesised over two steps from 5-hydroxy isophthalic acid using *t*-butylchlorodimethylsilane in an inert atmosphere, based upon literature methods.[24] Regeneration of the carboxylic acids was carried out under the mild hydrolysis conditions of acetic acid in THF and water (Figure 68).

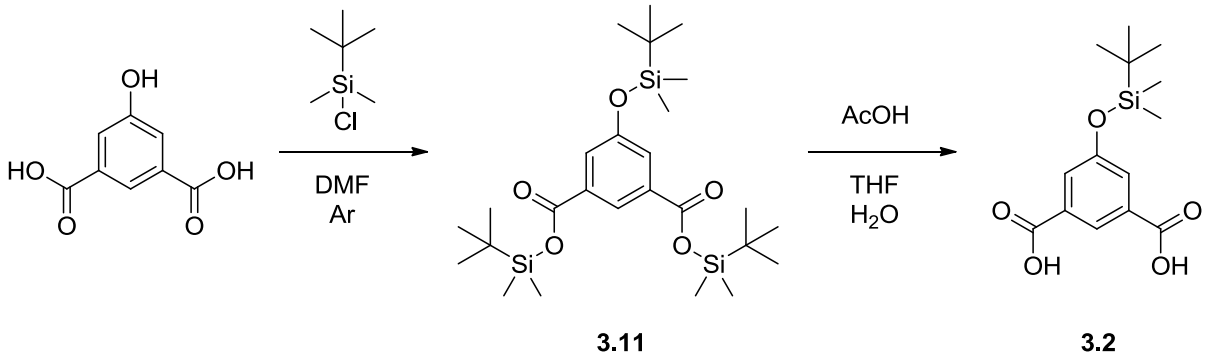

Figure 68. Synthesis of 5-((*tert*-butyldimethylsilyl)oxy)isophthalic acid (**3.2**)

*3.2.3. Synthesis of 5-(1,3-dioxoisoindolin-2-yl)isophthalic acid (**3.3**)*

The design rationale for compound **3.3** was similar to that of **3.2**. The structure of the isophthalic acid was designed to mimic that observed in Matrimid type polymers, which contain an imide bonding motif in the repeating unit.[25,26] Matrimid polymers, like PTMSP, are promising candidates for application in mixed matrix membranes and thus **3.3** was designed to maximise possible interactions between itself and the polymer through a combination of π-π interactions and hydrogen bonding.

3.3 was synthesised using procedures adapted from literature, converting 5-amino isophthalic acid in a single step using phthalic anhydride in DMF with a yield of 60% (Figure 69).[27] **3.3** was found to be insoluble in most common solvents, being only soluble in the polar organic solvents DMSO, DMF and DMA.

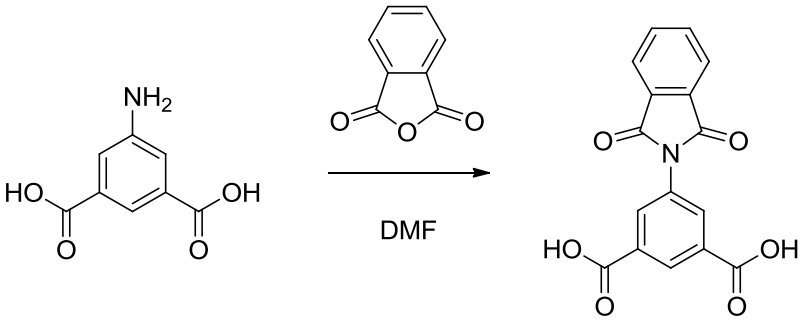

3.3

Figure 69. Synthesis of 5-(1,3-dioxoisoindolin-2-yl)isophthalic acid (**3.3**)

*3.2.4. Synthesis of 5-(benzyloxy)isophthalic acid (**3.4**)*

To study the potential influence of π-stacking between MOPs, **3.4** was synthesised to allow the inclusion of an aromatic system with a high degree of conformational freedom. While several of the other synthesised analogues contain extended π systems, they contain motifs capable of hydrogen bonding which could potentially disrupt or compete with π-π interactions. The oxygen atom on the O-benzyl motif is in close proximity to the isophthalate core and hence sterically restricted from participating in such hydrogen bonding interactions.

3.4 was synthesised in three steps from 5-hydroxy isophthalic acid by reaction with chloromethyl benzene in acetonitrile and acetone. Similar to the other organic compounds described in this section, protection and deprotection of the carboxylic acids was carried out under standard conditions in an overall yield of 60% (Figure 70).

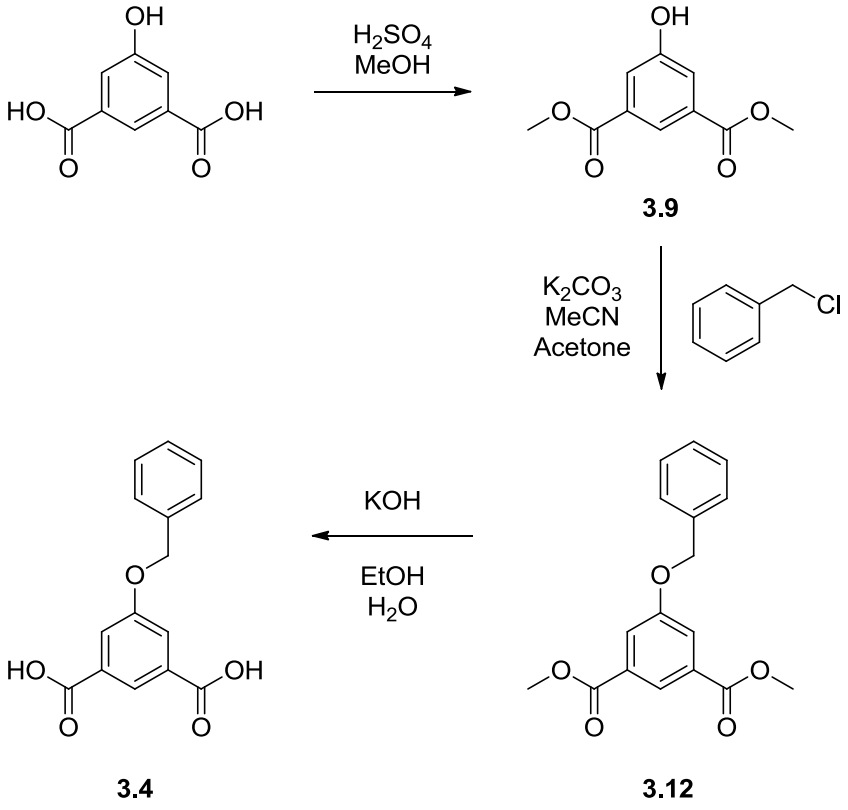

Figure 70. Synthesis of 5-(benzyloxy)isophthalic acid (**3.4**)

*3.2.5. Synthesis of 5-(phenyldiazenyl)isophthalic acid (**3.5**)*

Azobenzene groups have been shown to bestow interesting properties on porous materials allowing for photo-induced gating effects, which in turn provide the potential for

controlled host-guest interactions.[28] The geometric change associated with the *cis-trans* isomerisation can greatly influence the gas adsorption properties in metal-organic frameworks, due to opening or blocking of pores.[29,30] Due to the discrete form of MOPs however, the role of the azobenzene moiety could extend beyond simple pore blockage or opening due to isomerisation, to changes in cage packing which can influence the material's physical properties, such as volume and density, and its host-guest chemistry.

3.5 was synthesised in a single step from reaction of 5-amino isophthalic acid with nitrosobenzene in acetic acid and water (Figure 71), however purification by column chromotography resulted in poor yields (less than 5%). As such, the compound was esterified with H_2SO_4/MeOH and subsequently purified by column chromatography before saponification to obtain the pure compound as an orange solid in a 48% yield after purification.

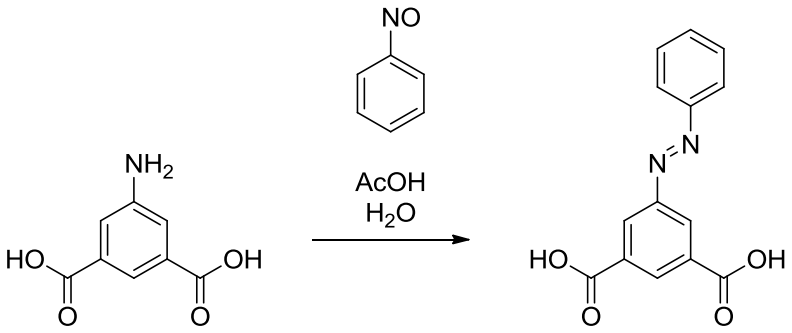

3.5

Figure 71. Synthesis of 5-(phenyldiazenyl)isophthalic acid (**3.5**)

*3.2.6. Synthesis of 5-((4-hydroxyphenyl)diazenyl)isophthalic acid (**3.6**)*

The azo compound **3.5** was found to be insoluble in most common laboratory solvents, limiting the options for synthesizing an azo functionalised MOP. In order to obtain a similar organic compound with increased solubility, **3.6** was synthesised containing an addition hydroxyl group on the phenyl system. Unfortunately, **3.6** was also found to have a low solubility in most common solvents.

Synthesis of **3.6** was performed over 3 steps based on a procedure described by Li *et al.* to generate an isophthalic acid derivative with appended azo-benzene functionality.[31] Following protection of the carboxylic acid groups, the isophthalate was reacted with phenol

to form the azobenzene motif. Subsequently the acid was deprotected to yield the desired compound **3.6** with an overall yield of 62% (Figure 72).

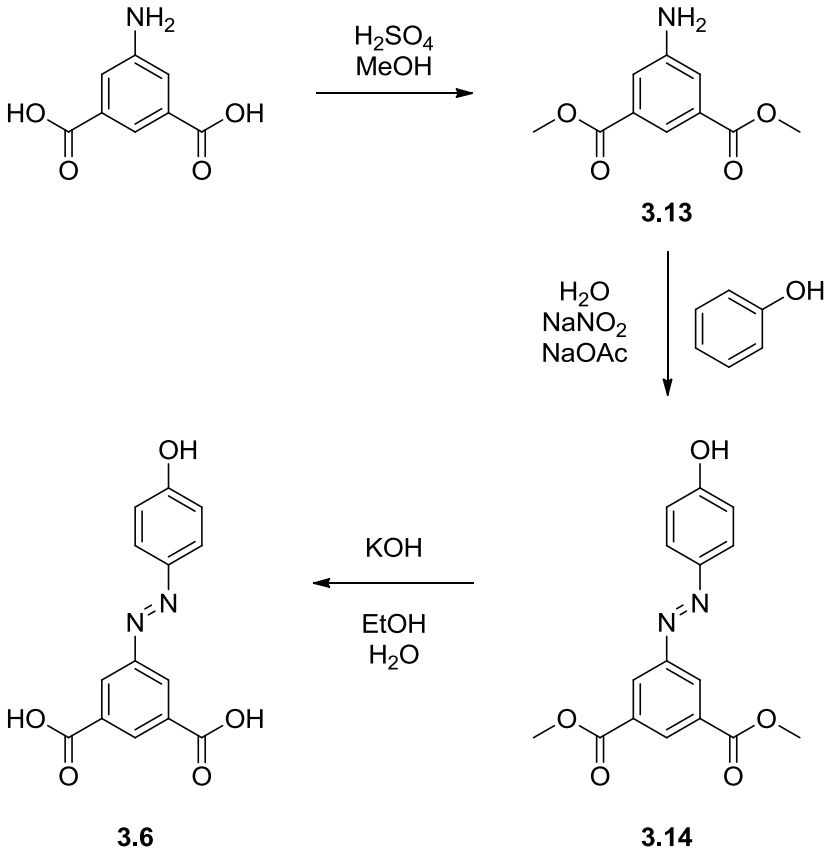

Figure 72. Synthesis of 5-((4-hydroxyphenyl)diazenyl)isophthalic acid (**3.6**)

*3.2.7. Synthesis of 5-((4-(phenyldiazenyl)benzyl)oxy)isophthalic acid (**3.7**)*

As with azo compounds **3.5** and **3.6**, **3.7** was synthesised as a means to introduce azobenzene functionality to a MOP surface. The structure of **3.7** features a benzyl spacer that is not present in the other azo compounds which, upon MOP formation, positions the azo group further from the MOP core. In doing so, it was proposed that the reduced steric constriction would better facilitate isomerisation of the azo motif.

Synthesis of **3.7** was carried out over three steps from 5-hydroxy isophthalic acid, coupling with a brominated azobenzene reagent in a microwave facilitated reaction. This brominated species was synthesised using a procedure adapted from Kaiser *et al.*[32] An overall yield of 35% was obtained, however the coupling reaction was not optimised and thus the yield could potentially be improved.

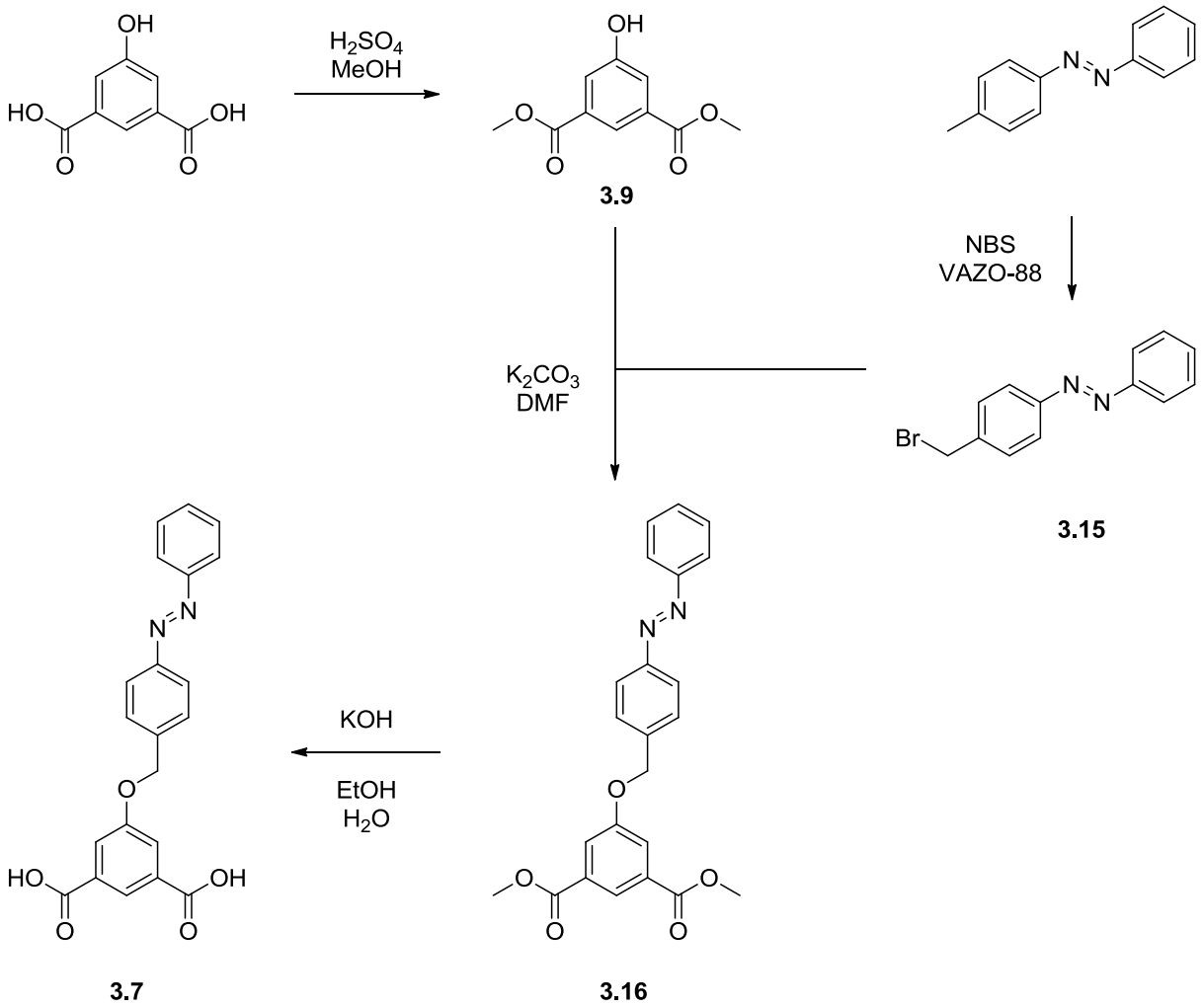

Figure 73. Synthesis of 5-((4-(phenyldiazenyl)benzyl)oxy)isophthalic acid (**3.7**)

*3.2.8. Synthesis of 5-((4-benzoylbenzyl)oxy)isophthalic acid (**3.8**)*

The majority of the organic units synthesised in this section were designed to facilitate weaker intermolecular forces such as hydrogen bonding and π-stacking. Contrary to this, **3.8** was synthesised as a route to covalently tether MOPs, through the use of UV driven radical bond formation. Benzophenones are used frequently as crosslinking moieties, as they exhibit many desirable features including reversible excitation, high stability and excellent crosslinking yields.[33-35] The UV induced bond formation for benzophenones is well established in the literature, in which a carbon based radical reacts with an unactivated C-H group (Figure 74).[36-38] In order to facilitate this mechanism, a methylene spacer was included in the ligand design to act as a suitable reaction site.

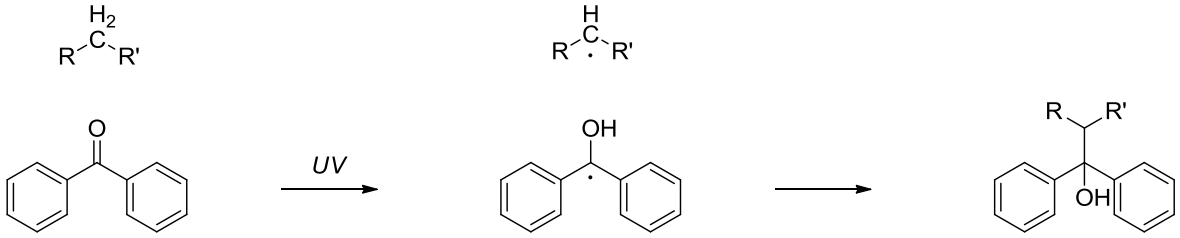

Figure 74. UV initiated carbon-carbon bond formation.

3.8 was synthesised from the reaction of the protected dimethyl 5-hydroxyisophthalate with 4-bromomethyl benzophenone, with the latter being synthesised via radical bromination using 1,1′-azo bis(cyclohexanecarbonitrile) (VAZO-88) and *N*-bromosuccinimide (NBS). Subsequent deprotection yielded the desired product in an overall yield of 24% (from 5-hydroxy isophthalic acid) (Figure 75).

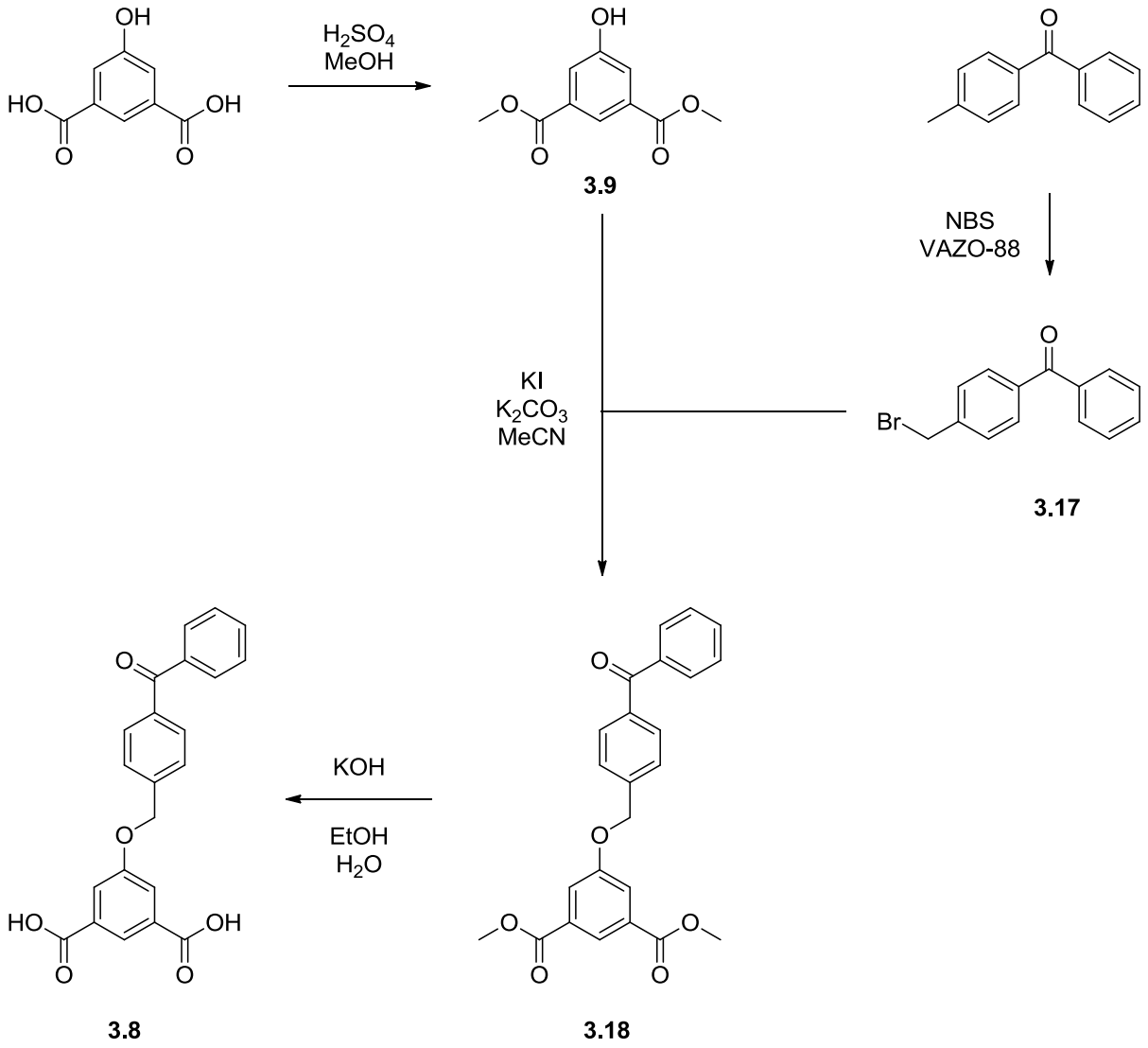

Figure 75. Synthesis of 5-((4-benzoylbenzyl)oxy)isophthalic acid (**3.8**)

3.3. Synthesis of Exohedrally Functionalised MOPs

Unlike the bimetallic materials described in the previous chapter which were synthesised using a shared methodology, the synthesis of MOPs with external functionality is reliant on a number of approaches. One of the major reasons for this is the difference in solubility between the MOP structures, as well as their respective building blocks. Importantly, all the synthesised MOPs were characterised by single crystal X-ray diffraction as this provides not only certainty in the three dimensional orientation and connectivity of the structures, but also elucidates the crystalline packing arrangements, which provides further insight into non-covalent interactions that determine solid-state packing.

*3.3.1. Synthesis of Cu_{24}(5-(2-(2-(2-hydroxyethoxy)ethoxy)ethoxy)isophthalate)$_{24}$ (**3.9**)*

MOP **3.9** was synthesised using a modified procedure based upon the method described by Tonigold and associates, as these materials both share ethylene glycol surface functionality and similar solubility.[16] This involves initial synthesis of the MOP by rapid precipitation using a non-coordinating base, followed by recrystallisation to allow single crystal structure analysis. Synthesis of **3.9** was carried out by dissolving equimolar amounts of **3.1** and copper nitrate in MeOH. The addition of 2,6-lutidine to this solution causes the precipitation of the desired product as an amorphous solid. The resulting MOP is insoluble in water and MeOH, but is soluble in polar organic solvents such as DMF and DMSO. Large block crystals suitable for single crystal X-ray diffraction studies were obtained by dissolving the MOP in DMSO and subsequent addition of isobutanol by slow vapour diffusion.

3.3.2. Attempted Synthesis of Cu_{24}(5-((tert-butyldimethylsilyl)oxy)isophthalate)$_{24}$

The reaction of copper nitrate and **3.2** did not result in the formation of the desired Cu_{24}(**3.2**)$_{24}$ structure. Interestingly, under specific conditions (described below) that result in the formation of large crystals, Cu_{24}(5-hydroxy isophthalate)$_{24}$ is formed instead of the silyl functionalised structure. **3.2** was dissolved with 0.5 equivalents of copper nitrate in a small amount of MeOH containing several drops of 2,6-lutidine. This reaction mixture was sonicated briefly before being allowed to rest at room temperature for a period of two weeks, after which small block shaped crystals were formed. The use of amide solvents in this reaction, such as DMF or DMA, resulted in the immediate formation of green precipitates which were not able to be structurally characterised. The relative concentrations of the constituent building blocks are important in this reaction as deviations from the aforementioned ratio results in the formation of non-crystalline material or the absence of solid product. Similarly the absence of 2,6-lutidine causes the reagents to remain in solution and no solid material to be formed.

The formation of Cu_{24}(5-hydroxy isophthalate)$_{24}$ can be rationalised by *in situ* cleavage of the silyl group; a side reaction that is unsurprising when considering the ubiquity of silyl-ether de-protection chemistry.[39,40] It is noteworthy that when formed in this method, Cu_{24}(5-hydroxy isophthalate)$_{24}$ crystallises in the *Fm*-3*m* space group as opposed to *I*4/*mmm* which is reported in the original synthesis of the hydroxy-MOP compound by Abourahma *et al.*[41]

*3.3.3. Synthesis of Cu_{24}(5-(1,3-dioxoisoindolin-2-yl)isophthalate)$_{24}$ (**3.10**)*

Interestingly, **3.10** is the only MOP synthesised in this work that required temperatures higher than ambient conditions. The elevated temperature, however; was needed because of the low solubility of the phthalymidyl acid **3.3** and not necessarily a prerequisite for synthesis of the supramolecular structure. **3.3** was suspended in a methanolic solution of copper nitrate in equimolar amounts before addition of a small amount of 2,6-lutidine. Stirring at reflux for several hours afforded a light blue solid which is sparingly soluble in MeOH. Block crystals that were suitable for single crystal X-ray diffraction studies were obtained by slow evaporation from a methanol solution. **3.10** exhibits a very low solubility in all common laboratory solvents which make it less than ideal for mixed membrane applications such as those discussed in Chapter 4.

*3.3.4. Synthesis of Cu_{24}(5-(benzyloxy)isophthalate)$_{24}$ (**3.11**)*

Crystals of **3.11** were grown at room temperature by dissolving a small amount of **3.4** in 4 mL of DMA with a molar equivalent of copper nitrate. A single drop of MeOH was added to the solvent with crystals forming over a 24 hour period. The addition of MeOH accelerates the crystal growth which takes approximately two weeks in neat DMA. It was found however that increasing the concentration of MeOH to 20% results in the slow formation of large polyhedral solids with a blue glass-like appearance. These solid materials were non-crystalline. Further increases in MeOH concentration bring about immediate precipitation of amorphous material.

3.3.5. Attempted Synthesis of MOPs with Azobenzene Functionality

Synthesis of a MOP with azobenzene functionality is a promising avenue for synthesizing materials with controllable gas adsorption characteristics; however this was unable to be achieved. The insolubility of organic azo-isophthalic acids in common laboratory solvents makes them difficult to employ as building units, using traditional techniques. This hurdle can be overcome by the addition of solubilising chemical motifs, such as the hydroxyl groups seen in **3.6**, which shows an increased solubility to that of **3.5** and **3.7**, however all the reactions of these azo-isophthalic acids yielded non-crystalline products. Two possible explanations for this are hence suggested.

Firstly, the azo syntheses reported in this chapter are not selective for a specific isomer. If the resulting azo-compounds were photo-stationary under ambient conditions, the subsequent MOP synthesis reactions would be carried out in an isomeric mixture resulting in

a mixture of MOPs with a distribution of *E* and *Z* ligands and thus a significant barrier to the formation of crystallised material. Conversely, a second rationale can be given if the azo compounds were photoactive under ambient conditions. Introduction of an isomerizing external group may produce a structurally dynamic MOP in which azo-isomerisation disrupts the crystal packing forces. This gives rise to the premise that crystal growth of azo-MOPs must be carried out in the absence of light, however even when such considerations are taken into account, suitable conditions could not be found to produce crystalline material. This theory is further evidenced by the work of Park and co-workers who, at the time of writing, successfully crystallised a MOP with azo-benzene surface functionality.[28] It was revealed in their study that the structural inclusion of a second ligand that inhibited isomerisation was necessary for growth of single crystals and as such, they were similarly unable to obtain single crystals of a MOP structure containing only azo-functionalised ligands.

*3.3.6. Synthesis of $Co_{12}Pd_{12}$(5-((4-benzoylbenzyl)oxy)isophthalate)$_{24}$ (**3.12**)*

Crystals of **3.12** containing exohedral benzophenone groups were synthesised from a 3:1 DMA:MeOH solvent mixture. Interestingly, the use of the preformed CoPd node described in Chapter 2 results in the aforementioned product, while the use of copper acetate or nitrate did not form materials that could be analyzed by X-ray crystallography. As such, a copper paddle-wheel MOP with benzophenone periphery was not able to be obtained, however **3.12** is an example with modification of both the internal and external surfaces.

Synthesis of **3.12** must be carried out with care, as the reaction is sensitive to many factors including reagent concentration and strict exclusion of oxygen. Increasing the concentration of the metallic building block tends to result in the formation of a secondary, non-crystalline phase which is very dark in colour and could not be successfully characterised. Similar to the bimetallic MOPs synthesised in Chapter 2, the presence of water or oxygen in the reaction results in the formation of a black non-crystalline product, presumably due to metal oxidation. The solvent system used was found to be reasonably forgiving, with crystalline MOP material forming with a DMA:MeOH ratio of up to 6:1, however the 3:1 ratio tended to yield the largest crystals, with the most consistent X-ray diffraction properties.

3.4. Structural Characterisation Methodology

There are several factors that need to be taken into account when characterizing such materials, as they exhibit many properties that can be troublesome for structural determination

by X-ray crystallography. Firstly, as with all the MOPs described in this thesis, the structures tend to produce very weak X-ray diffraction due to the very large void space present in these materials.[41] Secondly, the use of long flexible side chains introduces groups that have significant positional and conformational disorder throughout the crystalline matrix.[14,15] The latter issue has been tackled through several approaches in the literature including modelling software, crystallographic methods and geometric arguments.[42-44]

While such methods have shown success in the structural elucidation of disordered materials, a combinatorial approach that takes advantage of the strengths of several methods has been applied to several of the more disordered structures in this section. As such, a discussion of this approach is given in the following section.

3.4.1 Structure Elucidation by Combinatorial X-Ray Diffraction and Molecular Modelling

Structure solution through X-ray crystallographic methods allows for unambiguous structural determination of ordered motifs in a crystalline matrix.[45] In the absence of an ordered structure however, the conditions for diffraction are not met and the structure cannot be unambiguously determined. However, through the use of restraints and constraints, a structure model can often be generated that is based on the electron density map and adheres to chemical sensibility.[46,47] Unfortunately, this methodology reaches an effective limitation as structural order decreases, particularly in large void areas such as those seen in these MOP materials. Attempts to refine restrained models to areas of negligible electron density through common refinement software, such as SHELXL, tend to result in conformationally nonsensical solutions.[14,46,47]

To avoid this problem, molecular modelling packages can be used to generate solutions for highly disordered regions based on energetic arguments such as ideal bond lengths and angles.[48] If desired, the precision of such calculations can be improved through the use of more complex approaches, such as DFT, to better describe the chemical structure. However the resulting structure solution contains motifs that are a result of purely energetic arguments and not based upon any electron density observed in diffraction experiments.[49,50]

Attempts were made to use molecular modelling to calculate the structural properties of the external groups of the MOPs described in this chapter. As a first step, the core of each MOP structure was characterised by X-ray diffraction analysis, with the disordered external groups subsequently modelled using geometric and energetic arguments. It was found however that the resulting structure solutions were consistently the most sterically relaxed

structures in which the side chains point directly away from the MOP core, showing very little interaction with other structural motifs. These results, while being consistent with those seen in literature, are likely a simplified representation of the real packing forces experienced due to the chemical make-up of the side chains themselves, which would be expected to show significant attractive interactions.[17] The level of computational theory used in these solutions is largely the reason for the simplified conformations seen in the structural output. As MOP structures are quite large, containing hundreds of atoms each, calculations at DFT level are computationally expensive to the point of impracticality.[51] The associated computational expense is likely the reason that calculations for side chains that account for intermolecular packing forces are unseen in the literature. In order to allow atomistic calculation, it was necessary to use simplified force field descriptions that do not consider attraction between functional groups.

As a means of obtaining a more accurate description of the external groups, a combined approach that uses molecular modelling based on the X-ray diffraction electron density was developed, predominantly based on similar work by Furukawa *et al.*[14] Using traditional X-ray crystallographic methods, a structure solution was initially obtained using conventional restraints/constraints. This solution, which contains conformationally strained side chains, was then subject to a limited geometric optimisation using the Forcite module of the Materials Studio® software package.[52,53] The approach used in this work differs to that used by Furukawa in the maximum atomic displacement allowed during modelling. By limiting the displacement during optimisation, the external groups are not relocated to positions of low electron density in the final solution.

Caution must be exercised when using this approach for several reasons. Firstly, as with the aforementioned modelling techniques, the level of theory used in this work is limited, thus the side chain positions are determined largely by sterics in the absence of significant localised electron density. Secondly, the use of excessive restraints in the initial crystallographic structure solution can lead to unrealistic structure solutions, particularly due to the excessive density assignment in the void spaces of the preliminary structure solution. Thirdly, the resulting combinatorial structure solution suggests an ordered external structure which is not matched by the electron density map given by diffraction experiments. While this allows the solution to give useful information into the arrangement of the external groups in the crystalline state, this causes the structure to have a fit against the X-ray reflection data that is much lower than could be achieved through conventional means, such as removal of

disordered groups through the use of the SQUEEZE routine.[54] As such, the X-ray crystallographic data for **3.9** and **3.12** given in the relevant appendix is for the MOP core structures only, with the side chains treated as highly disordered motifs and removed via SQUEEZE. Expectedly, the corresponding removed electron density is much greater than would be expected for a standard X-ray structure. To maintain chemical sensibility in the structure solution, the atomic content from these side chains is included in the empirical formula, thus a discrepancy is generated between the unit cell contents and the molecular formula.

3.5 Structures of Exohedrally Functionalised MOPs

This section contains a discussion of the structures of the exohedrally functionalised MOPs. The structures of **3.10** and **3.11** were attained through conventional crystallography, while the structures of **3.9** and **3.12** were obtained using the combinatorial approach described in the previous section.

*3.5.1. Structure of Cu_{24}(5-(2-(2-(2-hydroxyethoxy)ethoxy)ethoxy)isophthalate)$_{24}$ (**3.9**)*

MOP **3.9**, which has ethylene glycol chains, crystallises in the monoclinic space group $P2_1/c$, with considerably lower symmetry than the MOP structures presented in Chapter 2. As a result of this, the asymmetric unit describes one half of a whole cage unit, containing 6 di-copper paddle-wheel nodes and 12 ligands. Due to the asymmetry of the MOP, none of the metal nodes are situated on symmetry sites and all atoms are fully occupied in the structure solution. Of the twelve ethylene glycol chains in the asymmetric unit, ten show only minor interactions with the surrounding environment being highly disordered and requiring modelling in the structure solution. In order to retain diffraction based positioning in the geometrically optimised model, the maximum displacement permitted during the optimisation process was set to 5 Å, through a maximum of 500 iterations.

The remaining two chains are ordered in the crystal structure and can be identified by refinement, showing strong interactions with the pores of adjacent MOPs. One of these chains penetrates into the core of an adjacent MOP, while a second is curled to block the pore window of a different cage. The interactions between adjacent MOPs causes them to pack in an inefficient manner, with a large extrinsic space as can be seen when viewed along the *a* axis (Figure 76). This inter-cage space is occupied by the disordered ethylene glycol groups that extend from the MOP exterior surfaces.

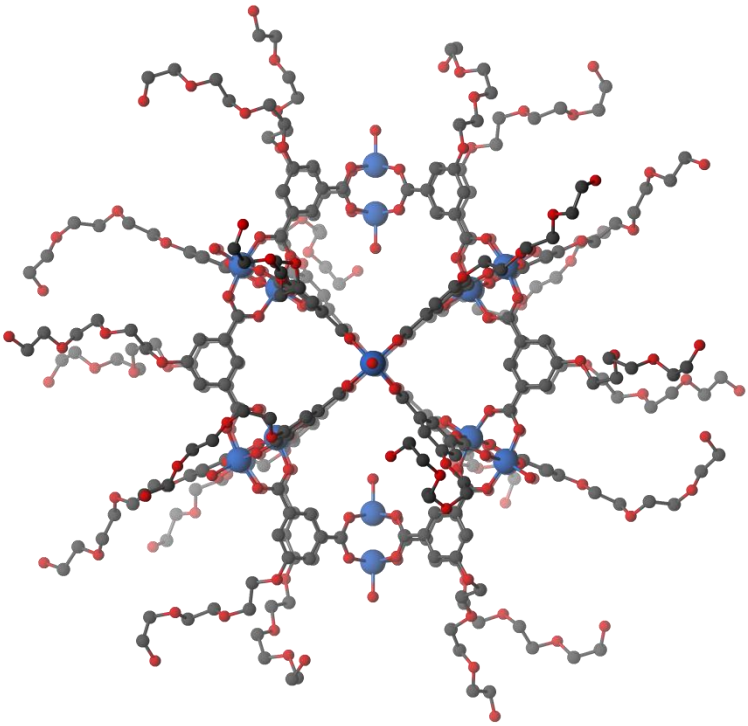

Figure 23. A perspective view of **3.9**. Hydrogen atoms are omitted for clarity. Only the oxygen atom of coordinating DMA molecules is shown.

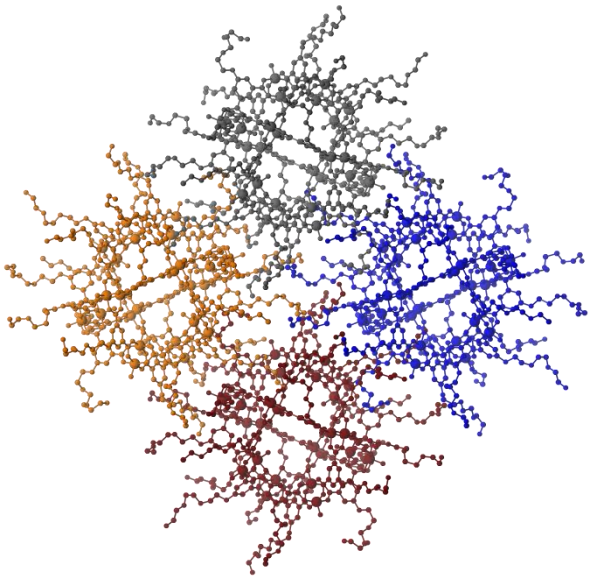

Figure 24. Crystal packing of **3.9** viewed along the crystallographic *a* axis. Polyhedra are individually coloured and hydrogen atoms omitted for clarity. Only the oxygen atom of coordinating solvent molecules is shown.

*3.5.2. Structure of Cu_{24}(5-(1,3-dioxoisoindolin-2-yl)isophthalate)$_{24}$ **3.10***

MOP **3.10** (Figure 78) crystallises in the trigonal space group *R*-3 with two di-copper metal nodes and four ligands in the asymmetric unit. Each copper ion exhibits a square pyramidal geometry, with coordinating solvent molecules in the axial positions. Unlike many of the other MOP structures described in this work such as those in Chapter 2, the metal nodes are not coincident with axes of symmetry and are fully occupied in the asymmetric unit. Three of the ligands display π-stacking interactions with the peripheral groups of neighbouring MOPs, with the chains themselves arranging in anti-parallel orientations. A fourth ligand is directed into the inter-polyhedral space formed as a result of the crystal packing. Interestingly, the rigid peripheral groups of **3.10** interact strongly with each other in the crystalline phase without penetrating the pore windows of adjacent cages, as is seen in the other MOP materials.

Two of the phthalimide groups in the asymmetric unit are ordered enough to be crystallographically resolved with minimal restraints, due to the relatively strong π-stacking forces. As the two remaining groups are disordered to a greater extent, a structure solution was obtained using the SAME command in the SHELXL software package, modelling the disordered structural motifs on the more ordered groups. As such, the position of the disordered phthalimide groups is refined based on the electron density, however structural parameters such as torsion angles and bond lengths are restrained by the template structural data.

Due to the strong interactions between side chains, individual cages are spaced in a way such that the pore windows are not blocked and the intrinsic pore space within each MOP is conserved. The extrinsic pore space between cages however is blocked by the bulky external groups thus no pore channels are seen in the structure. The influence of these external groups causes the individual polyhedra to pack in staggered layers as can be seen when viewing along the *b* axis (Figure 79).

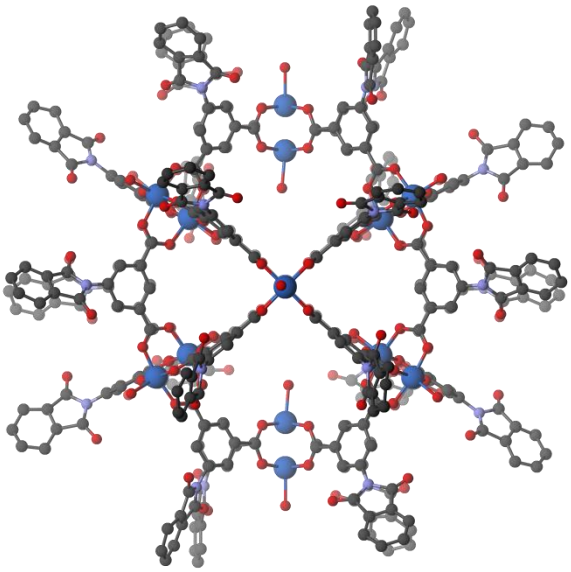

Figure 78. A perspective view of **3.10**. Hydrogen atoms are omitted for clarity. Only the oxygen atom of coordinating DMA molecules is shown.

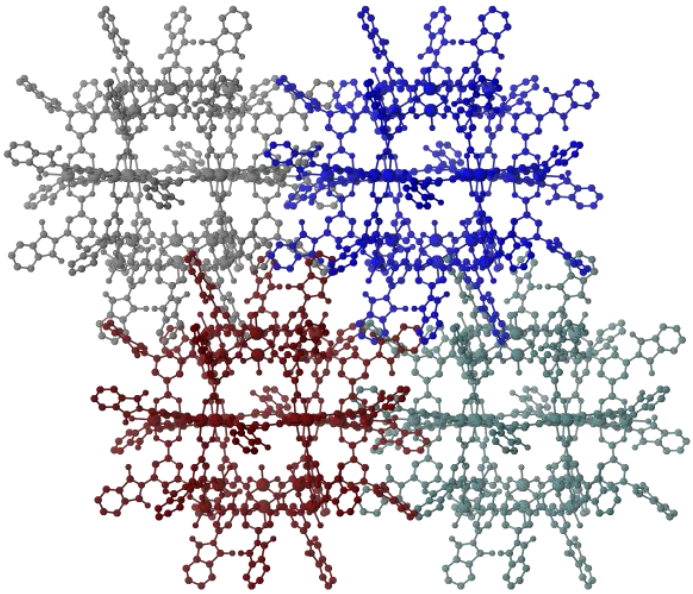

Figure 79. Crystal packing of **3.10** viewed along the crystallographic *b* axis. Polyhedra are individually coloured and hydrogen atoms omitted for clarity. Only the oxygem atom of coordinating solvent molecules is shown.

*3.5.3. Structure of Cu_{24}(5-(benzyloxy)isophthalate)$_{24}$ (**3.11**)*

The asymmetric unit of **3.11** contains two di-copper metal nodes and three ligands with O-benzyl groups extending from the cage exterior. The material crystallises in the tetragonal space group *P4/mnc* with one metal node situated on a symmetry site. The peripheral benzyl groups show significant disorder and as such, were restrained during refinement using SAME commands.[46,47] As with previously described materials in this chapter, the SAME command was used preferentially over more static restraints as it allows the crystallographic position to be determined by the electron density map. Unfortunately the high disorder of several of the benzyl groups means that the goodness of fit to the diffraction data is reduced when the structure solution contains the ordered side chains (Figure 80).

The significant disorder observed in the benzyl groups is due to several contributing factors. Firstly, the benzyl groups contain a sp^3 carbon provide significant flexibility and conformational freedom to the attached aromatic ring. Additionally, the crystal structure shows that the benzene rings are not suitably located to participate in π-stacking interactions, as observed in the aforementioned **3.10**. The absence of these interactions reduces the conformational restrictions that would otherwise add order to the benzyl groups.

Similar to **3.10**, the external groups are not positioned to block the pore windows of adjacent cages, and instead are localised in the inter-cage space such that the intrinsic pore space is retained. In addition, the cages pack in a similar manner, in which the polyhedra form staggered planes, as can be seen in Figure 81. However, unlike **3.10**, the relatively small benzyl side groups, in combination with the altered packing arrangement, does not result in a non-porous packing arrangement. As such, pore channels can be seen when viewing the structure along both the *a* and *b* axes.

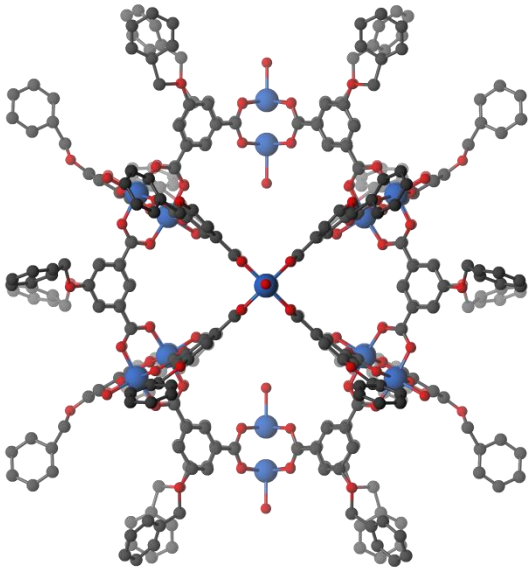

Figure 80. A perspective view of **3.11**. Hydrogen atoms are omitted for clarity. Only the oxygen atom of coordinating DMA molecules is shown.

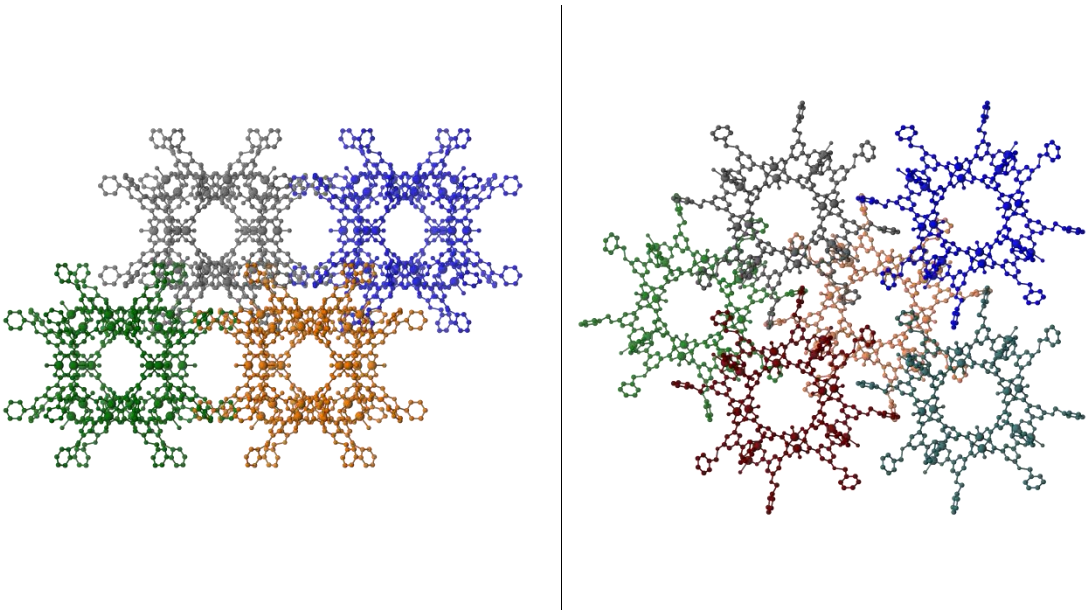

Figure 81. Crystal packing of **3.11** viewed along the crystallographic *b* (left) and *c* (right) axes. Polyhedra are individually coloured and hydrogen atoms omitted for clarity. Only the oxygen atom of coordinating solvent molecules is shown.

*3.5.4. Structure of $Co_{12}Pd_{12}$(5-((4-benzoylbenzyl)oxy)isophthalate)$_{24}$ (**3.12**)*

The structure solution for **3.12** (Figure 82) was determined using a combination of methods described in both the previous and current chapters. As with the materials in the former, **3.12** is a hetero-bimetallic structure. As such the cobalt and palladium elemental occupancy was determined crystallographically through the use of trial refinement which indicated an endo-Pd metal node configuration of approximately 75%, consistent with the hetero-metallic species in Chapter 2. Furthermore the peripheral benzophenone groups are disordered to varying degrees, thus the more disordered motifs were solved using the aforementioned combined crystallographic and modelling approach. It is worth noting that the most highly ordered side chain in the structure of **3.12** penetrates the larger pore window of an adjacent MOP (Figure 83).

During the modelling of **3.12**, a significant weakness in this combinatorial structure elucidation method was encountered. The hetero-metallic node, which was crystallographically characterised as displaying both endo- and exo-Pd configurations, could not be described accurately in Materials Studio as this requires that the relevant metal atom sites be partially occupied by either cobalt or palladium. In general, partial occupancy can be addressed in Materials Studio through the use of supercells, a construct of multiple unit cells. Fully occupied structural motifs are made present in every unit cell that constitutes the supercell, while partially occupied structural bodies are only present in the proportionate number of unit cells. For the purposes of this work however, the supercell would need to be collapsed into a single unit cell to produce a useful structure solution; a function that the software is not capable of. As the partial occupancy could not be used in the modelling software, the metal nodes were instead given a single endo-Pd conformation of fully occupied metal ions as this allowed for modelling of the disordered groups, while matching the crystallographically determined structure as closely as possible.

3.12 crystallises in the $P2_1/n$ space group with six hetero-metallic nodes and 12 ligands in the asymmetric unit. Four of these ligands are able to be solved crystallographically while the remaining eight require a modelling solution. Due to the large size of the benzopheneone groups and the resulting close packed arrangement, the modelling was carried out with a higher tolerance and number of refinement cycles than was used in the ethylene glycol modelling. For this structure, a maximum displacement of 15 Å over 1500 optimisation iterations was permitted, as this was found to give a stable structure that closely matched the diffraction data.

When compared to the bimetallic MOPs in Chapter 2, the structure of **3.12** is of relatively low symmetry due to the arrangement of the external groups. After modelling, the cobalt and palladium ions are positioned to more coincident locations due to the geometric arguments in the modelling process, however a more accurate description of the metal positions is obtained from the crystallographic data prior to modelling, indicating that the cobalt ions are not co-planar with the paddle-wheel oxygen atoms. Both the crystallographic and modelled solutions however are in agreement showing that the palladium and cobalt ions adopt square planar and square pyramidal geometries respectively.

3.12 forms an efficiently packed network with no accessible pore structure visible as the extrinsic void space is almost entirely occupied by the benzophenone motifs. While the modelled structure solution suggests that the benzophenone groups are located close enough to each other to interact, the level of theory used is unable to calculate aromatic interactions such as π-stacking. This highlights the potential inaccuracy of a computational approach as such interactions could greatly influence the conformation of the aromatic ligands.

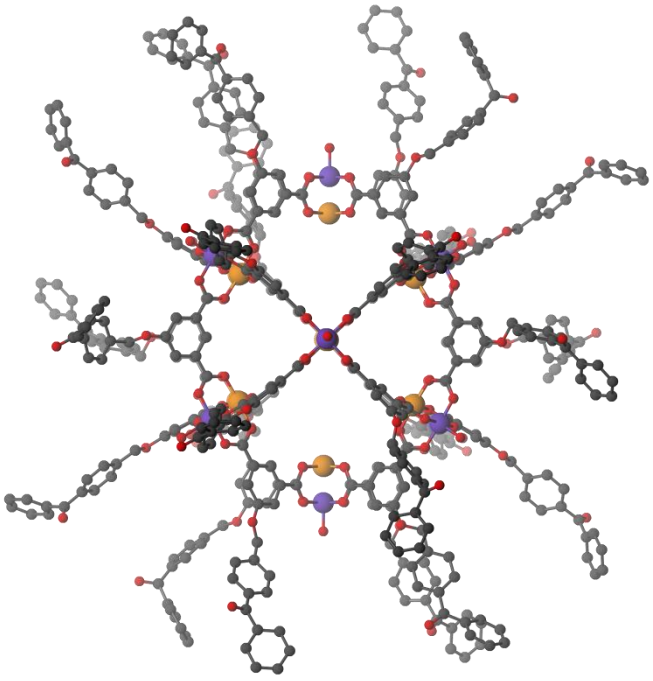

Figure 82. A perspective view of **3.12**. Hydrogen atoms are omitted for clarity. Only the oxygen atom of coordinating DMA molecules is shown.

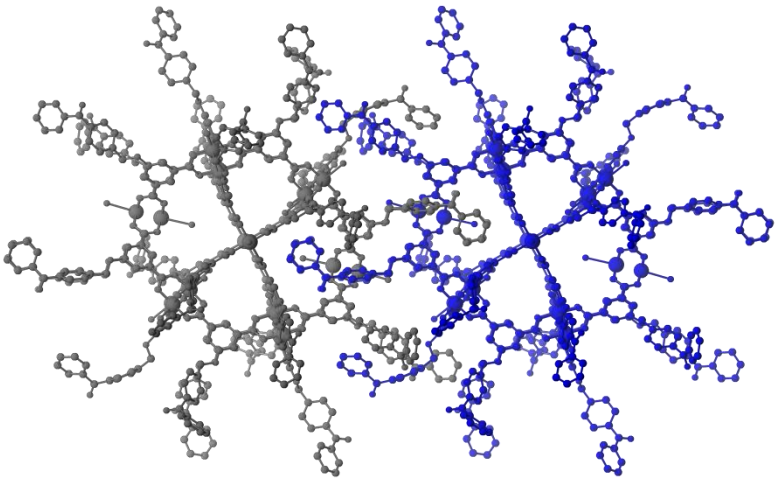

Figure 83. A perspective view of the crystal packing of adjacent **3.12** polyhedra, showing the penetration of internal void space by neighbouring benzophenone motifs. Polyhedra are individually coloured and hydrogen atoms omitted for clarity. A single atom is shown for coordinating solvent molecules.

3.6. Pore Blocking and Loss of Porosity Upon Activation

The materials described in this chapter show no permanent porosity upon removal of the solvent species. This was determined through gas sorption experiments, using both N_2 and CO_2 probe gases, both of which show no significant excess surface adsorption at cryogenic temperatures. As work in the previous chapter had shown that the solvation state of the metal ions can have an impact on porosity, each sample in this chapter was investigated in both a solvated-metal and activated-metal state to check for similar effects. It was found that, regardless of solvation state, the materials were non-porous to these probe gases.

The non-porous nature of the materials is a result of the exohedral motifs which are able to fill the void space created upon solvent removal. While this conclusion seems somewhat intuitive after consideration of the structural data, it is further evidenced through the use of computational investigation. The gas accessible surface area within the crystal structures can be visualised using a ‘rolling ball’ algorithm calculated using a gas molecule sized probe, producing a three-dimensional surface known as a Connolly surface. Connolly surfaces generated from the MOP crystal structures show that the structures of **3.9**, **3.10** and **3.11** (Fig. 79 & 80) are indeed porous in the crystalline state. Upon solvent removal the

crystalline packing collapses resulting in the loss of extrinsic void space. With the loss of interconnecting space between MOPs, the internal cavities within each structure become inaccessible conferring the non-porous behaviour.

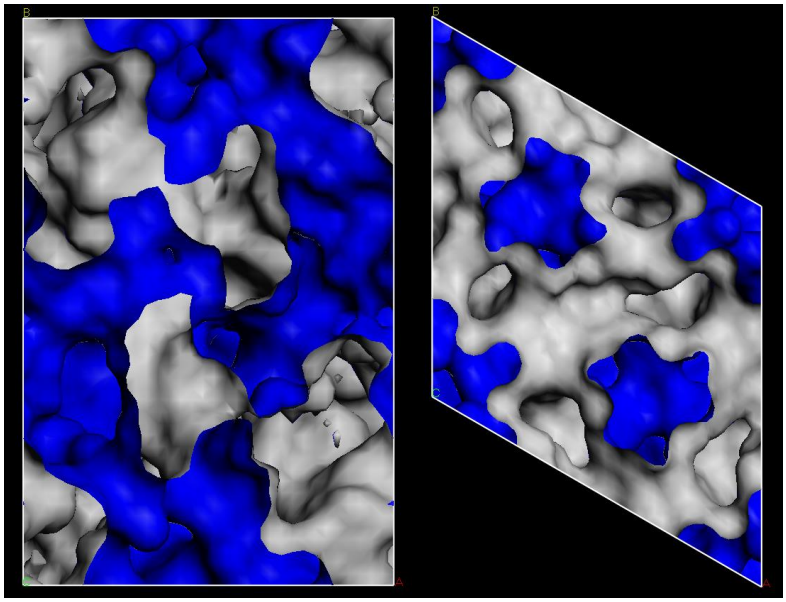

Figure 84. Unit cell Connolly surfaces generated from the crystal structures of **3.9** (left) and **3.10** (right). External Connolly surface is coloured grey, while internal surface is blue.

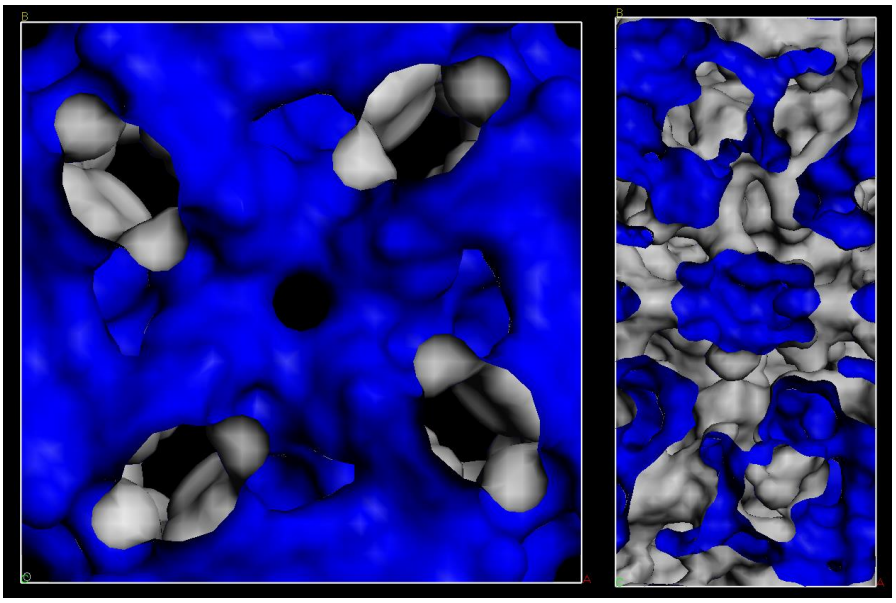

Figure 85. Unit cell Connolly surfaces generated from the crystal structures of **3.11** (left) and **3.12** (right). External Connolly surface is coloured grey, while internal surface is blue.

3.7. Summary

In summary, a series of isophthalic acid derivatives have been synthesised for use as secondary building units in MOPs. The synthesis of these organic compounds has been carried out using a variety of established methods, with the goal of adding chemically interesting motifs to the periphery of discrete supramolecular structures. To this end, the synthesis of four MOPs displaying exohedral functionality has been completed with characterisation by X-ray crystallography. These external groups are shown to have a dramatic influence on the packing of these MOPs in the crystalline phase, with contributing factors such as sterics and π-stacking, playing major roles in the crystal organisation.

A structural characterisation methodology involving combined X-ray crystallographic and computational geometric calculations has been explored and discussed in detail. This approach is used in this work to provide structural insight beyond the standard achieved through traditional crystallographic means. The bulky, flexible peripheral groups used in this work are found to reduce the permanent porosity of these materials, due to steric rearrangements brought about by the removal of solvent during activation procedures.

3.8. Experimental

Materials and Measurements

Unless otherwise stated, all chemicals were obtained from commercial sources and used as received. DMA and MeOH were distilled from CaH_2 and degassed with Ar. Acetone was dried over $CaSO_4$ and distilled under Ar. NMR spectra were recorded on a Varian 500 MHz spectrometer at 23 °C using a 5 mm probe. Powder X-ray diffraction data were collected on a Bruker D8 Advance diffractometer (capillary stage) using Cu Kα radiation (λ = 1.5418 Å, 50 kW/40mA, 2θ = 2 – 55°).

Single Crystal X-ray Diffraction

Single crystals were mounted in paratone-N oil on a nylon loop. X-ray diffraction data were collected at 150(2) K with Mo Kα radiation (λ = 0.7107 Å) at 100(2) K on the MX-1 beamline of the Australian Synchrotron (λ = 0.7107 Å).[55] Data sets were corrected for absorption using a multi-scan method, and all structures with the exception of **3.10** were solved by direct methods using SHELXS-2013, and refined by full-matrix least squares on F^2 by SHELXL-2014, interfaced through the program X-Seed.[46,47,56,57] **3.10** was solved by direct

methods using SHELXT software interfaced through the program OLEX-2 and refined in the same manner as the other data sets.[58,59]

In general, all non-hydrogen atoms were refined anisotropically and hydrogen atoms were included as invariants at geometrically estimated positions, unless specified otherwise. The solvent molecule associated with each transition metal was assigned as an oxygen atom due to a high degree of disorder. Disordered solvent molecules were accounted for prior to structure refinement using the SQUEEZE routine of Platon to remove electron density corresponding to these entities. Disorder of the external motifs was also common to all the structures and were restrained accordingly where possible.[54] Structural elucidation for highly disordered side groups were modelled using the Forcite module accessed by the Materials Studio software package.[52,53] Connolly surfaces were generated using the Materials Studio software package, using a 3.4 Å probe to simulate N_2 accessibility. All MOP crystals were only weakly diffracting despite the use of synchrotron radiation and this is noted as required for the individual structures.

Activation Protocol

In a typical activation to generate activated-metal materials, MOP crystals were washed in DMA (x3) over a 2 day period. The crystals were then exchanged into acetone (x5) over a 5 day period. The samples were dried with supercritical carbon dioxide and subsequently heated to 50°C for 200 min to yield the activated samples.

In a typical activation to generate solvated-metal materials, MOP crystals were washed in DMA (x3) over a 2 day period. The crystals were then washed with methanol (x5) and rested in methanol overnight. The samples were dried at 80°C for 180 min to yield the activated samples.

Gas Adsorption

Gas adsorption isotherms were measured using volumetric methods on a Micromeritics 3-Flex analyser or ASAP2020 analyser (Micromeritics Instrument Corporation, Norcross, GA, USA) at 77 K and 87 K (utilizing liquid N_2 and Ar baths respectively or a cryo-cooler circulator). Brunauer–Emmett–Teller (BET) surface areas were calculated using experimental points at a relative pressure of P/P_0=0.05–0.25. UHP grade (99.999%) N_2 and (99.999%) CO_2 was used for all measurements.

*Synthesis of Dimethyl 5-hydroxyisophthalate (**3.9**)*

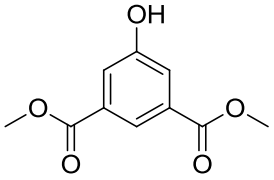

Concentrated sulfuric acid (2 mL) was added to a solution of 5-hydroxyisopthalic acid (10 g, 55 mmol) in methanol (100 mL). The resulting solution was heated at reflux overnight. The solvent was then removed leaving a white solid. The solid was dissolved in ethyl acetate (50 mL) and washed with sodium bicarbonate solution (50 mL), water (3 x 50 mL) and sodium chloride solution (50 mL). The organic layer was dried over magnesium sulfate, filtered and the solvent removed affording a white solid (9.2 g, 80%). ^{1}H NMR (500 MHz, $CDCl_3$): δ = 3.91 (6H, s), 7.59 (2H, d, *J* = 1.0 Hz) and 8.06 (1H, t, *J* = 1.0 Hz). ^{13}C NMR (125 MHz, $CDCl_3$): δ = 167.71, 159.35, 133.12, 122.51, 121.58, 59.22. m/z: 210.0.

*Synthesis of 5-(2-(2-(2-hydroxyethoxy)ethoxy)ethoxy)isophthalic acid (**3.1**)*

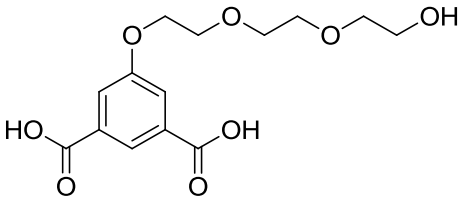

Dimethyl 5-hydroxyisophthalate (200 mg, 0.95 mmol) was mixed with potassium iodide (270 mg), potassium carbonate (140 mg), and 2-(2-(2-chloroethoxy)ethoxy)ethanol (0.3 mL, 2 mmol) were mixed in acetonitrile (10 mL) and stirred at reflux for 72 hours. The reaction mixture was filtered and the solvent removed under reduced pressure before addition of 1M HCl (10 mL). The product was extracted with ethyl acetate (2 x 20 mL), the combined organic extracts dried over $MgSO_4$, and the product concentrated under reduced pressure. The residue was taken up in 2:1 ethyl acetate:hexanes and filtered through silica to remove unreacted starting materials. The remaining material was dissolved in 1:1 EtOH:H_2O (20 mL) and potassium hydroxide (1g), and stirred at reflux for 16 hours. The ethanol was removed under vacuum and the remaining solution acidified (pH = 2) with concentrated HCl solution. The product was extracted with ethyl acetate, dried over $MgSO_4$ and isolated under reduced pressure as an orange solid (140 mg, 47% over two steps). ^{1}H NMR (500 MHz, $CDCl_3$): δ = 8.07 (1H, s), 7.65 (2H, s), 4.21 (2H, t, *J* = 5.0 Hz), 3.77 (2H, t, *J* = 5.0 Hz), 3.40 – 3.62 (8H,

m). (125 MHz, $CDCl_3$): δ = 166.13, 158.85, 131.71, 123.25, 120.04, 72.77, 69.55, 68.08, 66.01, 65.55, 61.83, 52.57. m/z: 314.1.

*Synthesis of bis(tert-butyldimethylsilyl) 5-((tert-butyldimethylsilyl)oxy)isophthalate (**3.11**)*

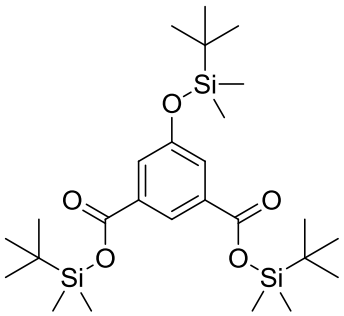

To a DMF solution (80 mL) of 5-hydroxyisopthalic acid (1.5 g, 7.38 mmol), under an argon atmosphere, imidazole (2.04 g, 29.55 mmol) and TBDMSCl (4.46 g, 31.01 mmol) were added. The reaction mixture was heated to 57 °C and stirred for 16 hours. The solvent was removed by evaporation and the residue was dissolved in CH_2Cl_2 (50 mL). The white precipitate was removed by filtration, and the organic solution was washed with H_2O (2 × 50 mL) and brine (2 × 50 mL), dried over $MgSO_4$ and filtered. The solvent was evaporated and the residue was dried under vacuum to yield a white solid (2.4 g, 50%). ^{1}H NMR (500 MHz $CDCl_3$): δ = 8.27 (1H, t, *J* = 1.5 Hz), 7.70 (2H, d, *J*=1.5 Hz), 1.03 (18H, s), 0.99 (9H, s), 0.30 (12H, s), 0.23 (6H, s). m/z: 524.2.

*Synthesis of 5-((tert-butyldimethylsilyl)oxy)isophthalic acid (**3.2**)*

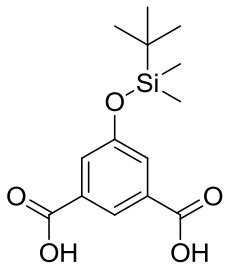

To a bis(*tert*-butyldimethylsilyl) 5-((*tert*-butyldimethylsilyl)oxy)isophthalate (2.4 g, 4.5 mmol) solution in THF (100 mL), glacial acetic acid (50 mL) and distilled water (18 mL) were added sequentially. The reaction mixture was stirred for 3 h and diluted with cold water (20 mL) and cooled to 0 °C in an ice bath. A white solid was precipitated which was isolated by filtration and dried under vacuum (1.3 g, 90%). ^{1}H NMR (500 MHz, DMSO-*d*6): δ = 8.09 (1H, t, *J* = 1.5 Hz), 7.54 (2H, d, *J* = 1.5 Hz), 0.95 (9H, s), 0.20 (6H, s). ^{13}C NMR (125 MHz, DMSO-*d*6): δ = 168.27, 159.54, 137.80, 134.52, 127.52, 32.61, 28.52, 7.51. m/z: 296.1.

*Synthesis of 5-(1,3-dioxoisoindolin-2-yl)isophthalic acid (**3.3**)*

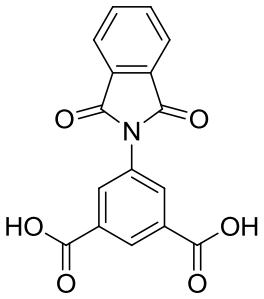

Phthalic anhydride (3.1 g, 17.11 mmol) and 1-amino 3,5-benzenedicarboxylic acid (2.5 g, 17.11 mmol) were dissolved in DMF (20 mL). The resulting solution was heated at reflux for 3 h. On cooling pure crystalline product was obtained (3.22 g, 60%). ^{1}H NMR (500 MHz, DMSO-*d*6): δ = 8.49 (1H, s), 8.28 (2H, s), 7.99 (2H, d, *J* = 3 Hz), 7.91 (2H, d, *J* = 3 Hz). ^{13}C NMR (125 MHz, DMSO-*d*6): δ = 166.56, 165.35, 136.25, 133.36, 131.78, 126.95, 122.74, 118.56. m/z: 311.0.

*Synthesis of Dimethyl 5-(benzyloxy)isophthalate (**3.12**)*

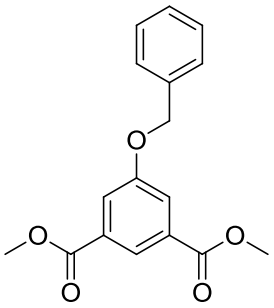

A mixture of dimethyl 5-hydroxyisophthalate (4 g, 14.5 mmol) and K_2CO_3 (3.4 g, 22.3 mmol) in CH_3CN/acetone (40 mL/30 mL) was refluxed 0.5 h. To this mixture was added of benzyl chloride (2.4 g, 19.3 mmol) dropwise. The resulting solution was heated at reflux overnight and the resulting light yellow suspension was concentrated by rotary evaporation. Water (40 mL) was added to the solution. The solution was extracted EtOAc (3 x 50 mL). The organic layed washed with brine solution (50 mL). After drying over anhydrous Na_2SO_4, the clear solution was concentrated under vacuum to give a pale yellow solid which was subsequently dried in a desiccator (5.0 g, 90%). ^{1}H NMR (500 MHz, $CDCl_3$): δ = 8.29 (1H, d, *J* = 5 Hz), 7.84 (2H, d, *J* = 5 Hz), 7.46 – 7.34 (5H, m), 5.15 (2H, s), 3.94 (6H, s). ^{13}C NMR (125 MHz, $CDCl_3$): δ = 166.54, 159.22, 136.50, 132.25, 129.12, 128.70, 128.02, 123.66, 120.61, 70.91, 52.87. m/z: 300.1.

*Synthesis of 5-(benzyloxy)isophthalic acid (**3.4**)*

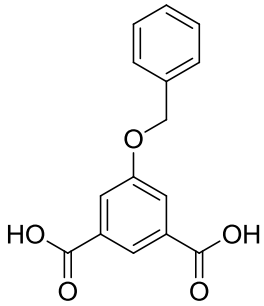

A solution of 4.0 g (13.2 mmol) of dimethyl 5-benzyloxyisophthalate and KOH (10.0 g, 53.5 mmol) were combined EtOH (100 mL) was heated to reflux for 4 h then cooled to rt. The solution was acidified with 2 M HCl to pH 3. The white precipitate was collected by filtration and dried under vacuum (3.05 g, 84%). ^{1}H NMR (500 MHz, DMSO-*d*6): δ = 13.30 (2H, s), 8.09 (1H, s), 7.74 (2H, d), 7.50 (2H, d), 7.39 (2H, m), 7.34 (1H, d), 5.24 ppm (2H, s); ^{13}C NMR (125 MHz, DMSO-*d*6): δ = 167.27, 159.38, 137.42, 133.53, 129.40, 128.87, 128.54, 123.35, 120.37, 70.59. m/z: 272.0.

*Synthesis of 5-(phenyldiazenyl)isophthalic acid (**3.5**)*

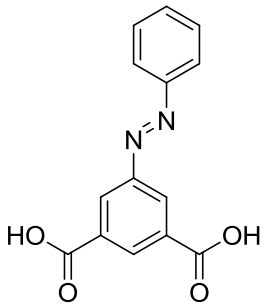

Nitrosobenzene (1.0 g, 9.3 mmol) and 5-aminoisophthalic acid (2.0 g, 11.2 mmol) were dissolved in a mixture of glacial acetic acid (70 mL) and H_2O (20 mL). The mixture was stirred at room temperature overnight. The crude product was isolated under vacuum and redissolved MeOH (50 mL) and a few drops of H_2SO_4. The mixture was stirred at room temperature for 3 hours before removal of the MeOH under vacuum. The residue was taken up in ethyl acetate and washed with water (2 x 20 mL). The washes were extracted with ethyl acetate (2 x 20 mL) and the organic extracts combined and concentrated under vacuum. The product was purified by column chromatography on silica (3:7 ethyl acetate:hexanes) yielding an orange solid which was dissolved in EtOH (10 mL) and 2M KOH (10 mL) and stirred and gentle reflux for 8 hours. The EtOH was subsequently removed under vacuum and the solution acidified with concentrated HCl. The yellow product was collected by filtration and

dried in a desiccator (1.2 g, 48%). ^{1}H NMR (500 MHz, DMSO-*d*6): δ = 8.81 (3H, m), 7.83 (2H, m), 7.64 (2H, m), 7.21 (1H, m). m/z: 270.0.

*Synthesis of dimethyl 5-aminoisophthalate (**3.13**)*

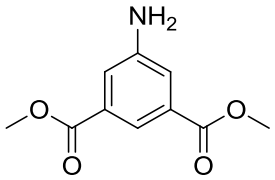

Concentrated sulfuric acid (2 mL) was added to a solution of 5-aminoisopthalic acid (4 g, 22.08 mmol) in methanol (100 mL). The resulting solution was heated at reflux overnight. The solvent was then removed leaving a white solid. The solid was dissolved in ethyl acetate (50 mL) and washed with sodium bicarbonate solution (50 mL), water (3 x 50 mL) and sodium chloride solution (50 mL) The organic layer was dried over $MgSO_4$, filtered and the solvent removed under vacuum leaving a white solid (3.88 g, 84 %). ^{1}H NMR (500 MHz, $CDCl_3$): δ = 8.04 (1H, s), 7.51 (2H, s) 3.90 (6H, s). ^{13}C NMR (125 MHz, $CDCl_3$): δ = 166.6, 146.8, 131.6, 120.7, 119.8, 52.4. m/z: 209.0.

*Synthesis of dimethyl 5-((4-hydroxyphenyl)diazenyl)isophthalate (**3.14**)*

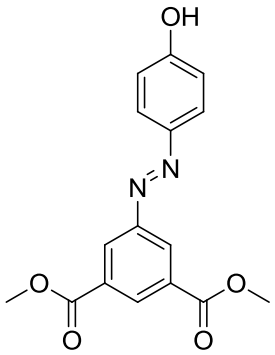

A solution of dimethyl 5-aminoisophthalate (2.1 g, 10 mmol) in H_2O (20 mL) was was cooled to 5 ºC and concentrated HCl (1 mL) added. $NaNO_2$ (0.75 g, 11 mmol) in ice water (4 mL) was added dropwise to the solution with vigorous stirring. Separately, a mixture of phenol (1.13 g, 12 mmol) and NaOAc (9 g, 110 mmol) in ice water (20 mL) was prepared. The first solution was added to the phenol mixture dropwise over 20 min with vigorous stirring. The mixture was allowed to warm to room temperature, filtered and washed with water (4 x 100 mL). The precipitate was dried in a dessicator yielding an orange solid (2.5 g, 80 %). ^{1}H NMR (500 MHz, DMSO-*d*6): δ = 10.48 (s), 8.50 (s), 8.41 (2H, s), 7.81 (2H, d, *J* =

7.2 Hz), 6.94 (2H, d, *J* = 7.2 Hz), 3.73 (6H, s). ^{13}C NMR (125 MHz, DMSO-*d*6): δ = 161.94, 159.60, 150.05, 142.34, 131.51, 130.21, 123.85, 123.52, 116.16, 48.6. m/z: 314.0.

*Synthesis of 5-((4-hydroxyphenyl)diazenyl)isophthalic acid (**3.6**)*

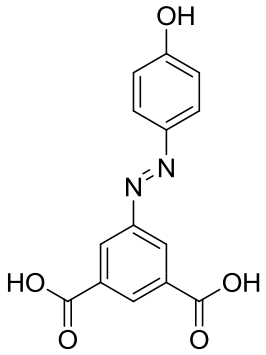

A solution of 2.5 g (7.95 mmol) of dimethyl 5-((4-hydroxyphenyl)diazenyl)isophthalate and KOH (10.0 g) were combined EtOH (100 mL) was heated to reflux for 4 h then cooled to room temperature. The solution was acidified with 2M HCl to pH = 3 and the white precipitate was collected by filtration and dried under vacuum (2.1 g, 92%). ^{1}H NMR (500 MHz, DMSO-*d*6): δ = 10.51 (s), 8.54 (s), 8.45 (2H, s), 7.87 (2H, d, *J* = 7.2 Hz), 6.97 (2H, d, *J* = 7.2 Hz). ^{13}C NMR (125 MHz, DMSO-*d*6): δ = 166.82, 161.80, 152.13, 145.10,134.23, 131.15, 125.71, 125.28, 116.16. m/z: 286.0.

*Synthesis of 1-(4-(bromomethyl)phenyl)-2-phenyldiazene (**3.15**)*

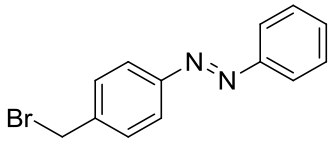

1-Phenyl-2-(*p*-tolyl)diazene (810 mg, 7.57 mmol) and N-bromosuccinimide (1.35 g, 7.57 mmol) were dissolved in degassed CCl_4 and VAZO-88 (186 mg, 0.76 mmol) was added. The reaction was heated at reflux under an inert atmosphere for 5 hours and the solid removed by filtration. The solvent was removed under vacuum to afford an orange product (1.92 g, 92%). ^{1}H NMR (500 MHz, $CDCl_3$): δ = 7.91 (m, 4H), 7.52 (m, 5H), 4.55 (s, 2H). m/z: 274.0.

*Synthesis of dimethyl 5-((4-(phenyldiazenyl)benzyl)oxy)isophthalate (**3.16**)*

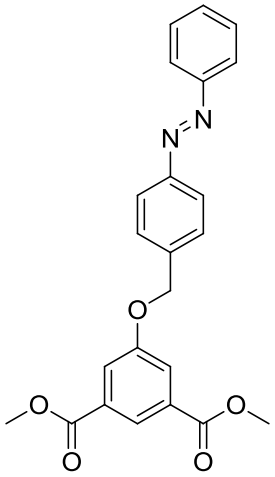

A mixture of 1-(4-(bromomethyl)phenyl)-2-phenyldiazene (340 mg, 1.22 mmol), dimethyl 5-hydroxyisophthalate (260 mg, 1.23 mmol) and K_2CO_3 (188mg, 1.35 mmol) in DMF (10 mL) was heated in a microwave at 120 °C for 2 hours. The solution was filtered and 1M HCl (20 mL) was added. The product was extracted with ethyl acetate (2 x 20 mL), dried over $MgSO_4$ and isolated under reduced pressure to yield a yellow solid (230 mg, 47%). ^{1}H NMR (500 MHz, $CDCl_3$): δ = 8.31 (1H, m), 7.95 - 7.35 (10H, m), 5.15 (2H, s), 3.94 (6H, s). m/z: 404.1.

*Synthesis of 5-((4-(phenyldiazenyl)benzyl)oxy)isophthalic acid (**3.7**)*

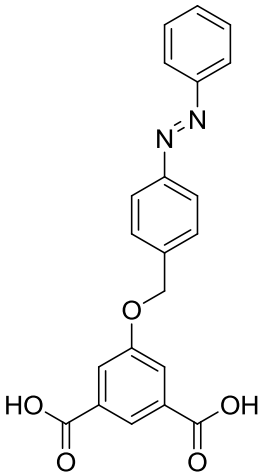

Dimethyl 5-((4-(phenyldiazenyl)benzyl)oxy)isophthalate (200 mg, 0.49 mmol) was dissolved in EtOH (20 mL) and 2M KOH solution (20 mL) and stirred at gentle reflux for 16 hours. The EtOH was removed under reduced pressure and the solution acidified with concentrated HCl. The precipitate was collected by filtration and dried under vacuum to yield a yellow solid (145 mg, 79%). ^{1}H NMR (500 MHz, DMSO-*d*6): δ = 8.27 (1H, m), 7.91 - 7.29

(10H, m), 4.90 (2H, s). ^{13}C NMR (125 MHz, DMSO-*d*6): δ = 167.31, 160.54, 144.58 137.42, 133.63, 126.91, 124.76, 120.37, 71.02 m/z: 376.1.

*Synthesis of (4-(bromomethyl)phenyl)phenylmethanone (**3.17**)*

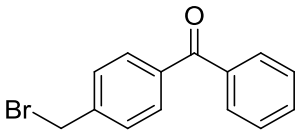

Phenyl(*p*-tolyl)methanone (500 mg, 2.54 mmol) and N-bromosuccinimide (544 mg, 3.06 mmol) were dissolved in degassed $CHCl_3$ (10 mL) followed by the addition of VAZO-88 (62 mg, 0.25 mmol). The mixture was stirred at reflux under an inert atmosphere for 16 hours, then allowed to cool to room temperature. The mixture was diluted with DCM (100 mL) and washed with saturated sodium bicarbonate solution (2 x 50 mL) and saturated sodium chloride solution (2 x 50 mL). The organic fraction was dried over Na_2SO_4 and the solvent removed under reduced pressure. The product was washed sparingly with cold EtOH affording a white solid (374 mg, 54%). ^{1}H NMR (500 MHz, $CDCl_3$): δ = 7.77 – 7.81 (4H, m), 7.57 – 7.63 (1H, m), 7.46 – 7.52 (4H, m), 4.53 (2H, s). ^{13}C NMR (125 MHz, $CDCl_3$): δ = 196.0, 142.1, 137.4, 136.4, 132.5, 130.6, 130.0, 128.9, 128.3, 32.2. m/z: 274.0.

*Synthesis of dimethyl 5-((4-benzoylbenzyl)oxy)isophthalate (**3.18**)*

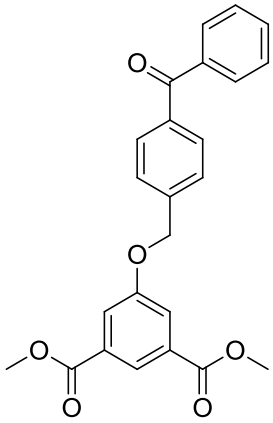

(4-(Bromomethyl)phenyl)phenylmethanone (187 mg, 0.67 mmol) and dimethyl 5-hydroxyisophthalate (124 mg, 0.67 mmol) were dissolved in acetonitrile (10 mL) with potassium hydroxide (268 mg) and potassium carbonate (142 mg). The reaction mixture was stirred at reflux for 16 hours, filtered and the solvent removed under vacuum. 1M HCl (50 ml) was added and the product extracted with ethyl acetate (2 x 50 mL). The organic phase was dried over Na_2SO_4, the solvent removed under vacuum to afford a pale yellow solid (180 mg,

66%).[1]H NMR (500 MHz, $CDCl_3$): δ = 8.48 (1H, s), 8.00 – 7.75 (6H, m), 7.68 – 7.47 (5H, m), 5.51 (2H, s), 3.96 (6H, s). m/z: 404.4.

*Synthesis of 5-((4-benzoylbenzyl)oxy)isophthalic acid (**3.8**)*

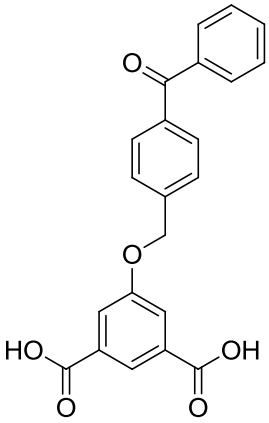

Dimethyl 5-((4-benzoylbenzyl)oxy)isophthalate (180 mg, 0.45 mmol) was dissolved in a mixture of H_2O (5 mL), EtOH (10 mL) and KOH (185 mg) and stirred at 45 °C for 16 hours. The EtOH was removed under reduced pressure and the solution was washed with DCM (10 mL). 1M HCl (50 mL) was added and the product extracted with ethyl acetate (2 x 25 mL), dried over Na_2SO_4 and isolated under reduced pressure yielding a white solid (90 mg, 46%). [1]H NMR (500 MHz, DMSO-*d*6): δ = 8.43 (1H, s), 7.95 – 7.73 (6H, m), 7.64 – 7.45 (5H, m), 5.24 (2H, s). m/z: 376.0.

*Synthesis of Cu_{24}(5-(2-(2-(2-hydroxyethoxy)ethoxy)ethoxy)isophthalate)$_{24}$.xS (**3.9**)*

5-(2-(2-(2-Hydroxyethoxy)ethoxy)ethoxy)isophthalic acid **3.1** (140 mg, 0.45 mmol) and $Cu(NO_3)_2 \cdot 3H_2O$ (122 mg, 0.45 mmol) were dissolved in MeOH (13 mL). Under vigorous stirring, 2,6-lutidine (0.11 mL, 0.9 mmol) was added dropwise and the reaction stirred for 30 minutes. The solvated product was collected by filtration as a blue solid and dried in a dessicator for 12 hours (204 mg). Crystals suitable for single crystal X-ray diffraction studies were obtained by slow vapour diffusion of isobutanol into a solution of the MOP in DMSO.

*Synthesis of Cu_{24}(5-(1,3-dioxoisoindolin-2-yl)isophthalate)$_{24}$.xS (**3.10**)*

5-(1,3-Dioxoisoindolin-2-yl)isophthalic acid **3.3** (140 mg, 0.45 mmol) and $Cu(NO_3)_2 \cdot 3H_2O$ (122 mg, 0.45 mmol) were dissolved in MeOH (15 mL). Under vigorous stirring, 2,6-lutidine (0.2 mL, 1.6 mmol) was added dropwise and the reaction stirred at reflux overnight. The excess solvent was removed under reduced pressure to afford the solvated product as a blue solid (192 mg). Crystals suitable for single crystal X-ray diffraction studies were obtained by slow evaporation of a methanolic MOP solution.

*Synthesis of Cu_{24}(5-(benzyloxy)isophthalate)$_{24}$.xS (**3.11**)*

5-(Benzyloxy)isophthalic acid **3.4** (29 mg, 0.1 mmol) and $Cu(NO_3)_2 \cdot 3H_2O$ (24 mg, 0.1 mmol) were dissolved in 4 mL of DMA. A single drop of MeOH was added and the mixture was stood undisturbed for 24 hours. The resulting crystals of **3.11** were analyzed by single crystal X-ray diffraction. Bulk **3.11** can be prepared by further addition of MeOH to the solution, which precipitates the solvated product as a blue solid which can be collected by filtration (40 mg).

*Synthesis of $Co_{12}Pd_{12}$(5-((4-benzoylbenzyl)oxy)isophthalate)$_{24}$.xS (**3.12**)*

In a screw cap vial, a solution of $[Pd(\mu\text{-}OOCMe)_4Co(OH_2)(HOOCMe)_2]$ **2.1** (13 mg, 0.024 mmol) in DMA (3 mL) and MeOH (1 mL) was added 5-((4-benzoylbenzyl)oxy)isophthalic acid **3.8** (10 mg, 0.026 mmol). The mixture was left at room temperature overnight resulting in small block-shaped violet crystals of **3.12** suitable for single crystal X-ray diffraction analysis.

3.9. References

(1) De Zorzi, R.; Guidolin, N.; Randaccio, L.; Geremia, S. *Cryst. Eng. Comm.* **2010**, *12*, 4056.

(2) Dobrzańska, L.; Lloyd, G. O.; Raubenheimer, H. G.; Barbour, L. J. *J. Am. Chem. Soc.* **2005**, *127*, 13134.

(3) Yaghi, O. M.; Li, H.; Davis, C.; Richardson, D.; Groy, T. L. *Acc. Chem. Res.* **1998**, *31*, 474.

(4) Sudik, A. C.; Millward, A. R.; Ockwig, N. W.; Côté, A. P.; Kim, J.; Yaghi, O. M. *J. Am. Chem. Soc.* **2005**, *127*, 7110.

(5) Mastalerz, M. *Chem.- Eur. J.* **2012**, *18*, 10082.

(6) Zhang, G.; Presly, O.; White, F.; Oppel, I. M.; Mastalerz, M. *Angew. Chem., Int. Ed.* **2014**, *53*, 5126.

(7) Desiraju, G. R. *Angew. Chem., Int. Ed.* **2007**, *46*, 8342.

(8) R. Desiraju, G. *Chem. Commun.* **1997**, 1475.

(9) Aakeroy, C. B.; Champness, N. R.; Janiak, C. *Cryst. Eng. Comm.* **2010**, *12*, 22.

(10) Karmakar, A.; Illathvalappil, R.; Anothumakkool, B.; Sen, A.; Samanta, P.; Desai, A. V.; Kurungot, S.; Ghosh, S. K. *Angew. Chem., Int. Ed.* **2016**, *55*, 10667.

(11) Marti-Rujas, J.; Colombo, L.; Lu, J.; Dey, A.; Terraneo, G.; Metrangolo, P.; Pilati, T.; Resnati, G. *Chem. Commun.* **2012**, *48*, 8207.

(12) Pigge, F. C.; Vangala, V. R.; Kapadia, P. P.; Swenson, D. C.; Rath, N. P. *Chem. Commun.* **2008**, 4726.

(13) Eddaoudi, M.; Kim, J.; Wachter, J. B.; Chae, H. K.; O'Keeffe, M.; Yaghi, O. M. *J. Am. Chem. Soc.* **2001**, *123*, 4368.

(14) Furukawa, H.; Kim, J.; Plass, K. E.; Yaghi, O. M. *J. Am. Chem. Soc.* **2006**, *128*, 8398.

(15) Perry, J. J.; Kravtsov, V. C.; Zaworotko, M. J.; Larsen, R. W. *Cryst. Growth Des.* **2011**, *11*, 3183.

(16) Tonigold, M.; Hitzbleck, J.; Bahnmuller, S.; Langstein, G.; Volkmer, D. *Dalton Trans.* **2009**, *0*, 1363.

(17) Tonigold, M.; Volkmer, D. *Inorg. Chim. Acta* **2010**, *363*, 4220.

(18) Lin, R.; Ge, L.; Hou, L.; Strounina, E.; Rudolph, V.; Zhu, Z. *ACS App. Mater. Interfaces* **2014**, *6*, 5609.

(19) Hoare, T. R.; Kohane, D. S. *Polymer* **2008**, *49*, 1993.

(20) Karcher, S.; Kornmüller, A.; Jekel, M. *Water Research* **2001**, *35*, 3309.

(21) Masuda, T.; Isobe, E.; Higashimura, T.; Takada, K. *J. Am. Chem. Soc.* **1983**, *105*, 7473.

(22) Nik, O. G.; Chen, X. Y.; Kaliaguine, S. *J. Membr. Sci.* **2012**, *413–414*, 48.

(23) Ren, H.; Jin, J.; Hu, J.; Liu, H. *Ind. Eng. Chem. Res.* **2012**, *51*, 10156.

(24) Bury, I.; Heinrich, B.; Bourgogne, C.; Mehl, G. H.; Guillon, D.; Donnio, B. *New J. Chem.* **2012**, *36*, 452.

(25) Bos, A.; Pünt, I. G. M.; Wessling, M.; Strathmann, H. *J. Polym. Sci. Part B: Polym. Phys.* **1998**, *36*, 1547.

(26) Wind, J. D.; Paul, D. R.; Koros, W. J. *J. Membr. Sci.* **2004**, *228*, 227.

(27) Singh, D.; Bhattacharyya, P. K.; Baruah, J. B. *Cryst. Growth Des.* **2010**, *10*, 348.

(28) Park, J.; Sun, L.-B.; Chen, Y.-P.; Perry, Z.; Zhou, H.-C. *Angew. Chem., Int. Ed.* **2014**, *53*, 5842.

(29) Lyndon, R.; Konstas, K.; Ladewig, B. P.; Southon, P. D.; Kepert, P. C. J.; Hill, M. R. *Angew. Chem., Int. Ed.* **2013**, *52*, 3695.

(30) Brown, J. W.; Henderson, B. L.; Kiesz, M. D.; Whalley, A. C.; Morris, W.; Grunder, S.; Deng, H.; Furukawa, H.; Zink, J. I.; Stoddart, J. F.; Yaghi, O. M. *Chem. Sci.* **2013**, *4*, 2858.

(31) Li, Z.-y.; Quan, H.-j.; Gong, C.-b.; Yang, Y.-z.; Tang, Q.; Wei, Y.-b.; Ma, X.-b.; Lam, H.-w. *Food Chemistry* **2015**, *172*, 56.

(32) Kaiser, M.; Leitner, S. P.; Hirtenlehner, C.; List, M.; Gerisch, A.; Monkowius, U. *Dalton Trans.* **2013**, *42*, 14749.

(33) Dorman, G.; Prestwich, G. D. *Biochemistry* **1994**, *33*, 5661.

(34) Prucker, O.; Naumann, C. A.; Rühe, J.; Knoll, W.; Frank, C. W. *J. Am. Chem. Soc.* **1999**, *121*, 8766.

(35) Horie, K.; Takagi, T.; Mita, I.; Shindo, Y.; Sato, H.; Tanaka, Y. *Polym. J.* **1984**, *16*, 887.

(36) Porter, G.; Suppan, P. *Trans. Faraday Soc.* **1965**, *61*, 1664.

(37) Lin, A. A.; Sastri, V. R.; Tesoro, G.; Reiser, A.; Eachus, R. *Macromolecules* **1988**, *21*, 1165.

(38) Horie, K.; Tsukamoto, M.; Morishita, K.; Mita, I. *Polym J* **1985**, *17*, 517.

(39) Guindon, Y.; Fortin, R.; Yoakim, C.; Gillard, J. W. *Tetrahedron Lett.* **1984**, *25*, 4717.

(40) Corey, E. J.; Venkateswarlu, A. *J. Am. Chem. Soc.* **1972**, *94*, 6190.

(41) Abourahma, H.; Coleman, A. W.; Moulton, B.; Rather, B.; Shahgaldian, P.; Zaworotko, M. J. *Chem. Commun.* **2001**, 2380.

(42) Takeda, N.; Umemoto, K.; Yamaguchi, K.; Fujita, M. *Nature* **1999**, *398*, 794.

(43) Li, J.-R.; Zhou, H.-C. *Nat. Chem.* **2010**, *2*, 893.

(44) Edwards, A. J.; Dhayal, R. S.; Liao, P.-K.; Liao, J.-H.; Chiang, M.-H.; Piltz, R. O.; Kahlal, S.; Saillard, J.-Y.; Liu, C. W. *Angew. Chem., Int. Ed.* **2014**, *53*, 7214.

(45) Bragg, W. H.; Bragg, W. L. *X Rays and Crystal Structure*; London : G. Bell, **1915**.

(46) Sheldrick, G. M.; University of Gottingen: 2014.

(47) Sheldrick, G. M. *Acta Crystallogr.* **2015**, *C71*, 3.

(48) Kostenko, M. G.; Rempel, A. A.; Sharf, S. V.; Lukoyanov, A. V. *Phys. Solid State* **2015**, *57*, 637.

(49) Boeyens, J. C. A.; Levendis, D. C. *J. Chem. Phys.* **1986**, *84*, 3986.

(50) Gilson, M. K.; Given, J. A.; Bush, B. L.; McCammon, J. A. *Biophys. J.* **1997**, *72*, 1047.

(51) Teo, J. M.; Coghlan, C. J.; Evans, J. D.; Tsivion, E.; Head-Gordon, M.; Sumby, C. J.; Doonan, C. J. *Chem. Commun.* **2015**, 52, 276.

(52) Accelrys Software Inc.: *Materials Studio ver. 5.5.3*, **2010**

(53) Accelrys Software Inc.: *Forcite Module for Materials Studio*, **2010**

(54) Spek, A. L. *Acta Crystallogr.* **2009**, *D65*, 148.

(55) McPhillips, T. M., McPhillips, S.E., Chiu, J. H., Cohen, A.E., Deacon, A. M., Ellis, P. J., Garman, E., Gonzalez, A., Sauter, N. K., Phizackerley, R. P., Soltis, S. M., Kuhn, P. *J. Synchrotron Rad.* **2002**, 401.

(56) Sheldrick, G. M. *Acta Crystallogr.* **2008**, *A64*, 112.

(57) Barbour, L. J. *J. Supramol. Chem.* **2001**, *1*, 189.

(58) Sheldrick, G. *Acta Crystallogr. Section A* **2015**, *71*, 3.

(59) Dolomanov, O. V.; Bourhis, L. J.; Gildea, R. J.; Howard, J. A. K.; Puschmann, H. *J. Appl. Crystallogr.* **2009**, *42*, 339.

3.10. Appendices

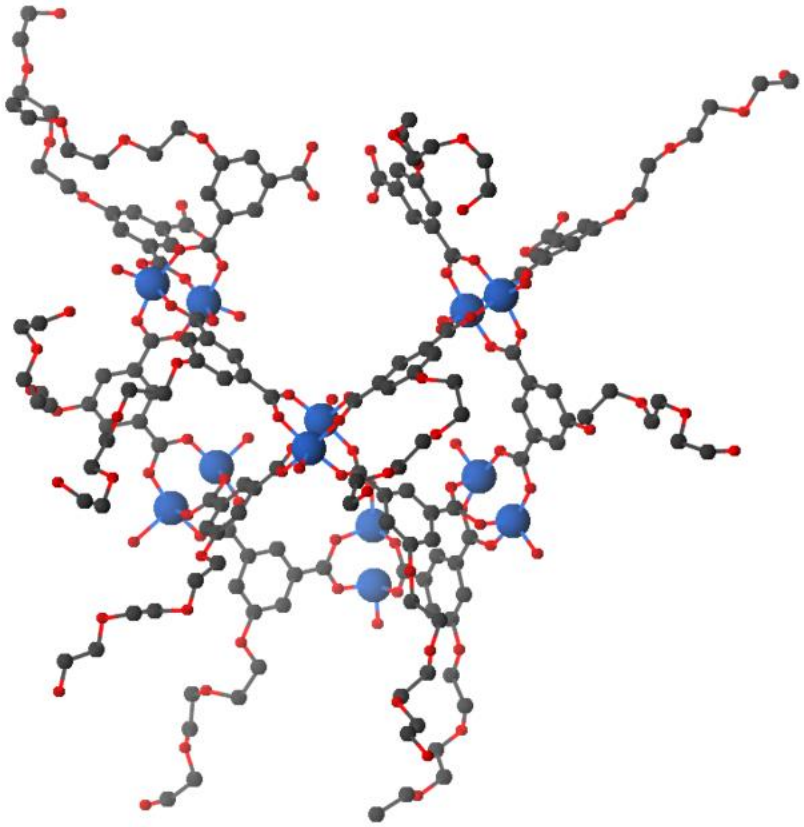

Figure 86. A perspective view of the asymmetric unit of **3.9**. Only the oxygen atom of coordinating solvent molecules were located in the structure solution. Copper atoms are shown in dark blue and hydrogen atoms have been omitted for clarity.

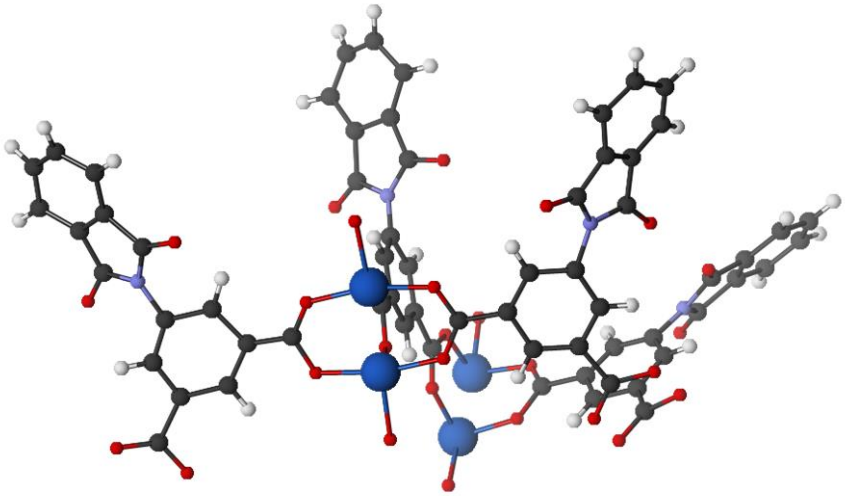

Figure 87. A perspective view of the asymmetric unit of **3.10**. Only the oxygen atom of coordinating solvent molecules were located in the structure solution. Copper and nitrogen atoms are shown in dark and pale blue respectively.

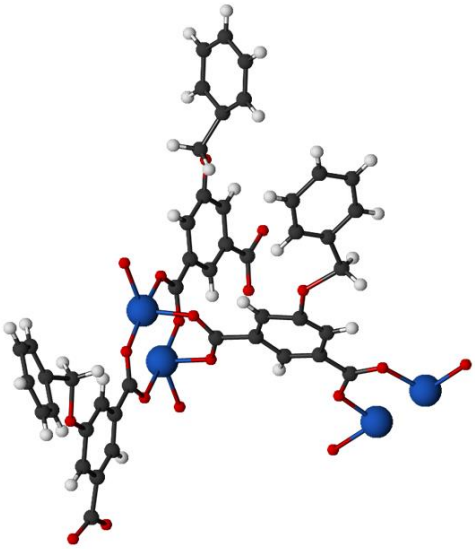

Figure 88. A perspective view of the asymmetric unit of **3.11**. Only the oxygen atom of coordinating solvent molecules were located in the structure solution. Copper atoms are shown in dark blue.

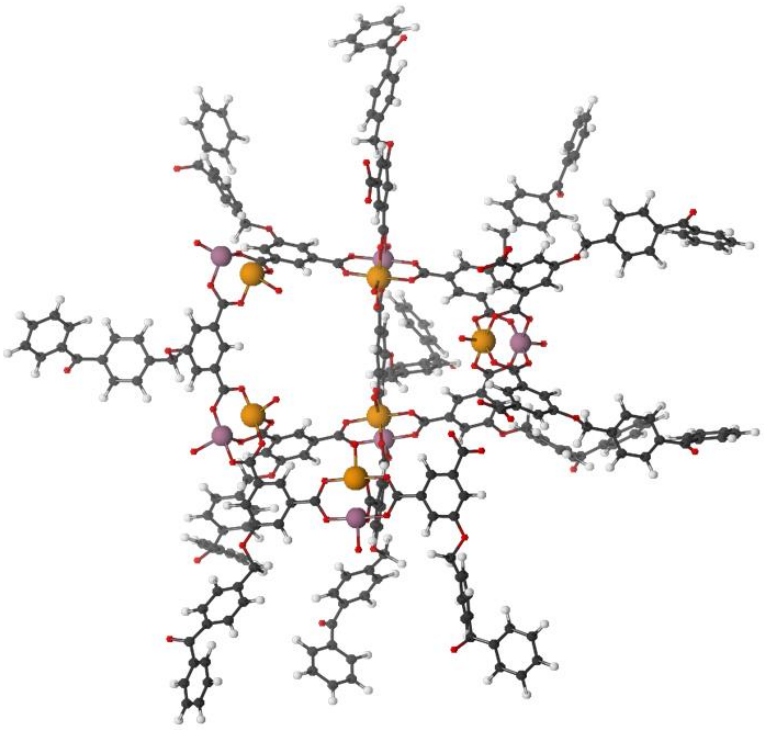

Figure 89. A perspective view of the asymmetric unit of **3.12**. Only the oxygen atom of coordinating solvent molecules were located in the structure solution. Cobalt and palladium atoms are shown in mauve and orange respectively.

Table 11. Crystallographic data for exohedrally functionalised MOPS. Indicated structures (*) have the electron density associated with the disordered side chains removed via SQUEEZE routine.

Compound	Cu_{24}(**3.1**)$_{24}$*	Cu_{24}(**3.3**)$_{24}$	Cu_{24}(**3.4**)$_{24}$	$Co_{12}Pd_{12}$(**3.8**)$_{24}$*
Empirical formula	$C_{168}H_{192}O_{96}Cu_{12}$	$C_{192}H_{108}Cu_{12}N_{12}O_{84}$	$C_{180}H_{120}O_{72}Cu_{12}$	$C_{264}H_{168}Co_6O_{72}Pd_6$
Formula weight	4509.82	4689.38	4197.23	5484.23
Crystal system	Monoclinic	Trigonal	Tetragonal	Monoclinic
Space group	$P2_1/c$	R-3	$P4/mnc$	$P2_1/n$
a (Å)	24.3976(13)	29.973(5)	27.860(4)	25.791(5)
b (Å)	36.464(2)	29.973(5)	27.860(4)	55.407(11)
c (Å)	36.625(2)	73.485(15)	39.580(8)	27.455(6)
α (°)	90	90	90	90
β (°)	102.075(5)	90	90	100.90(3)
γ (°)	90	120	90	90
Volume (Å^3)	31862(3)	57173(22)	30721(11)	38526(14)
Z	4	6	4	4
Density (calc.) (mg/m^3)	0.640	0.817	0.907	0.580
Absorption coefficient (mm^{-1})	0.824	0.707	0.868	0.558
F(000)	6001	14184	8496	6616
θ range for data collection (°)	2.4 to 29.2	0.8 to 17.6	1.0 to 22.4	1.1 to 20.5
Observed reflections	4724	6206	8548	18297
Reflections collected	76484	8191	10129	26692
[R(int)]	0.3475	0.1118	0.0869	0.124
Restraints/parameters	33/1522	174/893	51/565	6/1620
Completeness (%)	0.991	0.992	0.998	0.993
Goodness-of-fit on F^2	0.549	0.97	2.652	1.04
R_1 [I>2σ(I)]	0.1325	0.0737	0.110	0.068
wR_2 (all data)	0.3746	0.2204	0.3345	0.217
Largest peak (e.Å^{-3})	1.1	0.696	1.03	0.373
Deepest hole (e.Å^{-3})	-0.6	-0.327	-0.588	-0.357

CHAPTER 4.

CO_2/N_2 SEPARATIONS BY MOP-PTMSP MEMBRANES

Part of this work appears in the following publication:

AIMS: A New Strategy to Control Physical Aging and Gas Transport in Mixed-Matrix Membranes.[1]

Chapter 4. CO_2/N_2 Separations by MOP-PTMSP Membranes

4.1. Introduction

Separation of CO_2 from N_2 gas in a manner that is both efficient and effective is an issue of global significance.[2-5] As a known greenhouse gas, anthropogenic CO_2 has been a target of gas capture technology for several decades with a significant focus on the removal of CO_2 at points of primary energy production.[6] Despite advances in aqueous amine based carbon capture technology, much of the energy produced by the combustion process is used for regeneration of the amine absorbent which chemically binds the generated CO_2 (see section 1.6.1).[7] The energetic cost of absorbent regeneration is a result of both the high enthalpy of CO_2 chemisorption and the aqueous nature of the absorbent mixture and as such is intrinsic to the aqueous amine methodology.[8] By removing CO_2 from flue streams using a more efficient process, primary energy production can be made more cost effective, while simultaneously reducing the amount of fossil fuel that is consumed to satisfy a given energy requirement.[9] Membranes provide an attractive platform for this task through selective gas permeation (Figure 90).[10] In principle, a membrane can separate CO_2 directly from a post combustion flue stream without the requirement of a chemical absorbent, removing the energy intensive absorbent regeneration step. The work in this chapter explores the synthesis and characterisation of mixed matrix membranes for the purpose of separating gas phase mixtures, with particular focus on the environmentally significant CO_2/N_2 gas separation.

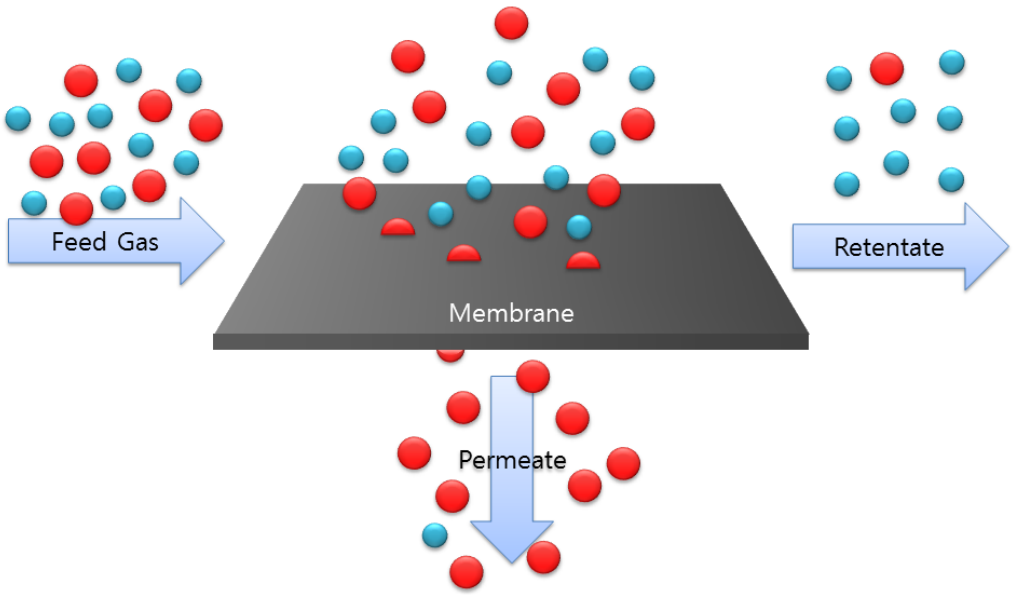

Figure 90. Schematic representation of membrane based gas separation.

4.2. Gas Separation by Selective Permeation

Membrane based gas separation is reliant on differences in permeation of the relevant gases. The effectiveness of a membrane is dependent on two opposing properties: the specific gas selectivity and the rate of gas permeation.[11] First described by Robeson, the trade-off between selectivity and permeability describes a limit known as the 'Robeson upper bound' of membrane performance.[12] As a membrane's gas permeability is unique for each gas, the upper bound is subsequently unique for each gas separation. The upper bound itself is not a fundamental limitation determined by physical constraint, but an empirical description of separation potential. As such, the upper bound is determined by existing materials and redefined as membrane technology advances.[13] Gas permeation through a membrane for a given gas is the product of the rate of gas diffusion and the gas solubility within the membrane.[13]

$$P = D \times S$$

Where: P = Gas permeation, D = Rate of gas diffusion, S = Gas solubility

By consideration of these properties, a membrane can be designed to allow selective permeation of a desired species. The rate of gas diffusion across a membrane is influenced by both the physical and electronic properties of the gas-membrane pair. The kinetic diameter of a permeant gas is often exploited as a means to limit diffusion, as a membranes pore apertures can be small enough to exclude a larger guest.[14-16] While this methodology is highly effective for species with greatly varying molecular sizes, the effectiveness is reduced when the kinetic diameters are closely matched. This difficulty becomes apparent when comparing N_2 and CO_2 gases, which have a difference in kinetic diameter of less than 0.4 Å.[17] To effectively separate mixtures in cases such as this, the membrane pore size must be finely tuned to control the selectivity of permeation, a particularly challenging task for materials designed using a 'top-down' approach.

Exploitation of electronic properties provides a second means with which to alter permeant diffusion rates. Highly charged pore interiors can exert an attractive force on polar species increasing the retention time at a given adsorption site, thus reducing the rate of diffusion.[18] More commonly however, increasing the strength of this interaction often has the

effect of increasing the solubility of a polar guest subsequently enhancing the permeation properties. Importantly, this behaviour is reliant on a Knudsen-type diffusion mechanism in which the gas-membrane interactions govern the diffusion process.[19] The net effect on permeation therefore is complex as several considerations need to be taken into account.

As advances are made in membrane development, new materials are giving further promise to the realisation of effective, membrane based CO_2/N_2 separation.Two promising materials for this application are the polymers of intrinsic microporosity (PIMs) PIM-1 and PIM-7.[20] The CO_2/N_2 separation performance of both of these polymers is close to the current upper-bound, due in part to their impressive ideal selectivites (see section 4.5) of 25 and 26.2 respectively. These selectivities are coupled with modest CO_2 permeabilities of 2300 and 1100 barrer respectively. A highly permeable example of near upper-bound performance is poly[1-(trimethylgermyl)-1-propyne] which has a CO_2 permeability of 14000 barrer, however the CO_2/N_2 ideal selectivity is 14, falling short of the aforementioned PIMs.

4.2.1. Poly[1-(trimethylsilyl)-1-propyne]and aging effects

Poly[1-(trimethylsilyl)-1-propyne] (PTMSP) is an organic polymer with exceptional CO_2/N_2 separation potential which has been used to define the upper bound of CO_2/N_2 performance (Figure 91).[13] When cast as a membrane, PTMSP polymer chains are captured in a meta-stable state with a high void space fraction. This highly accessible free volume within the membrane endows the membrane with exceptional gas transport properties. PTMSP membranes are extremely permeable to many gases including CO_2 however the CO_2/N_2 selectivity is lower than other high performing polymers. The differences in separation performance between highly selective and highly permeable membranes are quite dramatic, often differing greatly in these respective properties. Poly[bis(2-(2-methoxyethoxy)ethoxy)phosphazene] for example is a highly selective membrane boasting a CO_2/N_2 selectivity of 62.5, however the low CO_2 permeability of 250 barrer is prohibitively low for application in industrial CO_2 capture. In contrast, PTMSP displays a much more meagre ideal selectivity of close to 6, however the permeability of CO_2 is two orders of magnitude greater at 30000 barrer.

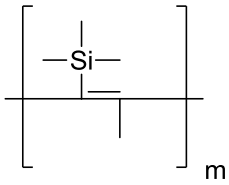

Figure 91. Chemical structure of poly[1-(trimethylsilyl)-1-propyne] (PTMSP)

PTMSP polymers exhibit promising gas separation properties due to the exceptionally high gas permeability of the polymer. This high permeability results from the physical structure of the polymer which, when cast, forms as a meta-stable network with a large void fraction.[21,22] Over time, the polymer chains that form the bulk material relax towards the thermodynamic form resulting in a closer packing of polymer chains, a subsequent reduction in void space and subsequently a dramatic reduction in gas permeability (Figure 92).[23,24] Due to the attractiveness of membranes as an energetically efficient medium for industrial separation processes, significant studies exist in the literature in an effort to understand the aging mechanisms and extend the longevity of such materials.[25-27]

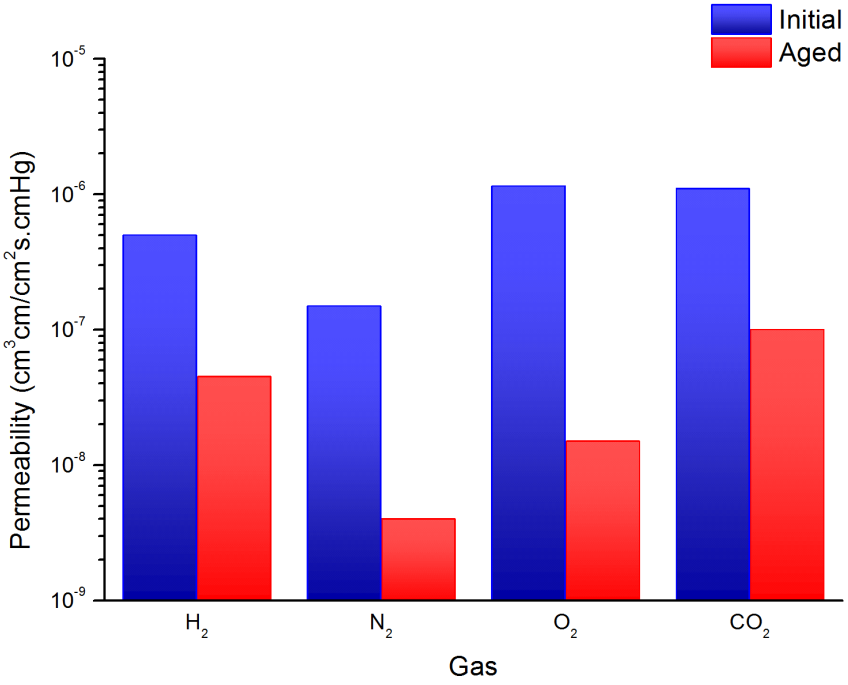

Figure 92. Aging effects on the gas permeability of PTMSP polymer.

4.3. Mixed Matrix Membranes

Organic polymers have been investigated for use in membranes for decades largely due to their macroscopic physical properties.[28,29] Such polymers are often highly processable and flexible which are both valued for large scale application. The addition of secondary phases within a membrane has shown significant potential as a means to enhance gas separation properties.[30,31] Such mixed matrix membranes, consisting of an organic polymer combined with an inorganic phase, have shown remarkable progress towards carbon capture applications due to synergistic effects of the two phases.[32] Typically the organic phase acts largely as a physical support for the inorganic phase, ensuring that the subsequent material is physically suitable for membrane-type application.[33,34] Many polymers, such as the polyimide Matrimid materials (Figure 93), have found extensive use in this role for CO_2 permeable membranes as they intrinsically possess significant separation performance.[35,36] The inclusion of an inorganic phase, such as a metal-organic framework, may potentially improve the performance of the resultant membrane by adding a phase which is highly selective for a particular component.[37] Due to their highly ordered, often crystalline nature, inorganic phases often possess much greater permselectivity than their organic counterparts, yet lack the physical robustness and flexibility required of a membrane.[38]

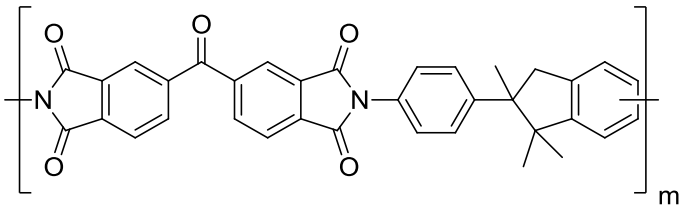

Figure 93. The chemical structure of Matrimid, commonly used in mixed matrix membranes.

4.3.1. Phase Interface and Compatibility

Ideally, the multiple phases in a mixed matrix membrane work synergistically to enhance the desired properties of the material. This is rarely true in reality however, due to incompatibility of the two phases.[39] Gas molecules passing through a material tend to follow the path of least resistance, which in a membrane represents the regions of highest

permeability.[40] As such, the regions of higher selectivity are often avoided by the permeant species where the rate of diffusion tends to be lower. In more extreme cases, this can lead to an overall reduction in performance of the membrane as one phase behaves like a non-permeable barrier, causing a reduction in net permeability with little to no increase in selectivity (Figure 94).[41] This type of interaction can be avoided by combining phases that have similar rates of gas diffusion as this reduces the phase preference for the permeating species.[42]

The phase interfacing within a mixed matrix membrane has a dramatic effect on overall membrane performance as poor interactions between matrices generate non-selective void space within the membrane.[43] Permeant species preferentially travel through these highly permeable void spaces and avoid the selective regions of the membrane, diminishing the separation properties of the material. Enhancing the interaction between the two matrices ensures that the presence of non-selective void space is minimised leading to improved performance.

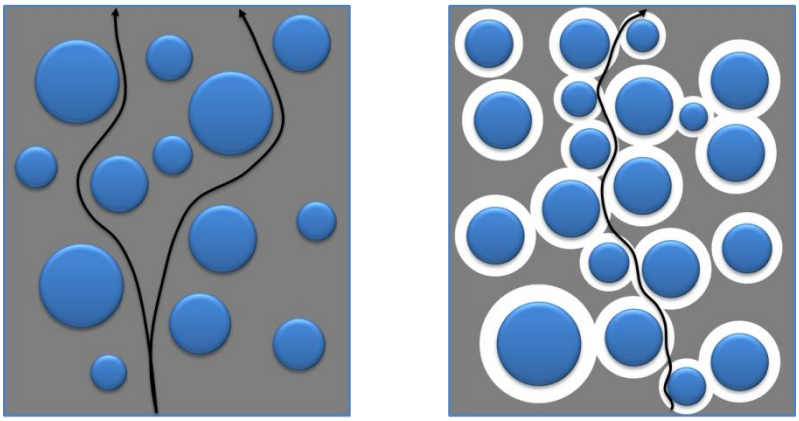

Figure 94. Representations of preferential gas transport through a high permeability phase (left) and void space generated by poor matrix interfacing (right).

4.3.2. MOP-Polymer Materials

Despite intense research into mixed matrix membranes containing metal-organic or inorganic phases, such as MOFs and zeolites, the application of MOPs in this area remains almost entirely unexplored.[44,45] As the phase interface has such a significant impact on the overall performance of a mixed matrix membrane, the work in this chapter explores the use of MOPs as an alternative to a MOF matrix to improve the interaction with an organic polymer

phase. MOFs are known for their highly ordered pore structure which can be tuned for specific host-guest interactions. This porosity however is a product of the polymeric structure, such that the framework cannot be reduced to a single pore 'unit' without significantly altering its properties. Conversely, MOPs are discrete entities in which the intrinsic void structure is preserved in each MOP unit. It is proposed that MOPs can be dispersed throughout a polymeric material uniformly such that individual MOP structures are embedded homogeneously throughout the polymer phase. This also allows for exploitation of the possible external functionality of MOP structures, such as those in Chapter 3, providing a route through which the MOP-polymer interaction can be tuned to prevent the formation of inter-phase void spaces.

4.4. Copper MOP-PTMSP Membranes

While the PTMSP polymer possesses many highly desirable attributes, it suffers from drawbacks such as low gas selectivity and dramatic aging effects. As such, the addition of a MOP to PTMSP polymer was proposed as a method of improving the selectivity of the membrane without sacrificing the intrinsically high permeability. The gas adsorption properties of copper based MOP-1 derivatives make them a promising partner for PTMSP in a mixed matrix material. As discussed in Chapter 3, exohedral functionality can be added to the cuboctahedral MOP-1 architecture through the use of 5-substituted isophthalic acids. The nature of this surface functionality can be used to control two significant aspects of the resultant mixed matrix membrane. Firstly, by using hydrophobic surface groups, the interaction between the MOP and PTMSP can be enhanced as the polymer structure itself is hydrophobic. Secondly, MOP dispersion throughout the polymer matrix can be influenced by the hydrophobicity of the external groups, as hydrophilic chains give preference to MOP-MOP interactions over MOP-polymer interactions, the effect of which was hypothesised to cause aggregation of the MOPs into a separate MOP phase, rather than a uniform dispersion of individual MOPs. To explore the properties of MOP-PTMSP membranes, copper MOPs with *t*-butyl (**4.1**), ethylene glycol (**4.2**) and alkyl (**4.3**) functionality were combined with PTMSP polymer to modify the gas permeation rate (Figure 95). Synthesis of these MOPs was carried out using the established methods of Li[46], Tonigold [47,48] and Furukawa[49].

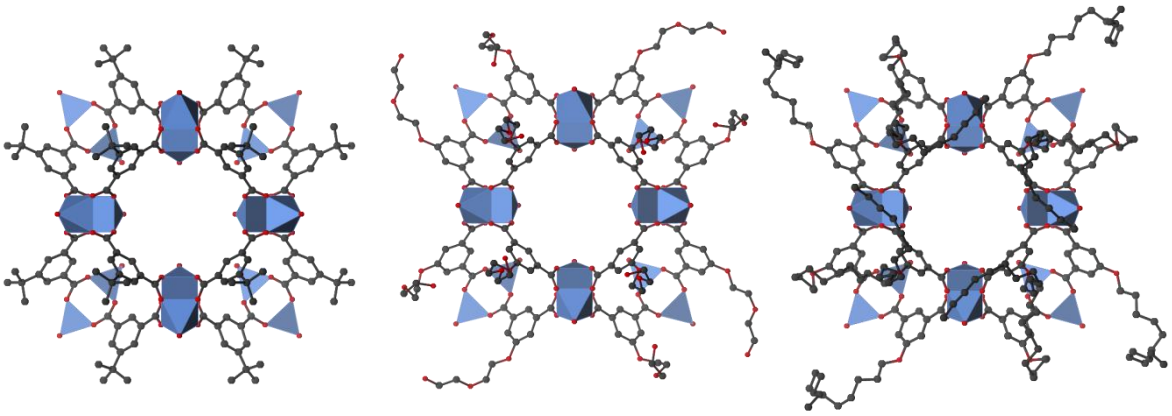

Figure 95. (Left to right) Copper MOPs with *t*-butyl (**4.1**), ethylene glycol (**4.2**) and alkyl (**4.3**) surface functional groups used in mixed matrix membranes.

In a DMA-solvated state, these MOPs exhibit high CO_2 uptake with reversible physisorption below atmospheric pressure. This behaviour suggests that the presence of these MOP additives to a membrane could facilitate high permeation of CO_2 by increasing the CO_2 capacity of the mixed matrix material. As a second benefit, the adsorption of N_2 gas is very low, and it would be anticipated that these additives would have a minimal effect on N_2 gas permeation and subsequently increase CO_2/N_2 selectivity.

4.4.1. Preparation of Mixed Matrix Membranes

Developing a method of membrane synthesis that yielded consistent material with suitable mechanical properties was crucial to this study. PTMSP membranes are typically cast from a polymer solution of an organic solvent and subsequently dried under vacuum. To allow uniform dispersion of the MOP throughout the membrane, a PTMSP solution was mixed with a solution of the relevant MOP and the resulting mixture cast in a polytetrafluoroethane (PTFE) lined dish, prior to evaporation of the solvent in a vacuum oven (Figure 96).

Figure 96. A MOP-PTMSP mixed matrix membrane cast from a PTFE dish.

Solvent selection was found to have a significant impact on the properties of the synthesised membrane. DMF, THF and $CHCl_3$ were used as casting solvents for MOP-PTMSP membranes and the resulting materials inspected for physical defects. Membranes cast from DMF were found to be relatively brittle with visible macroscopic aggregation of the MOP phase. Casting from a THF solution gave improvement in the mechanical properties compared to a DMF solution, however the material suffered from contraction during solvent removal and a distinct agglomeration of the MOP phase was apparent. $CHCl_3$ was found to be an ideal solvent for membrane casting as the resulting homogeneous materials did not suffer from distortions after the drying phase.

This fabrication methodology was similarly used to synthesise mixed matrix membranes based on Matrimid, however attempts to produce homogenous materials proved unsuccessful as differences in solubility between MOPs and the Matrimid polymer did not permit co-dissolution of the relevant materials. As such, the membranes which formed contained distinct separate phases with poor mechanical properties that were unsuitable for analysis.

4.4.2. Phase Dispersion in MOP-PTMSP Membranes

To determine whether MOP dispersion throughout the polymer matrix could be influenced by the MOP surface functionality, **4.1** and **4.2** were incorporated into MOP-PTMSP mixed matrix membranes and the extent of MOP aggregation was investigated using

scanning electron microscopy. PTMSP membranes doped with 5% and 20% (MOP wt.) **4.1** were analysed with secondary electron (SE) and back-scattered electron (BSE) detection for signs of MOP aggregation (Figure 97). While BSE detection reveals a very small amount of particulate matter, further inspection by EDX shows no co-localised increase in copper content, confirming that significant phase segregation had not occurred in these materials.

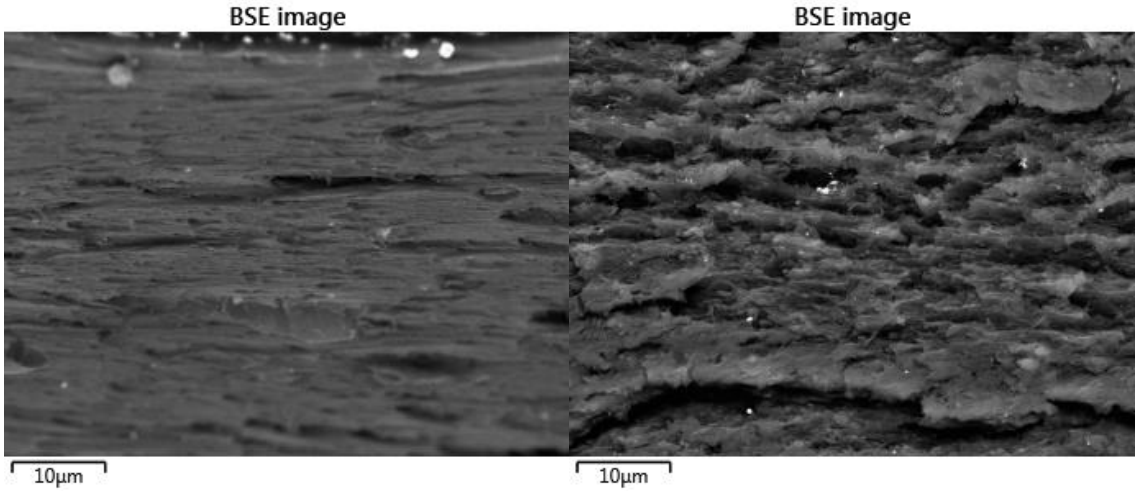

Figure 97. BSE image of **4.1**-PTMSP membranes with 5% (left) and 20% (right) MOP dopant.

PTMSP membranes cast with a **4.2** dopant exhibited phase segregation at all experimental concentrations, presumably due to the presence of the more hydrophilic ethylene glycol functionality. At 5%, 10% and 20% (MOP wt.), SEM shows the formation of MOP aggregates with significant void space between the polymer and MOP particles (Figure 98). Interestingly, in the prepared prototype samples, the size of the MOP aggregates was seen to decrease as MOP loading increases, with MOP crystals becoming dispersed periodically throughout the polymer. Whether this counter-intuitive finding represents a general trend for chemically incompatible MOP additives remains an area for further study.

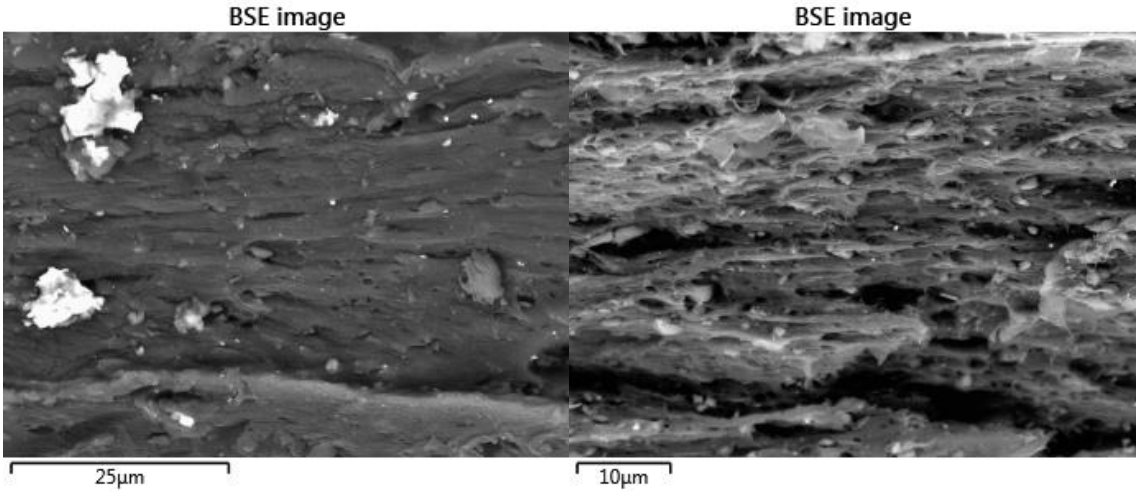

Figure 98. BSE image of **4.2**-PTMSP membranes with 5% (left) and 20% (right) MOP content.

4.3-PTMSP (5% wt.) membranes show almost no visible signs of MOP aggregation when analysed by SEM (Figure 99). At 20% weight loading, aggregates of **4.3** can be seen which are localised to one side of the membrane. This suggests that during the membrane synthesis, the aggregates of **4.3** precipitate before the polymer casting is complete. As such, it is expected that they would sink to the bottom of the casting dish and becomes trapped as the PTMSP membrane forms around it.

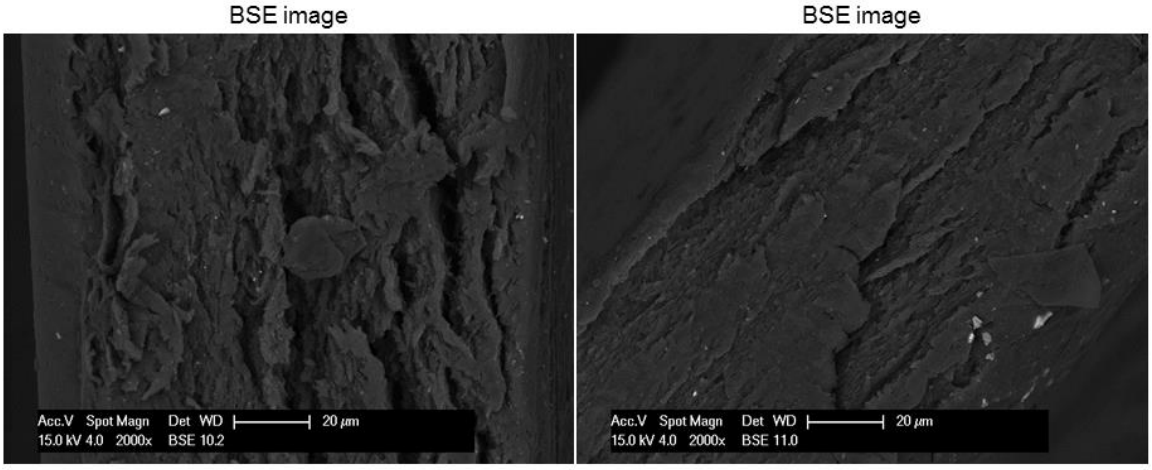

Figure 99. BSE image of **4.3**-PTMSP membranes with 5% (left) and 20% (right) MOP content.

4.5. CO_2/N_2 Separation Performance by MOP-PTMSP Membranes

The MOP-PTMSP mixed matrix membranes were tested for CO_2 and N_2 gas permeability to determine CO_2/N_2 separation performances. Relevant gases were measured individually, with the calculated ratios of CO_2/N_2 permeabilities used to determine the ideal selectivity of each membrane. This approach simplifies the experimental procedure, as the concentration of CO_2, as well as SO_x and NO_x impurities, is not considered expediting the analysis process. While this approach does not take into account more complex gas-gas interactions or the effect of lower concentration species present in industrial flue gas streams, the results provide substantial insight into performance under industrially relevant conditions. The selectivity for a two component separation is therefore given as:

$$\alpha_{A/B} = \frac{Permeability_A}{Permeability_B}$$

Where: α is the ideal selectivity of gas separation, A and B are single component gases under steady state conditions.

MOP-PTMSP membranes were cast from $CHCl_3$ with the following MOP loadings (wt.): **4.1** from 5% to 30%, **4.2** and **4.3** at 5% and 20%. MOP loading was limited by the physical properties of the synthesised membranes. At MOP loadings of **4.1** above 30%, the resulting membranes show signs of macroscopic aggregation and were very brittle. Similar effects were observed with loadings above 20% for **4.2** and **4.3**. To provide greater accuracy in results, samples from each membrane were analysed three times and the average permeability recorded. In all cases, the maximum deviation from the average permeation value was less than 5%. The single component CO_2 and N_2 permeabilities of these membranes are presented in Table 12.

Table 12. Single component N_2 and CO_2 gas permeabilities of MOP-PTMSP membranes.

MOP loading (% wt.)	N_2 Permeability (barrer)	CO_2 Permeability (barrer)	CO_2/N_2 Selectivity (α)
Neat PTMSP			
-	5083	29796	5.86
Cu_{24}((*t*-butyl)isophthalate)$_{24}$ (4.1) - PTMSP			
5	3595	27523	7.66
20	3505	24641	7.03
30	3227	24708	7.66
Cu_{24}(((hydroxyethoxy)ethoxy)isophthalate)$_{24}$ (4.2) - PTMSP			
5	1769	13038	7.37
20	3341	24917	7.46
Cu_{24}((dodecyloxy)isophthalate)$_{24}$ (4.3) - PTMSP			
5	3161	21779	6.89
20	802	8660	10.79

A neat PTMSP membrane was produced by the solvent casting method from $CHCl_3$, and gas permeabilities measured to ensure a valid comparison between the synthesised membranes and existing literature. The experimentally determined values for both N_2 and CO_2 permeability of 5100 and 30000 barrer respectively were found to be in agreement with literature,[50-52] validating the experimental setup. As predicted, neat PTMSP membranes exhibit a higher CO_2 permeability than the mixed matrix membranes, due to the absence of any MOP phase with a lower free void volume. CO_2/N_2 selectivity is also the lowest for neat PTMSP showing that the MOP additives improve membrane selectivity.

4.3-PTMSP membranes showed drastically reduced gas permeability, decreases of 27% and 71% for loadings of 5% and 20% respectively. While the hydrophobic MOPs can evenly disperse throughout the polymer at low concentration, the long aliphatic chains can fill both the polymer void space and the cage cavities resulting in a loss of transport pathways that becomes more severe with increased MOP loadings. Gains in CO_2/N_2 selectivity are observed, however this benefit is offset by the commensurate drops in gas permeability.

4.2-PTMSP membranes show a less predictable behaviour. At 5% loading, the mixed matrix membrane shows a drastically reduced permeability, while at 20% loading gas permeability is more similar to that of neat PTMSP. SEM images of the respective membranes provide an explanation for this phenomenon. At 5% loading, the MOPs are seen to aggregate into large crystalline clusters within the membrane. This aggregation causes the MOPs to act as a separate, low permeability phase which acts as a barrier to gas transport. In contrast to this, 20% loading produces a more even dispersion of smaller MOP particles. At a relatively high concentration, the interface properties dominate the difference in the individual phase permeability, resulting in the generation of non-selective voids within the membrane. These void spaces account for the significant increase in gas permeability seen in the 20% loading sample.

Up to a MOP loading of 30%, **4.1**-PTMSP membranes all show CO_2 permeabilities close to 25000 Barrer and CO_2/N_2 selectivities greater than 7. The highest performance in this study was achieved by membranes doped with 5% of the *t*-butyl functionalised MOP **4.1**. CO_2/N_2 selectivity was found to increase by approximately 30% with a loss in CO_2 permeability of 8%. Membranes with higher concentrations of **4.1** were shown to have similar increases in selectivity, yet suffer from substantially reduced gas permeability of almost 20%. The performance of the **4.1**-PTMSP membranes is such that they marginally exceed the current upper bound of performance for the CO_2/N_2 gas separation (Figure 100), however this performance still falls short of that required for industrial application.[13]

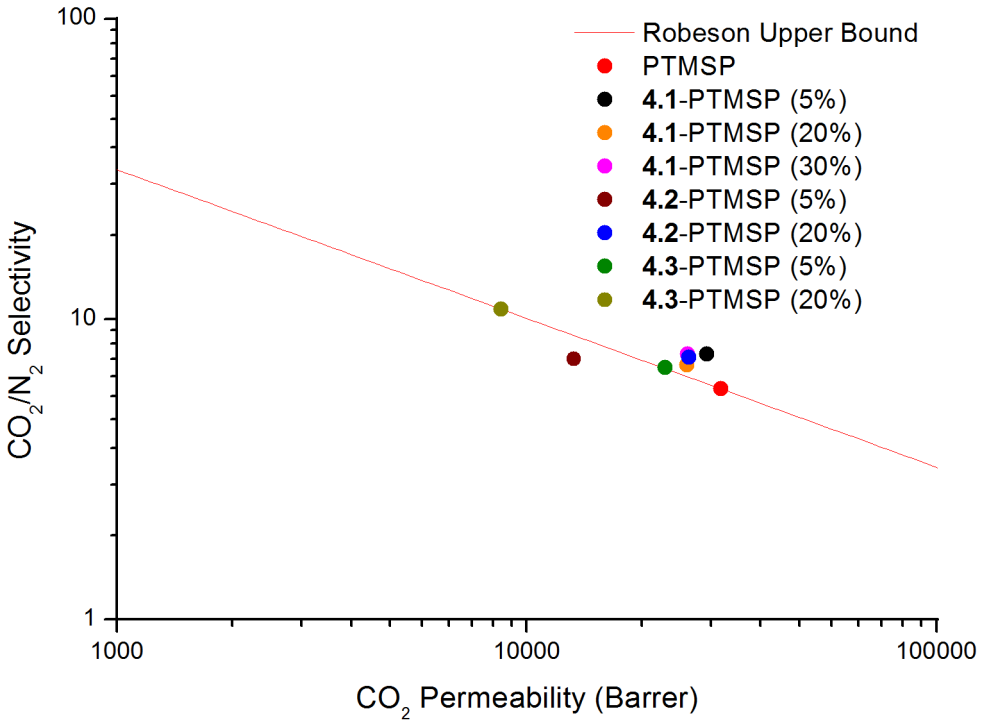

Figure 100. CO_2/N_2 Robeson plot[13] showing the performance of MOP-PTMSP membranes.

Analysis of the permeability results gives insight into the possible mechanism of gas diffusion through the membrane. In general, the addition of a MOP phase at a low loading results in an increase in selectivity, as is expected. However, as MOP loading is increased, a non-linear relationship is observed between permeability and selectivity. This shows that the gas diffusion rate and selectivity are not a linear function of the MOP loading and that the gas does exhibit preferential phase selection, as expected in a mixed matrix material. It also suggests that gas diffusion through the MOP phase is largely facilitated by the membrane void space, thus the selectivity may arise from gas interactions predominantly with the external surface of the MOP, rather than the interior.

4.6. Anti-aging Properties of MOP Additives to PTMSP Polymer

Polymer aging represents a significant barrier to the cost effective application of many membrane materials. As such, researchers have tried many approaches to enhance the longevity of such materials. One such example by Fu *et al*. recently showed that cross-linking of polymer chains through pyrolysis can form networks of carbon molecular sieves of increased rigidity, with significant anti-aging effects.[53] An alternative approach to extending polymer lifetime is to use a mixed matrix system, in which the void space within a polymer

phase is supported by an additive which stabilises the pore structure. Porous additives such as metal-organic frameworks and zeolitic imidazolate frameworks have hence been explored as stabilizing additives however the formation of two distinct phases often gives little improvement in performance of the aged material.[3,54] As the polymer ages, the collapsing polymer structure prevents gas transport to the inorganic phase, conferring no significant anti-aging benefit.

The uniform dispersion and solution processability of MOPs is highly advantageous for the stabilisation of polymer networks. As a MOP additive may not form a distinct phase within the polymer matrix, the phase interfacing is significantly improved over extended framework analogues, allowing more effective support of gas transport pathways. To explore the anti-aging effect of MOP additives on PTMSP polymers, the CO_2 permeabilities of **4.1**-PTMSP, **4.2**-PTMSP and **4.3**-PTMSP, each with a 20% loading in PTMSP, were measured after 365 days. Pure PTMSP was found to suffer from a 73% loss of permeability after a year due to aging, however it was found that all the MOP-PTMSP polymers retained a relatively high amount of their initial permeability (Figure 101). **4.3**-PTMSP with a low initial permeability of 8600 Barrer showed the largest relative decrease in permeability, which dropped 50% after aging. **4.1**-PTMSP and **4.2**-PTMSP however showed remarkable anti-aging properties, with permeabilities of 80% and 64% of their initial values after 365 days respectively. Comparing **4.1**-PTMSP (20%) to neat PTMSP, this translates to a relative permeability increase of 250% after the aging period, due to the stabilizing properties of the MOPs.

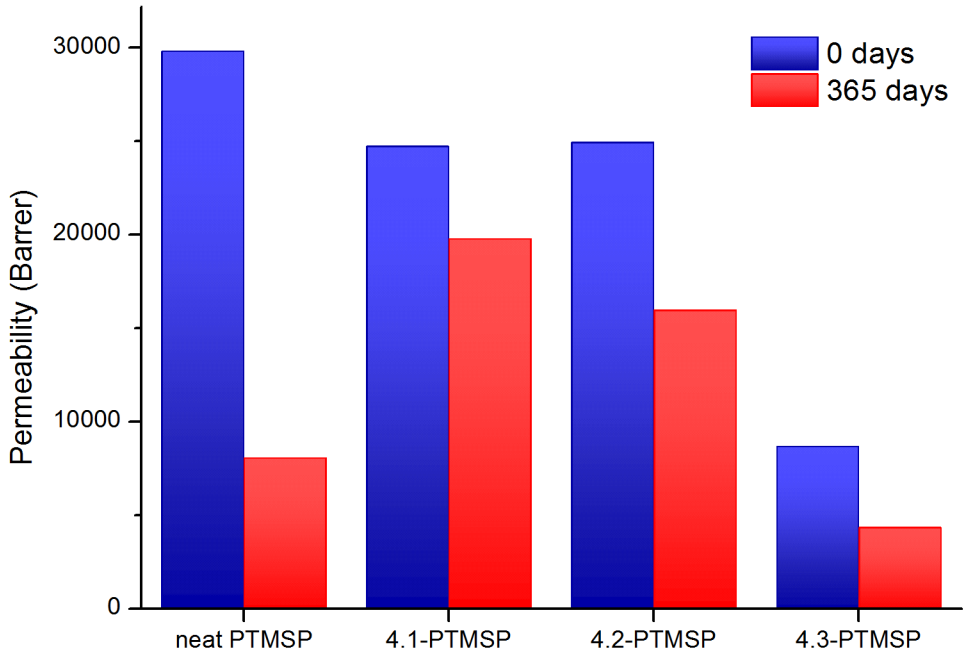

Figure 101. CO_2 permeability of MOP-PTMSP membranes in 'as-cast' state (blue) and after 1 year (red).

Further studies into the viscosity of MOP PTMSP co-solutions by co-workers have provided insight into the anti-aging mechanism of the MOPs. The individual polymer threads that constitute the polymer bulk are found to penetrate the MOP cavities thus the polymer chains, particularly those of high molecular weight, become encapsulated by the MOPs.[1] It is known that the kinetics of polymer aging are highly dependent on the molecular mobility of the polymer chains in the glassy state.[55,56] Restricting the mobility of the larger chains allows only chains of lower molecular weight to govern the bulk polymer phase. The lighter chains are shorter in length and thus are less flexible with reduced conformational freedom than their heavier counterparts. As such, the bulk material is less able to relax from the meta-stable state and relaxation into the denser, less permeable equilibrium state is slowed.

The proposed mechanism also explains the difference observed in the anti-aging effect of the different MOP structures. The long chains that decorate the surface of dodecyl functionalised **4.3** are able to penetrate MOP pores. This interaction reduces not only the intrinsic porosity of the MOP phase, but also the efficiency with which the MOPs can tether polymer chains. Where the polymer contains shorter or small bulky groups as is the case with

4.2 and **4.1**, the extent of polymer tethering is increased, preventing the physical aging of the polymer phase. While the anti-aging effect of **4.1** on PTMSP is significant, retaining 80% CO_2 permeability after 1 year, it falls short of the most successful anti-aging additive porous aromatic framework 1 (PAF-1) which allows PTMSP to retain over 90% of its initial CO_2 permeability.[57] The PAF-1-PTMSP composite is one of the less common examples of a mixed matrix membrane in which both matrices are of an organic nature. It is worth noting that this composite is a true mixed matrix material and not a co-polymer as the PAF-1 phase is porous, crystalline and structurally ordered in three dimsensions. Interestingly, the mechanism by which PAF-1 prevents aging is similar to that of MOPs, in which the polymer chains are tethered to the porous additive thus restricting chain mobility.

4.7. Summary

This chapter covers the preparation and gas separation potential of a series of mixed matrix membranes which are synthesised from PTMSP polymer doped with copper-based MOPs. The constituent MOPs share a common structural core but vary in external functionality, which has a strong influence on the MOP-polymer phase interaction. The discrete nature and resulting solubility of the MOPs allows for even dispersion throughout the polymer phase, allowing the synthesis of membranes that exhibit bulk homogeneity up to MOP loadings of 30% (wt.), however the maximum loading is influenced by the MOP chemical structure. The hydrophobicity of the external groups is shown to drastically affect the extent of microscopic aggregation. Hydrophilic groups lead to the formation of microscopic MOP-phase particles, while hydrophobic groups prevent such aggregation within the polymer matrix. CO_2 and N_2 permeabilities were measured to determine the ideal gas separation potential for each membrane, revealing that the surface chemistry of the MOPs as well as the loading concentration play key roles in the overall separative properties of the mixed matrix materials. The addition of MOPS to PTMSP polymer was also found to significantly slow the physical aging process, increasing the CO_2/N_2 performance of aged membranes by approximately 250%.

4.8. Experimental

Materials and Methods

MOP–PTMSP mixed-matrix membranes were produced through slow solvent evaporation following extensive pre-stirring of MOP–polymer solutions. Uniform distribution

of MOP nanoparticles throughout the polymer matrix was confirmed using energy-dispersive X-ray spectroscopy (EDX) and focused ion beam scanning electron microscopy (FIB-SEM).

PTMSP was purchased from Gelest Inc. (Morrisville PA, USA) and used without purification. Chloroform was purchased from Sigma-Aldrich. MOP-PTMSP membranes were fabricated through a typical solvent-casting method. Scanning electron microscopy (SEM) was performed on a Philips XL30 SEM operated at 15 kV using secondary electron (SE) or backscattered electron (BSE) detectors, or on a JEOL JEM 2100F TEM/SEM operated at 200 kV. EDX data was obtained using a JEOL 50 m^2 Si(Li) detector. SEM images were obtained at Adelaide Microscopy at the University of Adelaide (XL30) or at the Melbourne Centre for Nanofabrication (2100F).

Synthetic Methods

Metal-organic polyhedra (**4.1**, **4.2**, **4.3**)

The *t*-butyl functionalised MOP **4.1** was synthesised according to the method published by Li *et al*.[46]

The ethylene glycol functionalised MOP **4.2** was synthesised according to the method published by Tonigold *et al*.[47,48]

The dodecyloxy functionalised MOP **4.3** was synthesised according to the method published by Furukawa *et al*.[49]

MOP-PTMSP mixed matrix membranes

In a typical synthesis, 200 mg PTMSP was placed in a 20 mL vial with 5 g chloroform and an egg-shaped stirrer bar. The required amount of MOP sample (10, 20 or 40 mg) was placed in a separate 20 mL vial with 5 g chloroform and an egg-shaped stirrer bar. Each vial was closed and stirred for 24 hours under ambient conditions. Following this, the MOP–chloroform solution was added to the vial containing the stirred PTMSP–chloroform solution, and the mixed solution stirred for a further 24 hours under ambient conditions. ~100 micron films were formed via solution casting at ambient conditions. The membrane films were dried

in a vacuum oven at 40°C for 12 hours prior to single gas permeability measurements. Film thicknesses were measured using a Measumax digital micrometer.

Single component gas permeability measurements

Pure N_2 and CO_2 permeabilites were determined using a constant volume and variable pressure method.[58] Gas permeabilities were determined from the rate of downstream pressure build-up rate ($\frac{dp}{dt}$) obtained when permeation reached a steady state according to the following equation:[1]

$$P = D \times S = \frac{273 \times 10^{10} \times VL}{AT\left[\frac{p_2 \times 76}{14.7}\right]} \frac{dp}{dt}$$

Where: P = Membrane permeability to a gas (Barrer), D = Average effective diffusivity ($cm^2.s$), S = Apparent sorption coefficient/solubility (cm^3 (STP)/cm^3 polymer cm.Hg), V = Volume of the downstream chamber (cm^3), L = Film thickness (cm), A = effective area of the membrane (cm^2), T = Experimental temperature (K), p_2 = Feed gas pressure of the upstream chamber (psia).

4.9. References

(1) Kitchin, M.; Teo, J.; Konstas, K.; Lau, C. H.; Sumby, C. J.; Thornton, A. W.; Doonan, C. J.; Hill, M. R. *J. Mater. Chem. A* , **2015** , 3 ,15241.

(2) Choi, S.; Drese, J. H.; Jones, C. W. *Chem. Sus. Chem.* **2009**, *2*, 796.

(3) D'Alessandro, D. M.; Smit, B.; Long, J. R. *Angew. Chem., Int. Ed.* **2010**, *49*, 6058.

(4) Haszeldine, R. S. *Science* **2009**, *325*, 1647.

(5) IPCC *IPCC Special Report on Carbon Dioxide Capture and Storage*; Cambridge University Press: Cambridge, UK, **2005**.

(6) Mason, J. A.; Sumida, K.; Herm, Z. R.; Krishna, R.; Long, J. R. *Energy Environ. Sci.* **2011**, *4*, 3030.

(7) Demessence, A.; D'Alessandro, D. M.; Foo, M. L.; Long, J. R. *J. Am. Chem. Soc.* **2009**, *131*, 8784.

(8) Du, N.; Park, H. B.; Robertson, G. P.; Dal-Cin, M. M.; Visser, T.; Scoles, L.; Guiver, M. D. *Nat. Mater.* **2011**, *10*, 372.

(9) McDonald, T. M.; D'Alessandro, D. M.; Krishna, R.; Long, J. R. *Chem. Sci.* **2011**.

(10) Alexander Stern, S. *J. Membr. Sci.* **1994**, *94*, 1.

(11) Vaidhyanathan, R.; Iremonger, S. S.; Shimizu, G. K. H.; Boyd, P. G.; Alavi, S.; Woo, T. K. *Angew. Chem., Int. Ed.* **2012**, *51*, 1826.

(12) Robeson, L. M. *J. Membr. Sci.* **1991**, *62*, 165.

(13) Robeson, L. M. *J. Membr. Sci.* **2008**, *320*, 390.

(14) Kim, D.; Tzeng, P.; Barnett, K. J.; Yang, Y.-H.; Wilhite, B. A.; Grunlan, J. C. *Adv. Mater.* **2014**, *26*, 746.

(15) Yan, Q.; Wang, J.; Yin, Y.; Yuan, J. *Angew. Chem., Int. Ed.* **2013**, *52*, 5070.

(16) Ohta, Y.; Akamatsu, K.; Sugawara, T.; Nakao, A.; Miyoshi, A.; Nakao, S.-I. *J. Membr. Sci.* **2008**, *315*, 93.

(17) Kulprathipanja, S. *Ann. N. Y. Acad. Sci.* **2003**, *984*, 361.

(18) Tien-Binh, N.; Vinh-Thang, H.; Chen, X. Y.; Rodrigue, D.; Kaliaguine, S. *J. Mater. Chem. A* **2015**.

(19) Tanh Jeazet, H. B.; Staudt, C.; Janiak, C. *Dalton Trans.* **2012**, *41*, 14003.

(20) Budd, P. M.; Msayib, K. J.; Tattershall, C. E.; Ghanem, B. S.; Reynolds, K. J.; McKeown, N. B.; Fritsch, D. *J. Membr. Sci.* **2005**, *251*, 263.

(21) Kelman, S. D.; Rowe, B. W.; Bielawski, C. W.; Pas, S. J.; Hill, A. J.; Paul, D. R.; Freeman, B. D. *J. Membr. Sci.* **2008**, *320*, 123.

(22) Dorkenoo, K. D.; Pfromm, P. H. *Macromolecules* **2000**, *33*, 3747.

(23) Yampolskii, Y. *Macromolecules* **2012**, *45*, 3298.

(24) Struik, L. C. E. *Polym. Eng. Sci.* **1977**, *17*, 165.

(25) Allen, N. S.; Edge, M.; Corrales, T.; Childs, A.; Liauw, C. M.; Catalina, F.; Peinado, C.; Minihan, A.; Aldcroft, D. *Polym. Degrad. Stab.* **1998**, *61*, 183.

(26) Doghieri, F.; Biavati, D.; Sarti, G. C. *Ind. Eng. Chem. Res.* **1996**, *35*, 2420.

(27) Shelby, M. D.; Wilkes, G. L. *Polymer* **1998**, *39*, 6767.

(28) Henis, J. M. S.; Tripodi, M. K. *J. Membr. Sci.* **1981**, *8*, 233.

(29) Ghosal, K.; Freeman, B. D. *Polym. Adv. Tech.* **1994**, *5*, 673.

(30) Perez, E. V.; Balkus Jr, K. J.; Ferraris, J. P.; Musselman, I. H. *J. Membr. Sci.* **2009**, *328*, 165.

(31) Thornton, A. W.; Dubbeldam, D.; Liu, M. S.; Ladewig, B. P.; Hill, A. J.; Hill, M. R. *Energy Environ. Sci.* **2012**, *5*, 7637.

(32) Bae, T.-H.; Lee, J. S.; Qiu, W.; Koros, W. J.; Jones, C. W.; Nair, S. *Angew. Chem., Int. Ed.* **2010**, *49*, 9863.

(33) Julbe, A. In *Studies in Surface Science and Catalysis*; Jiří Čejka, H. v. B. A. C., Ferdi, S., Eds.; Elsevier: 2007; Vol. Volume 168, p 181.

(34) Tjong, S. C. *Mater. Sci. Eng. Reports* **2006**, *53*, 73.

(35) Khan, A. L.; Li, X.; Vankelecom, I. F. J. *J. Membr. Sci.* **2011**, *380*, 55.

(36) Vu, D. Q.; Koros, W. J.; Miller, S. J. *J. Membr. Sci.* **2003**, *211*, 311.

(37) Naseri, M.; Mousavi, S. F.; Mohammadi, T.; Bakhtiari, O. *J. Industrial and Eng. Chem.* **2015**, *29*, 249.

(38) Zhang, Y.; Musselman, I. H.; Ferraris, J. P.; Balkus Jr, K. J. *J. Membr. Sci.* **2008**, *313*, 170.

(39) Mahajan, R.; Koros, W. J. *Ind. Eng. Chem. Res.* **2000**, *39*, 2692.

(40) Aroon, M. A.; Ismail, A. F.; Matsuura, T.; Montazer-Rahmati, M. M. *Sep. Purif. Technol.* **2010**, *75*, 229.

(41) Huang, Z.; Li, Y.; Wen, R.; May Teoh, M.; Kulprathipanja, S. *J. Appl. Polym. Sci.* **2006**, *101*, 3800.

(42) Chung, T.-S.; Jiang, L. Y.; Li, Y.; Kulprathipanja, S. *Prog. Polym. Sci.* **2007**, *32*, 483.

(43) Mahajan, R.; Burns, R.; Schaeffer, M.; Koros, W. J. *J. Appl. Polym. Sci.* **2002**, *86*, 881.

(44) Perez, E. V.; Balkus Jr, K. J.; Ferraris, J. P.; Musselman, I. H. *J. Membr. Sci.* **2014**, *463*, 82.

(45) Ma, J.; Ying, Y.; Yang, Q.; Ban, Y.; Huang, H.; Guo, X.; Xiao, Y.; Liu, D.; Li, Y.; Yang, W.; Zhong, C. *Chem. Commun.* **2015**, *51*, 4249.

(46) Li, J.-R.; Zhou, H.-C. *Nat. Chem.* **2010**, *2*, 893.

(47) Tonigold, M.; Hitzbleck, J.; Bahnmuller, S.; Langstein, G.; Volkmer, D. *Dalton Trans.* **2009**, *0*, 1363.

(48) Tonigold, M.; Volkmer, D. *Inorg. Chim. Acta* **2010**, *363*, 4220.

(49) Furukawa, H.; Kim, J.; Plass, K. E.; Yaghi, O. M. *J. Am. Chem. Soc.* **2006**, *128*, 8398.

(50) Mizumoto, T.; Masuda, T.; Higashimura, T. *J. Polym. Sci., Part A: Polym. Chem.* **1993**, *31*, 2555.

(51) Qiu, J.; Zheng, J. M.; Peinemann, K. V. *Macromolecules* **2006**, *39*, 4093.

(52) De Sitter, K.; Winberg, P.; D'Haen, J.; Dotremont, C.; Leysen, R.; Martens, J. A.; Mullens, S.; Maurer, F. H. J.; Vankelecom, I. F. J. *J. Membr. Sci.* **2006**, *278*, 83.

(53) Fu, S.; Sanders, E. S.; Kulkarni, S. S.; Koros, W. J. *J. Membr. Sci.* **2015**, *487*, 60.

(54) Merkel, T. C.; He, Z.; Pinnau, I.; Freeman, B. D.; Meakin, P.; Hill, A. J. *Macromolecules* **2003**, *36*, 6844.

(55) Kovacs, A. J.; Aklonis, J. J.; Hutchinson, J. M.; Ramos, A. R. *J. Polym. Sci., Part B: Polym. Phys.* **1979**, *17*, 1097.

(56) Boucher, V. M.; Cangialosi, D.; Alegria, A.; Colmenero, J.; Gonzalez-Irun, J.; Liz-Marzan, L. M. *Soft Matter* **2010**, *6*, 3306.

(57) Lau, C. H.; Nguyen, P. T.; Hill, M. R.; Thornton, A. W.; Konstas, K.; Doherty, C. M.; Mulder, R. J.; Bourgeois, L.; Liu, A. C. Y.; Sprouster, D. J.; Sullivan, J. P.; Bastow, T. J.; Hill, A. J.; Gin, D. L.; Noble, R. D. *Angew. Chem., Int. Ed.* **2014**, *53*, 5322.

(58) Stern, S. A.; Gareis, P. J.; Sinclair, T. F.; Mohr, P. H. *J. Appl. Polym. Sci.* **1963**, *7*, 2035.

CHAPTER 5.

CONCLUSION

Chapter 5. Conclusion

5.1 Conclusion

A view of the historical development and significance of 0-dimensional porous materials has been given, showing that MOPs are an interesting and industrially promising class of materials that are still in their infancy from a research perspective. The potential of these materials has been introduced showcasing their prospective capabilities in the development of gas storage and separation. Two particular aspects of this field have been studied in depth in this work; that of H_2 storage using MOPs and the ability of MOPs to facilitate the separation of CO_2 from N_2. Each of these applications has global significance with the barriers to effective solutions being discussed in Chapter 1.

Chapter 2 has reported the synthesis of a family of metal-organic polyhedra that are constructed from hetero-bimetallic metal acetates. These bimetallic synthons each feature a palladium(II) ion partnered with a divalent first row metal atom in a paddle-wheel geometry, which is retained during MOP synthesis. Under ambient conditions, these hetero-metallic acetates react with ^{m}bdc derivatives that have H, OH or *t*-butyl groups in the 5-position. These substituents are positioned exohedrally in the formed structures and govern the crystal packing of each MOP. Characterisation of the MOP structures by X-ray diffraction indicates that the palladium ion is preferentially situated at the endohedral site as a result of the preferential square planar coordination environment. EDX analysis shows that while the Co, Ni and Zn analogues maintain a 1:1 M(II):Pd(II) content, the copper equivalent is found to contain a disproportionate amount of copper, which is attributed to the inherent instability of the copper-palladium paddle-wheel motif. The elegant synthetic approach that exploits preformed building units allows the inclusion of metallic elements that generally do not form MOP-1 architectures.

By modelling the paddle-wheel geometry, an in silico analysis of the interactions between metal atoms has been carried out, revealing that there is no inter-metal bonding across the hetero-metallic paddle-wheel unit, despite the short metal-metal distances. Analysis of the paddle-wheel cluster also reveals that the first row metals show strong interactions with H_2 molecules, and account for the strong hydrogen binding energies that characterise these MOPs. Gas adsorption experiments confirm the strong H_2 binding enthalpies suggested by the computational studies which range from -4.5 kJ/mol (for $Co_{12}Pd_{12}{}^{m}bdc_{24}$) to -12.1 kJ/mol (for $Zn_{12}Pd_{12}b^{m}bdc_{24}$), the greater of which is competitive with open-metal site MOFs such as

HKUST-1 and CPO-27-Ni. The strong adsorption enthalpies are coupled with high hydrogen capacities due to the large micropore volume that manifests in these MOPs after activation with acetone and supercritical CO_2. This activation protocol differs largely from the literature methods used to activate MOPs, but has been proven necessary to provide not only the highest accessible surface area, but also to remove the solvent ligands bound to the axial coordination site of the first row metals. This same activation method has also been shown to drastically alter the sorption properties of $Cu_{24}(b^mbdc)_{24}$. This material is non-porous to N_2 under standard methanol activation conditions, yet displays a N_2 accessible surface area of 300 m^2/g after acetone and supercritical CO_2 activation.

Chapter 3 focussed on the synthesis and structural characterisation of MOP structures that contain external functionality. The use of novel isophthalate ligands with 5-substituted functionality has played a pivotal role in the generation of these materials, and thus the successful synthesis of these compounds has been described. Unfortunately, not all of the desired functionality was able to be included into MOP structures, as the supramolecular synthesis reactions for many of these proved troublesome. In the case of the azo-benzene structures, this was due in part to the difficulties arising from crystallisation of the readily isomerising azo groups. Four MOPs with distinctive exohedral functionality have however been synthesised containing ethylene glycol, phthalamidyl, benzyl or benzophenone motifs.

In order to investigate the effect these external groups have on crystal packing, each of these structures was analysed by X-ray crystallography. In each case, the MOP core scaffolds were able to be modelled through standard crystallographic techniques; however the peripheral groups showed significant disorder. In the cases of the phthalimidyl and benzyl structures, the position and orientation of the side chains was able to be elucidated through the use of SAME commands, which applies significant restraints to the disordered parts of the X-ray crystallographic structure solution.

The highly disordered nature of the ethylene glycol and benzophenone motifs however, made full crystallographic structure determination unfeasible. In order to address this, an approach that combines X-ray crystallography with molecular modelling has been described and developed. A modelling algorithm that uses geometric and energetic arguments has been applied to the highly disordered structure to elucidate the favourable orientations and positions of the side chains. While it is acknowledged that this methodology attempts to give an ordered solution to a disordered material, the insight provided has shown to be useful in

predicting the porosity of a material, or rationalising the absence thereof. This characterisation and study has added to the growing body of literature that helps develop the field of supramolecular chemistry.

In contrast to the previous chapters which entail the synthesis of new MOP structures, Chapter 4 has focussed on the application of MOPs as part of a functional gas separation system. In the context of separating CO_2 and N_2, the advantages and challenges of membrane based processes that rely on selective permeation have been discussed. The performance limitations of current membranes giving rise to an 'upper bound' of separation has led to the development of mixed matrix membranes which aim to surpass current materials through the synergistic effect of two phases. Literature has shown that beneficial cooperation between the phases is theoretically limited when the two matrices interface poorly, due to the generation of non-selective void space, or through phase-preferential gas transport.

The discrete nature of MOPs and the highly tunable surface chemistry they possess gives them a distinct advantage over many other solids as part of a mixed matrix system. The nano-sized construction and potential solubility means that MOPs can be dispersed homogeneously through a polymer membrane, while a strong MOP-polymer interaction can be achieved through the use of external functional groups as is demonstrated by the copper MOP-PTMSP membranes described. Mixed matrix membranes with copper MOP and PTMSP constituents have hence been tested for CO_2/N_2 gas separation performance. These MOP-PTMSP membranes perform exceptionally well, surpassing both neat PTMSP polymer and the current 'upper bound' of separation. The addition of MOPs has also been shown to enhance the longevity of PTMSP polymer which is known to suffer from rapid physical aging effects, with a 250% performance increase being observed after 1 year over neat PTMSP polymer. While this is a step towards the development of a practical carbon capture system greater study and investigation needs to be carried out to further improve both the separation performance and lifetime of membrane based system.

The work in this thesis has explored MOPs that share a common architecture, which was displayed by the first porous $M_{24}L_{24}$ MOP structure, MOP-1. This focus however, has left a great number of potential structures unexplored and as such, there remains a vast amount of potential future study. Assemblies formed using radically different ligands, such as extended biphenyl systems, would possess drastically different properties due to increased pore dimensions. Similarly, deviating from the use of paddle-wheel metal nodes would result in

entirely different architectures forming. With dozens of discrete porous structures now in the published literature possessing different pore structures, stabilities and chemical motifs, similar studies can possibly be carried out in other fields such as petroleum refinement and drug delivery. Such further research could be bolstered by the novel metal nodes and characterisation techniques described in this thesis. As such, the study of MOPs and similar discrete porous materials is an interesting area that is worth exploring.

PUBLICATIONS

ChemComm

COMMUNICATION

View Article Online
View Journal | View Issue

Cite this: *Chem. Commun.*, 2016, 52, 276

Received 7th October 2015,
Accepted 24th October 2015

DOI: 10.1039/c5cc08336b

www.rsc.org/chemcomm

Hetero-bimetallic metal–organic polyhedra†

Jesse M. Teo,[a] Campbell J. Coghlan,[a] Jack D. Evans,[a] Ehud Tsivion,[b] Martin Head-Gordon,[b] Christopher J. Sumby*[a] and Christian J. Doonan*[a]

Porous metal–organic polyhedra (MOPs), constructed from hetero-metallic Pd^{II}–M^{II} (M = Cu, Ni, Zn) paddlewheel nodes and 5-*tert*-butyl-1,3-benzenedicarboxylate organic links, were prepared in which the Pd^{II} ions preferentially line the inner surface of the cage molecules. Careful activation produces co-ordinatively unsaturated 3d transition metal sites on the external MOP surfaces giving rise to H_2 adsorption enthalpies in excess of −12 kJ mol^{-1}.

Porous materials, such as metal–organic frameworks (MOFs) and their discrete counterparts metal–organic polyhedra (MOPs), that are constructed from co-ordinatively unsaturated inorganic nodes show great potential for application in gas adsorption/separation processes, catalysis, and emerging opportunities in electronics, optics, sensing and biotechnology.[1] A salient example is the M_2(dobdc) dobdc^{4-} = 2,5-dioxido-1,4-benzenedicarboxylate family of MOFs that possess 1D pore channels lined with a high density of open metal sites including Mg, Mn, Fe, Co, Ni, Zn.[2] Detailed theoretical and structural studies confirm that the exceptionally high affinities these materials exhibit towards gas molecules, such as H_2 and CO_2, originate from orbital and coulombic interactions between the adsorbate and the vacant coordination site of the metal oxide node.[3] In addition the dicopper paddlewheel node of HKUST-1 represents how accessible open metal sites can be exploited as Lewis acid catalysts.[4,5]

Although structurally well-defined, co-ordinatively unsaturated metal sites in molecular complexes are a rich source of fundamental research, they are relatively uncommon in porous framework materials.[6,7] Accordingly, novel porous solids comprised of such moieties are of significant interest to chemists. The metal paddlewheel unit is a common structural building block in porous framework materials due to its facile synthesis and topologically versatile square planar geometry.[8] Furthermore, the intrinsic vacant coordination sites have been used as a structural connection,[9] explored for their potential to enhance gas adsorption,[10] and in heterogeneous catalysis.[11,12] The most prevalent paddlewheel building unit for the synthesis of frameworks is based on Cu^{II}, however, Ni, Mo, Zn, Ru and Rh paddlewheel nodes have also been reported.[13–17] In an effort to expand the functional diversity of this common building block researchers have used a cation exchange approach to introduce extraneous metals into the paddlewheels of copper based MOFs.[18] Though this post-synthetic strategy was proven to be successful, if it can be achieved, the direct synthesis of materials offers more control over their composition and eliminates the need for additional synthetic steps that can result in degradation of the material.[19]

Here we describe the synthesis and characterisation of a series of porous metal–organic polyhedra constructed from bimetallic paddlewheels that are, hitherto, unprecedented building blocks for framework materials. The bimetallic metal units are based on a Pd^{II}–M^{II} (M = Ni, Cu or Zn) motif (Fig. 1), where the Pd^{II} ions predominantly reside on the interior of the cuboctahedral cages. As a consequence, the surface of the MOP can be selectively decorated with a series of first row transition metals that can be reacted to provide open coordination sites. We exploit this feature and determine the gas adsorption properties of these unique materials experimentally, using a theoretical analysis to further explain the adsorption. Notably, they show exceptionally high uptake of hydrogen for discrete porous molecules.

The bimetallic MOPs were synthesized by mixing 5-*tert*-butyl-1,3-benzenedicarboxylic acid (H_2L) and a precursor hetero-bimetallic paddlewheel acetate Pd^{II}–M^{II} (M = Ni, Cu or Zn)[20] in *N*,*N*-dimethylacetamide (DMA) at ambient temperature for 48 h under dry, anaerobic, conditions (20 days for M = Ni). This procedure afforded single crystals of the three Pd–M(L) MOPs

[a] *Centre for Advanced Nanomaterials, School of Physical Sciences, University of Adelaide, Adelaide, SA 5005, Australia. E-mail: christian.doonan@adelaide.edu.au*
[b] *Department of Chemistry, University of California Berkeley, Berkeley, California 94720, USA*

† Electronic supplementary information (ESI) available: Synthetic procedures, single crystal and powder X-ray diffraction data, gas adsorption data and computational data. CCDC 1423403–1423405. For ESI and crystallographic data in CIF or other electronic format see DOI: 10.1039/c5cc08336b

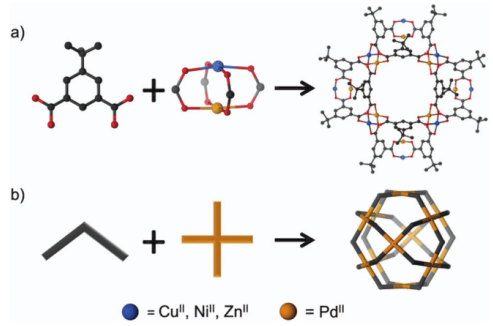

Fig. 1 (a) Structural and (b) schematic representations of the synthesis of the cuboctahedral bimetallic MOPs, which contain 12 heteronuclear paddlewheel nodes, from Pd(μ-OAc)$_4$M(OH$_2$) and 5-*tert*-butyl-1,3-benzenedicarboxylic acid (H$_2$L). In the resulting MOP, the Pd^{II} sites are preferentially positioned within the void cavity, while the divalent first row transition metal occupies the external sites.

that were suitable for X-ray diffraction studies. These new mixed-metal MOPs are isostructural with a number of known Cu$_2$(L′) analogues (L′ = 5-hydroxy-1,3-benzenedicarboxylate and 5-*tert*-butyl-1,3-benzenedicarboxylate) and crystallise in the tetragonal space group *I*4/*m* with two complete cage moieties in the unit cell.

Close analysis of the crystal structures obtained indicate that each MOP is best described by a cuboctahedral geometry with bimetallic paddlewheel units at 12 of the faces. The Pd^{II} and M^{II} ions, predominantly, adopt the *endo*- and *exo*-hedral positions of the 12 faces, respectively. The observed, systematic, distribution of metals can be explained by (i) a stepwise ligand exchange process that incorporates preformed bimetallic paddlewheel acetate into the MOP and (ii) the strong preference of d^8 Pd complexes towards square planar geometry; which can be accommodated at the endohedral sites of the MOP with least strain.[21] Ni, Cu and Zn are more co-ordinatively flexible, adopting 5-coordinate geometries in the presence of co-ordinating solvents, and thus favour the exohedral positions.[22,23] Indeed, the first row transition metals manifest significant distortions from square planar geometry that are most apparent in the Pd^{II}–Zn^{II} MOP which exhibits a O–Zn–O bond angle of 165.6° and least pronounced in the Pd^{II}–Ni^{II} structure which has a O–Ni–O bond angle of 171.2° (Table S2, ESI†). The distortions of the peripheral 3d metal sites in these materials compare favourably with the O–Cu–O angles for the Cu$_2$(L) MOP, which are the range 168.1–168.6°, and further explains why the Pd^{II}–M^{II} MOP structure is identical to previously reported Cu$_2$(L′) MOPs. Notably, the Pd centres can be accommodated on the endohedral surface without significant changes in the overall MOP structure.

Each bimetallic paddlewheel presents short intermetallic distances in the range of 2.46–2.56 Å (Table S3, ESI†). As expected, density functional theory (DFT) calculations of the paddlewheel cluster suggest the short metal–metal distances are due to geometric constraints imposed by the bridging carboxylate groups rather than a result of metal–metal bonding.[24] To satisfy the crystallographically assigned distribution of metals in the paddlewheel moieties a 1 : 1 Pd : M ratio is required. Energy-dispersive X-ray spectroscopy (EDX) was used to assess the metal composition for each MOP (Table S1, ESI†). For the PdZn(L) and PdNi(L) MOPs the anticipated Pd : M ratio of 1 : 1 was confirmed, however, for the CuPd(L) analogue the metal ratio heavily skewed towards Cu (62 : 38). This disparity in metal composition may be explained by the chemistry of the M–Pd bimetallic acetates. Synthesis of [Pd(μ-OAc)$_4$Cu(OH$_2$)](AcOH)$_2$ is found to be in competition with the trinuclear complex Pd$_2$Cu(μ-OAc)$_6$ and Cu^{II} acetate. However, such side reactions are not observed for the Ni or Zn analogues.[20] This additional [Cu$_2$(μ-OAc)$_4$] enhances the Cu ratio by affording some MOPs in which the M–Pd bimetallic node has been substituted by a Cu–Cu node.

An interesting difference arises in the crystal packing of the hetero-bimetallic MOPs compared to the Cu$_2$(L) MOP material (L = 5-*tert*-butyl-1,3-benzenedicarboxylate). The previously reported Cu$_2$(L) MOP material crystallises in the tetragonal space group *I*4/*mmm* under the conditions reported by Li *et al.* (DMA/methanol) with a body-centred cubic packing arrangement of the cuboctahedra.[25] The hetero-bimetallic paddlewheel structures reported here pack with a slight modification of this arrangement, presumably facilitated by subtle distortions of the cuboctahedral cage upon crystallisation, in which the cage centroids are translated slightly in the *a* and *b* axis directions. Intriguingly, hetero-bimetallic MOPs reported herein are isomorphous with the Cu$_2$(L′) MOPs (L′ = 5-hydroxy-1,3-benzenedicarboxylate).

H$_2$ and N$_2$ 77 K gas adsorption isotherms were performed to assess the permanent porosity of the bimetallic MOPs. Initially, a careful activation procedure was carried out to ensure complete removal of the co-ordinated solvent molecules. We found that a previously reported method for activating structurally analogous materials (solvent exchange with MeOH followed by heating)[25] was unsatisfactory for the bimetallic MOPs. Indeed, ^{1}H NMR analysis of digested MOP samples activated by this method revealed the presence of significant amounts of DMA. To completely remove these coordinated solvent molecules MOP crystals were soaked in a solution of dry acetone for 7 days, followed by supercritical CO$_2$ drying and finally heating at 50 °C under vacuum for 3 h (heating above this temperature leads to visual darkening of the samples but thermogravimetric data indicates thermal stability to higher temperatures). By employing this activation protocol only trace amounts of DMA were detected by ^{1}H NMR spectroscopy (Fig. S5–S8, ESI†). This procedure also led to dramatically increased H$_2$ and N$_2$ gas uptake for Cu$_2$(L) compared to previous reports.[25] It is noteworthy that subsequent to solvent removal powder X-ray diffraction experiments indicate that the MOPs are amorphous solids. Such 'crystalline-to-amorphous' transformations have been observed for other discrete porous materials and attributed to significant structural reorganisation upon solvent loss.[25,26] Fig. 2a shows the N$_2$ 77 K gas adsorption isotherms collected for the MPd(L) and Cu$_2$(L) MOPs. The shape of the isotherms are best described as type 1 with BET analysis of the isotherms yielding surface areas ranging from

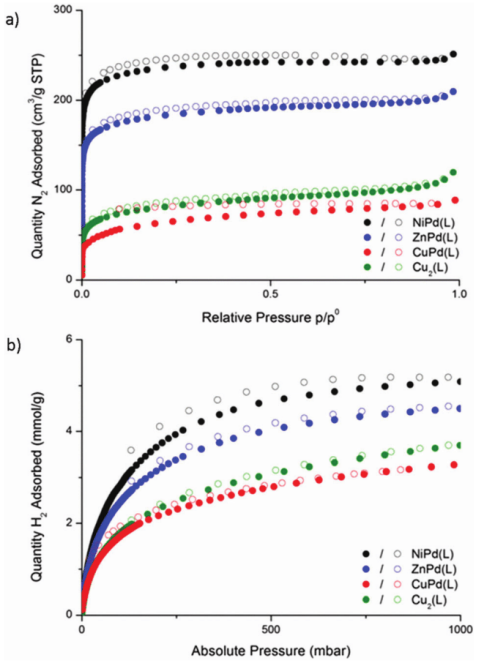

Fig. 2 (a) 77 K N_2 and (b) H_2 adsorption isotherms for the hetero-bimetallic MPd(L) and Cu_2(L) MOPs following activation. Closed and open symbols represent adsorption and desorption data, respectively.

200–1100 m^2 g^{-1}. A noticeable hysteresis is observed in the desorption of CuPd(L) in addition to its considerably lower surface area with respect to its MPd(L) counterparts (M = Ni^{II}, Zn^{II}). This data further supports the relative instability of the CuPd(L) paddlewheel unit. As the MOPs lack precise long-range order the origin of porosity in these materials cannot be described from X-ray diffraction data, however, insights from the pore size distribution suggest a significant reduction in microporosity for Cu_2(L) and CuPd(L) (Fig. S12, ESI†) compared to NiPd(L) and ZnPd(L), which is consistent with their lower surface areas. Fig. 2b shows the 77 K low pressure H_2 adsorption isotherms for Cu_2(L), NiPd(L), CuPd(L) and ZnPd(L). The isotherms for each MOP show reversible adsorption with steep uptake at low pressures. The H_2 uptake capacity of the MOPs range between 0.65 and 1.0 wt% at 77 K and 1 bar for CuPd(L) and NiPd(L), respectively. These results are consistent with the lower pore volume observed for the Cu_2(L) and CuPd(L) compared to the NiPd(L) and ZnPd(L) analogues. Isosteric heats of adsorption (Fig. 3) were obtained from temperature independent virial fits to the isotherms, as described in the ESI.† A virial analysis was employed as it provided the best fit to the adsorption isotherms exhibited by these disordered materials. The isosteric curves for ZnPd(L) and NiPd(L) indicate strong adsorption with initial Q_{st} values of −12.1 and −9.50 kJ mol^{-1}.

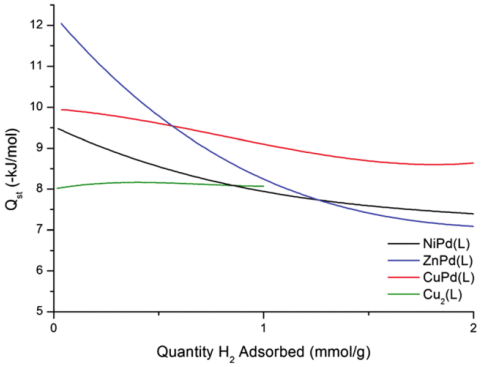

Fig. 3 Coverage dependencies of the isosteric heats of adsorption for H_2 in the MOPs (calculated from 77 and 87 K isotherm data).

As the hydrogen loading is increased, and the high affinity sites are saturated, the adsorption enthalpy decreases to approximately −7.5 kJ mol^{-1}. Such high adsorption enthalpies are competitive with exposed metal ion MOFs such as HKUST-1 and CPO-27-Ni, which have reported enthalpies of −10.1 and −13.5 kJ mol^{-1}, respectively.[27] Show significantly stronger affinity for hydrogen than the Cu_2(L) structure which has an enthalpy of approximately −8 kJ mol^{-1} over the hydrogen loading range. In contrast to the other bimetallic MOPs the adsorption enthalpy of CuPd(L) shows a gradual decline from −10 kJ mol^{-1} to a value of −8.60 kJ mol^{-1}. The different enthalpy profile, compared to the other bimetallic MOPs, is likely the result of the different pore structure present for CuPd(L), as evidenced by N_2 adsorption experiments. In this case the strong adsorption is consistent with small cavity sizes that bind hydrogen strongly by favourable 'wall–wall' overlaps rather than an open metal site.[5]

Preliminary DFT calculations were performed on modelled bimetallic paddlewheel clusters to provide insight into the hydrogen affinity observed in the bimetallic MOPs. Clusters comprised of Pd^{II}–M^{II} metals bridged by four formate ligands were optimized using Gaussian09 software with PBE0 and B97D3 functionals paired with the TZDVP basis set; a detailed description of this methodology is provided in the ESI.† The calculated parameters of water solvated optimised structures (Table S4, ESI†), showed excellent agreement with the experimental data, with only subtle structural changes observed for the optimized desolvated MOPs. A strong anti-bonding component was observed for the highest occupied molecular orbitals (HOMOs) (Fig. S15, ESI†), which supports previous suggestions that the metal centres do not interact in the bimetallic paddlewheels.[24] For the NiPd(L) paddlewheel there are two possible spin states and comparison of a number of DFT functionals suggest that the high-spin (HS) complexes are more energetically favourable. However, we note that DFT methods must be used with caution in this application and as a result we calculated the hydrogen affinity for both spin states.[28] For the bimetallic formate clusters no appreciable interaction between the Pd^{II} site and H_2 was

found. In contrast, H_2 showed a strong affinity for each of the M^{II} sites that followed the trend: Ni(HS) > Zn > Cu > Ni(LS), (Table S9, ESI†). Exceptionally high interaction energies, *ca.* −11.4 kJ mol^{-1}, were observed for the Ni^{II} high-spin structure. This can be explained by the partial occupation of σ* orbitals present that are able to stabilize the adsorption of H_2 through a Kubas-type bonding.[29] Indeed, this observation accounts for the substantially lower interaction energy (−2.04 kJ mol^{-1}) for low-spin Ni which cannot support Kubas-type bonding. The H_2–Zn and H_2–Cu interaction energies depend on the magnitude of partial positive charge on the metal (Table S11, ESI†) that produces an attractive polarizing binding site for H_2. This theoretical data is in good agreement with the experimental results obtained for ZnPd(L) and NiPd(L) but not CuPd(L). The discrepancy between the calculated and experimental data for CuPd(L) suggests that the H_2 adsorption enthalpies are dominated by the pore structure rather than by specific interactions with the open metal sites. This is supported by the adsorption data which clearly demonstrates the porosity of CuPd(L) is distinct from the ZnPd(L) and NiPd(L) analogues.

In summary, a series of permanently porous heterometallic MOPs have been synthesized. The reaction of H_2L with bimetallic Pd^{II}–M^{II} (M = Ni, Cu or Zn) paddlewheel acetates produces discrete cage molecules of cuboctahedral geometry. Structural determination reveals preferential localisation of the Pd^{II} ions to the cage interior, while the relevant first row M^{II} species are predominantly positioned on the cage periphery. Careful activation of these molecules yields cages with an external surface decorated with co-ordinatively unsaturated metal sites for interaction with gas molecules in the solid-state. H_2 gas adsorption experiments, combined with DFT modelling, show that these accessible M^{II} sites allow for high hydrogen adsorption enthalpies in excess of −12 kJ mol^{-1} for NiPd(L). These novel framework building blocks are poised for further exploration. For example, we are currently assessing potential the Pd^{II} site for catalysis.

This research is supported by the Science and Industry Endowment Fund (SIEF). CJD and CJS would like to acknowledge the Australian Research Council for funding FT100100400 and FT0991910, respectively. Aspects of this research were undertaken on the MX beamlines at the Australian Synchrotron, Victoria, Australia.

Notes and references

1 (*a*) B. L. Chen, N. W. Ockwig, A. R. Millward, D. S. Contreras and O. M. Yaghi, *Angew. Chem., Int. Ed.*, 2005, **44**, 4745–4749; B. L. Chen, N. W. Ockwig, A. R. Millward, D. S. Contreras and O. M. Yaghi, *Angew. Chem., Int. Ed.*, 2005, **44**, 4745–4749; (*b*) S. Xiang, W. Zhou, J. M. Gallegos, Y. Liu and B. Chen, *J. Am. Chem. Soc.*, 2009, **131**, 12415–12419; (*c*) Z. Zhang, S. Xiang and B. Chen, *CrystEngComm*, 2011, **13**, 5983–5992; (*d*) M. Dincă and J. R. Long, *Angew. Chem., Int. Ed.*, 2008, **47**, 6766–6779; (*e*) O. Kozachuk, I. Luz, F. X. Llabrés i Xamena, H. Noei, M. Kauer, H. B. Albada, E. D. Bloch, B. Marler, Y. Wang, M. Muhler and R. A. Fischer, *Angew. Chem., Int. Ed.*, 2014, **53**, 7058–7062; (*f*) A. A. Talin, A. Centrone, A. C. Ford, M. E. Foster, V. Stavila, P. Haney, R. A. Kinney, V. Szalai, F. El Gabaly, H. P. Yoon, F. Léonard and M. D. Allendorf, *Science*, 2014, **343**, 66; (*g*) P. Mahato, A. Monguzzi, N. Yanai, T. Yamada and N. Kimizuka, *Nat. Mater.*, 2015, **14**, 924–930; (*h*) K. Liang, R. Ricco, C. M. Doherty, M. J. Styles, S. Bell, N. Kirby, S. Mudie, D. Haylock, A. J. Hill, C. J. Doonan and P. Falcaro, *Nat. Commun.*, 2015, **6**, 7240.
2 N. L. Rosi, J. Kim, M. Eddaoudi, B. Chen, M. O'Keeffe and O. M. Yaghi, *J. Am. Chem. Soc.*, 2005, **127**, 1504–1518.
3 E. Tsivion, J. R. Long and M. Head-Gordon, *J. Am. Chem. Soc.*, 2014, **136**, 17827–17835.
4 S. Bordiga, L. Regli, F. Bonino, E. Groppo, C. Lamberti, B. Xiao, P. S. Wheatley, R. E. Morris and A. Zecchina, *Phys. Chem. Chem. Phys.*, 2007, **9**, 2676–2685.
5 J. L. C. Rowsell and O. M. Yaghi, *J. Am. Chem. Soc.*, 2006, **128**, 1304–1315.
6 O. K. Farha and J. T. Hupp, *Acc. Chem. Res.*, 2010, **43**, 1166–1175.
7 J. J. Perry IV, J. A. Perman and M. J. Zaworotko, *Chem. Soc. Rev.*, 2009, **38**, 1400–1417.
8 S. L. James, *Chem. Soc. Rev.*, 2003, **32**, 276–288.
9 F. N. Dai, H. Y. He, D. L. Gao, F. Ye, X. L. Qiu and D. F. Sun, *CrystEngComm*, 2009, **11**, 2516–2522.
10 J. R. Li, R. J. Kuppler and H. C. Zhou, *Chem. Soc. Rev.*, 2009, **38**, 1477–1504.
11 R. Yepez, S. Garcia, P. Schachat, M. Sanchez-Sanchez, J. H. Gonzalez-Estefan, E. Gonzalez-Zamora, I. A. Ibarra and J. Aguilar-Pliego, *New J. Chem.*, 2015, **39**, 5112–5115.
12 M. Položij, E. Pérez-Mayoral, J. Čejka, J. Hermann and P. Nachtigall, *Catal. Today*, 2013, **204**, 101–107.
13 S. Naito, T. Tanibe, E. Saito, T. Miyao and W. Mori, *Chem. Lett.*, 2001, 1178–1179.
14 O. Kozachuk, K. Yusenko, H. Noei, Y. Wang, S. Walleck, T. Glaser and R. A. Fischer, *Chem. Commun.*, 2011, **47**, 8509–8511.
15 Y. Ke, D. J. Collins and H.-C. Zhou, *Inorg. Chem.*, 2005, **44**, 4154–4156.
16 E.-Y. Choi, P. M. Barron, R. W. Novotny, H.-T. Son, C. Hu and W. Choe, *Inorg. Chem.*, 2009, **48**, 426–428.
17 K. Tan, P. Canepa, Q. Gong, J. Liu, D. H. Johnson, A. Dyevoich, P. K. Thallapally, T. Thonhauser, J. Li and Y. J. Chabal, *Chem. Mater.*, 2013, **25**, 4653–4662.
18 Q. Yao, J. Sun, K. Li, J. Su, M. V. Peskov and X. Zou, *Dalton Trans.*, 2012, **41**, 3953–3955.
19 M. Dincă and J. R. Long, *J. Am. Chem. Soc.*, 2007, **129**, 11172–11176.
20 N. S. Akhmadullina, N. V. Cherkashina, N. Y. Kozitsyna, I. P. Stolarov, E. V. Perova, A. E. Gekhman, S. E. Nefedov, M. N. Vargaftik and I. I. Moiseev, *Inorg. Chim. Acta*, 2009, **362**, 1943–1951.
21 P. Day, A. F. Orchard, A. J. Thomson and R. J. P. Williams, *J. Chem. Phys.*, 1965, **42**, 1973–1981.
22 A. J. Blake, N. R. Champness, P. Hubberstey, W.-S. Li, M. A. Withersby and M. Schröder, *Coord. Chem. Rev.*, 1999, **183**, 117–138.
23 T. Akitsu, *Polyhedron*, 2007, **26**, 2527–2535.
24 A. A. Markov, A. P. Klyagina, S. P. Dolin, N. S. Akhmadullina, N. Y. Kozitsyna, N. V. Cherkashina, S. E. Nefedov, M. N. Vargaftik and I. I. Moiseev, *Russ. J. Inorg. Chem.*, 2009, **54**, 885–892.
25 J.-R. Li and H.-C. Zhou, *Nat. Chem.*, 2010, **2**, 893–898.
26 F.-R. Dai, U. Sambasivam, A. J. Hammerstrom and Z. Wang, *J. Am. Chem. Soc.*, 2014, **136**, 7480–7491.
27 J. G. Vitillo, L. Regli, S. Chavan, G. Ricchiardi, G. Spoto, P. D. C. Dietzel, S. Bordiga and A. Zecchina, *J. Am. Chem. Soc.*, 2008, **130**, 8386–8396.
28 J. Harvey, *Principles and Applications of Density Functional Theory in Inorganic Chemistry I*, Springer, Berlin, Heidelberg, 2004, ch. 4, vol. 112, pp. 151–184.
29 G. J. Kubas, *Chem. Rev.*, 2007, **107**, 4152–4205.

Journal of Materials Chemistry A

PAPER

View Article Online
View Journal | View Issue

Cite this: J. Mater. Chem. A, 2015, 3, 15241

AIMs: a new strategy to control physical aging and gas transport in mixed-matrix membranes†‡§

Melanie Kitchin,[ab] Jesse Teo,[b] Kristina Konstas,[a] Cher Hon Lau,[ab] Christopher J. Sumby,[b] Aaron W. Thornton,[a] Christian J. Doonan*[ab] and Matthew R. Hill*[ab]

Received 30th March 2015
Accepted 19th June 2015

DOI: 10.1039/c5ta02286j

www.rsc.org/MaterialsA

The effect of controlling interactions between the components in a mixed-matrix membrane at the molecular level has been explored. A systematic series of soluble metal–organic polyhedra (MOPs) of varying external organic chain length were prepared and applied within polymer membranes to produce anti-aging intercalated membranes (AIMs). Use of a soluble porous additive allowed for intimate mixing between the polymer and the porous additive, eliminating the formation of non-selective gas transport voids at the interface, typically found in traditional mixed-matrix membranes. Moreover, the molecular interaction thus created provided a valuable tool for tailoring the physical aging rates of the membranes. Aging was slowed by a factor of three with the optimal ^{t}Bu-MOP additive, and viscosity measurements revealed they held the strongest MOP–polymer interaction, confirming the utility of the AIMs approach. MOP loading was therefore able to be optimized for the maximum anti-aging effect by monitoring the relative change in viscosity. Absolute gas permeability scaled with the MOP external organic chain length, revealing solubility-driven diffusion.

The realization of polymer-based membrane technologies in industrial applications requires sustainable performance of a material over an extended period of time. Unfortunately, the polymeric structures that demonstrate the most attractive initial permeability and selectivity properties are marred by physical aging processes that reduce fractional free volume content and increase chain packing density[1] as large cavities collapse towards an unattainable thermodynamic equilibrium.[2]

Given the potential application of polymeric membranes in low-energy separation processes, there has been a large amount of research aimed at locking as-cast polymers into place to retain initial high fractional free volume content, offsetting physical aging. One approach has been to post-synthetically pyrolyse precursor polymers at high temperatures to rigidify polymer chains and form dense carbon molecular sieves.[3] Another approach has been to use additives such as nanoparticles or microporous fillers, to prop open and increase transport pathways. Such composite materials, known as mixed-matrix membranes ('MMMs') have been prepared using metal–organic frameworks (MOFs), zeolitic imidazolate frameworks (ZIFs) and fused silica as the inorganic additive,[4,5] to mixed success. MOF-based MMMs are based around the adsorption and diffusion behaviour of gas molecules through the embedded MOFs rather than retaining the size-sieving properties of the surrounding polymer. As the polymer chains relax, access to the MOF pores throughout the film is restricted.

Another challenge faced by MOF- and ZIF-based MMMs is that of poor dispersion of, and in many cases interaction between, polymer and additive materials.[6] Poor adhesion at the additive–polymer interface generates voids that compromise membrane selectivity, thereby limiting industrial feasibility (Fig. 1).

Therefore, new additives that give rise to more intimate interactions with the polymer matrix are desirable for improving gas transport[7,8] and the rate of physical aging.[9] Adhesion between the additive and the matrix has previously been achieved using interfacial agents, modified particle surfaces, and ionic liquids.[6,10,11] We recently reported[9] that physical aging could be addressed through a strong interaction of the carbonaceous pores of PAF-1 [12] with polymer side-chains.

Unlike porous aromatic frameworks, MOFs and other related extended nanoporous frameworks, metal organic polyhedra (MOPs) are comprised of individual porous molecular cages.[13] As demonstrated by Balkus *et al.* their discrete molecular nature makes them amenable to solution processing, and as a result they can be homogeneously dispersed within the host

[a]Manufacturing, CSIRO, Bayview Avenue, Clayton, VIC, 3168, Australia. E-mail: Christian.Doonan@adelaide.edu.au; Matthew.Hill@csiro.au
[b]Centre for Advanced Nanomaterials, The School of Chemistry & Physics, The University of Adelaide, Adelaide, SA, 5005, Australia

† MRH acknowledges FT1300345. Parts of this work were funded by the Science and Industry Endowment Fund (SIEF).
‡ The manuscript was written through contributions of all authors. All authors have given approval to the final version of the manuscript.
§ Electronic supplementary information (ESI) available. See DOI: 10.1039/c5ta02286j

View Article Online
Journal of Materials Chemistry A Paper

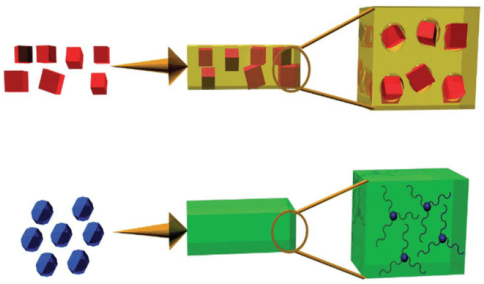

Fig. 1 Use of the soluble metal organic polyhedra (MOPs) in mixed matrix membranes (bottom) allows for intercalation that addresses physical aging, as opposed to the nonselective transport pathways created by insoluble additives such as MOFs (top).

polymer.[14] This offers the potential for a better interface to be formed, leading to enhanced gas transport properties and other effects.

Super glassy polymers such as polyacetylenes demonstrate attractive initial permeability and selectivity properties, ease of processability and a capacity to be produced at industrial scale. However, as mentioned above, the industrial viability of this class of polymers is impaired by rapid physical aging processes.[1,15] For example, the CO_2 permeability of the super glassy polymer poly(1-trimethylsilyl-1)propyne (PTMSP) decreases to 27% of its as-cast value over one year (29 796 Barrer to 8045 Barrer) (Fig. 5(a) and (b)) as the large cavities collapse towards an unattainable thermodynamic equilibrium.[15]

Here, we explore a new form of molecular interaction within PTMSP-based mixed-matrix membranes. A systematic series of MOPs with varying extrinsic organic chain lengths were synthesized (Fig. 2). Each MOP is of the general form $[Cu_{24}(A)_{24}(S)_{24}]\cdot x$S, where A represents one of four aromatic di-acid ligands, S represents a solvent molecule. Each of the di-acids can be differentiated by their side chain chemistry and chain length: (a) non-polar *tert* butyl (^{t}Bu MOP; Fig. 2(c)); (b) polar diethylene glycol (DEG MOP; Fig. 2(d)); (c) polar tri-ethylene glycol (TEG MOP; Fig. 2(e)) and non-polar dodecane (MOP-18; Fig. 2(f)). The ^{t}Bu MOP,[16] the DEG MOP[17] and MOP-18 [18] have been reported previously. The TEG MOP is a novel structure; differing from the DEG MOP, and the related tetra-ethylene glycol MOP[19] by one ethylene glycol group per di-acid ligand. Synthetic conditions and analytical data for the TEG MOP are available in the ESI.§

The nanoporous additives comprised of shorter side-groups were found to allow intercalation of polymer chains into the MOP pores, producing anti-aging intercalated membranes (AIMs) that exhibited superior anti-aging properties. The effect of polymer intercalation on the physical properties of the bulk of the polymer matrix was investigated using conventional analytical techniques. Of note, viscosity measurements provided a probing measure of additive–polymer interactions in solution form, and enabled additive loading optimization to

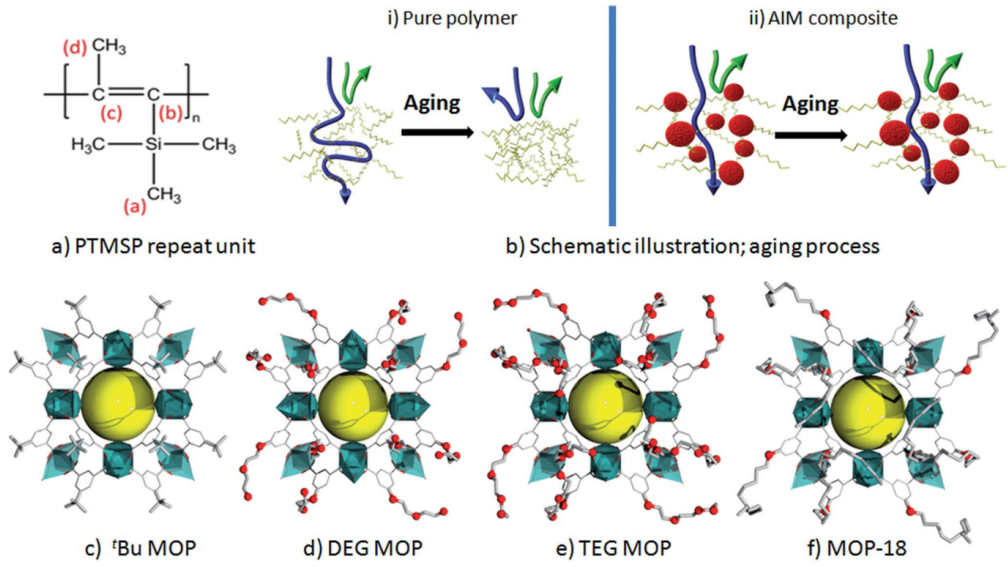

Fig. 2 (a) PTMSP repeat unit; (b) schematic illustrations of (i) pure polymer membrane exhibiting packing of polymer chains after aging, and (ii) MOP–MMM composite that prevents chain relaxation, maintaining membrane permeability; (c) ^{t}Bu MOP; (d) DEG-MOP; (e) TEG-MOP; and (f) MOP-18.

maximize anti-aging properties of the most successful AIM composition.

Experimental

MOP–PTMSP mixed-matrix membranes were produced through slow solvent evaporation following extensive pre-stirring of MOP–polymer solutions. Uniform distribution of MOP nanoparticles throughout the polymer matrix was confirmed using energy-dispersive X-ray spectroscopy (EDX) and focused ion beam scanning electron microscopy (FIB-SEM) (Fig. 4).

PTMSP was purchased from Gelest Inc. (Morrisville PA, USA) and used without purification. Chloroform was purchased from Sigma-Aldrich.

5 wt%, 10 wt%, 15 wt%, 20 wt%, 25 wt% and 30 wt% MOP + PTMSP membranes were fabricated through a typical spin casting method. The following is an example, for the 5 wt% loaded film.

200 mg PTMSP was placed in a 20 mL vial with 5 g chloroform and an egg-shaped stirrer bar and stirred overnight. A 10 mg ^{t}Bu MOP sample was placed in a separate 20 mL vial with 5 g chloroform and an egg-shaped stirrer bar. Each vial was closed and stirred for 24 hours under ambient conditions. Following this, the ^{t}Bu MOP–chloroform solution was added to the vial containing the stirred PTMSP–chloroform solution, and the mixed solution stirred for a further 24 hours under ambient conditions. ~100 micron films were formed *via* solution casting at ambient conditions. The membrane films were dried in a vacuum oven at 40 °C for 12 hours prior to single gas permeability measurements. Film thicknesses were measured using a Measumax digital micrometer.

Characterization methods

Scanning electron microscopy (SEM) was performed on a JEOL JEM 2100F TEM/SEM operated at 200 kV. EDS spectra were obtained using a JEOL 50 m^2 Si(Li) detector. FIB-SEM images were obtained at the Melbourne Centre for Nanofabrication. WAX experiments were performed on the SAX/WAX beamline at the Australian Synchrotron, Clayton, Victoria, Australia. Viscosity measurements were performed using an Ubbelohde viscometer at 25 °C, and calculated based on the ATSM D445 standard.

Results and discussion

One indicator of a beneficial polymer–particle interaction in a mixed-matrix membrane is the viscosity of a precursor solution. The viscosity of nanoparticle-filled polymer solutions drop in comparison to pure polymer melts where polymer chains can tether to the surface of the nanoporous additives and confine polymer chains within the mixed matrix.[20,21] Such an interaction involves an attraction between similar chemical groups of the polymer and additives that decreases the interchain entanglement of the bulk polymer solution.

To probe the extent of polymer–MOP interaction, viscosity tests were undertaken using an Ubbelohde Viscometer on pure PTMSP and additive–polymer blends stirred for 24 hours. This characterization technique has been used for several nanoparticle–membrane composites involving PAF-1, UiO-66 and fused silica as nanoporous additives.[9] These studies found that non-Newtonian behavior can arise in three situations: (1) where extra free volume is introduced;[20] (2) where polymer chains adsorb to the surface of the additive, decreasing polymer chain entanglement;[21] and (3) where polymer chains thread into the additives' pores.[21] In our previous work, we found that only in the case of the third interaction, that is, where polymer chains can thread into the additives' pores, is physical aging halted.[9,22]

The addition of MOPs with smaller chain lengths (^{t}Bu and DEG) led to an additive–polymer solution viscosity lower than that of pure PTMSP (11.725 cP and 12.244 cP compared to 12.733 cP) (Fig. 3(a)). The TEG + PTMSP blend was found to have a viscosity slightly above that of pure PTMSP (12.882 cP) In contrast, the MOP-18 + PTMSP blend was found to have a much higher viscosity (13.188 cP) than that of pure PTMSP (Fig. 3(a)).

The reduction in additive–polymer viscosity of solutions with smaller MOP side-chain lengths (^{t}Bu, DEG) indicates an interaction between additives and polymer chains. When compared with the anti-aging properties of the resulting films (Fig. 5(a) and (b)), we speculate that this decrease in viscosity results from

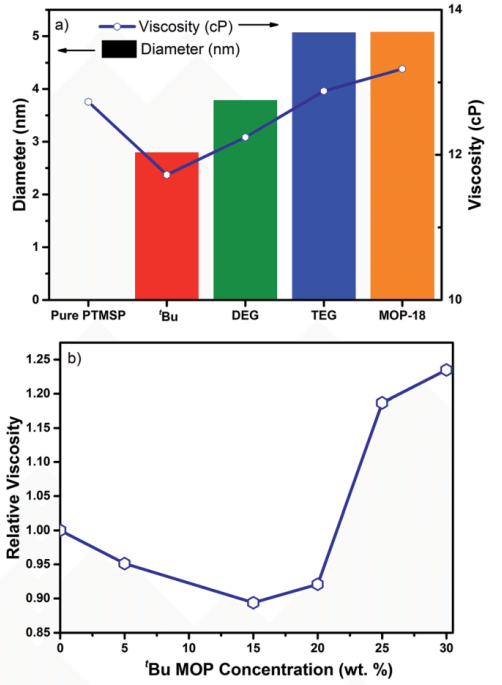

Fig. 3 (a) MOP–PTMSP solution viscosities (centiPoise) *vs.* MOP diameters; (b) ^{t}Bu MOP–PTMSP viscosities (centiPoise).

a decrease in inter-chain coupling of polymer chains through intercalation of polymer chains into the MOP pores. In contrast, the increase in viscosity of the 20 wt% MOP-18 + PTMSP blend, and the absence of anti-aging properties in the resulting membrane, suggests no interdigitation of polymer chains into the pores of the MOP.

The decrease in viscosity of the 20 wt% ^{t}Bu and DEG + PTMSP solutions can be explained through the concept of preferential tethering of polymer chains of higher molecular weight into the MOP pores, which leaves the lower molecular mass chains to constitute the bulk of the polymer matrix. This selective physisorption of high molar mass polymer fractions onto nanoporous additives is well documented.[23,24] Further, the resulting reduction in entanglement density of the lower molecular weight polymer bulk reduces viscosity through an increase in polymer flow.[25]

In this work, we also observed the concentration of nanoporous materials to have a significant effect on additive–polymer solution viscosities and resulting membrane properties. An increase in loading concentration of ^{t}Bu was found to decrease viscosities up to a minimum of 15 wt%. Above 20 wt%, loading, viscosity greatly increased (Fig. 3(b)).

Pore architecture effects of ^{t}Bu additives were studied with wide-angle X-ray scattering (WAXS) (Fig. 4(c)). Diffraction data of doped samples aged for 365 days was compared to that of pure PTMSP, and cross referenced with PTMSP WAX data found in literature.[26] The major peak at 9.8° corresponds to the small, channel-like cavities that have been found to be the transport pathway for gas molecules.[2] The smaller peaks at higher angles have been attributed to supramolecular ordering in PTMSP, arising from inter-chain spacing.[26] Importantly, the number of small holes decreases in the 5 wt% and 30 wt% samples over time, as indicated by the lower area under these peaks, and as represented by reduced gas permeabilities in these aged samples. Conversely, for the 20 wt% doped sample a large number of pores was maintained over time, as represented by the large area under the lower-angle peak.

The single gas permeabilities and ideal selectivities of MOP-loaded films taken of freshly-cast polymers and again after one year of exposure to the atmosphere can be seen in Fig. 5(a) and S3–S7.§ The corresponding data for a film of pure PTMSP treated under the same conditions is also provided for comparison.

The initial CO_2 permeabilities of 20 wt% loaded ^{t}Bu + PTMSP, DEG + PTMSP and TEG + PTMSP films are comparable, each being approximately 5000 Barrer lower than that of pure PTMSP (Fig. 5(a)). Altering MOP loadings of the ^{t}Bu series also had a negligible effect on initial permeabilities (Fig. 5(b)). This suggests that permeation is controlled by the polymer rather than the MOP additives, with pores of each MOP being inaccessible to these gases over the pressure range studied. On the contrary, the initial permeability of 20 wt% MOP-18 + PTMSP is much lower than that of pure PTMSP (Fig. 5(a)). This is attributed to the presence of the long dodecane chains of the MOP-18

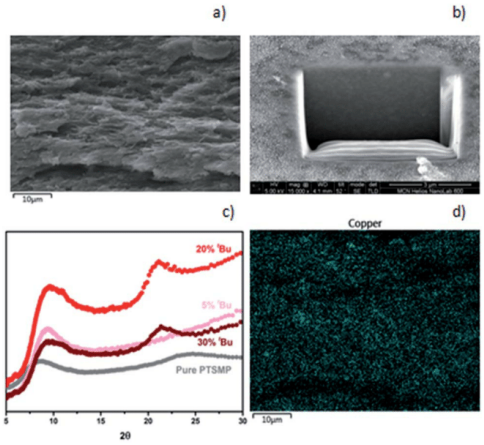

Fig. 4 (a) FIB-SEM of a milled 20 wt%-doped ^{t}Bu PTMSP membrane showing uniform dispersion of MOP nanoparticles (b) EDX data of a 20 wt% ^{t}Bu loaded PTMSP membrane, (c) WAX data of ^{t}Bu PTMSP samples. (d) EDS spectra of the cross section of a 20 wt% ^{t}Bu + PTMSP film showing even dispersion of MOP particles throughout the film.

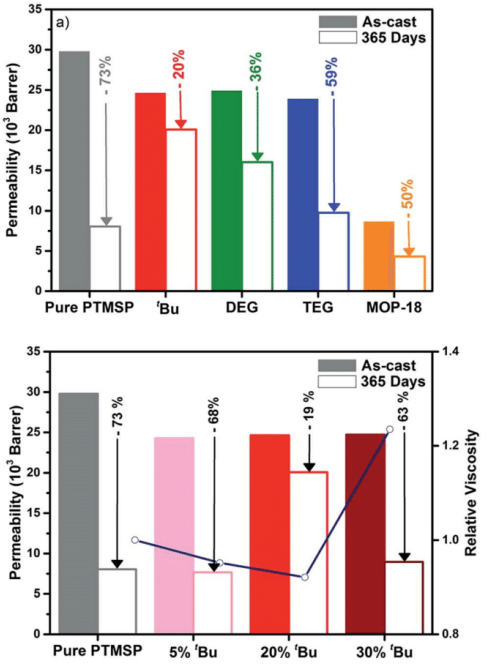

Fig. 5 (a) CO_2 permeability properties of 20 wt% MOP-loaded PTMSP membranes as cast *vs.* 365 days; (b) CO_2 permeability properties of ^{t}Bu–PTMSP membranes of different dopant loadings as cast *vs.* 365 days.

side groups, which block polymer pores, obstructing gas pathways.[14]

Addition of 20 wt% ^{t}Bu, DEG and TEG MOPs stopped the aging of PTMSP, to different degrees. Of the AIMs investigated, the 20 wt% loading of ^{t}Bu was most successful at freezing the super-glassy polymer in its initial state, with CO_2 permeability reducing to only 81% of its as-cast value over one year (Fig. 5(a)). This represents a 250% improvement when compared with the CO_2 permeability of a pure PTMSP film after one year (27% of its as-cast value). The DEG + PTMSP film, loaded with the shorter ethylene glycol-based MOP, had a greater anti-aging effect than the longer TEG + PTMSP film, with the CO_2 permeability of each reducing to 64% and 41% respectively (Fig. 5(a)). The CO_2 permeability of the MOP-18 + PTMSP film decreased to 50% of its as-cast value, which, given the low as-cast properties of the film, represents a permeability lower than that of pure PTMSP (Fig. 5(a)).

With the exception of MOP-18 + PTMSP, the selectivity of the MOP + PTMSP films changed proportionately over the space of a year, increasing as permeability decreased (Fig. S3–S7§). The change in CO_2/CH_4 selectivity of MOP-18 + PTMSP deviated from that of both the MOP-loaded films and the pure PTMSP film, showing a higher relative selectivity for CH_4 than that of the other films investigated, and therefore a decrease in selectivity despite the lower permeability of the aged film. This suggests that the CH_4 molecules compete for the sorption sites associated with MOP-18 alkyl chains in the polymer blend.[14]

Notably, the different chemical nature of the non-polar saturated hydrocarbons and the polar polyethylene glycol side chains did not dominate the aging properties of the MOP-loaded films. These results suggest that PTMSP–MOP pore intercalation is dominated by the length, rather than chemistry, of the additive side chain.

The kinetics of physical aging in a polymer is closely related to the molecular mobility of the polymer chains in the glassy state.[27,28] The preferential tethering of high molecular weight polymer chains into the pores of the ^{t}Bu, DEG and TEG + PTMSP solutions can therefore be regarded as complementing the observed anti-aging properties of their corresponding films. Confinement of these larger chains leaves those chains of lower molecular weight to make up the bulk of the polymer matrix. Polymer chains of lower molecular weight exhibit less flexibility than that of longer polymer chains, and as a result do not have the conformational freedom to relax into a more dense packing state. As observed from the permeability of aged ^{t}Bu + PTMSP, DEG + PTMSP and TEG + PTMSP films, this confinement of higher molecular mass polymer chains leads to a decrease in physical aging, resulting in less dense polymer films over time when compared to the 20 wt% MOP-18 + PTMSP and pure PTMSP films.

The concept of optimal loading fractions in polymer melts has been reported for several decades, and can be explained through a study of polymer interactions and interparticle distances.[20,29] Whereas intercalated polymer chains are rigidified, free polymer chains retain conformational flexibility, which drives physical aging. At additive concentrations below the percolation threshold, the relative number of intercalated polymer chains is low, and a large amount of the polymer bulk consists of free, large polymer chains. A reduction in chain entanglement of the resulting bulk solution results in a decrease in viscosity relative to pure PTMSP, as observed in Fig. 2(a). The reduction in chain entanglement of the bulk solution also loosens steric hindrances on the rotational motions of these free polymer chain side groups. This allows for greater chain flexibility, and therefore aging of the low-loaded films, as observed in Fig. 5(b).[30]

At an optimal loading concentration, all large polymer chains are intercalated. The lower viscosity of the solution can therefore be explained in terms of a further decrease in chain entanglements (Fig. 2(b)). The absence of free polymer chains also explains the suppression of physical aging in the 20 wt% loaded film, as polymer flexibility is restrained (Fig. 5(a) and (b)).

Above this optimal loading concentration, the MOP interparticle distances are reduced, leading to entanglement of intercalated chains. This results in a large increase in the viscosity, as observed in the 30 wt% loaded solution (Fig. 2(b)). Further, MOP interparticle distances are greatly reduced, and given the insufficient polymer chains present to fully interact with the MOP particles, multiple interactions with adjacent nanoparticles is possible.[31] The entanglement of intercalated chains into neighbouring MOPs allows aggregation of the additives, resulting in a reduction of polymer free volume and decreasing membrane permeability (Fig. 5(b)).

Mathematical modeling was used to further substantiate our results. Effective size calculations were carried out, which consider the van der Waals radii of each atom, as defined according to Bondi.[32] The trimethylsilyl (TMS) side group of PTMSP has an effective size of 6.3 Å. The effective size of the outer cavity of the ^{t}Bu MOP is 10 Å, suggesting that the trimethylsilyl side groups of the PTMSP polymer can intercalate into ^{t}Bu MOP pores, forming an interlocked configuration (Fig. 6).

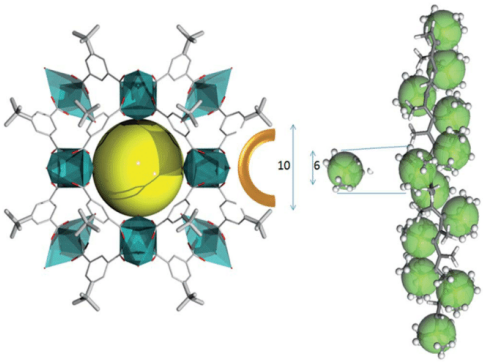

Fig. 6 The largest ^{t}Bu MOP pore windows are large enough (13.671 Å) to allow intercalation of PTMSP trimethylsilyl groups into the MOP pore.

Conclusions

Introducing MOP nanoparticles as inorganic additives, we synthesized a series of related AIMs. Varying the length and chemistry of nanoparticle side-groups allowed us probe the polymer–additive interfacial conditions required to allow for beneficial, non-covalent molecular interlocking of polymer chains. The effect of polymer intercalation on the physical properties of the bulk of the polymer matrix was also investigated.

Superior dispersion of MOP nanoparticles throughout PTMSP was observed using EDX and FIB-SEM. The large surface area to volume ratios of MOP nanoparticles was found to allow for increased interaction between polymer chains and nanoparticle pores. Viscosity results suggest a correlation between additive side-chain length and polymer chain interaction, with smaller side-chains of the ^{t}Bu nanoparticles allowing greater intercalation of the polymer chains into the MOP pores. No trend in polymer–additive interfacial properties was observed in relation to nanoparticle side-group chemistry. Comparing viscosity results with permeabilities of fresh and aged samples, it appears that the greater this intercalation, the more fractional free volume that is retained over time. Through comparison of different MOP loading concentrations, it was found that a decrease in interchain entanglement of polymer solutions resulting from preferential tethering of higher molecular weight polymer chains leads to a reduction in polymer aging, as smaller, less flexible chains remaining in the polymer bulk lack in conformational freedom required to relax into a more dense packing state.

Abbreviations

MOP	Metal-organic polyhedra
MMM	Mixed-matrix membrane
PTMSP	Poly(1-trimethylsilyl-1-propyne)

Acknowledgements

Parts of this work were conducted on the SAXS Beamline at the Australian Synchrotron and the Melbourne Centre for Nanofabrication. The authors acknowledge Dr Cameron Way for assistance with viscosity measurements.

Notes and references

1 H. B. Park, C. H. Jung, Y. M. Lee, A. J. Jill, S. J. Pas, S. T. Mudie, E. V. Wagner, B. D. Freeman and D. J. Cookson, *Science*, 2007, **318**, 254–258.
2 K. Nagai, T. Masuda, T. Nakagawa, B. D. Freeman and I. Pinnau, *Prog. Polym. Sci.*, 2001, **26**, 721–798.
3 S. Fu, E. S. Sanders, S. S. Kulkarni and W. J. Koros, *J. Membr. Sci.*, 2015, **487**, 60–73.
4 D. M. D'Alessandro, B. Smit and J. R. Long, *Angew. Chem., Int. Ed.*, 2010, **49**, 6058–6082.
5 T. C. Merkel, L. G. Toy, A. L. Andrady, H. Gracz and E. O. Stejksal, *Macromolecules*, 2003, **36**, 353–358.
6 Y. C. Hudiono, T. K. Carlisle, J. E. Bara, Y. Zhang, D. L. Gin and R. D. Noble, *J. Membr. Sci.*, 2010, **350**, 117–123.
7 T. C. Merkel, B. D. Freeman, R. J. Spontak, Z. He, I. Pinnau, P. Meakin and A. J. Hill, *Science*, 2002, **19**, 519–522.
8 G. Dong, H. Li and V. Chen, *J. Mater. Chem. A*, 2013, **1**, 4610–4630.
9 (*a*) C. H. Lau, P. T. Nguyen, M. R. Hill, A. W. Thornton, K. Konstas, C. M. Doherty, R. J. Mulder, L. Bourgeois, A. C. Y. Yiu, D. J. Sprouster, J. P. Sullivan, T. J. Bastow, A. J. Hill, D. L. Gin and R. D. Noble, *Angew. Chem., Int. Ed.*, 2014, **53**, 5322–5326; (*b*) C. H. Lau, K. Konstas, C. M. Doherty, S. Kanehashi, B. Ozcelik, S. E. Kentish, A. J. Hill and M. R. Hill, *Chem. Mat.*, 2015, DOI: 10.1021/acs.chemmater.5b01537.
10 S. Shu, S. Husain and W. J. Koros, *J. Phys. Chem. C*, 2007, **111**, 652–657.
11 J. S. Wall, B. Hu, J. A. Siddiqui and R. M. Ottenbrite, *Langmuir*, 2001, **17**, 6027–6029.
12 T. Ben, H. Ren, S. Ma, D. C. Prof, J. Lan, X. Jing, W. Wang, J. Xu, F. Deng, J. M. Simmons, S. Qiu and G. Zhu, *Angew. Chem., Int. Ed.*, 2009, **48**, 9457–9460.
13 M. Eddaoudi, J. Kim, J. B. Wachter, H. K. Chae, M. O'Keeffe and O. M. Yaghi, *J. Am. Chem. Soc.*, 2001, **123**, 4368–4369.
14 E. V. Perez, K. J. Balkus, J. P. Ferraris and I. H. Musselman, *J. Membr. Sci.*, 2014, **463**, 82–93.
15 K. Nagai, T. Masuda, T. Nakagawa, B. D. Freeman and I. Pinnau, *Prog. Polym. Sci.*, 2001, **26**, 721–798.
16 J.-R. Li and H.-C. Zhou, *Nat. Chem.*, 2010, **2**, 893–898.
17 M. Tonigold and D. Volkmer, *Inorg. Chim. Acta*, 2010, **363**, 4220–4229.
18 H. Furukawa, J. Kim, K. E. Plass and O. M. Yaghi, *J. Am. Chem. Soc.*, 2006, **128**, 8398–8399.
19 M. S. Tonigold, *Novel Copper- and Cobalt-based Metal-Organic Polyhedra and Frameworks: Synthesis, Structure, Properties and Applications*, Ulm University, 2011.
20 M. E. Mackay, T. T. Dao, A. Tuteja, D. L. Ho, B. V. Horn, H.-C. Kim and C. J. Hawker, *Nat. Mater.*, 2003, **2**, 762–766.
21 S. Jain, J. G. P. Goossens, G. W. M. Peters, M. V. Duin and P. J. Lemstra, *Soft Matter*, 2008, **4**, 1848–1854.
22 C. H. Lau, K. Konstas, A. W. Thornton, A. C. Liu, S. Mudie, D. F. Kennedy, S. C. Howard, A. J. Hill and M. R. Hill, *Angew. Chem., Int. Ed.*, 2015, **54**, 2669–2673.
23 F. H. J. Maurer, H. M. Schoffeleer, R. Kosfeld and T. Uhlenbroich, *Progress in Science and Engineering of Composites*, ICCM-Iv, Tokyo, 1982.
24 R. E. Felter, E. S. Moyer and Z. N. Ray, *J. Polym. Sci., Part B: Polym. Lett.*, 1969, **7**, 529–533.
25 O. Kramer, V. Ty and J. D. Ferry, *Proc. Natl. Acad. Sci. U. S. A.*, 1972, **69**, 2216–2218.
26 Y. U. P. Yampol'skii, S. M. Shishatskii, V. P. Shantorovich, E. M. Antipov, N. N. Kuzmin, S. V. Rykov, V. L. Khodjaeva and N. A. Plate, *J. Appl. Polym. Sci.*, 1993, **48**, 1935–1944.
27 A. J. Kovacs, J. J. Aklonis, J. M. Hutchinson and A. R. Ramos, *J. Polym. Sci., Polym. Phys. Ed.*, 2003, **17**, 1097–1162.

28 V. M. Boucher, D. Cangialosi, A. Alegria, J. Colmenero, J. Gonzalez-Irun and L. M. Liz-Marzan, *Soft Matter*, 2010, **6**, 3306–3317.
29 R. K. Iler, *J. Colloid Interface Sci.*, 1971, **37**, 364–373.
30 I. M. Kalogeras and A. Vassilikou-Dova, *J. Phys. Chem. B*, 2001, **105**, 7651–7662.
31 T. Cosgrove, P. C. Griffiths and P. M. Lloyd, *Langmuir*, 1995, **11**, 1457–1463.
32 A. Bondi, *J. Phys. Chem.*, 1964, **68**, 441–451.